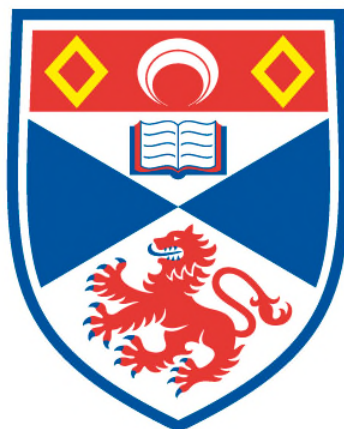


**SYNTHESIS AND CHARACTERIZATION OF CRYSTALLINE MICROPOROUS  
MATERIALS: INVESTIGATION OF NEW SYNTHETIC ROUTES**

**Yuyang Tian**

**A Thesis Submitted for the Degree of PhD  
at the  
University of St Andrews**



**2014**

**Full metadata for this item is available in  
St Andrews Research Repository  
at:**

**<http://research-repository.st-andrews.ac.uk/>**

**Please use this identifier to cite or link to this item:**

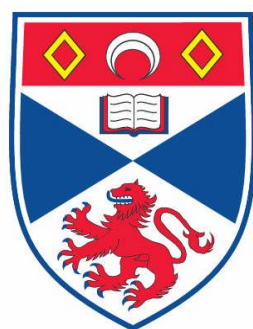
**<http://hdl.handle.net/10023/6371>**

**This item is protected by original copyright**

**This item is licensed under a  
Creative Commons Licence**

# Synthesis and Characterization of Crystalline Microporous Materials: Investigation of New Synthetic Routes

Yuyang Tian



This thesis is submitted in partial fulfilment for the degree of PhD  
at the  
University of St Andrews

April 2014

# Declarations

## 1. Candidate's declarations:

I, Yuyang Tian, hereby certify that this thesis, which is approximately 51000 words in length, has been written by me, and that it is the record of work carried out by me, or principally by myself in collaboration with others as acknowledged, and that it has not been submitted in any previous application for a higher degree.

I was admitted as a research student in September 2010 and as a candidate for the degree of PhD in September 2011; the higher study for which this is a record was carried out in the University of St Andrews between 2010 and 2014.

Date ..... signature of candidate .....

## 2. Supervisor's declaration:

I hereby certify that the candidate has fulfilled the conditions of the Resolution and Regulations appropriate for the degree of PhD in the University of St Andrews and that the candidate is qualified to submit this thesis in application for that degree.

Date ..... signature of supervisor .....

## 3. Permission for publication: *(to be signed by both candidate and supervisor)*

In submitting this thesis to the University of St Andrews I understand that I am giving permission for it to be made available for use in accordance with the regulations of the University Library for the time being in force, subject to any copyright vested in the work not being affected thereby. I also understand that the title and the abstract will be published, and that a copy of the work may be made and supplied to any bona fide library or research worker, that my thesis will be electronically accessible for personal or research use unless exempt by award of an embargo as requested below, and that the library has the right to migrate my thesis into new electronic forms as required to ensure continued access to the thesis. I have obtained any third-party copyright permissions that may be required in order to allow such access and migration, or have requested the appropriate embargo below.

The following is an agreed request by candidate and supervisor regarding the publication of this thesis:

**PRINTED COPY**

Embargo on all print copy for a period of 1 year on the following ground(s):

- Publication would preclude future publication

**ELECTRONIC COPY**

Embargo on all electronic copy for a period of 1 year on the following ground(s):

- Publication would preclude future publication

Date ..... signature of candidate .....

Date ..... signature of supervisor .....

## Courses Attended

The School of Chemistry at the University of St. Andrews requires that a postgraduate attend a number of taught courses. The courses attended were:

Nanostructural Materials	Prof. Wuzong Zhou and Prof. Manfred Buck
Electron Microscopy	Prof. Wuzong Zhou

## Publications

The Assembly-Disassembly-Organization-Reassembly Mechanism for 3D-2D-3D Transformation of Germanosilicate IWW Zeolite

Pavla Chlubná-Eliášová, **Yuyang Tian**, Dr. Ana B. Pinar, Dr. Martin Kubů, Prof. Jiří Čejka, Prof. Russell E. Morris. *Angew. Chem. Int. Ed.*, 2014, 53, 7048-7052.

Synthesis and structural characterization of a single-crystal to single-crystal transformable coordination polymer

**Yuyang Tian**, Phoebe K. Allan, Catherine L. Renouf, Xiang He, Laura J. McCormick, Russell E. Morris. *Dalton Trans.*, 2014, 43, 1519-1523.

Ionic Liquid assisted Synthesis of Zeolite-TON

**Yuyang Tian**, Matthew J. McPherson, Paul S. Wheatley, Russell E. Morris. *Z. Anorg. Allg. Chem.*, 2014, 640, 1177-1181.

## Acknowledgements

Firstly and foremost I would like to express my deepest gratitude to my supervisor, Prof. Russell Morris, for giving me the chance of studying under his supervision. I really appreciate his excellent guidance, encouragements and patience throughout my four-year study.

I also want to thank the Morris group members. My gratitude goes to Dr. Paul Wheatley, Dr. Laura McCormick, Dr. Morven Duncan and Dr. Stewart Warrender for their helpful suggestion and warm-hearted guidance during my experimental process. I would like to thank Dr. Phoebe Allan, Dr. Catherine Renouf, Dr. Laura McCormick and Samuel Morris for their hard work of collecting diffraction data for me in synchrotron light source. A special thank you goes to my collaborators working with the “adorable zeolites”, Paul Wheatley, Samuel Morris and Daniel Firth in St Andrews, Pavla Chlubná-Eliášová in Prague and Ana Pinar in Zürich, for their helpful discussions and data analysis. I also thank the other members in the group, in particular Dr. Farida Aidoudi, Dr. Mazlina Musa, Dr. Xiang He, Damiano Cattaneo, Katarzyna Mocniak, and Matthew McPherson.

The technical staff at the University of St Andrews give me a lot of help. I would like to particularly thank Dr. Daniel Dawson for his help in collecting the solid state NMR data, Mrs. Sylvia Williamson for TGA, Mrs. Melanja Smith for solution NMR, and Mr. Ross Blackley for his training on SEM/EDX and PXRD.

I am very thankful to the help from my friends in and out of St Andrews during the thesis writing. They help me to get through this difficult period. Prof. Guangshan Zhu in Jilin University gives me lots of suggestions and advice since I was an undergraduate. I would like to express my sincere appreciation to him.

My study is funded by China Scholarship Council (CSC). I am grateful to them for supporting my project.

Finally, a special thank you goes to my family, in particular my parents, Fengde Tian and Xiaoxia Wu, and my wife, Shuang Ding. They always patiently encourage me and make my daily life beautiful and sunny.

## Abstract

Conventionally, crystalline microporous materials such as zeolites and metal-organic frameworks (MOFs) are synthesized through the hydrothermal route or the trial-and-error approach. Other synthetic strategies may lead to the synthesis of microporous materials with new architectures or interesting properties. The general aim of this thesis is to investigate some new synthetic routes towards crystalline microporous materials.

A top-down and post-synthesis method is reported in Chapter 4. Some zeolites are built up by layers and double-4-ring pillars. Germanium is preferentially located in the double-4-ring sites of a zeolite framework and is hydrolytically unstable. The idea of the top-down method is to disassemble these zeolites to the layer structures by dissolving the Ge-containing pillars and reassemble them to a new framework. This method is applied to the germanosilicate **IWW** and **ITH** zeolites for the first time. The effects of framework chemical compositions, Ge distributions and disassembling conditions on the top-down treatment process are investigated. The products obtained from the top-down treatment are characterised.

An ionic liquid assisted strategy for the synthesis of zeolites is described in Chapter 5. The ionic liquid assisted strategy is a solvent free reaction. The raw materials are transformed to zeolites through a solid state reaction. The ionic liquids are first used as structure-directing agents (SDAs) in this solvent free reaction to replace the expensive quaternary ammonium hydroxide. A **TON** zeolite is synthesized using 1-ethyl-3-methylimidazolium bromide as the SDA. Moreover, the ionic liquid assisted strategy is considered as a “green chemistry” synthetic route due to the high yield of the zeolites and the minor production of waste water.

Many aluminophosphates have been successfully synthesized through ionothermal routes. Most of them are synthesized using 1-alkyl-3-methylimidazolium based ionic liquids. A new ionic liquid, 1-(2-hydroxyl-ethyl)-3-methylimidazolium chloride ([HOEmim]Cl), is prepared and used for the ionothermal synthesis of aluminophosphate materials. A zeolite analogue with the **CHA** framework has been synthesized. At high synthetic temperatures, the products are large single crystals. The structures of the framework and the SDA are investigated by single crystal diffraction and other

characterisation methods.

Flexible MOF materials are usually synthesized by a trial-and-error approach. Recently a flexible MOF compound was synthesized using 5-sulfoisophthalic acid (SIP) as the ligand. It was proposed the sulfonate is weakly coordinated to the metal, which brings flexibility to the compound, and the carboxylate groups keep the framework intact. 2-sulfoterephthalic acid (STP) which also contains one sulfonate group and two carboxylate groups is believed to be an alternative ligand for the targeted synthesis of flexible MOFs. In Chapter 7, a MOF compound is synthesized using STP and 4, 4'-bipyridine (Bpy) as ligands to validate the proposed strategy can be generalized. Variable temperature single crystal diffraction analysis solves the structure and reveals a reversible structure transformation upon dehydration and rehydration.

# Table of Contents

Chapter 1 Introduction .....	1
1.1 Overview of the crystalline microporous materials .....	1
1.2 Introductions to zeolites and zeolite analogues .....	1
1.2.1 Structural overview of zeolites and zeolite analogues .....	1
1.2.2 Historical developments of zeolites and zeolite analogues .....	8
1.2.3 Synthetic routes for zeolites and zeolite analogues.....	11
1.2.4 Applications of zeolites and zeolite analogues .....	23
1.3 Introductions to Metal-Organic Frameworks.....	24
1.3.1 A brief overview .....	24
1.3.2 The framework structure of MOFs.....	25
1.3.3 Guest molecules and the classification of MOFs .....	29
1.3.4 Synthesis of MOF materials .....	31
1.3.5 Applications of MOF materials.....	32
1.4 References.....	33
Chapter 2 Aims of the Thesis .....	40
2.1 Aims of the thesis.....	40
2.2 References.....	41
Chapter 3 Analytical Techniques .....	42
3.1 X-ray Diffraction .....	42
3.1.1 Crystallography.....	42
3.1.2 Theory of XRD .....	44
3.1.3 Single Crystal Structural Analysis.....	47
3.1.4 Powder X-ray Diffraction .....	51
3.1.5 Synchrotron Radiation Diffraction.....	54
3.2 Nuclear Magnetic Resonance Technique.....	55
3.2.1 Basic Theory .....	55
3.2.2 Solution phase NMR .....	56
3.2.3 Solid State NMR.....	56
3.3 Scanning Electron Microscopy and Energy Dispersive X-Ray Spectroscopy .....	58
3.4 Adsorption Analysis.....	59
3.4.1 Basic theory .....	59
3.4.2 Measurements of the porous properties.....	62
3.5 Thermogravimetric Analysis.....	63
3.6 CHNS Elemental Analysis.....	63
3.7 References.....	64
Chapter 4 Top-down and Post-Synthesis Treatment of Ge-zeolites .....	65
4.1 Introduction .....	65
4.2 Aims.....	66
4.3 Top-down and post-synthesis treatment of IWW-type zeolite.....	67
4.3.1. Framework structure introduction to IWW-type zeolite .....	67

4.3.2 Experimental methods .....	67
4.3.3 Results and Discussions.....	71
4.3.4 Summary.....	87
4.4 Top-down and post-synthesis treatment of ITH-type zeolites .....	89
4.4.1. Framework structure introduction to ITH-type zeolite.....	89
4.4.2 Experimental methods .....	90
4.4.3 Results and discussions .....	92
4.4.4 Summary.....	105
4.5 Summary of Chapter 4 .....	106
4.6 References.....	107
Chapter 5 Ionic Liquid Assisted Synthesis of Zeolites.....	109
5.1 Introduction .....	109
5.2 Aims.....	110
5.3 Ionic liquid assisted synthesis of zeolites.....	110
5.3.1 Experimental Sections.....	110
5.3.2 Results and discussions .....	112
5.4 Summary .....	124
5.5 References.....	126
Chapter 6 Ionothermal Synthesis of Aluminophosphates Large Single Crystals with a New Ionic Liquid .....	128
6.1 Introduction .....	128
6.2 Aims.....	131
6.3 Ionothermal synthesis of AlPOs with a new ionic liquid.....	131
6.3.1 Experimental methods .....	131
6.3.2 Results and discussions .....	132
6.4 Summary .....	143
6.5 References.....	144
Chapter 7 Targeted Synthesis of a Hemilabile Metal-Organic Frameworks.....	146
7.1 Introduction .....	146
7.2 Aims.....	148
7.3 Cu-STP-Bpy.....	148
7.3.1 Experimental methods .....	148
7.3.2 Results and discussions .....	150
7.4 Summary .....	160
7.5 References.....	161
Chapter 8 Conclusions and Future Work.....	163
8.1 Conclusions.....	163
8.2 Future work .....	165
8.3 References.....	166
APPENDIX.....	167

# Chapter 1 Introduction

## *1.1 Overview of the crystalline microporous materials*

Solid materials with porous architectures are generally defined as porous solids. According to the definition from the International Union of Pure and Applied Chemistry (IUPAC),<sup>1,2</sup> pore sizes of the porous solids are classified as: (a) micropores if the pore sizes are smaller than 2 nm; (b) mesopores if the pore sizes are between 2 and 50 nm and (c) macropores if the pore sizes are larger than 50 nm.

Common crystalline microporous materials include the inorganic microporous materials, such as zeolites and zeolite analogues,<sup>3-6</sup> and the Metal Organic Frameworks (MOFs) which are the coordination polymers also including Zeolitic Imidazolate Frameworks (ZIFs), Materials Institute Lavoisier (MILs) and Porous Coordination Polymers (PCPs).<sup>7-11</sup> These materials possess certain similarities including uniformly distributed nanosized pores, high surface areas and well defined structures. However, there are also some major differences between the two kinds of materials. For instance, in zeolites and their analogues, the central atoms are usually tetrahedrally coordinated while the MOFs possess various coordination modes and diverse structural geometries;<sup>12</sup> zeolites and zeolite analogues are of rigid inorganic skeletons while the frameworks of MOFs are made of both inorganic and organic compounds, which are more flexible and have versatile chemical compositions.<sup>10</sup> Due to these key differences, these two kinds of materials will be discussed separately in this thesis.

## *1.2 Introductions to zeolites and zeolite analogues*

### *1.2.1 Structural overview of zeolites and zeolite analogues*

A well-known family of the crystalline microporous materials which will be focused on in this chapter is the zeolites and the zeolite analogues. For a strict definition, zeolites are crystalline aluminosilicates with three dimensional frameworks that possess channels and cages.<sup>13</sup> The frameworks are built up of corner-sharing silicate and aluminate tetrahedra which are linked together by bridging oxygen atoms.<sup>14</sup> The zeolite analogues, also known as zeotype materials, exhibit similar corner-sharing 4-connected structures to zeolites, but have different chemical compositions due to the replacement

of Si and Al with other elements, including P, Ge, In, Ga and transition metals.<sup>15-20</sup> A typical example of zeolite analogues is the aluminophosphate (AlPO<sub>4</sub>) family which are built from corner-sharing AlO<sub>4</sub> and PO<sub>4</sub> tetrahedral units.<sup>3</sup> Some AlPO<sub>4</sub> materials have identical framework structures to those of zeolites,<sup>21, 22</sup> while new structures that have never been synthesized as aluminosilicates are also reported.<sup>23, 24</sup> Besides the new structures, elements including Si and various transition metals are incorporated into the AlPO<sub>4</sub> frameworks, resulting in microporous silicoaluminophosphate (SAPO-n)<sup>25</sup> and metal-aluminophosphates (MeAPO-n)<sup>22</sup> materials, respectively. Successful synthesis of AlPO<sub>4</sub> materials and their derivatives dramatically enrich the structures and compositions of the crystalline microporous materials.

### ***1.2.1.1 Framework type codes***

For each zeolite framework, a three-capital-letter code is designated as the Framework Type Code.<sup>26</sup> They are approved and collected by the structure commission of the International Zeolite Association (IZA). These codes are only assigned to confirmed framework topologies. Up to now 218 framework type codes have been approved. It is noteworthy that the framework type codes only define the network of the zeolites rather than the real materials. The real zeolite materials with different chemical parameters such as Si/Al ratios, cations in the pores and framework elements *etc.* are assigned to an individual name. For example the real zeolite ZSM-5, which is the abbreviation of Zeolite Socony Mobil No. 5, is structurally identical to another real zeolite, Silicalite. Both of them are assigned to the framework type of **MFI**, wherein the ZSM-5 is an aluminosilicate material<sup>27</sup> but Silicalite is a purely siliceous one.<sup>28</sup> Another example is the zeolites IM-12 and ITQ-15, which are both germanosilicates of same intersecting 14- and 12-membered ring channels. They are both designated as **UTL** type structure, but synthesized using different structure directing agents (SDAs).<sup>29, 30</sup>

### ***1.2.1.2 Concepts of building units***

The structures of zeolites and zeolite analogues can be described using the concepts of building units. The primary building unit (PBU) is the TO<sub>4</sub> tetrahedron where T is silica and aluminium for zeolites or other central atoms such as phosphorus for zeolite analogues. The PBUs connected to each other by bridging oxygen atoms. Fig. 1-1 shows a single TO<sub>4</sub> tetrahedron unit (Fig. 1-1a) and two TO<sub>4</sub> tetrahedra linked by corner-sharing oxygen, resulting in the bridging oxygen between them (Fig. 1-1b).

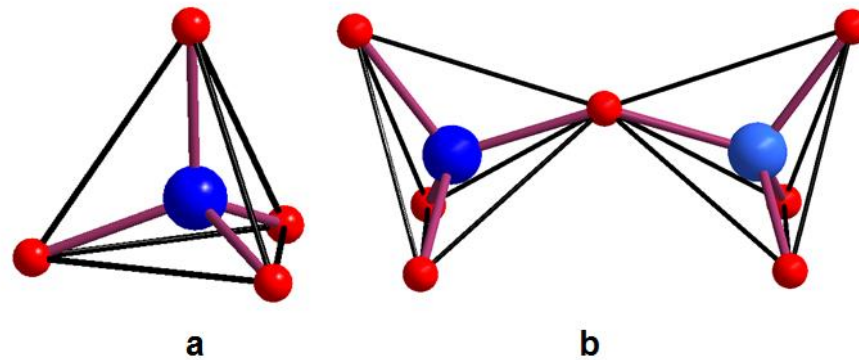


Fig. 1-1. (a) a  $\text{TO}_4$  PBU shows its tetrahedral geometry; (b) two PBUs are connected in the corner-sharing modes by bridging oxygen. (Blue ball: central T atom; red ball: oxygen atom)

Several corner-sharing  $\text{TO}_4$  tetrahedra (up to 16) assemble to form the secondary building units (SBUs).<sup>31</sup> The principles of selecting SBUs to describe the zeolite frameworks are (a): the entire framework is usually built up from one SBU type only (though some exceptions are present at the moment, such as **LOV**<sup>32</sup> and **MEP**<sup>33</sup>); (b): the structure of the SBU is non-chiral and (c): there are always integral numbers of SBUs in the unit cell.<sup>34</sup> The symbols of the SBUs indicate the rings and atoms in the units. All of the 23 SBUs that have been observed from the zeolite frameworks up to now and their symbols are listed in Fig. 1-2 (in next page).

When a ring is formed by connecting  $n$  tetrahedral atoms, it is called an  $n$ -membered ring or  $n$ -ring. Zeolites with 8-, 10-, 12-membered rings are defined as small-, medium- and large-pore zeolites, respectively.<sup>35</sup> Zeolites with rings that contain more than 12 tetrahedral atoms are termed extra-large pore zeolites.<sup>36</sup> The pores extend along one direction to form 1-dimensional channels. If these channels intersect other channels running in different directions, 2- or 3-dimensional pore systems can be created.<sup>37</sup>

In zeolite framework structures, some polyhedral units are frequently observed. These polyhedra can be considered as  $m$  of edge-sharing  $n$ -rings and labelled as  $[n_i^m]$ .<sup>37</sup> For example, in Chapter 4 and Chapter 6 of this thesis, two polyhedra named  $[4^15^26^2]$  and  $[4^{12}6^28^6]$  will be mentioned. They are applied to present the structures made of one 4-ring, two 5-rings and two 6-rings for  $[4^15^26^2]$  and twelve 4-rings, two 6-rings and six 8-rings for  $[4^{12}6^28^6]$ , respectively. The structures of these two polyhedra are shown in Fig. 1-3.

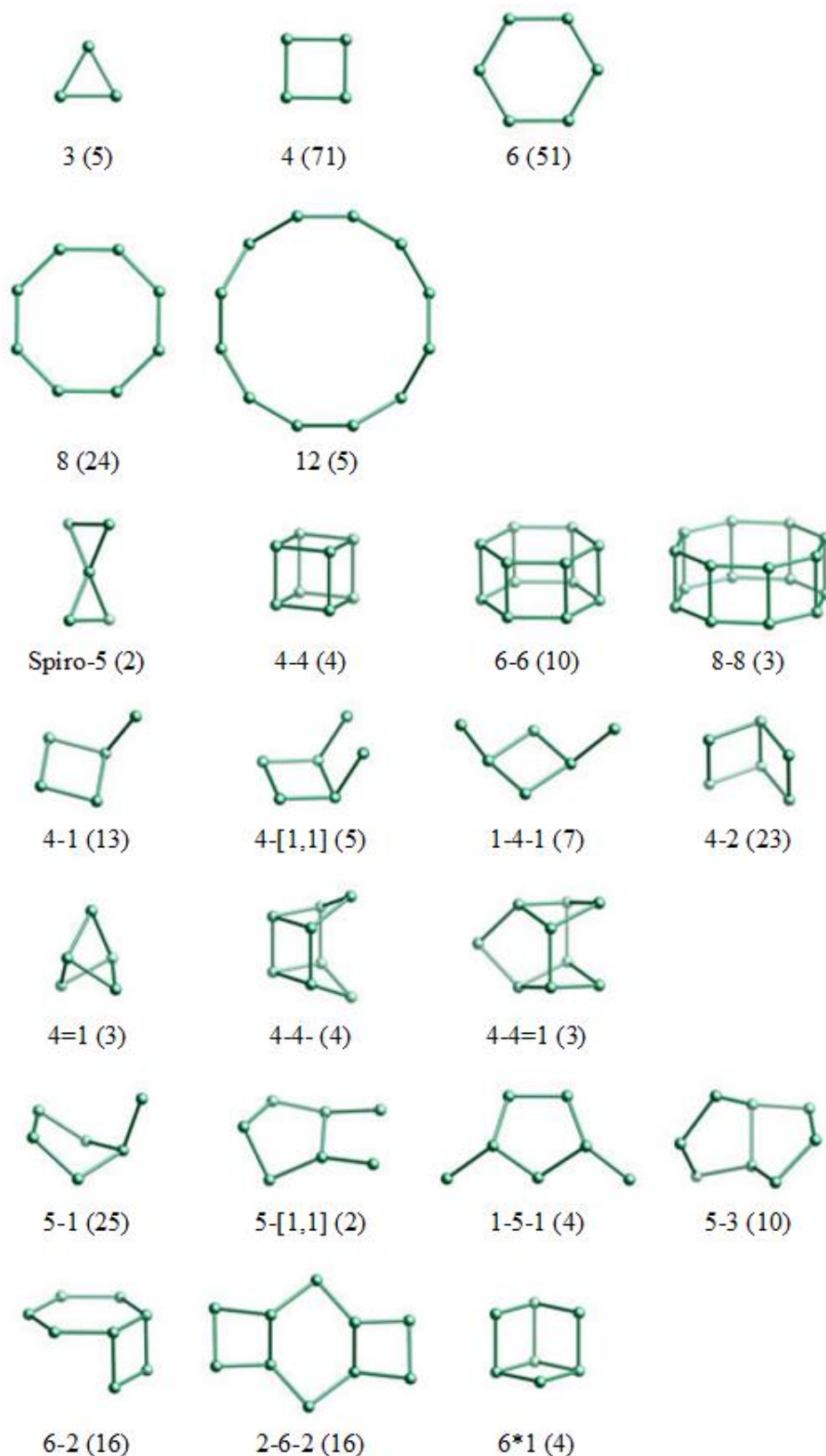


Fig. 1-2. All the observed SBUs and their names.<sup>34</sup> The number in the parentheses represents the frequency of occurrence. The vertices represent the tetrahedral atoms and the T-O-T bridges are drawn as straight lines for clarity. The picture is copied from the IZA website.

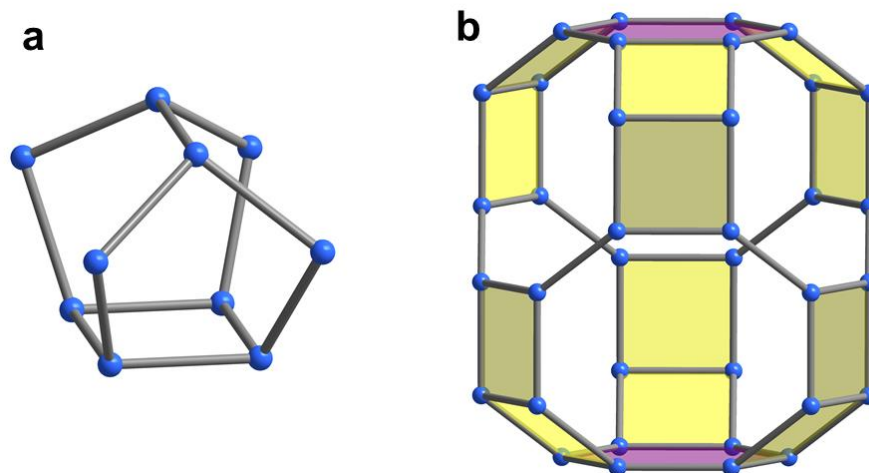


Fig. 1-3. Schematics show the structures of (a)  $[4^{15}2^66^2]$  and (b)  $[4^{12}6^28^6]$ . The blue balls represent the tetrahedral atoms; the T-O-T bridges are drawn as straight lines. For  $[4^{12}6^28^6]$ , the twelve 4-rings and two 6-rings are coloured yellow and purple, respectively.

In general, guest molecules which are larger than water could be blocked by rings with less than 6 members. Polyhedron that contains only 6-membered rings or smaller is termed cage while that possesses at least one ring with more than 6 members is defined as cavity. These polyhedral units are described as composite building units (CBUs).<sup>37</sup> The combinations of different CBUs in various modes are helpful to identify different zeolite frameworks.

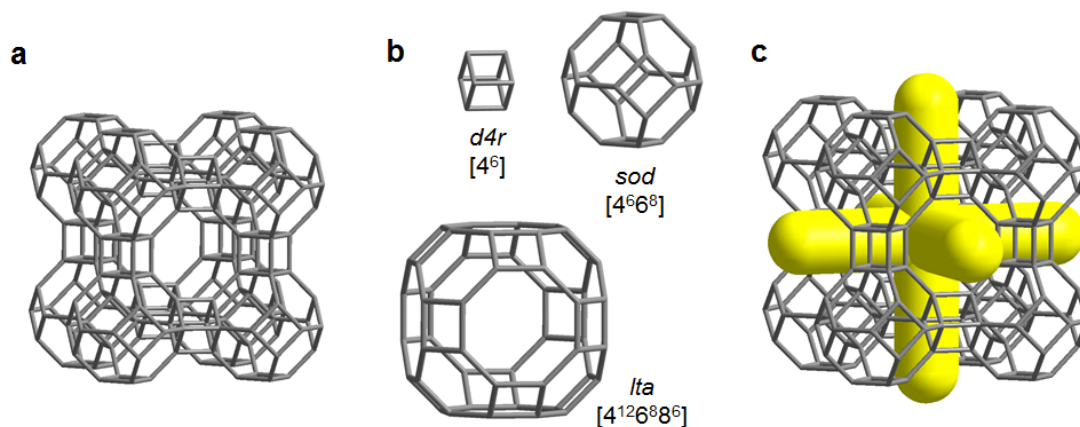


Fig. 1-4. Schematic shows (a) the structure of zeolite **LTA**; (b) the CBUs that are characteristic to the **LTA** topology and (c) the 3-dimensional channels in the **LTA** structures. The vertices represent the tetrahedral atoms and the T-O-T bridges are drawn as straight lines.

These concepts are exemplified in Fig. 1-4, which illustrates the structure of **LTA** type zeolite framework. Zeolite **LTA** has a 3-dimensional structure with 8-membered rings (Fig. 1-4a).<sup>38</sup> The **LTA** structure can be independently built up by the SBUs of 4-4, 6-2,

1-4-1, 8, 6 or 4. In the structure, *sod* cages which are built up by six 4-membered rings and eight 6-membered rings ( $[4^6 6^8]$ ) are connected in 3 directions by double 4-membered ring (*d4r* or  $[4^6]$ ), forming an *lta* cavity ( $[4^{12} 6^8 8^6]$ ) inside (Fig. 1-4b). The yellow cylinders in Fig. 1-4c denote the intersecting 3-dimensional, 8-ring channels in the **LTA** structure.

### 1.2.1.3 Extra-framework species

In zeolite frameworks, the tetrahedral  $[\text{SiO}_4]$  units are neutral while the  $[\text{AlO}_4]^-$  units are negative univalent, which results in the zeolite framework being negatively charged. Extra-framework cations are therefore required to balance this charge. These cations, either inorganic or organic, are usually introduced in the form of hydroxide solution during the synthesis process.<sup>39</sup> When pure silica zeolites are synthesized in the presence of ammonium cations, defects are often formed to maintain charge balance.<sup>40, 41</sup> Besides being located in the negatively charged framework, quaternary ammonium cations or amines can also be present in the channels of the neutral framework such as in aluminophosphates and pure silica zeolites. This indicates that besides existing in the channel to compensate the framework charge, the extra-framework species are also important for directing the formation of particular framework types.

M. E. Davis and R. F. Lobo suggest that in the zeolite synthetic process the organic compounds play the roles of (a) space-filling species; (b) structure-directing agents and (c) real templates.<sup>13</sup> The last two names are usually used in literatures and generate the notions of structure-directing agents (SDAs) and templates to describe these extra-framework species.

Unlike the structure-directing effect, which implies that a given molecule will induce the formation of only one structure type, the notion of space-filling species implies that different molecules may induce the same zeolite structure. An example is AlPO-5, which is a 12-ring aluminophosphate and can be synthesized in the presence of over 85 different SDAs.<sup>42</sup> Moreover, one space-filling compound can direct the formation of many different structure types. For example, hexamethonium cations are used for the synthesis of EU-1, ZSM-48, ITQ-13, IM-10, ITQ-22 and ITQ-24, by changing the ratios of  $\text{SiO}_2/\text{H}_2\text{O}$ ,  $\text{SiO}_2/\text{Al}_2\text{O}_3$ , and  $\text{SiO}_2/\text{NaO}_2$ .<sup>43-45</sup>

According to the classification of Davis and Lobo, the extra-framework species are defined as SDAs only if the compounds lead to one specific structure. One example is the synthesis of **EMT** using 18-crown-6 as SDA.<sup>46</sup> However, some exceptions are considered. For example in Chapter 4 of this thesis, two organic compounds, hexamethonium hydroxide [HM(OH)<sub>2</sub>] and N, N, N', N'-tetramethyl-1, 6-hexanediamine (TMHDA), were used independently for the synthesis of **ITH** type zeolites. Although the products possess identical framework structure, the framework Si/Ge ratios are in two distinct ranges. Clearly this shows not only a space-filling effect and sometimes the role of the extra-framework species needs to be examined cautiously. Moreover, the SDA is more precise than template in most cases as the word “template” implies geometric correspondence between the host framework and guest molecules. To simplify the discussion, in this thesis the notion of SDA will be used.

Examples of true templates are rare. The most well-known example is the triquateryary amine C<sub>18</sub>H<sub>30</sub>N<sub>3</sub><sup>3+</sup> (compound **I** in Fig. 1-5a), which is considered to be a true template for ZSM-18 (type code **MEI**).<sup>47</sup> This compound possesses 3-fold rotational symmetry and locates in a cage of ZSM-18 which has the same symmetry. Compound **I** was found to be static in the cage due to the motion being confined by the framework.<sup>48</sup> Another recently reported template is the diquinuclidinium cations for the synthesis of STA-2 (type code **SAT**), of which the cations fit closely in the cavities of the framework.<sup>49</sup>

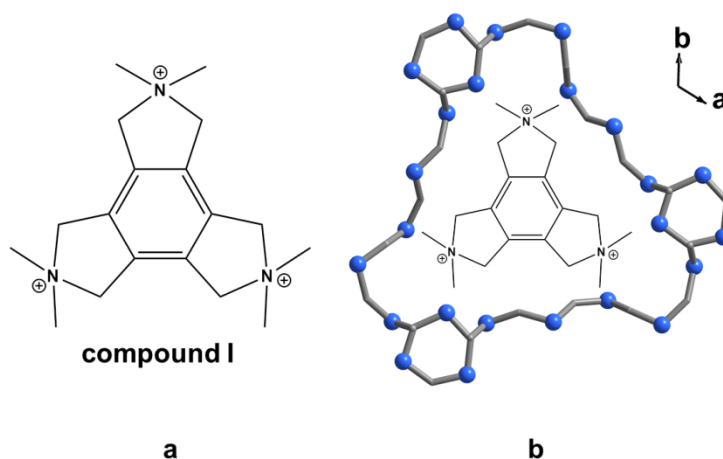


Fig. 1-5. (a) the structure of the triquateryary cation C<sub>18</sub>H<sub>30</sub>N<sub>3</sub><sup>3+</sup> (compound **I**) and (b) the cavity structure of ZSM-18 with the compound **I** inside. The blue balls represent for the tetrahedral atoms; the bonds are the bridging oxygen.

In conclusion zeolites and zeolite analogues are diverse in their chemical compositions, structures and the guest species in the pores. To distinguish zeolites and zeolite analogues, the related materials are given the chemical formulae in the form of  $|\text{SDA}_a(\text{H}_2\text{O})_{b|l} [\text{M}_x \text{N}_y \text{O}_z]_j\text{-code}$ . The extra-framework guest molecules are enclosed by the bracket of  $| |$  and the framework molecules are enclosed by the bracket of  $[ ]$ . The type code is followed to identify the structures.<sup>37</sup>

### ***1.2.2 Historical developments of zeolites and zeolite analogues***

In a historical perspective, the development of zeolites and zeolite analogues undergoes several milestones including natural zeolites, synthetic aluminosilicate, high silica zeolites, AIPOs and Ge-containing zeolites. Each of these materials enriched the zeolite structural architectures and promoted their applications in diverse fields. These materials will be introduced in this part.

#### ***1.2.2.1 Natural zeolites***

In 1756, Swedish mineralogist A. F. Cronstedt discovered that a mineral, stilbite, releases gas when heated in water. He named this material zeolite which is derived from Greek *zeo* (to boil) and *lithos* (stone).<sup>50</sup> Subsequently many more naturally occurring zeolites were discovered around the globe.<sup>51</sup> Currently there are 67 natural zeolites recorded on the IZA commission's natural zeolite datasheet. Most of them have a synthetic counterpart but some are still unique in nature.<sup>52,53</sup> They are usually discovered in sedimentary tuffs and marine sediments, which are rich in inorganic cations during their formation ages. Therefore all natural zeolites are aluminosilicates containing inorganic cations in their channels, and are defined as such.

#### ***1.2.2.2 Synthetic aluminosilicates***

Compared to natural zeolites, synthetic zeolites are of high purity, unique pore size distribution and have better ion-exchange performance so they are in high demand in industrial fields. After the discovery of natural zeolites the synthesis of zeolite materials in the laboratory was always attractive to scientists. This is not only because of the increasing demand for zeolites in various industrial fields, but also the enthusiasm of creating new materials for potentially new applications. Inspired by natural zeolites, scientists tried to simulate the formation environments of the natural minerals. In the 1940s, R. M. Barrer reported the first synthesis of zeolitic materials from basic solution at high temperature.<sup>54</sup> The reactions were carried out in stainless-steel autoclaves to

stand the high temperature range from 180 to 270 °C. R. M. Milton's work in 1950s directed the way to preparing zeolites at milder conditions.<sup>55</sup> By using a highly reactive synthetic gel formed in strong basic solution, they reduced the synthesis temperature down to about 100 °C. Synthesis of zeolites A (**LTA**), P (**KFI**) and X (**FAU**) were achieved. Subsequently many zeolite materials with different structure types were synthesized.<sup>56, 57</sup> At the same time, the industrial applications of zeolites were being investigated and commercialized in various areas including sorbents, gas separation and catalysis.<sup>58-60</sup>

### ***1.2.2.3 High silica zeolites***

In 1961, R. M. Barrer and P. J. Denny synthesized a number of zeolites in the presence of alkylammonium hydroxide.<sup>61</sup> They noted that the zeolites, which were synthesized with organic cations, contained higher Si/Al ratios than the zeolites synthesized using only inorganic cations. The organic cations usually possess larger volume but the same positive charge as the inorganic cations. Such “low charge density” species can fill the same space with a lower positive charge. When the zeolites formed around the organic cations, fewer [AlO<sub>4</sub>] units are required to neutralise the framework charge. This results in the formation of zeolites that are rich in silica. Not only did they obtain zeolites with high Si/Al ratios, but the employment of diverse organic compounds also induced the creation of new zeolite structures. For example, quaternary ammonium cations of tetramethylammonium (TMA<sup>+</sup>), tetraethylammonium (TEA<sup>+</sup>), tetrapropylammonium (TPA<sup>+</sup>) and tetrabutylammonium (TBA<sup>+</sup>) were successful in preparing zeolite ZK-4 (**LTA**),<sup>62</sup> Beta (**\*BEA**),<sup>63</sup> ZSM-5 (**MFI**)<sup>64</sup> and ZSM-11 (**MEL**),<sup>65</sup> respectively. Pure siliceous zeolites of silicalite (**MFI**) and silicalite-2 (**MEL**) were synthesized in 1978 and 1979.<sup>28, 66</sup> The high silica and pure siliceous zeolites have some unique properties such as high hydrothermal stabilities and hydrophobic surfaces.

### ***1.2.2.4 Aluminophosphates (AIPOs) and heteroatom-substituted AIPOs***

In addition to aluminate and silicate, other elements can also form microporous materials. To distinguish these compounds from zeolites, which are strictly defined as aluminosilicate microporous materials, they are named zeolite analogues. The most famous family of zeolite analogues is the aluminophosphates (AIPOs), which was first reported by Wilson *et al.*<sup>3</sup> Most AIPOs are crystalline materials composed of alternating AlO<sub>4</sub> and PO<sub>4</sub> tetrahedra. Moreover, heteroatoms such as Si, Ga, and transition metals

can fully or partially replace the central atoms to form various materials, including SAPOs (Si-substituted aluminophosphates),<sup>25</sup> MeAPOs (Metal-substituted aluminophosphates, Me= Fe, Mg, Mn, Zn, Co, Ti, V, *etc.* ),<sup>22</sup> GaPOs (Gallophosphates)<sup>67</sup> and so on. Some of them are structurally related to existing zeolites, but some of them possess unique structures for which no zeolite counterparts had been reported before the corresponding AlPOs were synthesized.<sup>23, 25</sup> In addition to the conventional 4-connected zeolitic structures, some materials also exhibit 5- or 6-coordinated geometry and result in terminal hydroxyl groups in the structure. These attributes make the zeolite analogues structurally and compositionally attractive. For example, cloverite is an extra-large 20-membered ring gallophosphate microporous material. The name comes from the unusual four-leafed clover shaped pore opening, which is due to the terminal hydroxyl groups (Fig. 1-6).<sup>68</sup> The cloverite has the type code of **-CLO** and the hyphen indicates the structure is an interrupted framework.<sup>34</sup>

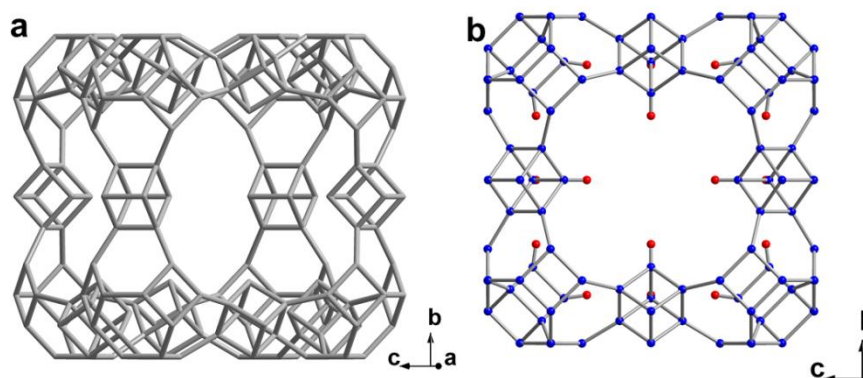


Fig. 1-6. (a) a cavity structure of cloverite; (b) clover shaped opening and the terminal hydroxyl groups pointed at the centre of the cavity. The T-O-T bridges are drawn as straight lines Blue balls: tetrahedral atoms; red balls: terminal oxygen atoms.

#### 1.2.2.5 Ge-containing zeolites and the structure-directing effect of germanium

At the beginning, incorporation of Ge atoms into the zeolite framework was only of interest to extend their chemical compositions.<sup>56</sup> The significant event about the substitution of Ge in zeolite framework started from Corma's work on synthesizing the Polymorph C of Zeolite Beta (type code **BEC**).<sup>69</sup> The polymorph C of zeolite Beta contains double 4-membered rings (*d4rs*) in the structure (Fig. 1-7). The synthesis of purely siliceous **BEC** structure was rarely reported, which are probably because the [8Si] *d4rs* would be energetically unfavourable. When Ge atoms replaced some Si atoms in

the *d4r* sites, the structure was stabilized due to the formation of smaller T-O-T angle ( $\sim 130^\circ$  compared to  $145^\circ$  for Si-O-Si) in the presence of larger Ge atoms.<sup>70</sup> Therefore the germanium plays the role of SDA which directs the formation of *d4r*s in the frameworks.

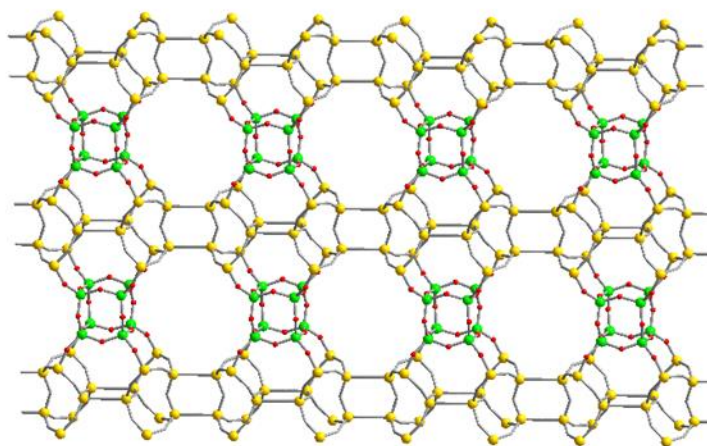


Fig. 1-7. Structure of **BEC** framework. The tetrahedral atoms of the *d4r*s are shown in green, other tetrahedral atoms are yellow, red balls represent the oxygen atoms around *d4r*s.

Many hypothetical structures were unattainable in their purely siliceous form. Incorporation of Ge extends the synthesized zeolite structures. Moreover, a statistical analysis indicated the correlation between the framework density (the number of tetrahedra per  $\text{nm}^3$ , FD) and the size of the smallest ring in the structure.<sup>71</sup> The zeolites with lower framework density tend to form in the structures containing 3- and 4-membered rings. Incorporation of Ge is thus of benefit for synthesizing zeolites with highly open frameworks, such as extra-large pore zeolites and 3-dimensional zeolites.<sup>36</sup> More zeolite frameworks that contain *d4r*s or even smaller *d3r*s were subsequently synthesized such as **UTL**, **UOS**, **IWW**, **ITT**, **IRR**, **-IRY**, **UWY**, and *etc.*<sup>29, 72-77</sup>

### ***1.2.3 Synthetic routes for zeolites and zeolite analogues***

#### ***1.2.3.1 Hydrothermal synthesis***

The most extensively applied synthetic route for zeolite is hydrothermal synthesis.<sup>78</sup> In general, tetrahedral species ( $\text{SiO}_4$ ,  $\text{AlO}_4$ ,  $\text{PO}_4$ , and *etc.*) of different reagents are mixed in an aqueous solution which contains structure directing agents. The solution is sealed in a vessel such as Teflon lined autoclave or closed tube, and heated to high temperature (above  $100^\circ\text{C}$ ) under autogenous pressure. For aluminosilicate zeolites, the solution is basic or nearly neutral, depending on whether  $\text{OH}^-$  or  $\text{F}^-$  is used as mineralizer. For

AlPOs materials, acidic and weakly basic synthetic precursors are both reported for the synthesis of different materials.<sup>79</sup>

The mechanism of zeolite crystallization is sophisticated and is affected by many parameters, such as concentration of the tetrahedral species, reactivity of the tetrahedral sources, SDAs, pH values, crystallization temperature, crystallization time, aging time, and so on. In general there are three steps for zeolites crystallization in hydrothermal synthetic route (shown in Fig. 1-8): (a) The concentration of the reactant species reaches supersaturated; (b) tetrahedral species form the nuclei; and (c) the crystals grow. The typical crystallization curve of zeolites (zeolite crystallinity presents as a function of crystallization time) usually exhibits an S-shaped plot,<sup>80</sup> which indicates the zeolite crystallization starts with an induction step to overcome an energy barrier for nucleation and follows a crystal growth step with the crystallinity increasing rapidly.<sup>81</sup>

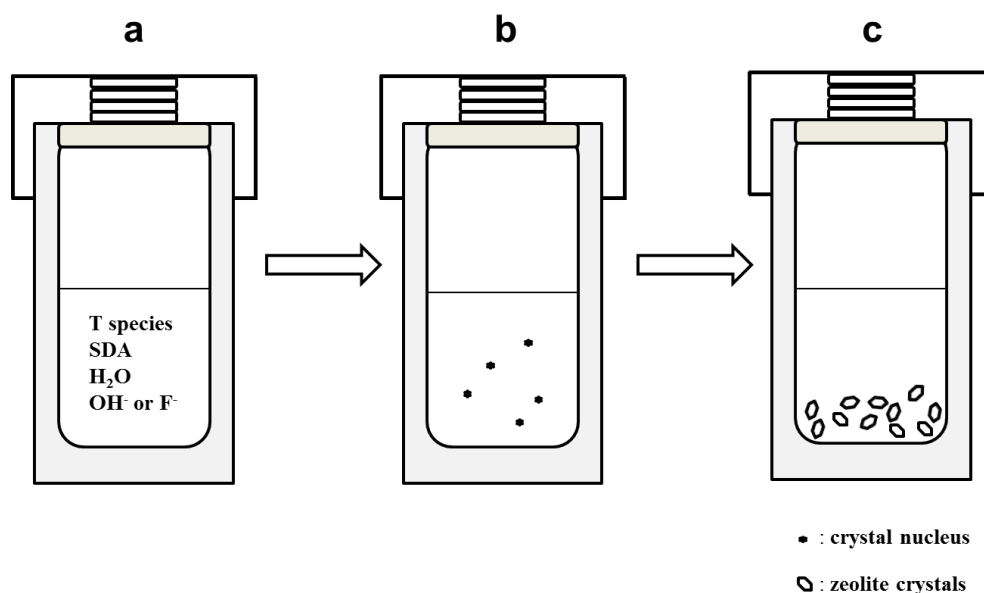


Fig. 1-8. Scheme shows the general procedure of hydrothermally synthesizing zeolite crystals. (a) the reagents are mixed and the tetrahedral species reach supersaturated; (b) nucleation and (c) crystal growth.

There exist two proposed mechanisms for zeolite crystallization: the solid-phase transformation mechanism and the solution-mediated transformation mechanism.<sup>79</sup> The main divergence between the two opinions is whether tetrahedral species which are dissolved in the liquid phase attend the crystallization. The solid-phase transformation mechanism suggests the tetrahedral species in the hydrogel form the nuclei and grow up without the participation of the species dissolved in the liquid.<sup>81</sup> The solution-mediated

transformation mechanism suggests the tetrahedral solids first dissolve in the alkaline solution and then form the nuclei and provide the nutrients for crystal growth.<sup>82, 83</sup> Both of the two mechanisms are supported by several experimental results. Xu *et al.* reported a dry gel converted to ZSM-5 in the presence of the mixed vapour of water and volatile SDAs.<sup>84</sup> The gel was kept away from the solvent thus the dry gel conversions<sup>85</sup> are considered to belong to the solid-phase transformation process. The zeolites synthesized from clear solution unambiguously support the solution-mediated transformation mechanism.<sup>86-88</sup> Moreover, Angell and Flank utilized Raman spectra and other techniques to investigate the synthesis of zeolite A.<sup>89</sup> They observed the changes of the SiO<sub>2</sub>/Al<sub>2</sub>O<sub>3</sub> ratios in both solid and liquid phase during the synthesis; the Raman spectra also indicated the structure changes of the silicate species in the solution. These results support the solution-mediated transformation mechanism.

In the zeolite synthesis process, the cation species has significant effects on the structure of the products. Most importantly, they play the role of structure directing agents. Inorganic cations are used as SDAs for the synthesis of zeolites with low SiO<sub>2</sub>/Al<sub>2</sub>O<sub>3</sub> ratios.<sup>90</sup> In addition, Davis *et al.* reported that the synthesis of zeolites can be accelerated by adding the inorganic cations.<sup>91</sup> Using the quaternary ammonium salts as the organic SDAs dramatically increases the number of the new zeolite framework types and makes the synthesis of high silica zeolites available. Although it is widely considered that the structure of organic SDAs is a decisive parameter to the synthesized zeolite architecture, predicting the zeolite framework from the SDA is still elusive. A mechanism proposed by Davis and Burkett is schematically illustrated in Fig. 1-9.<sup>92, 93</sup> In the proposed mechanism, the organic SDAs form hydrophobic hydration spheres in the solution; the soluble silicate species form hydrophobically hydrated domains; the spheres and the domains overlap and the soluble silicate species replace the water molecules in the SDA-water hydration spheres; the inorganic-organic composites are formed due to the van der Waals interactions between SDAs and soluble silicate species; these inorganic-organic composites subsequently assemble to zeolite nuclei and grow to bulk crystals.

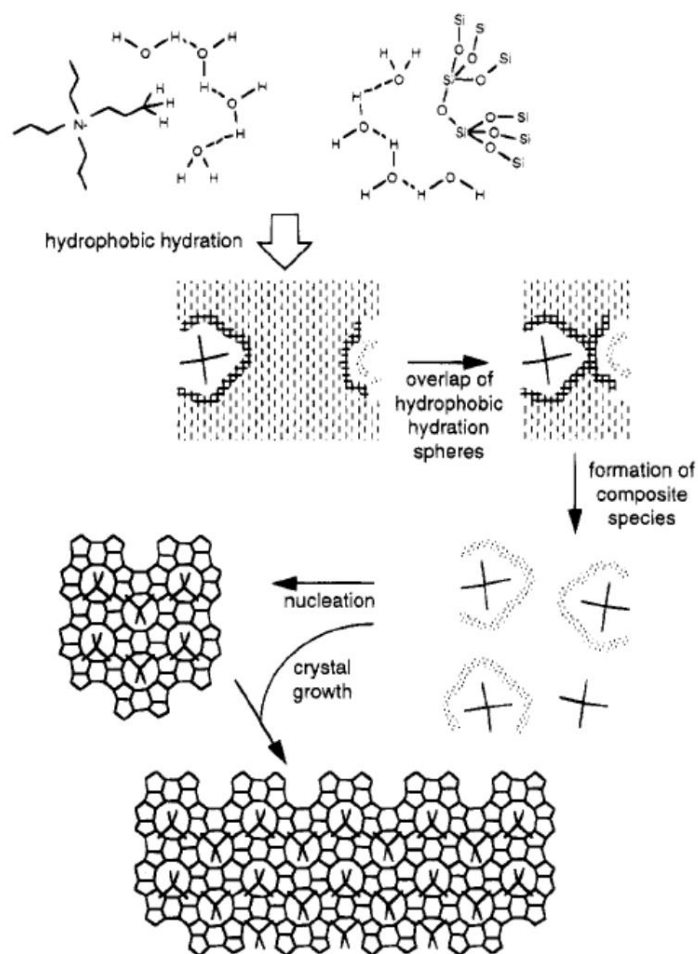


Fig. 1-9. Schematic illustration of the SDA effect of  $\text{TPA}^+$  in the synthesis of ZSM-5. The picture is adopted from reference 92.

The proposed mechanism explains the phenomenon that some molecules, such as tetraethanolammonium and diethanoldipropylammonium, which are structurally similar to TPA, are unable to direct the synthesis of ZSM-5.<sup>92, 94</sup> It also implies that adequate SDAs should possess intermediate interaction with water. A criterion of selecting SDAs is the organic cations with the  $\text{C}/\text{N}^+$  ratios between 11 and 16 are likely to be suitable SDAs.<sup>95</sup> This is probably because these organic compounds possess sufficient solubility in the aqueous solution and the appropriate hydrophobicity to keep the balance of the interactions with solvent and tetrahedral species. Many organic cations were synthesized and their usages as SDAs for zeolite synthesis were reviewed.<sup>96-98</sup> Systematic investigations on the design of various SDAs and their directing effects to the zeolite structures were carried out. Many zeolites with novel architectures were reported, such as the SSZ-n,<sup>99-104</sup> ITQ-n family (Instituto de Tecnología Química)<sup>69, 72-74, 98, 105</sup> and IM-n family (Institut Français du Pétrole/Mulhouse).<sup>29, 76, 77, 106</sup>

Beside the quaternary ammonium salts, several other cationic compounds are used as SDAs: phosphorus-derived cationic compounds were applied. Phosphonium hydroxide or phosphazanium hydroxide were successfully used as SDAs for novel zeolite structures;<sup>107, 108</sup> Polymorph structure was selectively synthesized where the corresponding structure is more favourable in the presence of novel ammonium SDAs.<sup>109</sup> Another kind of SDAs that has been used is the organometallic complexes. For example, bis-(pentamethyl-cyclopentadienyl) cobalt (III) hydroxide was used for synthesizing a novel structure with 14-membered rings, UTD-1 (type code **DON**);<sup>110</sup> the complex formed by 18-crown-6 and a sodium cation were used for selectively synthesizing the EMC-2, which is a polymorph of **FAU**.<sup>111</sup> Recently, Ryoo et al. reported the organic species which possess both quaternary ammonium and long alkyl chains play the roles of SDA and surfactant at the same time.<sup>112, 113</sup> Either **MFI** zeolites with the thickness of a single unit cell or zeolite materials with hierarchical structures were synthesized (Fig. 1-10). Such “bifunctional” SDAs indicate the organic species are also helpful to control the morphologies of the zeolite materials.

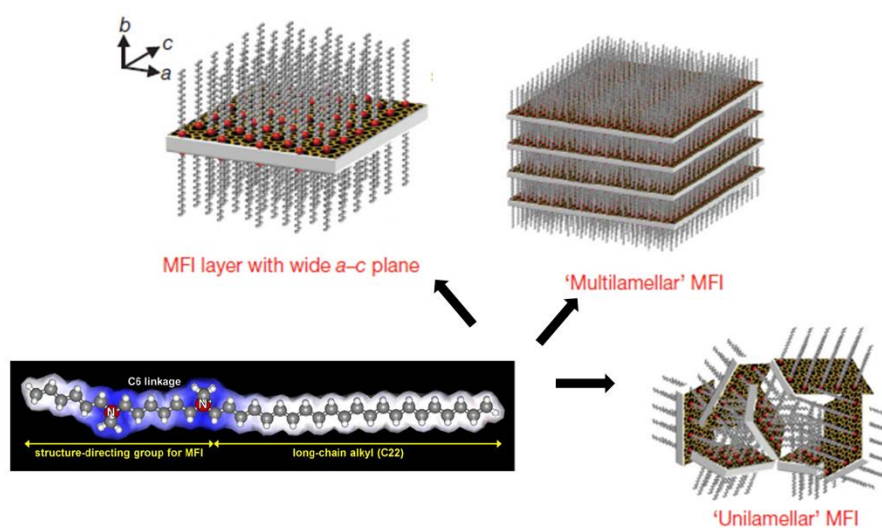


Fig. 1-10. The “Bifunctional” cationic surfactant SDA and the lamellar zeolites structures synthesized using this SDA. Picture adopted from reference 112.

The utilization of the micropores of zeolites requires removing the extra-framework species from the channels, usually attained by combustion. Although presently such novel SDAs are expensive and are limited in practical applications, the successes of synthesizing new materials and structures infer their importance in the zeolite synthesis process. Current interests of the investigations about the SDAs include: preparing new

compounds that can direct new zeolites, such as chiral structures;<sup>114-116</sup> synthesis of zeolites with recyclable SDAs<sup>117</sup> or under the organic free synthetic conditions<sup>118-120</sup> to reduce the cost; and the rational design of the suitable SDA for zeolite synthesis.<sup>98, 121</sup>

Another important species for zeolite synthesis are the mineralizers. The most common mineralizer is the hydroxide anion. It is usually introduced into the synthetic system in the form of the counter ions of the SDA cations, such as NaOH, KOH, and  $R(OH)_n$  where  $R^{n+}$  is the organic SDA cations. It provides sufficient alkalinity for the dissolution of the tetrahedral species and the formation of the T-O-T bonds.<sup>122</sup> Using  $F^-$  as the mineralizer was first reported by Flanigen *et al.*<sup>123</sup> Guth *et al.* reported the synthesis of **MFI** zeolite large single crystals in the presence of HF and the pH value below 10.<sup>124</sup> The large single crystals were obtained because the  $F^-$  can form complexes with the tetrahedral species and release them gradually as the nutrients for crystal growth.<sup>125</sup> Large single crystals of zeolite analogues such as  $AlPO_4-5$ ,  $AlPO_4-11$  and  $AlPO_4-34$  were also synthesized through the fluoride route.<sup>125, 126</sup> Moreover, the quality of the zeolites and zeolite analogues which were obtained through the fluoride route is usually better than the ones synthesized under strongly alkaline conditions. This is because under the high hydroxide concentration the zeolite frameworks are more likely to form Si-O<sup>-</sup> defects, but the high silica zeolites synthesized from the  $F^-$  medium contain 5-coordinated silicon  $SiO_{4/2}F^-$  units instead of the Si-O<sup>-</sup> defects to balance the extra-framework positive charge.<sup>127, 128</sup>

Besides it can assist the formation of crystals with large size and good quality, the structure-directing effect of  $F^-$  has attracted much attention recently.  $AlPO_4-34$  which possesses a triclinic **CHA** type structure can only be synthesized in the presence of fluoride. The fluorine is incorporated in the framework, resulting in an octahedral Al in the framework.<sup>129</sup> The fluorine was also observed to locate inside the building units such as *d4rs* and stabilize them, such as in ITQ-7,<sup>70</sup> ITQ-17,<sup>130</sup> cloverite,<sup>68</sup> and so on. Morris *et al.* reported the synthesis of the  $GeO_2$  *d4r* building units, and the structure analysis by both Rietveld refinement and <sup>19</sup>F NMR indicated the  $F^-$  was located inside the *d4r*.<sup>131</sup> Another interesting investigation was carried out by Cambor and co-workers. They reported a trend that zeolites with lower framework density are synthesized with decreasing  $H_2O/SiO_2$  ratios and interestingly this trend was only observed for the zeolites synthesized in F medium rather than hydroxide medium, although the F doesn't affect the selectivity of the phases.<sup>127</sup>

### 1.2.3.2 Solvothermal synthesis

The influence of the hydrothermal synthetic route for zeolites and zeolite analogues is obvious and profound. Almost all of the zeolite structures can be hydrothermally synthesized. However, the importance of other synthetic routes is unable to be ignored. Several novel synthetic routes were reported. Compared with the conventional hydrothermal synthesis, they exhibited some different features. The first synthetic route that is going to be introduced is solvothermal synthesis. In this synthetic route, organic solvents are used instead of water. Bibby and Dale first reported the synthesis of silica sodalite in ethylene glycol.<sup>132</sup> Xu *et al.* reported the syntheses of silicalite, ZSM-39 and ZSM-48, using ethylene glycol, glycerol and butyl alcohol as the solvent, respectively.<sup>133</sup>

In general organic solvents are less polar but more viscous than water. The behaviour of the starting materials in organic solvent such as the solubility and the mass transfer rates are different. These differences reduce the rates of nucleation and crystal growth and result in the formation of large single crystals. Some large single crystals of zeolites and zeolite analogues were prepared from the solvothermal route. Kuperman and co-workers reported the synthesis of giant crystals of the aluminosilicate ferrierite, silicalite, dodecasil-3C and a novel microporous aluminophosphate in the solvents of pyridine, propylamine or triethylamine.<sup>134</sup>

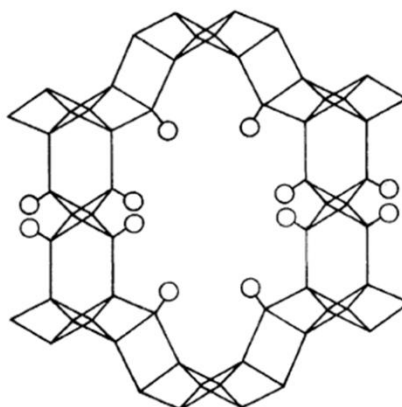


Fig. 1-11. The schematic shows the 20-membered ring of JDF-20 and the terminal hydroxyl groups (the open circles). Picture is adapted from reference 135.

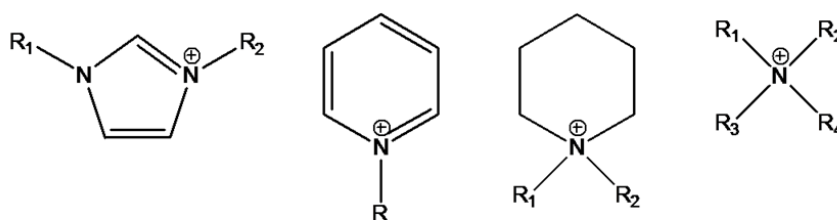
The solvothermal route also leads to the synthesis of novel structures. Xu and co-workers reported the synthesis of JDF-20, which is an extra-large pore aluminophosphate possessing 20 T-atoms channel, using di-, tri-, and tetra-ethylene

glycol and butane-1, 4-diol as the solvent.<sup>135</sup> Similar to the cloverite, JDF-20 is also an interrupted structure with the terminal hydroxyl groups which are shown as the open circles in Fig. 1-11. Moreover, the JDF-20 has the unusual chemical compositions, of which the Al/P ratio is 5/6.<sup>136</sup>

### 1.2.3.3 Ionothermal synthesis

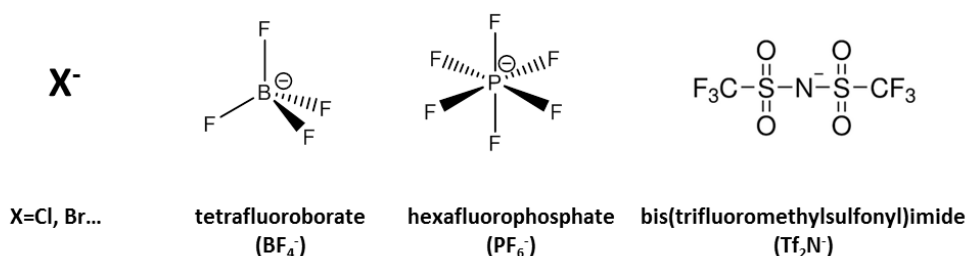
The ionic liquids (ILs), usually referring to the room-temperature ionic liquids (RTILs), are ionic salts which possess melting points below 100 °C.<sup>137</sup> The first report of ionic liquids goes back to 1914, but only in recent decades have the investigations of ionic liquids developed.<sup>138, 139</sup> Besides their good thermal stability, non-flammability and wide liquidus ranges, ionic liquids are also considered as multi-functional and environment-benign solvents because they are structurally flexible and eco-friendly. Some cations and anions of commonly used ionic liquids are shown in Fig. 1-12. The alkyl-groups of cations can be modified and functionalized, and enormous cations and anions can be combined to give over 10<sup>18</sup> possible ionic liquids. Ionic liquids possess negligible vapour pressure so they are a good choice to replace the volatile organic compounds.<sup>140, 141</sup>

#### Cations:



1-alkyl-3-methylimidazolium    N-alkyl-3-pyridinium    N-alkyl-N-piperidinium    tetraalkylammonium

#### Anion:



X=Cl, Br...

tetrafluoroborate  
(BF<sub>4</sub><sup>-</sup>)

hexafluorophosphate  
(PF<sub>6</sub><sup>-</sup>)

bis(trifluoromethylsulfonyl)imide  
(Tf<sub>2</sub>N<sup>-</sup>)

Fig. 1-12. Several cations and anions of commonly used ionic liquids.

Ionic liquids have been used as catalysts for organic reactions,<sup>142</sup> electrolytes<sup>143</sup> and green solvents for the synthesis of inorganic materials such as metal nanoparticles, metal oxides and silica aerogel.<sup>144</sup> Moreover, ionic liquids contain organic cations which can play the role of SDA for the synthesis of microporous materials. Zeolite IM-16 and IM-20 have been synthesized using the most commonly ionic liquid cations, 1-ethyl-3-methylimidazolium and 1-butyl-3-methylimidazolium, as the SDAs.<sup>76, 77</sup> The synthesis processes are still classified as hydrothermal routes as water is the dominant solvent.

The ionothermal synthesis was first reported by Morris *et al.* in 2004. Several zeolite analogues were synthesized using ionic liquids or eutectic mixtures as the solvents.<sup>145</sup> In ionothermal synthesis procedures, ionic liquids are the main solvents and play the roles of SDAs and solvent at the same time.

Compared with the conventional hydrothermal synthesis, ionothermal synthesis has some unique properties. For instance, the ionic liquids possess negligible vapour pressure so sealed reaction vessels are not necessary. The synthesis is able to be scaled up for industrial production at ambient pressure. It also reduces the safety concerns of the reactions in autoclaves. A good example is the research on ionothermal synthesis of **AEL** film on metal surface for anti-corrosion coating;<sup>146</sup> Ionic liquids are good microwave absorbers therefore they are suitable for the rapid microwave assisted synthesis;<sup>147</sup> moreover, the ionic liquids can be easily recycled and repeatedly used.<sup>145</sup>

Another proposed effect of ionothermal synthesis is “improved templating”.<sup>148</sup> The framework species in the synthetic precursor interact with the SDAs directly, instead of forming the hydration domains under hydrothermal conditions. The direct van der Waals interactions between ionic liquids and tetrahedral species may lead to different structures from the ones synthesized hydrothermally.

Although plenty of research on ionothermal synthesis of zeolite analogues has been reported until now, synthesis of zeolites through ionothermal route is still a challenge. This is probably because of the poor solubility of the silicate species in the commonly used ionic liquids and the decreased water reactivity in ionic liquids obstruct the nucleation and growth of zeolite crystals.<sup>149</sup> Only a few successful examples have been reported.<sup>150-152</sup> Yan *et al.* reported the synthesis of zeolite silicalite-1 in ionic liquid and water by dry gel conversion method. The reaction occurred under ambient pressure due

to the presence of ionic liquid.<sup>152</sup> Wheatley *et al.* reported the synthesis of siliceous **MFI** and **TON**-type zeolites in a partially hydroxide anion-exchanged ionic liquid. The hydroxide anions were used as mineralizer and constructive for the dissolution of silicate species.<sup>151</sup>

#### 1.2.3.4 Solvent free synthesis

The conventional hydrothermal synthesis produces plenty of waste water and organic compounds. Under the consideration of the environmental sustainability, “green” methods for zeolite synthesis are desired. In 2012, Xiao *et al.* reported a solvent free synthesis of zeolite materials.<sup>153</sup> In this strategy, raw materials of the tetrahedral atoms and the SDAs were mechanically mixed and heated in autoclaves without the addition of any solvent (Fig. 1-13). The water required for crystallization was provided from the hydrated raw materials. Zeolites with various framework types including **MFI**, **\*BEA**, **MOR** and **FAU** were prepared with minimal production of waste solvent. The recent research from the same group has confirmed that this strategy is also feasible for the preparation of zeolite analogues.<sup>154</sup> This solvent free strategy is considered as a “green” manner because of some advantages such as high yields of the products, high utilization of autoclaves, simplification of the synthetic procedure and minimal production of waste solvent.<sup>119</sup>

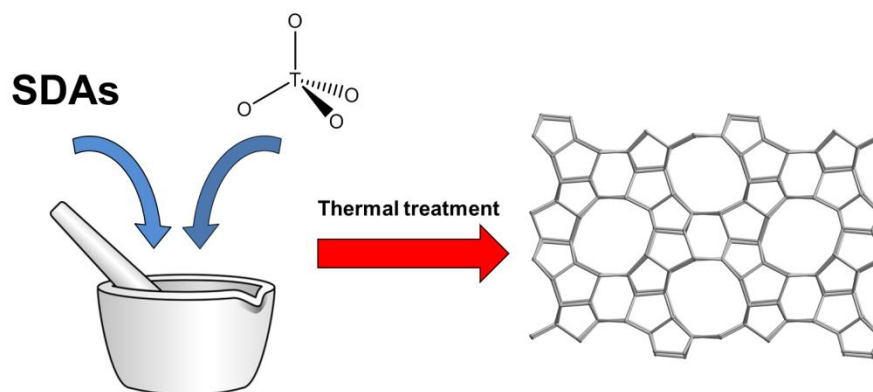


Fig. 1-13. Schematic illustration shows the procedure of solvent free synthetic route.

#### 1.2.3.5 2D-3D transformation

The conventional hydrothermal synthesis of zeolites can be considered as a transformation from the 0-dimensional  $\text{TO}_4$  species to the 3-dimensional frameworks. Most of the zeolites are synthesized from this 0D to 3D procedure. However, some zeolites can be prepared from the condensation of 2-dimensional layer structures as well.

The first example is zeolite MCM-22, which can be synthesized from a layer material MCM-22(P).<sup>155, 156</sup> The structure of the MCM-22(P) is shown in Fig. 1-14. It is a layer structure formed by two bottom to bottom connected cup-like cavities which possess 12-membered ring top openings and 6-membered ring bottoms. The direct calcination of the MCM-22(P) leads to the condensation of the layers at the positions of the cup openings and results in the 3D MCM-22 zeolite. The MCM-22 zeolites have two independent 2D 10-membered ring channels. One is around the cup bottom connections and the other one is formed at the connection of the openings. The two cup-like cavities form the unique supercage of 18.2 Å in height and 7.1 Å in diameter.<sup>157</sup> The similar procedures of the 2D to 3D transformation were also observed in the synthesis of **FER** from the layered **PREFER**<sup>158</sup> and the synthesis of **CAS** type zeolite NU-6(2) from the precursor of NU-6(1).<sup>159</sup> Besides being directly condensed to the zeolite structures, the layered structures can also be swelled and pillared to form some interlayer-expanded materials. The MCM-22(P) can be swelled by surfactant and pillared by silicate species to form mesoporous MCM-36;<sup>160</sup> The **PREFER** layers can be swelled and pillared to form an **ITQ-36** material.<sup>161</sup> The 2D to 3D transformation provides a way to tailor the porous properties of the materials.

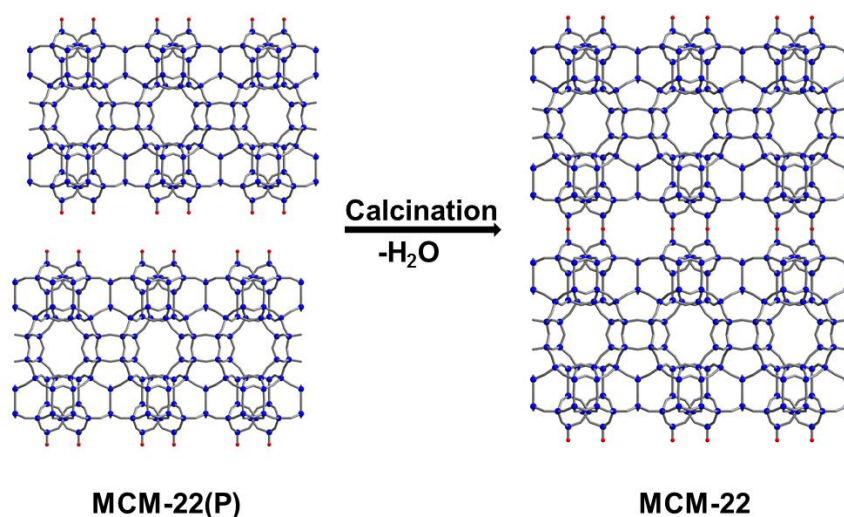


Fig. 1-14. Schematic representation of the transformation from MCM-22(P) to MCM-22.

Synthesis of zeolites from the 2D to 3D route requires the successful preparation of the layer structures. However, the targeted synthesis towards layered zeolite precursors is elusive. Moreover, up to now all the zeolites synthesized from 2D condensation are also available from the conventional hydrothermal route. Recently, the synthesis of the

“ADORable” zeolite was reported, where the “ADOR” refers to an “Assembly, Disassembly, Organization and Reassembly” process.<sup>162</sup> The **UTL** zeolite was used as the parental material and two new zeolite structures which have never been synthesized through hydrothermal route were obtained. The synthetic strategy is shown in Fig. 1-15. The **UTL** is hydrothermally synthesized from a hydrothermal procedure of the  $TO_4$  assembly. The structure can be considered as layer structures pillared by *d4rs*.<sup>29</sup> The *d4rs* are preferentially occupied by Ge atoms and are hydrolytically sensitive.<sup>163</sup> After hydrolysis in an acidic medium the *d4rs* dissolve, and the **UTL** structure is disassembled to the layer precursors. The subsequent organization and reassembly processes can lead to two new structures with different pore sizes: When the layer materials were treated with some organosilane compounds such as diethoxydimethylsilane (DEDMS), single 4-membered rings (S4Rs) were formed and connected the layers, resulting in an IPC-2 (structure type **OKO**<sup>164</sup>) with  $12 \times 10$  ring system structure; When no extra tetrahedral atom species was added during the process, the layers were directly condensed by forming the bridging oxygen and an IPC-4 (structure type **PCR**<sup>162</sup>) with even smaller  $10 \times 8$  ring system structure was obtained.

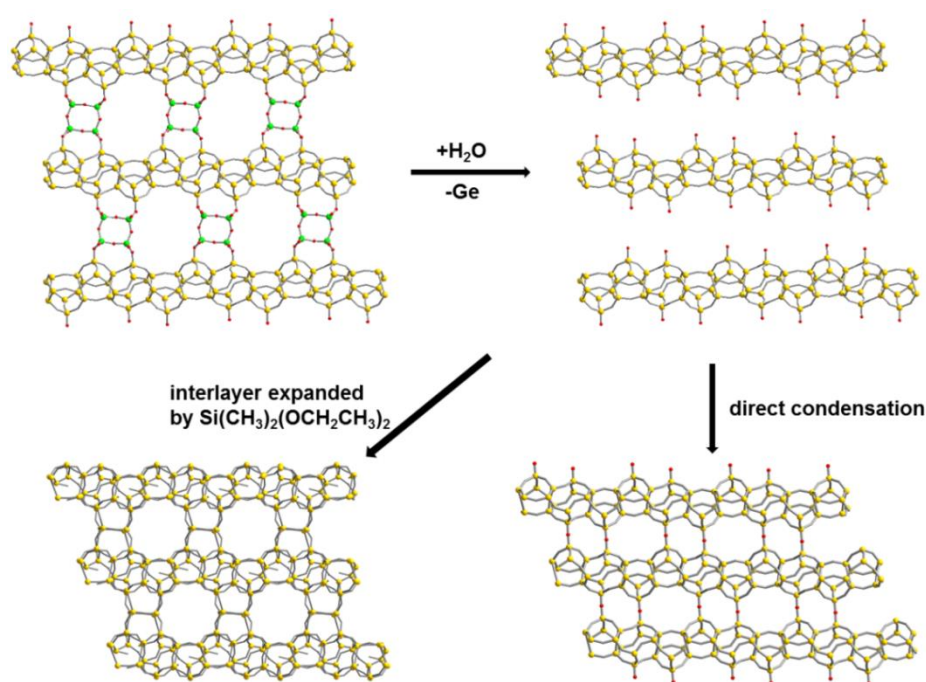


Fig. 1-15. Schematic shows the ADOR treatment of **UTL**-type zeolite. The zeolite **UTL** (top left) possesses the structure constructed by the 2D layers (shown in yellow) and the hydrolytically sensitive Ge-*d4rs* (shown in green); chemically selective cleavage leads to the layer structures (top right); connection of the layers by single 4-membered rings or bridging oxygen atoms (red balls) leads to the formation of zeolite **OKO** (bottom left) and **PCR** (bottom right), respectively.

The ADOR route establishes a new method to synthesize zeolites which cannot be achieved through hydrothermal route and will lead to more novel zeolite structures. Moreover, such a top-down and reassembly treatment provides a strategy to control and rationally design zeolites with desired pore sizes and chemical compositions. Another advantage is the structure of the “ADORable zeolites” obtained from the known zeolite is predictable by varying the limited connecting manners of the layers. The structure can be simply solved by comparing the experimental powder diffraction pattern with the calculated ones.

#### ***1.2.4 Applications of zeolites and zeolite analogues***

Zeolites and zeolite analogues possess some unique properties including the micropores of the molecular scale, the uniformly distributed pore sizes, and high surface area. Most of the zeolites are also of good thermal and chemical stability. Due to their structural characters and chemical compositions, these solids are of industrial and academic interest in many areas including ion-exchange,<sup>165-167</sup> catalysis,<sup>168-172</sup> adsorption<sup>173-176</sup> and host materials,<sup>177-180</sup> to name but a few.

The common inorganic cations present in natural zeolites are  $\text{Li}^+$ ,  $\text{Na}^+$ ,  $\text{K}^+$ ,  $\text{Mg}^{2+}$ ,  $\text{Ca}^{2+}$ ,  $\text{Ba}^{2+}$ , *etc.* These alkali and alkaline-earth metal cations can be readily exchanged by other cations. Therefore one important application of natural zeolites is removal of heavy metal elements from waste water.<sup>165-167</sup> The synthetic zeolites are also used for water softening in detergent powder by replacing the phosphates.<sup>181</sup>

In aluminosilicate zeolites, the framework is negatively charged due to the presence of the trivalent Al cations. A proton is attached to the oxygen atoms of the  $[\text{AlO}_4]^-$  and create a Brønsted acidic site (Fig. 1-16).<sup>168</sup> The acidic sites in the zeolite framework are of catalytic activity for oil refining and petrochemical reactions. For instance, zeolite Y (FAU) is the catalyst most used for the fluidized catalytic cracking (FCC) reaction to produce gasoline.<sup>182</sup> Moreover, the zeolites with various pore sizes and structural topologies can selectively interact with molecules depending on whether the shape and size of the molecule matches the dimensions and geometry of their pores. This feature results in the “shape selective catalysis” of zeolites for reagents with different sizes and shapes.<sup>170, 183</sup>

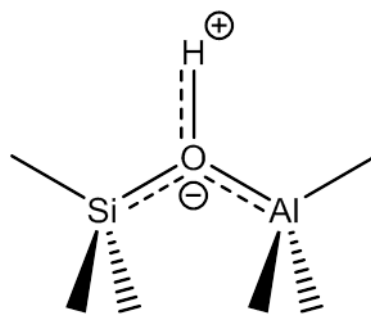


Fig. 1-16. Schematic shows the formation of the Brønsted acidic site in the zeolite framework.

The zeolite materials are also used as adsorbents and host materials due to their porous property and high surface area. Pressure Swing Adsorption (PSA) with zeolites is an effective method for gaseous mixture separation and hydrogen purification.<sup>184, 185</sup> Zeolite membranes are also used for effective separation of gaseous mixtures.<sup>186, 187</sup> As host materials, the channels and cavities of zeolite materials can constrain the reactions in the nano-sized spaces, leading to the formation of quantum dots, nano wires and some unusual molecules through a “ship in the bottle” synthetic strategies.<sup>179</sup> Dye molecules can be assembled in the channel of zeolites and zeolite analogues to give multi-functional materials with nonlinear optical or light harvesting properties.<sup>188, 189</sup>

### ***1.3 Introductions to Metal-Organic Frameworks (MOFs)***

#### ***1.3.1 A brief overview***

Another interesting research topic in the area of porous solids is the Metal-Organic Frameworks (MOFs). Since the first MOF material was reported by Robson *et al.* in 1994,<sup>190</sup> in the following two decades, thousands of MOF compounds with different structures were synthesized.<sup>191</sup> Many of them have different names such as Metal-Organic Frameworks (MOFs), Zeolitic Imidazolate Frameworks (ZIFs), Materials Institute Lavoisier (MILs) and Porous Coordination Polymers (PCPs).<sup>7-11</sup> The MOFs are usually constructed by the repeating motifs of central metal atoms (metal centres) and organic spacers (ligands) coordinated to the metals. Therefore the MOF is a subset of the coordination polymers, and is considered as a coordination network structure with potential voids.<sup>192</sup> The definitions of the related materials including the coordination polymers, coordination networks and the MOFs were recommended by IUPAC recently.<sup>192</sup>

The structures and properties of the MOFs have attracted much attention, owing to their potential applications in areas such as gas adsorption, drug delivery, separation and catalysis.<sup>174, 193-195</sup> As crystalline porous materials, the MOFs possess properties such as high surface area, uniform pore size distribution, and well crystalline porous structures, which make them similar to the zeolite materials in research interests. Nevertheless, the MOFs are different from the zeolite materials in many aspects: Compared to the zeolites, the MOFs have diverse chemical compositions of metal ions or clusters; the pore sizes of the MOF materials are controllable in a wide range which even goes to the mesoporous scales due to the feasibly tailored organic ligands;<sup>8, 196</sup> and the MOFs possess abundant structural topologies due to the multifarious coordination modes of the organic ligands to metal centres.<sup>12</sup>

### 1.3.2 The framework structure of MOFs

#### 1.3.2.1 The organic ligands

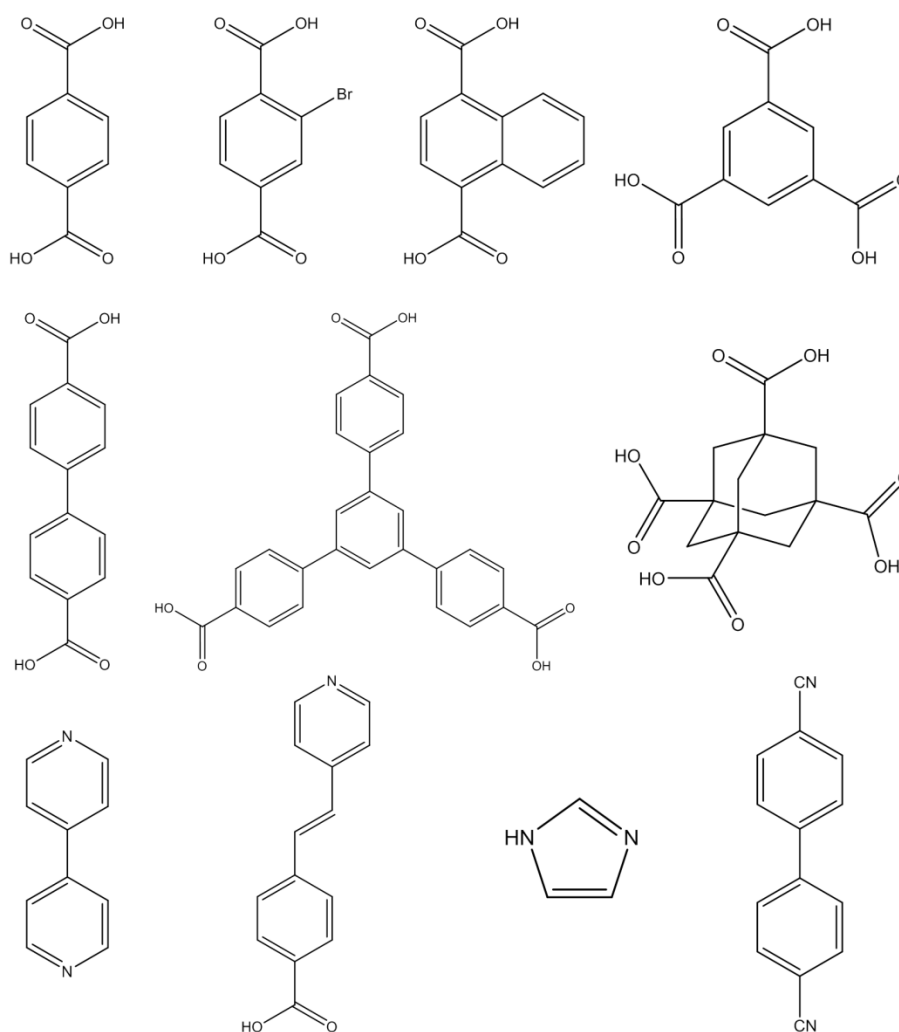


Fig. 1-17. Several commonly used organic ligands.

In MOF materials, the ligands usually have at least two donor atoms to link the discrete metal centres together. The ligands are called di-, tri- or tetrapodal depending on the number of the donor atoms.<sup>197</sup> The ligands usually possess rigid parts such as aromatic rings or adamantane in order to build up the network structures. The sizes of the rigid parts and the geometries of donor groups in the ligands are important to the pore sizes and the structures of the MOFs.<sup>198</sup> The organic ligands are readily tailored and functionalized, which is one reason of the presence of the numerous MOF compounds. Some references concluded the commonly used organic ligands in detail, and some typical ones are listed in Fig. 1-17.<sup>197, 199, 200</sup>

One of the most commonly used organic ligands is the compounds with the carboxylate groups. Each carboxylate group contains two oxygen atoms and can attach to one or more metal atoms in versatile modes.<sup>201</sup> Some of the coordination modes are shown in Fig. 1-18. Besides the carboxylate ligands, other ligands contain N-donor atoms such as bipyridine, imidazole and cyanide and ligands containing phosphate or sulfonate groups are also used for construction of MOF materials.<sup>202-206</sup> The versatile coordination modes of the ligand groups to the metals contribute to the structures of the MOF materials.

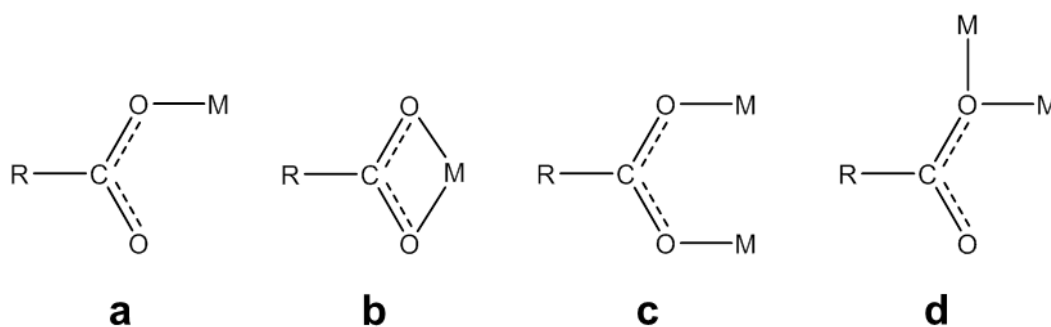


Fig. 1-18. Some coordination modes of carboxylate groups: (a) Monodentate coordination; (b) bidentate chelating; (c) bidentate bridging and (d) monatomic bridging.

### 1.3.2.2 The metal centres, the SBUs and the structures of MOF materials

The metal atoms in MOF material are the “nodes” of the network structure. The geometries of these nodes are important to the whole structure. The nodes can be either a single atom or a cluster which are surrounded by the coordination groups. In order to facilitate the description of the whole network structures, the concept of the secondary building units (SBUs) are introduced to describe the complete motifs including the metal centres and the coordination groups.<sup>207</sup> A review by Yaghi *et al.* identified 131

SBUs from crystals with carboxylate ligands.<sup>12</sup> The diversity of the SBU geometry and their compositions greatly enrich the structure of the MOF materials. The SBUs are extended to 3-dimensional structures by the linkage of the ligands. Two well-known MOF structures, their ligands and SBUs are shown in Fig. 1-19 as examples.

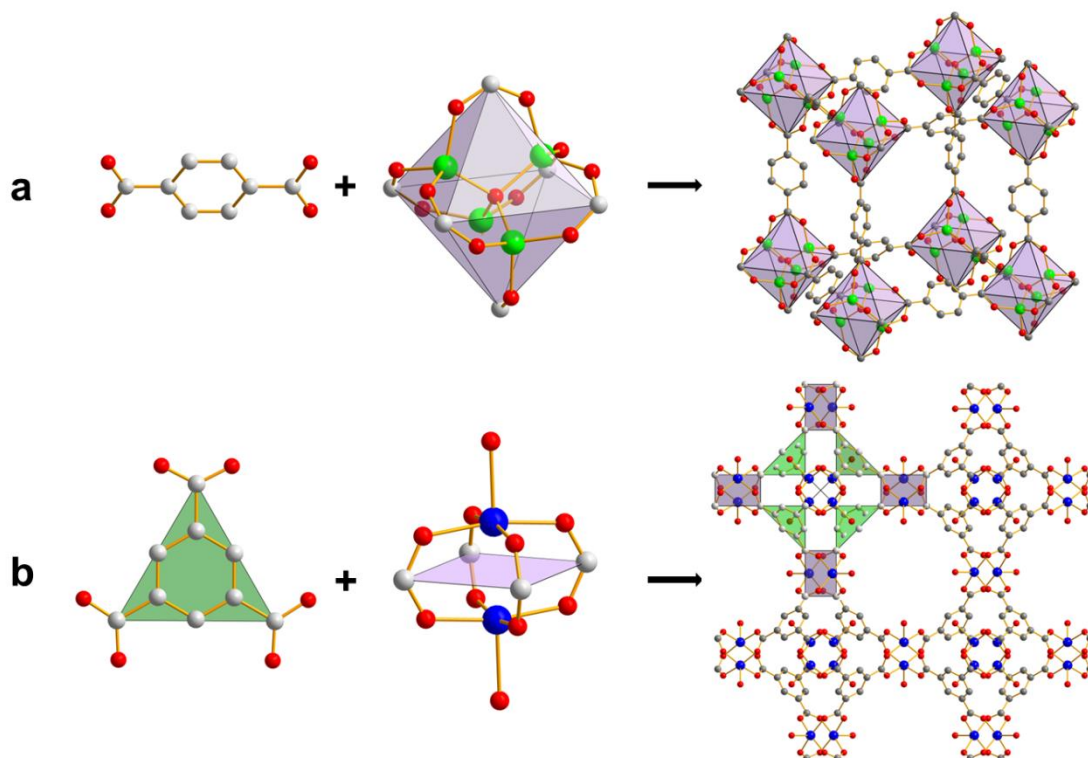


Fig. 1-19. (a) The ligand, SBU and the entire structure of MOF-5 framework; (b) the ligands, SBU and the structure of HKUST-1 viewed along the [100] direction. (Zn, green; Cu: blue; O: red; C: grey. H atoms are omitted for clarity.)

Fig. 1-19a is the structure of MOF-5.<sup>208</sup> Four Zn atoms (green balls) bond to one oxygen atom (red ball) forming a Zn<sub>4</sub>O tetrahedral cluster. Each edge of this tetrahedron is bidentate bridged by a carboxylate group from the ligand of 1, 4-benzenedicarboxylate (BDC). The resulting Zn<sub>4</sub>O(CO<sub>2</sub>)<sub>6</sub> cluster is an octahedral SBU with six extension points. These octahedral SBUs are connected by the benzene ring of BDC at the six vertexes, forming the cubic 3D infinite network structure.

Fig. 1-19b is the structure of HKUST-1, which represents the [Cu<sub>3</sub>(TMA)<sub>2</sub>(H<sub>2</sub>O)<sub>3</sub>]<sub>n</sub> (TMA is benzene-1, 3, 5-tricarboxylate). The compound was first reported by Williams *et al.* in 1999.<sup>209</sup> The carboxylate groups coordinate to the Cu<sub>2</sub> dimers in the bidentate bridging mode, resulting in a well-known paddle-wheel structure. Each Cu atom is square pyramidal coordinated, and its apical vertex is terminated by a water molecule. Therefore the SBU of the HKUST-1 is a square plane defined by the C atoms of the

TMA. The TMA ligands are the triangular shaped linkers which are shown as the green triangles in Fig. 1-19b. The SBUs and the ligands form the octahedral cages which stack to a cubic 3D structure. The structure shows a  $9 \times 9 \text{ \AA}^2$  window when viewed along [100] direction.

### 1.3.2.3 The IRMOFs

Compared with inorganic microporous materials, one advantage of MOFs is that the pore sizes and the surface area of a MOF material can be readily controlled while keeping the network topology identical to the original one. This can be achieved by replacing the ligands of the original MOF material with some carefully selected or modified organic compounds. This route is named isorecticular synthesis.

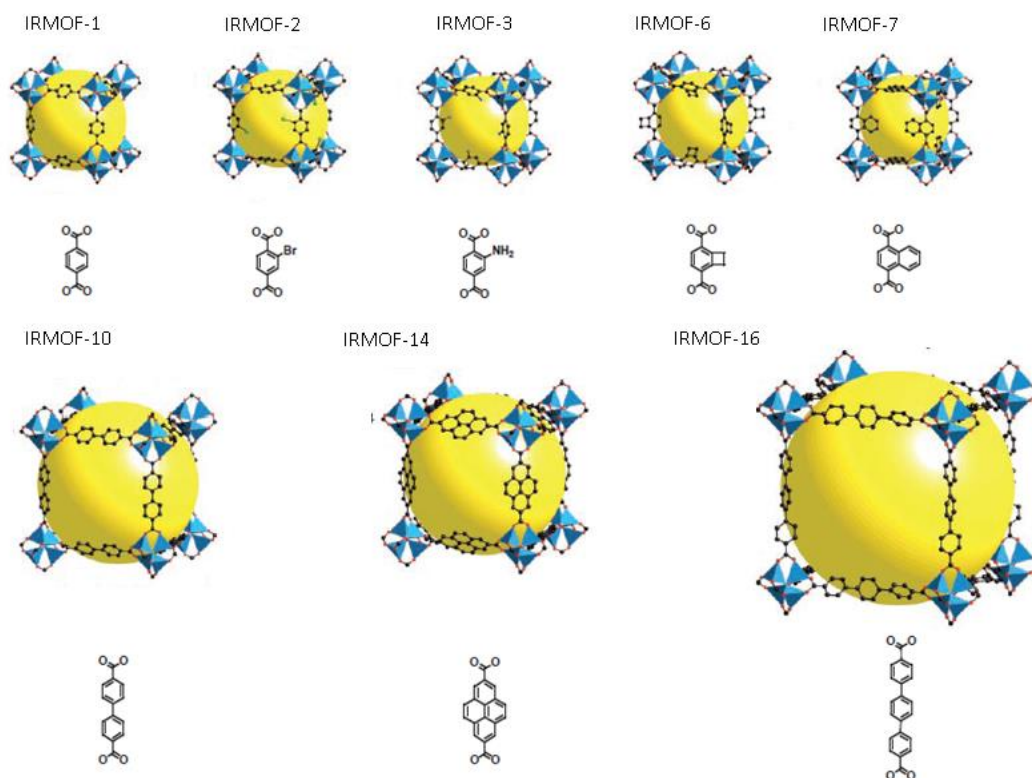


Fig. 1-20. The structures of several isorecticular MOFs (IRMOF-n, n=1, 2, 3, 6, 7, 10, 14, 16). The corresponding ligand of each structure is shown under the scheme. The picture is adopted from reference 8.

In 2002, a series of isorecticular MOFs (IRMOF-n) with the same framework topology to MOF-5 were systematically prepared by keeping the SBUs identical but modifying or expanding the ligands.<sup>8</sup> The obtained IRMOFs possess pore sizes varying from 0.38 nm to 2.88 nm (Fig.1-20). Some IRMOF compounds show good surface properties for gas adsorption. The pore size of IRMOF-6 (0.59nm) is considered suitable for methane

storage and the isotherm shows methane uptake of IRMOF-6 is 240 cm<sup>3</sup> (STP)/g at 298 K and 36 atm.

### 1.3.3 Guest molecules and the classification of MOFs

Usually there are some guest molecules located in the void space of the MOF materials. To activate the pores of the MOF materials, these guests need to be removed. Based on the structure transformation after removal of the guest molecules, the MOFs are classified in three categories, named first, second and third generation.<sup>210, 211</sup>

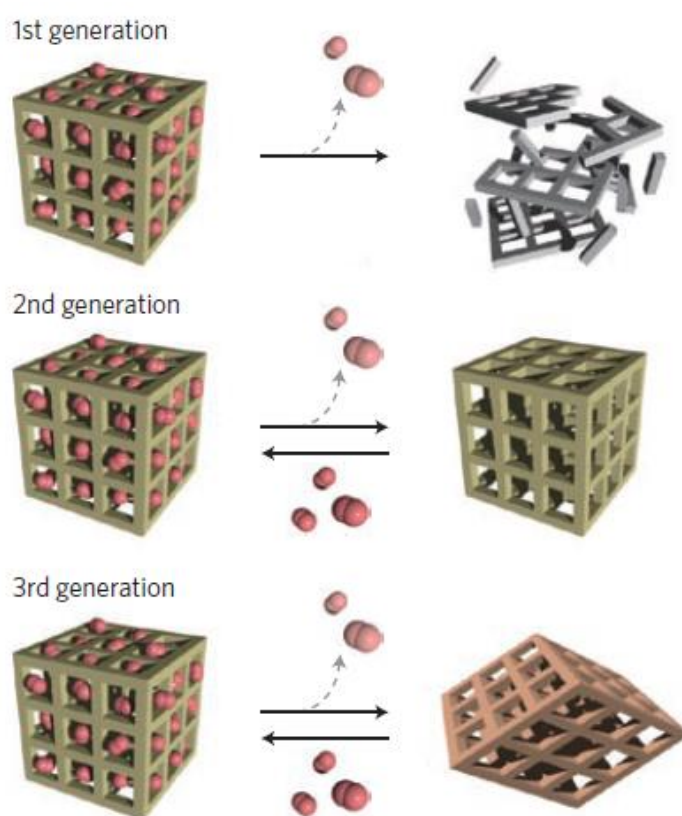


Fig. 1-21. Three categories of the MOF materials. The first generation materials collapse irreversibly after guest removal; the second generation materials possess robust structures when the guest molecules are removed and adsorbed; the third generation materials exhibit reversible structural flexibility. The picture is adopted from reference 211.

A representative illustration of the three generations of the MOF materials is shown in Fig. 1-21. The first generation compounds are unable to preserve their crystallinity after the removal of the guest molecules. The second generation compounds keep the original structures after removal or adsorption of the guest molecules. They possess robust network structures and have permanent pores. The third generation compounds are flexible structures and contain dynamic pores. They show a structural rearrangement

when the guest molecules are removed from the framework or are exchanged by other molecules.

Compared to the rigid and robust 2nd generation coordination polymers, the 3rd generation compounds are especially interesting for their adsorption. Their structures are changed in response to the different chemical interactions between the guests and the frameworks. This character is seen as a breathing effect or gate-opening effect.<sup>7, 212</sup> The dynamic porosity of the 3rd generation compounds is also potentially interesting for diverse areas such as drug delivery and sensing.<sup>213, 214</sup>

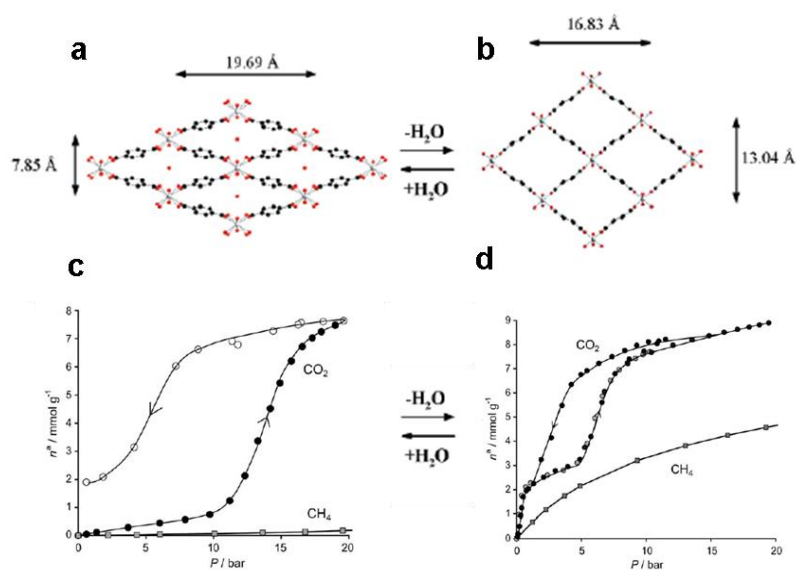


Fig. 1-22. Crystal structures of (a) hydrated MIL-53 and (b) dehydrated MIL-53. (c) is the adsorption isotherms of hydrated MIL-53(Cr) on CO<sub>2</sub> and CH<sub>4</sub>; (d) is the adsorption isotherms of dehydrated MIL-53(Cr) on CO<sub>2</sub> and CH<sub>4</sub>. The picture is adopted from references 7 and 215.

A classical 3rd generation MOF is the MIL-53, which was first reported by Ferey *et al.* in 2002.<sup>7</sup> The structure of the MIL-53 is built up by the metal centres of Cr<sup>3+</sup>, Al<sup>3+</sup> or Fe<sup>3+</sup> and the ligands of BDC. The metal centres (M) and the bridging OH groups form the 1D M(OH) chain. The carboxylate groups of the BDC coordinate to the metal centres and form the diamond shaped 1D channels along the direction of the M(OH) chains. Water molecules are located in the channels. A breathing phenomenon was observed in the dehydrate-hydrate process caused by the hydrogen-bond interactions between the water molecules and the framework. The pore dimension of the channels changes from  $7.85 \times 19.69 \text{ \AA}^2$  to  $13.04 \times 16.83 \text{ \AA}^2$  after the removal of the water molecules (Fig. 1-22 a and b). The adsorption selectivity for CO<sub>2</sub> over CH<sub>4</sub> of the MIL-53(Cr) was investigated.<sup>215</sup> The MIL-53(Cr) exhibits selective adsorption behaviour on

CO<sub>2</sub> over CH<sub>4</sub>. For the polar CO<sub>2</sub> molecules, the hydrated MIL-53(Cr) adsorbs very few CO<sub>2</sub> (less than 1 mmol/g) when the pressure is under 10 bar. While in the pressure range of 12 to 18 bar, the uptake of CO<sub>2</sub> dramatically increases to 7.7 mmol/g. The adsorption of CO<sub>2</sub> on dehydrated MIL-53(Cr) shows two steps at the pressure ranges of 0 to 5 bar and 5 to 20 bar, respectively. The uptake of CO<sub>2</sub> finally reaches to 8.5 mmol/g when the pressure is 20 bar. For the nonpolar CH<sub>4</sub> molecules, the uptake of methane on the hydrated MIL-53(Cr) is very low, which is probably because the channels are blocked by water. The uptake of methane on the dehydrated MIL-53(Cr) increases gradually to 4.6 mmol/g when the pressure is 20 bar (Fig. 1-22 c and d).

### ***1.3.4 Synthesis of MOF materials***

Some of the MOF materials are synthesized from the diffusion method. Solvent, organic amine or reagents are diffused into the synthetic system slowly for nucleation and crystal growth. This method usually takes very long time in order to obtain large single crystals, sometimes up to several weeks or months. Also the MOFs can be synthesized through hydrothermal or solvothermal routes. The metal salts, organic ligands and solvents are put in the sealed vessels and heated at a certain temperature. Sometimes temperature gradients are required. The advantages of these routes are the crystallization time is shortened to several days or even hours, and the solubility of the solvent to the reactant can be dramatically improved.

The diffusion method and the hydrothermal/solvothermal methods are the most commonly used methods for MOF synthesis. Recently other synthetic methods are also investigated. The ionothermal synthetic route is applied for the preparation of MOFs encouraged by the successes in their syntheses of zeolite analogues.<sup>216, 217</sup> Other novel synthetic routes such as microwave-assisted heating,<sup>218</sup> sonochemical synthesis<sup>219</sup> and mechanochemical synthesis<sup>220</sup> are also reported.

Although the formation of some special SBUs such as the paddle-wheel unit and the Zn<sub>4</sub>O(CO<sub>2</sub>)<sub>6</sub> have been reported, synthesis of novel structures is always unpredictable and challenging due to the various coordination modes of the ligands to the metal centres. Most of the MOFs are synthesized by trial-and-error. In 2008, Yaghi *et al.* reported the high-throughput method for synthesis of the zeolitic imidazolate frameworks (ZIFs) which are the MOF materials with imidazolate-based ligands.<sup>202</sup> 25

crystals were synthesized among 9600 micro-reactions, and 16 of them are new structures. Before this only 24 ZIF structures were reported. This high-throughput protocol is considered to be an efficient method for synthesis of MOF materials.

### ***1.3.5 Applications of MOF materials***

Compared to the inorganic microporous materials, some MOF materials exhibit extremely high surface areas. The zeolites usually have the surface areas below 1000 m<sup>2</sup>/g, while the surface areas of many MOFs are beyond this scale.<sup>191</sup> Therefore the MOF materials are greatly interested in the area of gas adsorptions. At present the methane storage and carbon dioxide uptake are the most interesting research topics due to the growing concerns on energy utilization and environmental protection. The MOF materials with high porosities and surface areas show good gas adsorption properties.<sup>8, 173, 221</sup>

Due to their well-defined crystalline structures, the MOF materials have uniform pore size distribution, which is similar to the zeolites. Therefore the MOFs possess some applications as “molecular sieves”. They are used as the matrix of the membrane or fixed bed for gaseous mixture separation.<sup>173, 174</sup> For example, Caro *et al.* reported the synthesis of a ZIF-8 membrane on the titania-alumina support and investigated its separation performance for ethene/ethane mixtures. The selectivity of the membrane at room temperature under 1 and 6 bar feed pressure are 2.8 and 2.4, respectively.<sup>222</sup> The molecular sieve separations for gaseous mixtures are considered as a cost-effective and environmentally benign method and have attracted increasing attention nowadays. The porous properties of the MOFs are also utilized for the application of catalysis.<sup>195</sup> The diverse compositions of the MOFs also make them as important luminescent and magnetic materials.<sup>223, 224</sup>

Recently the biology and medicinal applications of the MOF materials are developed by several research groups.<sup>213</sup> The MOFs are used for drug delivery due to their high surface areas. Moreover, the unsaturated metal sites of some MOF materials can adsorb the gas molecules with biology activities, such as Nitric Oxide (NO),<sup>225</sup> which is highly reactive with air. The NO adsorbed by MOF materials can be gradually released and its lifetime is dramatically extended.<sup>226</sup>

## 1.4 References

1. R. Pierotti and J. Rouquerol, *Pure Appl. Chem.*, 1985, **57**, 603-619.
2. J. Haber, *Pure Appl. Chem.*, 1991, **63**, 1227-1246.
3. S. T. Wilson, B. M. Lok, C. A. Messina, T. R. Cannan and E. M. Flanigen, *J. Am. Chem. Soc.*, 1982, **104**, 1146-1147.
4. M. E. Davis, *Nature*, 2002, **417**, 813-821.
5. P. Feng, X. Bu and G. D. Stucky, *Nature*, 1997, **388**, 735-741.
6. M. E. Davis, *Chem. Mater.*, 2013, **26**, 239-245.
7. C. Serre, F. Millange, C. Thouvenot, M. Noguès, G. Marsolier, D. Louër and G. Férey, *J. Am. Chem. Soc.*, 2002, **124**, 13519-13526.
8. M. Eddaoudi, K. Jaheon, N. Rosi, D. Vodak, J. Wachter, M. O'Keeffe and O. M. Yaghi, *Science*, 2002, **295**, 469-472.
9. A. Phan, C. J. Doonan, F. J. Uribe-Romo, C. B. Knobler, M. O'Keeffe and O. M. Yaghi, *Acc. Chem. Res.*, 2009, **43**, 58-67.
10. G. Férey, *Chem. Soc. Rev.*, 2008, **37**, 191-214.
11. S. Kitagawa, R. Kitaura and S. Noro, *Angew. Chem. Int. Ed. Engl.*, 2004, **43**, 2334-2375.
12. D. J. Tranchemontagne, J. L. Mendoza-Cortes, M. O'Keeffe and O. M. Yaghi, *Chem. Soc. Rev.*, 2009, **38**, 1257-1283.
13. M. E. Davis and R. F. Lobo, *Chem. Mater.*, 1992, **4**, 756-768.
14. A. Corma, in *Stud. Surf. Sci. Catal.*, eds. I. M. C. E. van Steen and L. H. Callanan, Elsevier, 2004, vol. Volume 154, Part A, pp. 25-40.
15. A. K. Cheetham, G. Férey and T. Loiseau, *Angew. Chem. Int. Ed.*, 1999, **38**, 3268-3292.
16. E. M. Flanigen, R. L. Patton and S. T. Wilson, in *Stud. Surf. Sci. Catal.*, eds. W. J. M. E. F. V. P.J. Grobet and G. Schulz-Ekloff, Elsevier, 1988, vol. Volume 37, pp. 13-27.
17. J. B. Parise, *Inorg. Chem.*, 1985, **24**, 4312-4316.
18. S. Feng and M. Greenblatt, *Chem. Mater.*, 1992, **4**, 462-468.
19. K.-H. Lii, *J. Chem. Soc., Dalton Trans.*, 1996, 819-822.
20. S. S. Dhingra and R. C. Haushalter, *J. Chem. Soc., Chem. Commun.*, 1993, 1665-1667.
21. M. M. Harding and B. M. Kariuki, *Acta Crystallographica Section C*, 1994, **50**, 852-854.
22. E. M. Flanigen, B. M. Lok, R. L. Patton and S. T. Wilson, in *Stud. Surf. Sci. Catal.*, eds. A. I. Y. Murakami and J. W. Ward, Elsevier, 1986, vol. Volume 28, pp. 103-112.
23. M. E. Davis, C. Saldarriaga, C. Montes, J. Garces and C. Crowdert, *Nature*, 1988, **331**, 698-699.
24. J. M. Bennett, J. W. Richardson Jr, J. J. Pluth and J. V. Smith, *Zeolites*, 1987, **7**, 160-162.
25. B. M. Lok, C. A. Messina, R. L. Patton, R. T. Gajek, T. R. Cannan and E. M. Flanigen, *J. Am. Chem. Soc.*, 1984, **106**, 6092-6093.
26. R.M. Barrer, *Pure Appl. Chem.* 51, 1979, 1091-1100.
27. G. T. Kokotailo, S. L. Lawton, D. H. Olson and W. M. Meier, *Nature*, 1978, **272**, 437-438.
28. E. M. Flanigen, J. M. Bennett, R. W. Grose, J. P. Cohen, R. L. Patton, R. M. Kirchner and J. V. Smith, *Nature*, 1978, **271**, 512-516.
29. J.-L. Paillaud, B. Harbuzaru, J. Patarin and N. Bats, *Science*, 2004, **304**, 990-992.
30. A. Corma, M. J. Diaz-Cabanas, F. Rey, S. Nicolopoulos and K. Boulaya, *Chem. Commun.*, 2004, 1356-1357.
31. H. van Koningsveld, *Compendium of Zeolite Framework Types. Building Schemes and Type Characteristics*, Elsevier, Amsterdam, 2007
32. S. Merlino, *Acta Cryst A.* (1981). A37, C189
33. T. Nakagawa, K. Kihara and K. Harada, *Am. Mineral.*, 2001, **86**, 1506-1512.
34. C. Baerlocher, L. B. McCusker and D. H. Olson, *Atlas of zeolite framework types*, Elsevier, 2007.
35. M. E. Davis, *Chem.-Eur. J.*, 1997, **3**, 1745-1750.
36. J. Jiang, J. Yu and A. Corma, *Angew. Chem. Int. Ed.*, 2010, **49**, 3120-3145.
37. L. McCusker, F. Liebau and G. Engelhardt, *Pure Appl. Chem.*, 2001, **73**, 381-394.

38. T. B. Reed and D. W. Breck, *J. Am. Chem. Soc.*, 1956, **78**, 5972-5977.
39. C. S. Cundy and P. A. Cox, *Microporous Mesoporous Mater.*, 2005, **82**, 1-78.
40. J. C. van der Waal, M. S. Rigutto and H. van Bekkum, *J. Chem. Soc., Chem. Commun.*, 1994, 1241-1242.
41. M. A. Camblor, M. Costantini, A. Corma, L. Gilbert, P. Esteve, A. Martinez and S. Valencia, *Chem. Commun.*, 1996, 1339-1340.
42. S. T. Wilson, in *Stud. Surf. Sci. Catal.*, eds. E. M. F. P. A. J. H. van Bekkum and J. C. Jansen, Elsevier, 2001, vol. Volume 137, pp. 229-260.
43. N. Bats, L. Rouleau, J. L. Paillaud, P. Caullet, Y. Mathieu and S. Lacombe, in *Stud. Surf. Sci. Catal.*, eds. I. M. C. E. van Steen and L. H. Callanan, Elsevier, 2004, vol. Volume 154, Part A, pp. 283-288.
44. R. Castañeda, A. Corma, V. Fornés, F. Rey and J. Rius, *J. Am. Chem. Soc.*, 2003, **125**, 7820-7821.
45. G. Sastre, A. Pulido, R. Castañeda and A. Corma, *J. Phys. Chem. B*, 2004, **108**, 8830-8835.
46. F. Delprato, L. Delmotte, J. L. Guth and L. Huve, *Zeolites*, 1990, **10**, 546-552.
47. S. L. Lawton and W. J. Rohrbaugh, *Science*, 1990, **247**, 1319-1322.
48. S. B. Hong, H. M. Cho and M. E. Davis, *J. Phys. Chem.*, 1993, **97**, 1622-1628.
49. G. W. Noble, P. A. Wright and A. Kvik, *J. Chem. Soc., Dalton Trans.*, 1997, 4485-4490.
50. A. F. Cronstedt, *Akad. Handl. Stockholm*, 17 (1756) 120.
51. S. Wang and Y. Peng, *Chem. Eng. J.*, 2010, **156**, 11-24.
52. Pluth, J.J. and Smith, J.V., *Am. Mineral.*, 75, 501-507 (1990)
53. Effenberger, H., Giester, G., Krause, W. and Bernhardt, H.J., *Am. Mineral.*, 83, 607-617 (1998)
54. R. M. Barrer, *J. Chem. Soc.*, 1948, 127-132.
55. E. M. Flanigen, in *Stud. Surf. Sci. Catal.*, eds. E. M. F. H. van Bekkum and J. C. Jansen, Elsevier, 1991, vol. Volume 58, pp. 13-34.
56. R. M. Barrer, J. W. Baynham, F. W. Bultitude and W. M. Meier, *J. Chem. Soc.*, 1959, 195-208.
57. J. A. Rabo and M. W. Schoonover, *Applied Catalysis A: General*, 2001, **222**, 261-275.
58. V. J. Frilette, P. B. Weisz and R. L. Golden, *J. Catal.*, 1962, **1**, 301-306.
59. P. B. Weisz and V. J. Frilette, *J. Phys. Chem.*, 1960, **64**, 382-382.
60. A. J. Kidnay and M. J. Hiza, *AIChE J.*, 1966, **12**, 58-63.
61. R. M. Barrer and P. J. Denny, *J. Chem. Soc.*, 1961, 971-982.
62. G. T. Kerr, *Inorg. Chem.*, 1966, **5**, 1537-1539.
63. J. M. Newsam, M. M. J. Treacy, W. T. Koetsier and C. B. D. Gruyter, *Proceedings of the Royal Society of London. A. Mathematical and Physical Sciences*, 1988, **420**, 375-405.
64. H. van Koningsveld, H. van Bekkum and J. C. Jansen, *Acta Crystallographica Section B*, 1987, **43**, 127-132.
65. G. T. Kokotailo, P. Chu, S. L. Lawton and W. M. Meier, *Nature*, 1978, **275**, 119-120.
66. D. M. Bibby, N. B. Milestone and L. P. Aldridge, *Nature*, 1979, **280**, 664-665.
67. R. Fricke, H. Kosslick, G. Lischke and M. Richter, *Chem. Rev.*, 2000, **100**, 2303-2406.
68. M. Estermann, L. B. McCusker, C. Baerlocher, A. Merrouche and H. Kessler, *Nature*, 1991, **352**, 320-323.
69. A. Corma, M. T. Navarro, F. Rey, J. Rius and S. Valencia, *Angew. Chem. Int. Ed.*, 2001, **40**, 2277-2280.
70. T. Blasco, A. Corma, M. J. Díaz-Cabañas, F. Rey, J. A. Vidal-Moya and C. M. Zicovich-Wilson, *J. Phys. Chem. B*, 2002, **106**, 2634-2642.
71. G. O. Bnmner and W. M. Meier, *Nature*, 1989, **337**, 146-147.
72. A. Corma, F. Rey, S. Valencia, J. L. Jorda and J. Rius, *Nat. Mater.*, 2003, **2**, 493-497.
73. A. Corma, M. J. Díaz-Cabanás, J. L. Jorda, C. Martinez and M. Moliner, *Nature*, 2006, **443**, 842-845.
74. A. Corma, M. J. Díaz-Cabañas, J. Jiang, M. Afeworki, D. L. Dorset, S. L. Soled and K. G. Strohmaier, *Proceedings of the National Academy of Sciences*, 2010, **107**, 13997-14002.

75. J. Jiang, J. L. Jorda, M. J. Diaz-Cabanas, J. Yu and A. Corma, *Angew. Chem. Int. Ed.*, 2010, **49**, 4986-4988.
76. M. Dodin, J.-L. Paillaud, Y. Lorgouilloux, P. Caullet, E. Elkaïm and N. Bats, *J. Am. Chem. Soc.*, 2010, **132**, 10221-10223.
77. Y. Lorgouilloux, M. Dodin, J.-L. Paillaud, P. Caullet, L. Michelin, L. Josien, O. Ersen and N. Bats, *J. Solid State Chem.*, 2009, **182**, 622-629.
78. C. S. Cundy and P. A. Cox, *Chem. Rev.*, 2003, **103**, 663-702.
79. J. Yu, in *Stud. Surf. Sci. Catal.*, eds. H. v. B. A. C. Jiří Čejka and S. Ferdi, Elsevier, 2007, vol. Volume 168, pp. 39-103.
80. R. I. Walton, F. Millange, D. O'Hare, A. T. Davies, G. Sankar and C. R. A. Catlow, *J. Phys. Chem. B*, 2000, **105**, 83-90.
81. D. W. Breck, *J. Chem. Educ.*, 1964, **41**, 678.
82. G. T. Kerr, *J. Phys. Chem.*, 1966, **70**, 1047-1050.
83. J. Ciric, *J. Colloid Interface Sci.*, 1968, **28**, 315-324.
84. W. Xu, J. Dong, J. Li, J. Li and F. Wu, *J. Chem. Soc., Chem. Commun.*, 1990, 755-756.
85. M. Matsukata, M. Ogura, T. Osaki, P. Hari Prasad Rao, M. Nomura and E. Kikuchi, *Top. Catal.*, 1999, **9**, 77-92.
86. P. Wenqin, S. Ueda and M. Koizumi, in *Stud. Surf. Sci. Catal.*, eds. A. I. Y. Murakami and J. W. Ward, Elsevier, 1986, vol. Volume 28, pp. 177-184.
87. S. Kasahara, K. Itabashi and K. Igawa, in *Stud. Surf. Sci. Catal.*, eds. A. I. Y. Murakami and J. W. Ward, Elsevier, 1986, vol. Volume 28, pp. 185-192.
88. S. Ueda, N. Kageyama, M. Koizumi, S. Kobayashi, Y. Fujiwara and Y. Kyogoku, *J. Phys. Chem.*, 1984, **88**, 2128-2131.
89. L. Angell C and H. Flank W, in *Molecular Sieves?II*, American Chemical Society, 1977, vol. 40, pp. 194-206.
90. R. M. Barrer, R. Beaumont and C. Collela, *J. Chem. Soc., Dalton Trans.*, 1974, 934-941.
91. M. Goepper, H.-X. Li and M. E. Davis, *J. Chem. Soc., Chem. Commun.*, 1992, 1665-1666.
92. S. L. Burkett and M. E. Davis, *Chem. Mater.*, 1995, **7**, 1453-1463.
93. S. L. Burkett and M. E. Davis, *J. Phys. Chem.*, 1994, **98**, 4647-4653.
94. A. V. Goretsky, L. W. Beck, S. I. Zones and M. E. Davis, *Microporous Mesoporous Mater.*, 1999, **28**, 387-393.
95. Y. Kubota, M. M. Helmkamp, S. I. Zones and M. E. Davis, *Microporous Mater.*, 1996, **6**, 213-229.
96. A. W. Burton, S. I. Zones and S. Elomari, *Curr. Opin. Colloid Interface Sci.*, 2005, **10**, 211-219.
97. A. W. Burton and S. I. Zones, in *Stud. Surf. Sci. Catal.*, eds. H. v. B. A. C. Jiří Čejka and S. Ferdi, Elsevier, 2007, vol. Volume 168, pp. 137-179.
98. M. Moliner, F. Rey and A. Corma, *Angew. Chem. Int. Ed.*, 2013, **52**, 13880-13889.
99. M. A. Camblor, M.-J. Díaz-Cabañas, J. Perez-Pariente, S. J. Teat, W. Clegg, I. J. Shannon, P. Lightfoot, P. A. Wright and R. E. Morris, *Angew. Chem. Int. Ed.*, 1998, **37**, 2122-2126.
100. P. Wagner, S. I. Zones, M. E. Davis and R. C. Medrud, *Angew. Chem. Int. Ed.*, 1999, **38**, 1269-1272.
101. A. Burton, S. Elomari, R. C. Medrud, I. Y. Chan, C.-Y. Chen, L. M. Bull and E. S. Vittoratos, *J. Am. Chem. Soc.*, 2003, **125**, 1633-1642.
102. A. Burton, S. Elomari, C.-Y. Chen, R. C. Medrud, I. Y. Chan, L. M. Bull, C. Kibby, T. V. Harris, S. I. Zones and E. S. Vittoratos, *Chem.-Eur. J.*, 2003, **9**, 5737-5748.
103. A. Burton and S. Elomari, *Chem. Commun.*, 2004, 2618-2619.
104. D. J. Earl, A. W. Burton, T. Rea, K. Ong, M. W. Deem, S.-J. Hwang and S. I. Zones, *J. Phys. Chem. C*, 2008, **112**, 9099-9105.
105. C. Avelino, P. Marta, R. Fernando, S. Gopinathan and J. T. Simon, *Angew. Chem. Int. Ed.*, 2003, **42**, 1156-1159.
106. Y. Mathieu, J.-L. Paillaud, P. Caullet and N. Bats, *Microporous Mesoporous Mater.*, 2004, **75**, 13-22.
107. R. Simancas, D. Dari, N. Velamazán, M. T. Navarro, A. Cantín, J. L. Jordá, G. Sastre, A. Corma and F. Rey, *Science*, 2010, **330**, 1219-1222.

108. D. L. Dorset, G. J. Kennedy, K. G. Strohmaier, M. J. Diaz-Cabañas, F. Rey and A. Corma, *J. Am. Chem. Soc.*, 2006, **128**, 8862-8867.
109. A. Corma, M. J. Diaz-Cabanás, J. L. Jorda, F. Rey, G. Sastre and K. G. Strohmaier, *J. Am. Chem. Soc.*, 2008, **130**, 16482-16483.
110. C. C. Freyhardt, M. Tsapatsis, R. F. Lobo, K. J. Balkus and M. E. Davis, *Nature*, 1996, **381**, 295-298.
111. C. Baerlocher, L. B. McCusker and R. Chiappetta, *Microporous Mater.*, 1994, **2**, 269-280.
112. M. Choi, K. Na, J. Kim, Y. Sakamoto, O. Terasaki and R. Ryoo, *Nature*, 2009, **461**, 246-249.
113. K. Na, C. Jo, J. Kim, K. Cho, J. Jung, Y. Seo, R. J. Messinger, B. F. Chmelka and R. Ryoo, *Science*, 2011, **333**, 328-332.
114. R. Morris, *Top. Catal.*, 2010, **53**, 1291-1296.
115. Z. Lin, A. M. Z. Slawin and R. E. Morris, *J. Am. Chem. Soc.*, 2007, **129**, 4880-4881.
116. R. E. Morris and X. Bu, *Nature Chem.*, 2010, **2**, 353-361.
117. H. Lee, S. I. Zones and M. E. Davis, *Nature*, 2003, **425**, 385-388.
118. B. Xie, J. Song, L. Ren, Y. Ji, J. Li and F.-S. Xiao, *Chem. Mater.*, 2008, **20**, 4533-4535.
119. X. Meng and F.-S. Xiao, *Chem. Rev.*, 2013, **114**, 1521-1543.
120. G. Majano, A. Darwiche, S. Mintova and V. Valtchev, *Ind. Eng. Chem. Res.*, 2009, **48**, 7084-7091.
121. M. B. Park, S. J. Cho and S. B. Hong, *J. Am. Chem. Soc.*, 2011, **133**, 1917-1934.
122. A. Corma and M. E. Davis, *ChemPhysChem*, 2004, **5**, 304-313.
123. E. Flanigen, R. L. Patton, US Patent 4 073 684, 1978.
124. J. L. Guth, H. Kessler and R. Wey, in *Stud. Surf. Sci. Catal.*, eds. A. I. Y. Murakami and J. W. Ward, Elsevier, 1986, vol. Volume 28, pp. 121-128.
125. S. Qiu, J. Yu, G. Zhu, O. Terasaki, Y. Nozue, W. Pang and R. Xu, *Microporous Mesoporous Mater.*, 1998, **21**, 245-251.
126. S. Qiu, W. Pang, H. Kessler and J.-L. Guth, *Zeolites*, 1989, **9**, 440-444.
127. M. A. Cambor, L. A. Villaescusa and M. J. Díaz-Cabañas, *Top. Catal.*, 1999, **9**, 59-76.
128. H. Koller, A. Wölker, L. A. Villaescusa, M. J. Díaz-Cabañas, S. Valencia and M. A. Cambor, *J. Am. Chem. Soc.*, 1999, **121**, 3368-3376.
129. N. Rajić, R. Gabrovšek, A. Ristić and V. Kaučič, *Thermochim. Acta*, 1997, **306**, 31-36.
130. G. Sastre, J. A. Vidal-Moya, T. Blasco, J. Rius, J. L. Jordá, M. T. Navarro, F. Rey and A. Corma, *Angew. Chem. Int. Ed.*, 2002, **41**, 4722-4726.
131. L. A. Villaescusa, P. Lightfoot and R. E. Morris, *Chem. Commun.*, 2002, 2220-2221.
132. D. M. Bibby and M. P. Dale, *Nature*, 1985, **317**, 157-158.
133. H. Qisheng, F. Shouhua and X. Ruren, *J. Chem. Soc., Chem. Commun.*, 1988, 1486-1487.
134. A. Kuperman, S. Nadimi, S. Oliver, G. A. Ozin, J. M. Garces and M. M. Olken, *Nature*, 1993, **365**, 239-242.
135. Q. Huo, R. Xu, S. Li, Z. Ma, J. M. Thomas, R. H. Jones and A. M. Chippindale, *J. Chem. Soc., Chem. Commun.*, 1992, 875-876.
136. R. H. Jones, J. M. Thomas, J. Chen, R. Xu, Q. Huo, S. Li, Z. Ma and A. M. Chippindale, *J. Solid State Chem.*, 1993, **102**, 204-208.
137. N. V. Plechkova and K. R. Seddon, *Chem. Soc. Rev.*, 2008, **37**, 123-150.
138. P. Wasserscheid and W. Keim, *Angew. Chem. Int. Ed.*, 2000, **39**, 3772-3789.
139. T. Welton, *Chem. Rev.*, 1999, **99**, 2071-2084.
140. J. D. Holbrey and K. R. Seddon, *Clean Products and Processes*, 1999, **1**, 223-236.
141. J. G. Huddleston and R. D. Rogers, *Chem. Commun.*, 1998, 1765-1766.
142. R. Sheldon, *Chem. Commun.*, 2001, 2399-2407.
143. J. S. Wilkes, J. A. Levisky, R. A. Wilson and C. L. Hussey, *Inorg. Chem.*, 1982, **21**, 1263-1264.
144. Z. Ma, J. Yu and S. Dai, *Adv. Mater.*, 2010, **22**, 261-285.
145. E. R. Cooper, C. D. Andrews, P. S. Wheatley, P. B. Webb, P. Wormald and R. E. Morris, *Nature*, 2004, **430**, 1012-1016.
146. R. Cai, M. Sun, Z. Chen, R. Munoz, C. O'Neill, D. E. Beving and Y. Yan, *Angew. Chem. Int. Ed.*, 2008, **47**, 525-528.

147. J. Hoffmann, M. Nuchter, B. Ondruschka and P. Wasserscheid, *Green Chem.*, 2003, **5**, 296-299.
148. R. E. Morris, *Chem. Commun.*, 2009, 2990-2998.
149. R. E. Morris, in *Stud. Surf. Sci. Catal.*, eds. P. M. Antoine Gédéon and B. Florence, Elsevier, 2008, vol. Volume 174, Part A, pp. 33-42.
150. Y. C. Ma, Y. P. Xu, S. J. Wang, B. C. Wang, Z. J. Tian, J. Y. Yu and L. W. Lin, *Chemical Journal of Chinese Universities-Chinese*, 2006, **27**, 739-741.
151. P. S. Wheatley, P. K. Allan, S. J. Teat, S. E. Ashbrook and R. E. Morris, *Chem. Sci.*, 2010, **1**, 483-487.
152. R. Cai, Y. Liu, S. Gu and Y. Yan, *J. Am. Chem. Soc.*, 2010, **132**, 12776-12777.
153. L. Ren, Q. Wu, C. Yang, L. Zhu, C. Li, P. Zhang, H. Zhang, X. Meng and F.-S. Xiao, *J. Am. Chem. Soc.*, 2012, **134**, 15173-15176.
154. Y. Jin, Q. Sun, G. Qi, C. Yang, J. Xu, F. Chen, X. Meng, F. Deng and F.-S. Xiao, *Angew. Chem. Int. Ed.*, 2013, **52**, 9172-9175.
155. R. Millini, G. Perego, W. O. Parker Jr, G. Bellussi and L. Carluccio, *Microporous Mater.*, 1995, **4**, 221-230.
156. A. Corma, V. Fornés, J. Martínez-Triguero and S. B. Pergher, *J. Catal.*, 1999, **186**, 57-63.
157. M. E. Leonowicz, J. A. Lawton, S. L. Lawton and M. K. Rubin, *Science*, 1994, **264**, 1910-1913.
158. L. Schreyeck, P. Caullet, J. C. Mougénel, J. L. Guth and B. Marler, *Microporous Mater.*, 1996, **6**, 259-271.
159. S. Zanardi, A. Alberti, G. Cruciani, A. Corma, V. Fornés and M. Brunelli, *Angew. Chem. Int. Ed.*, 2004, **43**, 4933-4937.
160. Y. J. He, G. S. Nivarthi, F. Eder, K. Seshan and J. A. Lercher, *Microporous Mesoporous Mater.*, 1998, **25**, 207-224.
161. C. T. Kresge and W. J. Roth, US Patent No. 5266541 (1993).
162. W. J. Roth, P. Nachtigall, R. E. Morris, P. S. Wheatley, V. R. Seymour, S. E. Ashbrook, P. Chlubná, L. Grajciar, M. Položij, A. Zukal, O. Shvets and J. Čejka, *Nature Chem.*, 2013, **5**, 628-633.
163. W. J. Roth, O. V. Shvets, M. Shamzhy, P. Chlubná, M. Kubů, P. Nachtigall and J. Čejka, *J. Am. Chem. Soc.*, 2011, **133**, 6130-6133.
164. E. Verheyen, L. Joos, K. Van Havenbergh, E. Breynaert, N. Kasian, E. Gobechiya, K. Houthoofd, C. Martineau, M. Hinterstein, F. Taulelle, V. Van Speybroeck, M. Waroquier, S. Bals, G. Van Tendeloo, C. E. A. Kirschhock and J. A. Martens, *Nat. Mater.*, 2012, **11**, 1059-1064.
165. L. Čurković, Š. Cerjan-Stefanović and T. Filipan, *Water Res.*, 1997, **31**, 1379-1382.
166. G. Blanchard, M. Maunay and G. Martin, *Water Res.*, 1984, **18**, 1501-1507.
167. E. Álvarez-Ayuso, A. García-Sánchez and X. Querol, *Water Res.*, 2003, **37**, 4855-4862.
168. A. Corma, *Chem. Rev.*, 1995, **95**, 559-614.
169. R. J. Davis, *J. Catal.*, 2003, **216**, 396-405.
170. A. Corma, *J. Catal.*, 2003, **216**, 298-312.
171. R. Gounder and M. E. Davis, *AIChE J.*, 2013, **59**, 3349-3358.
172. L. Ma, C. Abney and W. Lin, *Chem. Soc. Rev.*, 2009, **38**, 1248-1256.
173. A. U. Czaja, N. Trukhan and U. Muller, *Chem. Soc. Rev.*, 2009, **38**, 1284-1293.
174. J.-R. Li, R. J. Kuppler and H.-C. Zhou, *Chem. Soc. Rev.*, 2009, **38**, 1477-1504.
175. K. T. Chue, J. N. Kim, Y. J. Yoo, S. H. Cho and R. T. Yang, *Ind. Eng. Chem. Res.*, 1995, **34**, 591-598.
176. V. Cottier, J.-P. Bellat, M.-H. Simonot-Grange and A. Méthivier, *J. Phys. Chem. B*, 1997, **101**, 4798-4802.
177. G. Calzaferri, S. Huber, H. Maas and C. Minkowski, *Angew. Chem. Int. Ed.*, 2003, **42**, 3732-3758.
178. N. Herron, Y. Wang, M. M. Eddy, G. D. Stucky, D. E. Cox, K. Moller and T. Bein, *J. Am. Chem. Soc.*, 1989, **111**, 530-540.
179. A. Corma and H. Garcia, *Eur. J. Inorg. Chem.*, 2004, **2004**, 1143-1164.

180. Z. M. Li, Z. K. Tang, H. J. Liu, N. Wang, C. T. Chan, R. Saito, S. Okada, G. D. Li, J. S. Chen, N. Nagasawa and S. Tsuda, *Phys. Rev. Lett.*, 2001, **87**, 127401.
181. C. Fruijtier-Pöllöth, *Arch. Toxicol.*, 2009, **83**, 23-35.
182. C. J. Plank, E. J. Rosinski and W. P. Hawthorne, *I&EC Product Research and Development*, 1964, **3**, 165-169.
183. J. Dwyer, *Nature*, 1989, **339**, 174-175.
184. M. W. Ackley, S. U. Rege and H. Saxena, *Microporous Mesoporous Mater.*, 2003, **61**, 25-42.
185. S. Sircar and T. C. Golden, *Sep. Sci. Technol.*, 2000, **35**, 667-687.
186. X. Yin, G. S. Zhu, W. Yang, Y. Li, G. Q. Zhu, R. Xu, J. Sun, S. Qiu and R. R. Xu, *Adv. Mater.*, 2005, **17**, 2006-2010.
187. K. Kusakabe, T. Kuroda, A. Murata and S. Morooka, *Ind. Eng. Chem. Res.*, 1997, **36**, 649-655.
188. S. D. Cox, T. E. Gier, G. D. Stucky and J. Bierlein, *J. Am. Chem. Soc.*, 1988, **110**, 2986-2987.
189. S. Megelski and G. Calzaferri, *Adv. Funct. Mater.*, 2001, **11**, 277-286.
190. B. F. Abrahams, B. F. Hoskins, D. M. Michail and R. Robson, *Nature*, 1994, **369**, 727-729.
191. H. Furukawa, K. E. Cordova, M. O'Keeffe and O. M. Yaghi, *Science*, 2013, **341**, 6149.
192. S. R. Batten, N. R. Champness, X.-M. Chen, J. Garcia-Martinez, S. Kitagawa, L. Öhrström, M. O'Keeffe, M. P. Suh and J. Reedijk, *Pure Appl. Chem.*, 2013, **85**.
193. R. E. Morris and P. S. Wheatley, *Angew. Chem. Int. Ed.*, 2008, **47**, 4966-4981.
194. P. Horcajada, R. Gref, T. Baati, P. K. Allan, G. Maurin, P. Couvreur, G. Férey, R. E. Morris and C. Serre, *Chem. Rev.*, 2011, **112**, 1232-1268.
195. J. Lee, O. K. Farha, J. Roberts, K. A. Scheidt, S. T. Nguyen and J. T. Hupp, *Chem. Soc. Rev.*, 2009, **38**, 1450-1459.
196. H. Deng, S. Grunder, K. E. Cordova, C. Valente, H. Furukawa, M. Hmadeh, F. Gándara, A. C. Whalley, Z. Liu, S. Asahina, H. Kazumori, M. O'Keeffe, O. Terasaki, J. F. Stoddart and O. M. Yaghi, *Science*, 2012, **336**, 1018-1023.
197. C. Janiak, *Dalton Trans.*, 2003, 2781-2804.
198. M. Eddaoudi, J. Kim, N. Rosi, D. Vodak, J. Wachter, M. O'Keeffe and O. M. Yaghi, *Science*, 2002, **295**, 469-472.
199. O. M. Yaghi, M. O'Keeffe, N. W. Ockwig, H. K. Chae, M. Eddaoudi and J. Kim, *Nature*, 2003, **423**, 705-714.
200. A. Y. Robin and K. M. Fromm, *Coord. Chem. Rev.*, 2006, **250**, 2127-2157.
201. G. B. Deacon and R. J. Phillips, *Coord. Chem. Rev.*, 1980, **33**, 227-250.
202. R. Banerjee, A. Phan, B. Wang, C. Knobler, H. Furukawa, M. O'Keeffe and O. M. Yaghi, *Science*, 2008, **319**, 939-943.
203. K. R. Dunbar and R. A. Heintz, in *Prog. Inorg. Chem.*, John Wiley & Sons, Inc., 2007, pp. 283-391.
204. S.-i. Noro, S. Kitagawa, T. Akutagawa and T. Nakamura, *Prog. Polym. Sci.*, 2009, **34**, 240-279.
205. A. P. Côté and G. K. H. Shimizu, *Coord. Chem. Rev.*, 2003, **245**, 49-64.
206. A. Clearfield, *Current Opinion in Solid State and Materials Science*, 1996, **1**, 268-278.
207. J. Kim, B. Chen, T. M. Reineke, H. Li, M. Eddaoudi, D. B. Moler, M. O'Keeffe and O. M. Yaghi, *J. Am. Chem. Soc.*, 2001, **123**, 8239-8247.
208. H. Li, M. Eddaoudi, M. O'Keeffe and O. M. Yaghi, *Nature*, 1999, **402**, 276-279.
209. S. S.-Y. Chui, S. M.-F. Lo, J. P. H. Charmant, A. G. Orpen and I. D. Williams, *Science*, 1999, **283**, 1148-1150.
210. K. Uemura, R. Matsuda and S. Kitagawa, *J. Solid State Chem.*, 2005, **178**, 2420-2429.
211. S. Horike, S. Shimomura and S. Kitagawa, *Nature Chem.*, 2009, **1**, 695-704.
212. D. Tanaka, K. Nakagawa, M. Higuchi, S. Horike, Y. Kubota, T. C. Kobayashi, M. Takata and S. Kitagawa, *Angew. Chem. Int. Ed.*, 2008, **47**, 3914-3918.
213. P. Horcajada, C. Serre, G. Maurin, N. A. Ramsahye, F. Balas, M. Vallet-Regí, M. Sebban, F. Taulelle and G. Férey, *J. Am. Chem. Soc.*, 2008, **130**, 6774-6780.

214. M. D. Allendorf, R. J. T. Houk, L. Andruszkiewicz, A. A. Talin, J. Pikarsky, A. Choudhury, K. A. Gall and P. J. Hesketh, *J. Am. Chem. Soc.*, 2008, **130**, 14404-14405.
215. P. L. Llewellyn, S. Bourrelly, C. Serre, Y. Filinchuk and G. Férey, *Angew. Chem.*, 2006, **118**, 7915-7918.
216. Z. Lin, D. S. Wragg and R. E. Morris, *Chem. Commun.*, 2006, 2021-2023.
217. E. R. Parnham and R. E. Morris, *Acc. Chem. Res.*, 2007, **40**, 1005-1013.
218. Z. Ni and R. I. Masel, *J. Am. Chem. Soc.*, 2006, **128**, 12394-12395.
219. W.-J. Son, J. Kim, J. Kim and W.-S. Ahn, *Chem. Commun.*, 2008, 6336-6338.
220. M. Klimakow, P. Klobes, A. F. Thünemann, K. Rademann and F. Emmerling, *Chem. Mater.*, 2010, **22**, 5216-5221.
221. P. L. Llewellyn, S. Bourrelly, C. Serre, A. Vimont, M. Daturi, L. Hamon, G. De Weireld, J.-S. Chang, D.-Y. Hong, Y. Kyu Hwang, S. Hwa Jung and G. r. Férey, *Langmuir*, 2008, **24**, 7245-7250.
222. H. Bux, C. Chmelik, R. Krishna and J. Caro, *J. Membr. Sci.*, 2011, **369**, 284-289.
223. M. D. Allendorf, C. A. Bauer, R. K. Bhakta and R. J. T. Houk, *Chem. Soc. Rev.*, 2009, **38**, 1330-1352.
224. M. Kurmoo, *Chem. Soc. Rev.*, 2009, **38**, 1353-1379.
225. P. S. Wheatley, A. R. Butler, M. S. Crane, S. Fox, B. Xiao, A. G. Rossi, I. L. Megson and R. E. Morris, *J. Am. Chem. Soc.*, 2005, **128**, 502-509.
226. A. C. McKinlay, B. Xiao, D. S. Wragg, P. S. Wheatley, I. L. Megson and R. E. Morris, *J. Am. Chem. Soc.*, 2008, **130**, 10440-10444.

## Chapter 2 Aims of the Thesis

### *2.1 Aims of the thesis*

At present, the most prevalent strategy for the synthesis of zeolites and zeolite analogues is hydrothermal synthesis. Almost all of the reported zeolite framework structures can be synthesized hydrothermally. Water is a low cost, readily available solvent for hydrothermal synthesis. Hydrothermal syntheses of zeolites and zeolite analogues have been widely studied in the aim of seeking new framework architectures, controlling the morphology and size, and preparing materials for diverse applications. Recently, new synthetic techniques other than the hydrothermal method have been reported. Some of them, such as top-down treatment,<sup>1</sup> solvent free strategy<sup>2</sup> and ionothermal synthesis,<sup>3</sup> were introduced in Chapter 1. They possess some unique features which make them different from the conventional hydrothermal synthesis. Materials with new structures and properties can be synthesized through these novel synthetic routes.

The aim of this thesis is to synthesize crystalline microporous materials through those new synthetic strategies. Three methods will be described in the following chapters, aiming at different purposes based on the unique feature of each method:

In Chapter 4, the top-down and post-synthesis treatment will be applied to some germanosilicate zeolites which are built up by layers and pillars. **IWW**<sup>4</sup> and **ITH**<sup>5</sup> zeolites with different chemical compositions and Ge distributions will be prepared as the starting material for the top-down treatment. The main aim is to synthesize zeolite materials with predicted architectures. This may be possible because the layers of the selected zeolites should be more hydrolytically stable than the pillars and retained after a disassembly process. The original structures are already known so the products will be mainly characterised by means of powder X-ray diffraction.

In Chapter 5, a solvent free method will be carried out using ionic liquids as the SDAs. The method is named the “ionic liquid assisted” route. The aim is to synthesize zeolites with the aid of ionic liquids in a solid state reaction. The products will be characterised by PXRD, solid state NMR, SEM, N<sub>2</sub> adsorption and so on. The roles of the ionic liquids and other synthetic conditions will be investigated. It is hoped to develop a new

“green chemistry” synthetic route for zeolites and to improve our understanding of the ionothermal synthesis of silicate based zeolites.

The content of Chapter 6 is about ionothermal synthesis of AlPO materials. A new ionic liquid, 1-(2-hydroxyl-ethyl)-3-methylimidazolium chloride ([HOEmim]Cl), will be used as solvent and SDA. This ionic liquid contains a hydroxyl group and thus may have higher interaction strength with the framework species over alkyl imidazolium based ionic liquids. This kind of compound is usually considered not adequate as an SDA in hydrothermal synthesis.<sup>6</sup> Single crystal X-ray diffraction will be applied to investigate the relationship between the ionic liquid and the framework.

A flexible MOF compound has been synthesized by the strategy of selecting the ligands with both weaker and stronger coordinating groups.<sup>7</sup> The aim of this chapter is to prove this strategy can be generalized to other compounds and can prepare flexible MOFs. In Chapter 7 other ligands which also contain both stronger and weaker coordinating groups will be selected to build MOF materials. Variable temperature single crystal structure analysis will be carried out to investigate the flexibility of the synthesized MOFs.

## 2.2 References

1. W. J. Roth, P. Nachtigall, R. E. Morris, P. S. Wheatley, V. R. Seymour, S. E. Ashbrook, P. Chlubná, L. Grajciar, M. Položij, A. Zukal, O. Shvets and J. Čejka, *Nature Chem.*, 2013, **5**, 628-633.
2. L. Ren, Q. Wu, C. Yang, L. Zhu, C. Li, P. Zhang, H. Zhang, X. Meng and F.-S. Xiao, *J. Am. Chem. Soc.*, 2012, **134**, 15173-15176.
3. E. R. Cooper, C. D. Andrews, P. S. Wheatley, P. B. Webb, P. Wormald and R. E. Morris, *Nature*, 2004, **430**, 1012-1016.
4. A. Corma, F. Rey, S. Valencia, J. L. Jorda and J. Rius, *Nat. Mater.*, 2003, **2**, 493-497.
5. C. Avelino, P. Marta, R. Fernando, S. Gopinathan and J. T. Simon, *Angew. Chem. Int. Ed.*, 2003, **42**, 1156-1159.
6. S. L. Burkett and M. E. Davis, *Chem. Mater.*, 1995, **7**, 1453-1463.
7. B. Xiao, P. J. Byrne, P. S. Wheatley, D. S. Wragg, X. Zhao, A. J. Fletcher, K. M. Thomas, L. Peters, J. S. O. Evans, J. E. Warren, W. Zhou and R. E. Morris, *Nature Chem.*, 2009, **1**, 289-294.

## Chapter 3 Analytical Techniques

### 3.1 X-ray Diffraction (XRD)<sup>1, 2</sup>

#### 3.1.1 Crystallography<sup>3</sup>

##### 3.1.1.1 Crystal structure and unit cell

A crystal is a solid material which is constructed by repeated motifs in a long-range ordered way. The motifs can be atoms, ions or molecules and are identical throughout the whole structure. If each of these identical motifs is considered as a point, an array of regularly repeating points in the space is formed and named lattice. The crystal structure can be described by the combination of the lattice and the motif.

The lattice points of a crystal expand in three dimensions of the space. Three vectors, **a**, **b** and **c** which connect an arbitrary point (as the origin) to its nearest lattice points at 3 different directions, represent the basis vectors. A parallelepiped using the basis vectors as its edges confines a range that can construct the entire crystal by repeating itself in 3 dimensions. This range is a unit cell. The cell parameters, which describe the size and shape of the unit cell, including the magnitudes of the vectors and the angles between them, are designated  $a$ ,  $b$ ,  $c$ ,  $\alpha$ ,  $\beta$  and  $\gamma$  (Fig. 3-1).

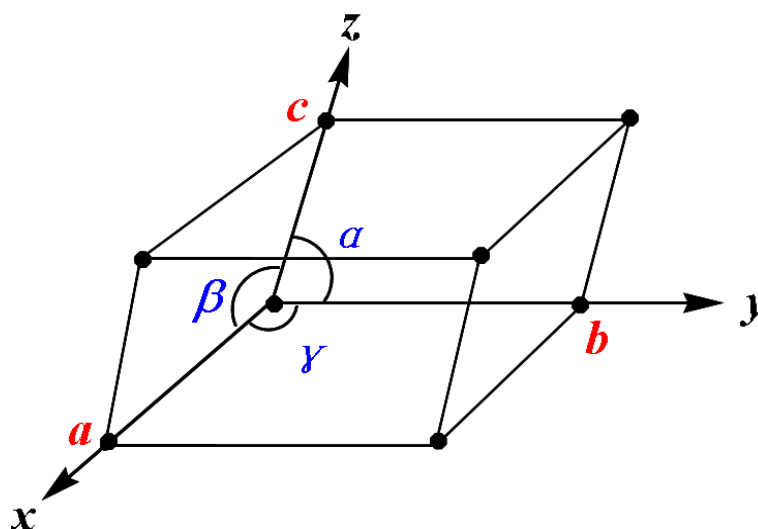


Fig. 3-1. A unit cell and the cell parameters.

The unit cell can be classified according to the positions of the lattice points in the parallelepiped: Primitive cell ( $P$ ): the lattice points only occupy the corners; Body

centred (*I*): the lattice points occupy the corners and the centre of the unit cell; Face centred (*F*): the lattice points occupy the corners and the centre of each face of the unit cell and Base centred (*C*): the lattice points occupy the corners and the centre of one pair of opposite faces of the unit cell.

### ***3.1.1.2 Symmetry, point groups and space groups***

If a shape moved following some rules and generated a new shape which is exactly same as the original one, this shape is symmetric. The movements are the symmetry operations. For some symmetry operations including rotation, reflection, inversion and their combinations (improper rotations), there is at least one point which keeps its position. These operations are classified as point symmetry operations. The corresponding symmetry elements are rotation axes, mirror plane, inversion point and rotation-reflection axes, respectively. For the long range ordered crystal structural, translational symmetry and their combinations (screw and glide) are also considered.

The crystals need to fill the entire space in 3 dimensions. Thus some symmetry operations, for example 5 fold rotation, are not possible for crystals. This makes the limited combinations of the symmetry operations. The combinations of the different point symmetry operations are named point groups. There are 32 point groups. If the translational symmetry operations are taken into account, the combinations are named space groups and there are 230 space groups in total. These space groups describe all the possible discrete symmetries that a crystal may have.<sup>4</sup>

### ***3.1.1.3 Crystal systems and Bravais lattices***

According to the characteristic symmetry elements of the crystals, they are classified into 7 crystal systems. The 7 crystal systems include cubic, tetragonal, orthorhombic, trigonal, hexagonal, monoclinic and triclinic. Each crystal system possesses some characteristic symmetries except for triclinic which has no symmetry. To satisfy the symmetry the unit cell must possess specific cell parameters. The lattices can be made up of non-primitive cell (*I*, *F* and *C*) or the primitive cell (*P*). The combinations of these cells and the crystal systems result in different lattice types named Bravais lattices. However in order to keep the unit cell as simple as possible, not all the combinations are necessary. 14 Bravais lattices are obtained by the combination of the crystal systems and the different unit cells. The 14 Bravais lattices describe the translational symmetry of the lattices and can be considered as applying certain translational symmetries to the

7 crystal systems. The 7 crystal systems, their characteristic symmetries, the possible Bravais lattices of each crystal system and the cell parameters of the crystal systems are listed in Table 3-1.

Table 3-1. Crystal systems, their characteristic symmetries, the corresponding Bravais lattices and the cell parameters.

Crystal systems	Characteristic symmetry	Bravais lattices	Cell parameters
Cubic	Four 3-fold axes	$P, I, F$	$a = b = c$ $\alpha = \beta = \gamma = 90^\circ$
Tetragonal	One 4-fold axis	$P, I$	$a = b \neq c$ $\alpha = \beta = \gamma = 90^\circ$
Orthorhombic	Three 2-fold axes	$P, I, F, C$	$a \neq b \neq c$ $\alpha = \beta = \gamma = 90^\circ$
Trigonal	One 3-fold axis	$P$	$a = b = c$ $\alpha = \beta = \gamma \neq 90^\circ$
Hexagonal	One 6-fold axis	$P$	$a = b \neq c$ $\alpha = \beta = 90^\circ, \gamma = 120^\circ$
Monoclinic	One 2-fold axis	$P, C$	$a \neq b \neq c$ $\alpha = \gamma = 90^\circ \neq \beta > 90^\circ$
Triclinic	None	$P$	$a \neq b \neq c$ $\alpha \neq \beta \neq \gamma \neq 90^\circ$

### 3.1.2 Theory of XRD<sup>5, 6</sup>

#### 3.1.2.1 XRD and Bragg's law

X-ray diffraction is an important and widely used technique for structure resolution. X-rays are electromagnetic radiation. The wavelength of the typical X-rays for crystal structure analysis is in the range of 0.1 to 1 nm. The magnitude of the wavelength is comparable with the distance between the atoms in the molecules (0.1 ~ 0.3 nm). Meanwhile crystalline materials possess long range order. Therefore the crystals can be used as a diffraction grating for X-rays. Diffraction theory indicates that the constructive interference can occur when the path difference of the coherent waves is an integral multiple of their wavelength.

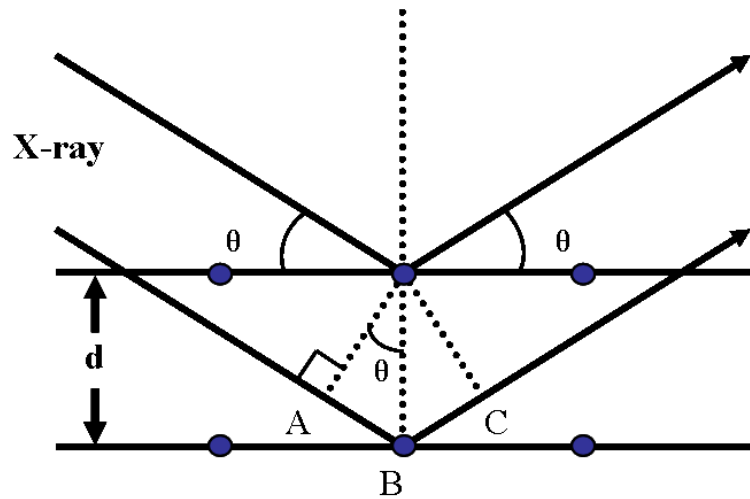


Fig. 3-2. The schematic shows the reflection of the X-ray beams by the adjacent lattice planes. The blue circles represent the atoms in a crystal.

Fig. 3-2 illustrates what happens to an X-ray beam when it incidents on the crystals. The atoms of crystalline materials which are shown in blue circles can be envisaged as a group of parallel lattice planes. Here the distance between the two planes is  $d$ , which denotes the  $d$ -spacing between the two adjacent planes. The wavelength of the X-ray is  $\lambda$  and the angle of the incident beam to the planes is  $\theta$ . When the X-ray beams strike on the surfaces of these planes, one beam is reflected by the top plane. Another beam penetrates the top plane but reflected by the second plane. The reflected X-rays have the same wavelength as the incident beam so they are coherent beams. The path difference of these two beams is  $AB + BC = 2d \sin \theta$ . Constructive interference of the reflected beam occurs when this path difference is the integral multiple ( $n$ ) of the wavelength  $\lambda$ . Bragg's Law in eq. 3-1 describes the relationship between the incident angle and the  $d$ -spacing of the lattice planes:<sup>7</sup>

$$n\lambda = 2d \sin \theta \quad (\text{eq. 3-1})$$

### 3.1.2.2 Miller indices

The group of the parallel lattice planes that reflect the X-rays can be described using the Miller indices. In a group of parallel planes, select the one which is the nearest to the origin but not pass through the origin, the plane will intercept with the three axes at  $xa$ ,  $yb$  and  $zc$ , respectively, where  $a$ ,  $b$  and  $c$  are the cell parameters of the unit cell. The lowest whole number form of  $(1/x \ 1/y \ 1/z)$  is written as  $(hkl)$ , which represents the group of these parallel atomic planes. For the planes that are parallel to one axis, the

corresponding intercept is infinity and the value of  $h$ ,  $k$  or  $l$  equals to zero. For example, the planes parallel to the  $c$  axis but intercept the  $a$  and  $b$  axes is  $(hk0)$ . A more general example of a  $(332)$  plane is shown in Fig. 3-3.

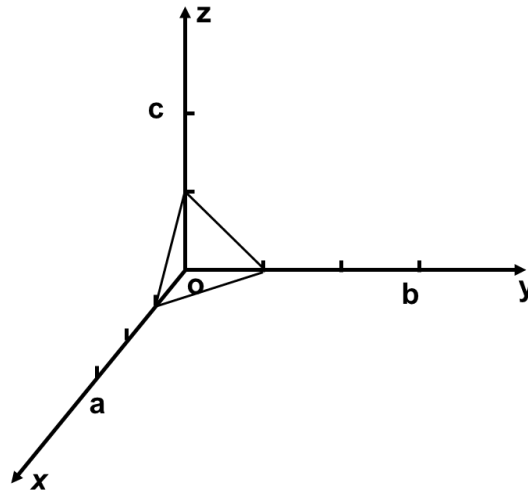


Fig. 3-3.  $(332)$  plane which intercepts three axes at  $1/3a$ ,  $1/3b$  and  $1/2c$ , respectively.

### 3.1.2.3 Generation of X-rays, characteristic lines and monochromatic X-rays

In the laboratory, X-rays are generated when a metal target is bombarded by an accelerated electron beam. The apparatus for generating the X-ray in laboratory is an X-ray tube, which is shown in Fig. 3-4. The cathode is a filament which can emit electron beam upon a current flowing through and heating it. The anode is a metal such as Cu or Mo. Both cathode and anode are sealed in a vacuum tube. The electron beam can be accelerated by a high voltage between the cathode and the anode to collide with the anode. The generated X-ray comes out through the Beryllium windows.

Two kinds of X-rays are generated by two mechanisms. One is bremsstrahlung. The bremsstrahlung is caused by energy conversion from the kinetic energy loss of the electron deceleration. It is a continuous spectrum. The other is the characteristic X-rays. The excitation of inner shell electrons of the target metal atoms results in a vacancy in the inner shell. Electrons from the outer shell with higher energy then fall into the inner shell. Energy is released in the form of X-ray radiation. These X-rays have some specific discrete wavelengths which are correlated to the differences of the energy between different shells. Therefore these X-rays are characteristic X-rays of the target metal. The X-ray caused by the electron transition from L shell to K shell is the  $K\alpha$  radiation and the electron transition from M shell to K shell generates the  $K\beta$  radiation.

The  $K\alpha$  radiation is usually used as its higher intensity. The  $K\alpha$  radiation splits to several fine spectra caused by the electrons from different orbitals of the L shell. For copper target two  $K\alpha$  lines with the wavelength of  $K\alpha_1 = 1.5406 \text{ \AA}$  and  $K\alpha_2 = 1.5444 \text{ \AA}$  are present. The pure X-ray of single wavelength is obtained by a monochromator.

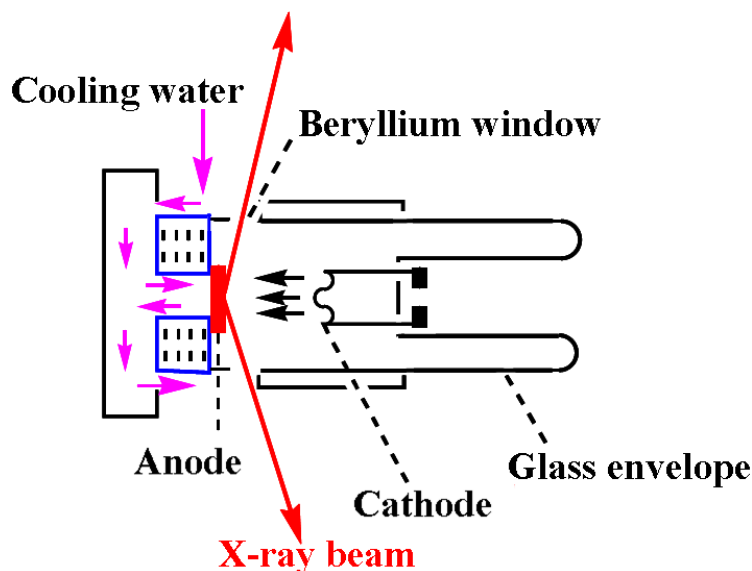


Fig. 3-4. Schematic shows the structure of an X-ray tube.

### 3.1.3 Single Crystal Structural Analysis

#### 3.1.3.1 The phase problem

Single crystal diffraction is probably the most powerful tool for structural analysis of crystalline materials. Single crystal diffraction gives a series of diffraction images from different directions. Both the  $\theta$  angles and the intensities of the diffraction spots are recorded. Each spot is the diffraction of a group of miller planes ( $hkl$ ). Full description of a crystal structure requires the information of both the lattice and the motif. The lattice information such as the cell parameters,  $a$ ,  $b$ ,  $c$ ,  $\alpha$ ,  $\beta$  and  $\gamma$  can be calculated through Bragg's law by the recorded diffraction spot positions (diffraction angle of  $2\theta$ ). Most of the space groups can be determined by checking the systematic extinction which is the phenomenon of the disappearance of some ( $hkl$ ) reflections caused by the crystal symmetry.

In order to determine the atoms and their coordinates in a crystal, the intensities of the diffraction spots are used. When the motif of a crystal is only one atom, the intensity of

each  $(hkl)$  plane is correlated with the atomic number (the scattering factor,  $f$ ) and the atomic displacement caused by thermal vibration (atomic temperature factor,  $U$ ).

When the motif is a molecule or a group of atoms, the position of the atom in the unit cell (atomic coordinates) will also affect the intensities of the  $(hkl)$  reflections. For a crystal structure with the atom  $j$  ( $x_j, y_j, z_j$ ) in the unit cell, the structure factor  $F_{(hkl)}$  is:

$$F_{(hkl)} = \sum_{j=1}^{\infty} f_j [\cos 2\pi(hx_j + ky_j + lz_j) + i \sin 2\pi(hx_j + ky_j + lz_j)] \quad (\text{eq. 3-2a})$$

or

$$F_{(hkl)} = \sum_{j=1}^{\infty} f_j e^{i\varphi_{(hkl)}} \quad (\text{eq. 3-2b})$$

where:  $\varphi_{(hkl)} = 2\pi(hx_j + ky_j + lz_j)$  is the phase of the  $(hkl)$  reflection

$i$  is the imaginary unit.

Eq. 3-2 shows the structure factor is the coefficient of the scattering factors (atomic number) and the phase (atomic coordinates) of all the atoms in the unit cell. Therefore the electron density,  $\rho_{(hkl)}$ , which is the number of the electrons in the unit volume (electrons per  $\text{\AA}^3$ ) can be obtained by the inverse Fourier transform of the structure factor (in eq. 3-2b). For a unit cell with the volume of  $V$ , the electron density is:

$$\rho_{(hkl)} = \frac{1}{V} \sum_{hkl} F_{(hkl)} e^{-i\varphi_{(hkl)}} \quad (\text{eq. 3-3})$$

Eq. 3-3 indicates the electron density of any position ( $x, y, z$ ) in the unit cell can be calculated if the structure factors  $F_{(hkl)}$  of the  $(hkl)$  reflections were measured. The results would be an electron density map of which the peaks would indicate the atoms with different atomic number (the numbers of the electrons) and their distribution in the unit cell (atomic coordinates). The amplitude of the structure factor  $|F_{(hkl)}|$  can be obtained from a series of reductions and corrections of the corresponding  $(hkl)$  intensity,  $I$ . However, the phases are unknown from the single crystal diffraction. In order to solve the structure, first we need to solve this “phase problem”.

### 3.1.3.2 Patterson method<sup>8</sup> and direct methods<sup>9</sup>

Two methods used for solving the phase problem will be introduced: Patterson method and direct methods. In Patterson method, the Patterson function is the inverse Fourier transform of the intensity which can be obtained from the measured data:

$$P_{(uvw)} = \frac{1}{V} \sum_{hkl} |F_{(hkl)}|^2 e^{-2\pi i(hu+kv+lw)} \quad (\text{eq. 3-4})$$

The  $(u, v, w)$  are essentially the vectors between any two points at  $(x, y, z)$  and  $(x+u, y+v, z+w)$  in the unit cell. The Patterson function  $P_{(uvw)}$  and the electron densities of these two points will have the correlation of:

$$P_{(uvw)} = \sum_{j=1}^{\infty} \rho_{(xyz)} \rho_{(x+u, y+v, z+w)} \quad (\text{eq. 3-5})$$

When the Patterson function exhibits a peak, it indicates neither of these two point has an electron density of zero. Therefore the  $(u, v, w)$  are the interatomic vectors with opposite directions. In a unit cell with  $N$  atoms, each atom forms  $N$  vectors with other atoms, including the atom itself. Thus there would be  $N^2$  peaks in the Patterson space. It is clear that the heavier atoms will have higher Patterson peaks. The coordinates of these heavier atoms can be determined first, resulting in an initial structure model to solve the phase problem.

The Patterson method is especially suitable for the crystals with a limited number of heavier atoms. However, it is impossible to solve the structure of the crystals whose atoms have almost the similar scattering factors, such as zeolites. In this case, direct methods are usually used. In direct methods, the phase problem is solved by the statistical analysis of the intensities. Direct methods are based on two properties of the electron density: (a) the electron density at any point is always non-negative; and (b) the electron density is always discrete at the positions of atoms. The Sayre equation (eq. 3-6)<sup>10</sup> is deduced:

$$F_{(hkl)} = k \sum_{h'k'l'} F_{(h'k'l')} F_{(h-h', k-k', l-l')} \quad (\text{eq. 3-6})$$

In the Sayre equation the strong reflections contribute more than the weak reflections do. For centrosymmetric structures, the phase problem is simplified as the “sign problem” as the  $\varphi_{(hkl)}$  is either 0 or  $\pi$ . It is only required to determine if the structure factors are

positive or negative. If  $S_{(hkl)}$  is the sign of the  $F_{(hkl)}$ , the Sayre equation is simplified as the structural invariants triplet:

$$S_{(hkl)} \cong S_{(h'k'l')}S_{(h-h',k-k',l-l')} \quad (\text{eq. 3-7})$$

For the non-centrosymmetric structures, other relationships such as tangent formula<sup>11</sup> are used. These relationships indicate the phase problem can be solved by the trial-and-error route based on a starting set of some strong reflections' phases. Many sets of phases can be guesses and the correct set is identified by the figure of merit (FOM). The complex calculations are accomplished by computers.

### 3.1.3.3 Structure refinement<sup>12, 13</sup>

After solving the phase problem, the crystal structure is solved and the structure factors can be calculated. However, the amplitudes of the calculated structure factors  $|F_c|$  will show a certain differences from the observed amplitudes,  $|F_o|$ . These differences are caused by inaccurate atom positions, unsolved atoms, atomic displacements, and so on. The unsolved atoms such as some light atoms can be solved by using the inverse Fourier transform of the difference between the observed structure factor  $F_o$  (obtained by using the calculated phase  $\varphi_c$  and the observed amplitude  $|F_o|$ ) and the calculated  $F_c$ . The completion of the structure solution is usually completed simultaneously with the refinement. The structure solution completion and the refinement will achieve a best fit of the experimental results. The least-squares technique is usually used for structural refinement. Nowadays the refinement on  $F^2$  is preferred as it is believed more suitable for the weak reflections and more accurate than the refinement on  $F$ . For the refinement on  $F^2$ , the summation of  $M$  in eq. 3-8 should be minimized:

$$M(\Delta) = \sum w\Delta^2 = \sum w(F_o^2 - F_c^2) \quad (\text{eq. 3-8})$$

The  $w$  is the weight factor of the reflection, which is introduced to increase the weight of the reflections with less error. Several weight schemes are used for refinements. For example when the error of  $F_o$  is  $\sigma$ , the weight factor could be:

$$w = \frac{1}{\sigma^2} \quad (\text{eq. 3-9})$$

The structural refinement will provide some results which can verify the quality of the refined model, including the residual factors ( $R$ -factors), the weighted  $R$ -factors and the goodness of fit (GOOF). The conventional  $R$ -factor is defined as:

$$R = \frac{\sum ||F_o| - |F_c||}{\sum |F_o|} \times 100\% \quad (\text{eq. 3-10})$$

The weighted  $R$ -factor of the refinement on  $F^2$  is  $wR_2$ :

$$wR_2 = \sqrt{\frac{\sum w(F_o^2 - F_c^2)^2}{\sum w(F_o^2)^2}} \quad (\text{eq. 3-11})$$

For a well refined structure, the  $R$ -factor can be refined to a value below 0.05 and the  $wR_2$  below 0.15. It is noteworthy that lower  $R$ -factors are not the validation of the correct structures. The chemical properties of the refined structure such as bond lengths and angles should be examined carefully.

The GOOF values  $S$  are also employed to evaluate the quality of the refinement results and are defined as:

$$S = \sqrt{\frac{\sum w(F_o^2 - F_c^2)^2}{(m - n)}} \quad (\text{eq. 3-12})$$

Here  $m$  is the amount of the reflections and  $n$  is the amount of the parameters for the refinement. For the appropriate weight scheme and correct structure model, the  $S$  should be close to 1.

### **3.1.4 Powder X-ray Diffraction (PXRD)<sup>14</sup>**

Single crystals with suitable sizes are required for the single crystal diffraction analysis. However, sometimes adequate samples are unable to be obtained. This is particularly common for zeolites of which the sub-micrometre crystals or polycrystalline particles are often synthesized. In this case powder X-ray diffraction analysis can still provide some necessary information, such as the phase identification of the samples by comparing with the database and the structure refinement by the Rietveld refinement for known structures. The reflections in PXRD are a series of cones with the semi-vertex angles of  $2\theta$  (Debye-Scherrer cones) instead of the independent spots in single crystal diffraction. This is because the miller planes in powder samples are arranged in random orientations. When the signals are detected along the direction from the centre of the

cone to the edge, a PXRD pattern is recorded. The  $x$ -axis is the diffraction angle in  $2\theta$  and the  $y$ -axis is the intensity of the diffraction (Fig. 3-5).

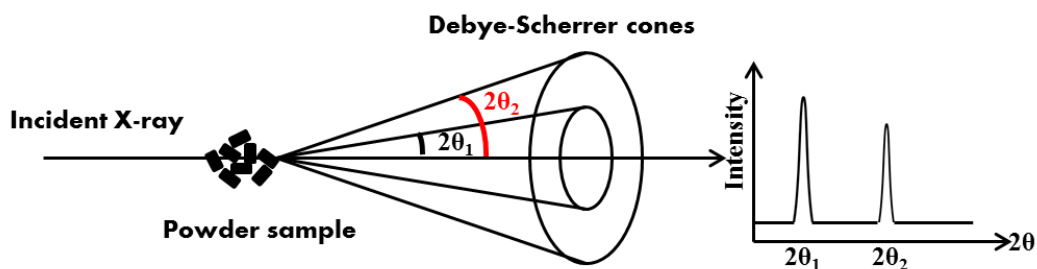


Fig. 3-5. Scheme shows the Debye-Scherrer cones and the way they transform to the PXRD patterns.

### 3.1.4.1 Diffraction geometry and the equipment

The PXRD data are usually collected using diffraction geometries such as the Debye-Scherrer geometry and the Bragg-Brentano geometry. The experiments in this thesis were carried out in Debye-Scherrer mode as shown in Fig. 3-6. In Debye-Scherrer mode, a monochromated beam illuminates the samples which are filled in a capillary. The diffraction signal was collected by a detector. The Debye-Scherrer geometry is considered as the best geometry for obtaining the accurate peak positions. Moreover, the preferred orientation can be eliminated to some extent by rotating the capillary and only a small amount of the samples are required as the thinner capillaries are preferred. The samples were characterised using the Cu-K $\alpha$ 1 radiation ( $\lambda = 1.5406 \text{ \AA}$ ) on a STOE STADI-P diffractometer equipped with a curved germanium (111) primary monochromator and a linear position-sensitive detector (PSD).

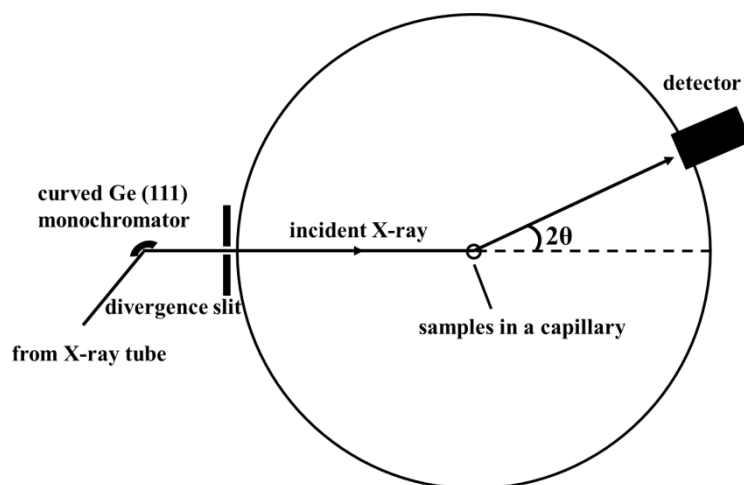


Fig. 3-6. Schematic shows the Debye-Scherrer geometry for PXRD data acquisition.

### 3.1.4.2 Phase identification

One application of the PXRD technique is to identify the phases of the samples. The peaks of a PXRD pattern reveal the information of the cell parameters of a material so the pattern is considered as the “fingerprint” of the corresponding compound. If the sample is a known compound, some information such as the structure and the purity can be identified by comparing with some databases. The most famous database is the Powder Diffraction File (PDF) which is published by the International Centre for Diffraction Data (ICDD). The latest release contains 778,883 unique data sets of both inorganic and organic materials. For the zeolite frameworks the data can be obtained in either a handbook of “Collection of Simulated XRD Powder Patterns for Zeolites”<sup>15</sup> or on the website of structure commission of IZA. At the moment the handbook contains data of 176 frameworks and the website collected 218 frameworks.

### 3.1.4.3 Rietveld refinement<sup>16</sup>

In the powder X-ray diffraction analysis, the structure solutions are complicated due to the overlapping of the peaks. However, if a starting model of the structure is known, the structure can be refined using the Rietveld method.<sup>17</sup> The Rietveld refinement is a least-squares technique for the best fitted parameters of a structure by comparing the calculated powder pattern profile with the observed one. The single crystal structure is refined on the squares of the structure factors which are proportional to the intensities of the spots of the Bragg reflections. Being different from the single crystal refinement, in the Rietveld refinement the parameters are refined on individual intensities of each of the diffraction increments to minimize the residual  $S_y$ . For a powder X-ray diffraction with  $i$  steps, the residual  $S_y$  is defined as:

$$S_y = \sum_i w_i (y_{i \text{ obs}} - y_{i \text{ calc}})^2 \quad (\text{eq. 3-13})$$

where:  $w_i$  is the weight of the  $i$ th step;

$y_{i \text{ obs}}$  is the observed intensity of the  $i$ th step;

$y_{i \text{ calc}}$  is the calculated intensity of the  $i$ th step.

There are many parameters that can affect the intensities of each step, including the features of the instrument, the features of the specimen and the structure factors. Thus the intensities of each step can be calculated by eq. 3-14:

$$y_{i\text{ calc}} = S \sum_k L_k |F_k|^2 \phi(2\theta_i - 2\theta_k) P_k A + y_{bi} \quad (\text{eq. 3-14})$$

where  $k$  represents a Bragg reflection ( $hkl$ );  $S$  is the scale factor;  $L_k$  is affected by Lorentz, polarization and multiplicity factors;  $F_k$  is the structure factor of the ( $hkl$ ) reflection;  $\phi$  is the reflection profile function;  $P_k$  is the preferred orientation function;  $A$  is the adsorption factor and  $y_{bi}$  is the background intensity.

Similar to the single crystal refinement, a series of R-factors and the goodness of fit,  $\chi$ , are employed to evaluate the Rietveld refinement. The weighted pattern R index,  $R_{wp}$ , and the expected R index,  $R_e$ , are defined as:

$$R_{wp} = \left[ \frac{\sum w_i (y_{i\text{ obs}} - y_{i\text{ calc}})^2}{\sum w_i y_{i\text{ obs}}^2} \right]^{1/2} \quad (\text{eq. 3-15})$$

and 
$$R_e = \left[ \frac{N-P}{\sum w_i y_{i\text{ obs}}^2} \right]^{1/2} \quad (\text{eq. 3-16})$$

where  $N$  is the number of the profile points and  $P$  is the number of the parameters. The goodness of fit  $\chi$  is defined as eq. 3-17. It indicates how the  $R_{wp}$  matches to the  $R_e$  and a value of  $\chi$  between 1.3 and 1 is usually satisfied.

$$\chi = \frac{R_{wp}}{R_e} = \frac{\sum w_i (y_{i\text{ obs}} - y_{i\text{ calc}})^2}{N - P} \quad (\text{eq. 3-17})$$

### 3.1.5 Synchrotron Radiation Diffraction<sup>18</sup>

When the electrons are accelerated to the relativistic speeds and curved by a magnetic field, a radiation will be emitted. This radiation is named synchrotron radiation as it was first discovered in the synchrotron accelerator. The synchrotron radiation has a broad spectrum and the synchrotron X-ray radiation is considered as a powerful X-ray source for crystal structure analysis. Compared with the X-rays generated in the X-ray tube, the synchrotron radiation has several advantages:

- (1) The synchrotron radiation is of high intensity and highly collimated. Therefore some crystals with small sizes or weak diffraction intensities can be solved using synchrotron radiation. Moreover, the high intensity of the radiation can decrease the time for data collection. Therefore with the aid of the synchrotron radiation, some complex *in-situ* analysis such as variable temperature single crystal analysis can be carried out.

- (2) The synchrotron radiation is of high purity and the wavelength can be tuned in a wide range. This feature increases the resolution for the X-ray diffraction and the Rietveld refinement.<sup>19</sup>

In this thesis the synchrotron diffraction data for Rietveld refinement was collected at the Materials Science-Powder X04SA Beamline at the Swiss Light Source (SLS), Paul Scherrer Institut in Villigen, Switzerland in Debye-Scherrer geometry with the wavelength of 1.000 Å. The single crystal diffraction data were collected at the Station 11.3.1 of the Advanced Light Source (ALS), Lawrence Berkeley National Laboratory, using a wavelength of  $\lambda = 0.7749$  Å.

## 3.2 Nuclear Magnetic Resonance (NMR) Technique

### 3.2.1 Basic Theory<sup>20</sup>

Nuclear magnetic resonance (NMR) spectroscopy is an adsorption spectroscopy technique for characterising the chemical environments of a certain nuclei. The atomic nuclei have the intrinsic property of spin and the corresponding spin quantum number of  $I$ . A nucleus with an even number of both protons and neutrons possesses an  $I$  of zero; for the nucleus where the number of either the protons or neutrons is even but the other is odd,  $I$  is a half-odd integer;  $I$  is an integer when both the number of protons and neutrons is odd. The nuclei with non-zero  $I$  are used for NMR characterisation.  $I$  is quantized and the corresponding magnetic quantum number,  $m$ , can adopt values from  $-I$  to  $+I$ . Therefore the nuclei will have  $2I+1$  of different values of magnetic moments,  $\mu$ . Normally these magnetic moments are degenerate. When an external magnetic field  $B_0$  is applied, the energy levels are split. The energy  $E$  of each of the energy levels is:

$$E = -\mu B_0 = -\gamma m \frac{h}{2\pi} B_0 \quad (\text{eq. 3-18})$$

where:  $\gamma$  is the gyromagnetic ratio of the given nucleus;

$h$  is the Planck constant.

The energy difference  $\Delta E$  for the quantum transition is:

$$\Delta E = -\mu_2 B_0 - (-\mu_1 B_0) = \gamma(m_1 - m_2) \frac{h}{2\pi} B_0 = \gamma \frac{h}{2\pi} B_0 \quad (\text{eq. 3-19})$$

Meanwhile the energy of the radiation with frequency of  $\nu$  (Hz) is:

$$E = h\nu \quad (\text{eq. 3-20})$$

Therefore the resonance occurred when the nuclei adsorb the energy of suitable radio-frequency (rf) radiation. The resonant frequency is:

$$\nu = \frac{\gamma}{2\pi} B_0 \quad (\text{eq. 3-21})$$

Eq. 3-21 indicates that the resonant frequency of a given nucleus should be same if an external magnetic field is applied. However, same atomic nuclei of different compounds will have different environments due to the electrons around the nuclei producing a local magnetic field  $B_e$  which is opposite to the external magnetic field and contributes to the overall magnetic field. This phenomenon is called chemical shielding. The apparent magnetic field  $B$  is:

$$B = B_0 - B_e = (1 - \sigma)B_0 \quad (\text{eq. 3-22})$$

Here  $\sigma$  is the shielding constant which is related to the chemical environment of the nucleus. Eq.3-22 indicates the same nuclei of different compounds would be excited by different resonant frequency,  $\nu$ . A compound with the resonant frequency  $\nu_{ref}$  is used as the reference and the chemical shift,  $\delta$ , is defined as:

$$\delta = \frac{\nu - \nu_{ref}}{\nu_{ref}} \times 10^6 \text{ ppm} \quad (\text{eq. 3-23})$$

The chemical shifts of the compound are characteristic to the chemical environments of the nuclei such as their structures and chemical bonding. For organic compounds, the  $^1\text{H}$  and  $^{13}\text{C}$  NMR are widely used for structure identification and analysis.

### **3.2.2 Solution phase NMR**

The  $^1\text{H}$  solution phase NMR experiments were carried out on a Bruker Avance 300 instrument with the operating frequency of 300 MHz. The compounds were dissolved in deuterated solvents which contain tetramethylsilane (TMS) as the reference.

### **3.2.3 Solid State NMR<sup>21, 22</sup>**

For the microporous materials such as zeolites and AlPOs, the NMR can detect the chemical shift of the framework atoms such as  $^{29}\text{Si}$ ,  $^{27}\text{Al}$ ,  $^{31}\text{P}$ ,  $^{19}\text{F}$  and so on. The chemical properties of the SDA molecules can be investigated by  $^1\text{H}$  and  $^{13}\text{C}$  NMR. The characterisation must be carried out with the solid compounds. However, the spatial configurations of the nuclei are constrained in the solid phase. Unlike the compounds

dissolved in the solution phase, the anisotropic interactions of the nuclei such as chemical shift interaction, dipolar-dipolar interaction and the quadrupolar interaction in the solid phase cannot be averaged. Therefore in solid phase NMR the spectra are dramatically broadened.

The dipolar-dipolar coupling is the interaction between the magnetic fields of two nuclei. This interaction in the solid phase can be averaged when the NMR sample is spinning at an angle of  $54.74^\circ$   $\theta$  with respect to the direction of the external magnetic field  $B_0$  (Fig. 3-7). This is because the average perturbation is proportional to  $(3\cos^2\theta-1)$  and when  $\theta=54.74^\circ$  this factor equals to 0. The  $54.74^\circ$   $\theta$  is called the “magic angle”. Meanwhile, the chemical shift anisotropic interactions are also removed when the sample is spinning under the magic angle. This Magic Angle Spinning (MAS) technique is especially useful for nuclei with the spin quantum number  $I=1/2$ .

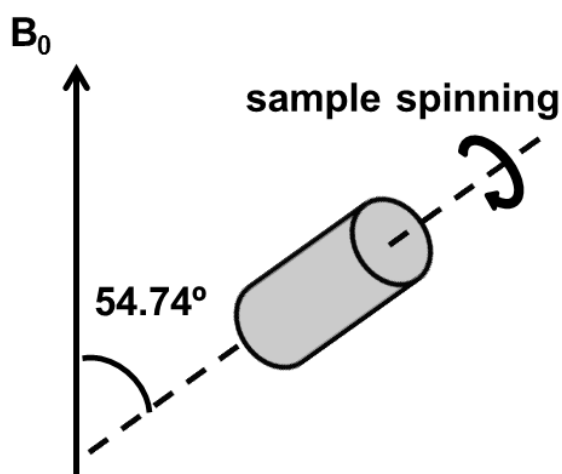


Fig. 3-7. Schematic shows the MAS experiment.

Some nuclei for NMR experiments including  $^{29}\text{Si}$  and  $^{13}\text{C}$ , which are of interest in zeolite materials, are naturally low in abundance (dilute spins). These nuclei will have a low signal/noise ratio. If a pulse is applied to an abundant nucleus such as proton, a polarization of the proton is created. The polarization can be transferred to the dilute spins through the dipolar interaction during a carefully optimized contact time (the spin locking period). The result is the signals of the dilute spins which are close to the protons are enhanced. This technique is cross polarization (CP) and usually combined with the MAS (CP/MAS) for characterising the solid materials.<sup>23</sup> It can give a better signal/noise ratio of the dilute spins and also provide the structure information of the nuclei's connections in space.

For the nuclei with  $I$  greater than  $1/2$  such as  $^{27}\text{Al}$ , they are quadrupolar due to the nonspherical charge distribution. The quadrupolar interactions are unable to be removed only by MAS. Other strategies combined with MAS were developed to narrow the spectrum lines. For example in 1995 Multiple-Quantum Magic Angle Spinning (MQMAS) NMR was developed by Frydman *et al.*<sup>24,25</sup> It is a 2-dimensional technique which combines the “multiple-quantum” spectroscopy and MAS. In the experiment the purely isotropic echo is observed therefore the narrow peak is obtained.

Solid-state NMR experiments in this thesis were recorded using a Bruker Avance III spectrometer equipped with either a 9.4 T superconducting magnet ( $^1\text{H}$  Larmor frequency of 400.13 MHz) or a wide-bore 14.1 T magnet ( $^1\text{H}$  Larmor frequency of 600 MHz). The samples were packed into standard  $\text{ZrO}_2$  rotors with outer diameters of 4 mm and rotated at the magic angle at different rates (from 10 to 14 kHz).

### ***3.3 Scanning Electron Microscopy and Energy Dispersive X-Ray Spectroscopy***<sup>26</sup>

Crystalline materials usually possess well defined morphologies. Meanwhile, the sizes of the porous materials such as zeolites are of great interest as the catalytic properties are affected by the sizes of the particles. The morphology and the size of a solid material can be detected by scanning electron microscopy (SEM). In SEM, an electron beam is emitted from an electron gun. This beam is focused to be very thin in a vacuum chamber, and accelerated by the high voltage to hit on a small spot of the sample surface. The contact of the sample and the beam will produce signals such as secondary electrons and backscattered electrons. These signals contain the surface information of the contact spot and can be recorded by different detectors. The beam is scanning on the sample surface, which is achieved by the deflection coils between the electron gun and the sample. As a result, the information of every spot in a rectangular area is obtained.

As it has been described in **3.1.2.3** of this chapter, a characteristic X-ray is generated when the electron transition between the atomic inner and outer orbitals occurred. In SEM the same procedure happens as well when the electron beam hits on the surface of the sample. Qualitative and quantitative analysis of the sample compositions can be achieved by recording the characteristic X-rays from different atoms. This technique is known as Energy Dispersive X-Ray Spectroscopy (EDX). A typical EDX spectrum

from a Ge-zeolite (the **ITH** framework with Si/Ge ratio of 15) is shown in Fig. 3-8. The characteristic peaks indicate the presence of the elements from the sample. Their composition in the sample can be detected by recording the intensities of the X-rays.

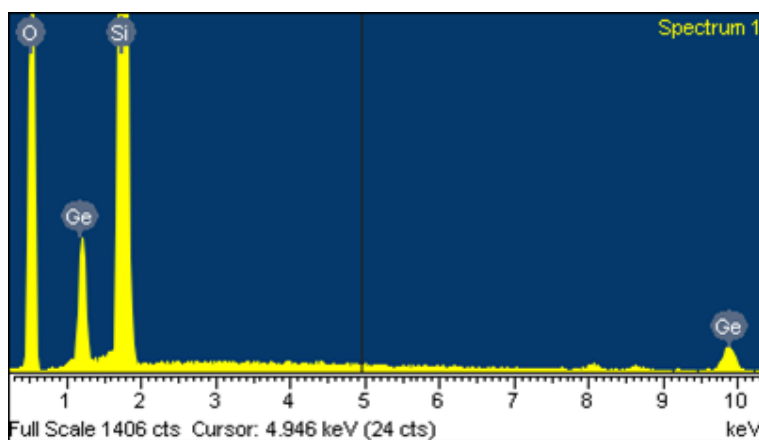


Fig. 3-8. An EDX spectrum of an ITH type Ge-zeolite sample.

The SEM images were recorded with a Jeol JSM-5600 scanning electron microscope. A tungsten filament electron gun was used. The operating high voltage was 5 kV. Chemical composition analysis by EDX was carried out with an Oxford Inca Energy system on the same SEM instrument at the operating voltage of 25 kV.

### ***3.4 Adsorption Analysis***

#### ***3.4.1 Basic theory***

##### ***3.4.1.1 Adsorption isotherms<sup>27</sup>***

Microporous materials possess large surface areas and unique pore size distributions which are of interest in their applications for gas adsorption, gas separation and shape-selective catalysis. The most widely used technique for characterising the porous features is gas adsorption. The adsorption experiment is usually carried out by measuring the sorption isotherm of a probe gas such as N<sub>2</sub> at a constant temperature. The isothermal curve describes the equilibrium adsorption amount of the gas (volume at standard temperature and pressure) as a function of the relative pressure  $p/p_0$  where  $p$  is the partial pressure of the gas and  $p_0$  is the saturated vapour pressure of the gas at the measuring temperature. IUPAC classified the isotherms into six types, which are shown in Fig. 3-9.

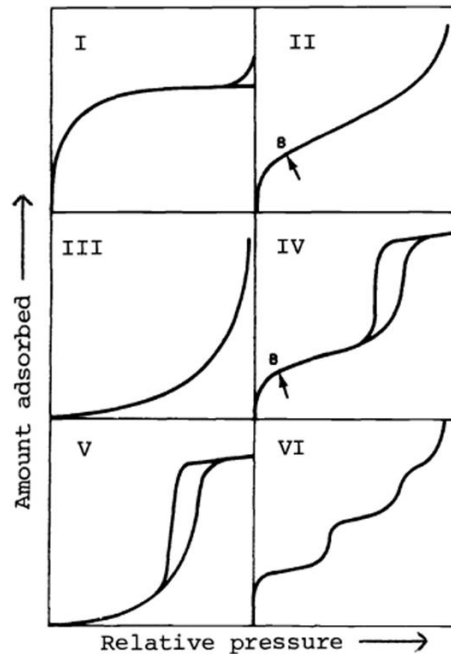


Fig. 3-9. Different types of isotherms. (The picture is adopted from reference 27.)

The shapes of the isotherms are correlated to the structure of the absorbents. A microporous material exhibits an isotherm of type I, which shows a rapid increase of the adsorbed quantity at low relative pressure. This is because the inner wall of the micropores has a stronger affinity to the adsorbate and the monolayer adsorption of the gas molecules occurs at low relative pressure. A plateau of the adsorption is present when the pressure increases. It indicates the adsorption amount is governed by the filling of the micropores. When the pressure is close to the saturated vapour pressure of the adsorptive, an increase which results from the condensation of the gas molecules could be observed. The shape of the type II isotherm is similar to the shape of type I but a gradual increase of the adsorption amount is observed instead of the plateau in type I. This type of isotherm is obtained with a non-porous material or a macroporous material as the absorbent. After the monolayer adsorption which is indicated by the point B, the gas uptake increases continuously due to the occurrence of multilayer adsorption. Type IV isotherm is characteristic of a mesoporous material. The shape of type IV isotherm is similar to type II but has two unique features: first, type IV isothermal has a hysteresis loop which is caused by the different procedures of the adsorption and desorption processes, and the shapes of the hysteresis loops are related to the structures of the mesopores; secondly, at high relative pressure region, an increase of the gas uptake is present due to the capillary condensation. The isotherms of type III and V are convex to

the relative pressure axis. These kinds of isotherms usually happen when the adsorbate has weak interaction with the surface of the adsorbent and type III and V are correlated to the non-porous and porous materials, respectively. Type VI isotherm shows a stepwise adsorption due to the multilayer adsorption on a uniform non-porous surface.

### 3.4.1.2 Determination of porous properties

There are many theories that were proposed to evaluate the surface areas of the adsorbents from their isotherms. However at present no single theory is perfectly suitable for this aim. It should be noticed the different methods for porous properties are calculated based on different pore size ranges and shapes. The Brunauer-Emmett-Teller (BET) method is a most widely used theory for porous materials.<sup>28</sup> It was derived from the Langmuir method<sup>29</sup> which describes monolayer adsorption of the gas molecules on an energetically identical surface without considering the interactions between the gas molecules. The BET method improved the Langmuir method by involving multilayer adsorption. In the BET method the main assumption is the binding energy between the layers of the adsorbed gas is about the same as the energy between the gas and the adsorbent. The correlation between the adsorption amount of  $V$  at the relative pressure of  $p/p_0$  and the partial pressure of  $p$  is shown in eq. 3-24:

$$\frac{p}{V(p_0-p)} = \frac{1}{V_m C} + \frac{C-1}{V_m C} \cdot \frac{p}{p_0} \quad (\text{eq. 3-24})$$

where  $V_m$  is the adsorbed amount of a monolayer adsorption and  $C$  is a constant which is related to the enthalpy of adsorption between the gas and the adsorbent.

The eq. 3-24 indicates the  $p/V_m(p_0-p)$  and  $p/p_0$  have a linear relationship with the slope of  $(C-1)/V_m C$  and  $1/V_m C$  as the intercept. The linear region is usually restricted in the  $p/p_0$  range of 0.05 to 0.30. By making a plot of  $p/V_m(p_0-p)$  versus  $p/p_0$  with three or more points in this linear region, the  $V_m$  can be calculated. The BET surface area ( $S_{BET}$ ) can be obtained by eq. 3-25:

$$S_{BET} = \frac{V_m N_A}{22.4} A_m \quad (\text{eq. 3-25})$$

where  $N_A$  is the Avogadro constant and  $A_m$  is the molecular cross-section area of the adsorbed gas molecules. For  $N_2$  adsorption at 77 K,  $A_m = 0.162 \text{ nm}^2$ .

There are also many methods to evaluate the pore volumes of the porous materials. One widely used method is the  $t$ -method.<sup>30</sup> Here the  $t$  is the statistical thickness of the gas

multilayer and is related with the relative pressure of  $p/p_0$  by some empirical formula. In the  $t$ -method, a plot of the adsorption amount  $V$  as a function of  $t$  at the corresponding relative pressure is drawn. The shape of the plot is correlated with the structure of the adsorbent: for a non-porous material, the plot is a straight line with a constant slope; for a microporous material, the slope decreases and the intercept of the plot is considered to be the micropore volume; for the mesoporous material the slope increases. The volume and the pore size distribution of the materials with mesopores above 5 nm are usually calculated by the BJH method.<sup>31</sup> Recently, computational modelling methods such as density functional theory (DFT) and Monte Carlo algorithm have been developed and are able to analyse both microporous and mesoporous materials.<sup>32</sup>

### ***3.4.2 Measurements of the porous properties***

#### ***3.4.2.1 Methods of measurements***

The adsorption amounts could be measured either by volumetric or gravimetric methods. In the volumetric method, the probe gas with known amount is introduced into the measuring system which contains the adsorbent. The system is maintained at a constant temperature for a period until the establishment of equilibrium. The volumetric measurement usually takes place at a cryogenic temperature such as the boiling point of the probe gas. The pressures before and after equilibrium are recorded, from which the adsorption amount can be calculated. In the gravimetric method, the adsorption amount is recorded by a microbalance. The gravimetric method is suitable for measurement at high temperatures.

Before the adsorption measurement, an important treatment is the outgassing. The species adsorbed in the adsorbent should be removed under high vacuum and high temperature. The thermal stability of the sample should be examined carefully before choosing the outgassing conditions.

#### ***3.4.2.2 N<sub>2</sub> adsorption***

Nitrogen is a widely used probe molecule for measuring the adsorption isotherms. The N<sub>2</sub> adsorption experiments in this thesis were carried out at -196 °C in a liquid nitrogen bath using a Micromeritics ASAP 2020 surface area and porosity analyser.

### ***3.4.2.3 Ar adsorption***

Compared to nitrogen which is a non-spherical molecule and has quadrupole, argon is considered as a better probe gas due to its spherical shape and the weaker interactions with the surface of the adsorbents. Moreover, for the adsorption measurement of microporous materials such as zeolites, the smaller Ar atoms can diffuse into the cages through the 6-membered-ring, which is inaccessible to N<sub>2</sub>. Therefore the Ar adsorption is an accurate measurement for microporous materials. In this thesis the argon adsorption isotherms were measured on a Micromeritics ASAP 2020 static volumetric instrument in a liquid argon bath at -186 °C.

## ***3.5 Thermogravimetric Analysis (TGA)***

The volatile species located in the void space of the porous materials are characterised by TGA. The as-synthesized samples are put in an inert crucible and heated under required gas atmosphere. The weight loss of the sample is recorded by a microbalance. The weight losses of the microporous materials at different temperature can be attributed to many reasons, such as the removal of the guest molecules in the MOF materials, the decomposition of the organic SDAs in inorganic frameworks and the decomposition of the organic ligands of the MOF materials. The TGA experiments were measured on a Netzsch TG 209 instrument under the atmosphere of air. The samples were heated in alumina crucibles at the heating ramp of 10 °C·min<sup>-1</sup>.

## ***3.6 CHNS Elemental Analysis***

The atomic compositions of C, H, N and S of the organic compounds can be obtained by determining the combustion products of the materials. The elemental analysis on C, H, N and S of the MOF materials was carried out by a Carlo Erba CHNS analyser.

### 3.7 References

1. W. Clegg, A. J. Blake and J. M. Cole, *Crystal structure analysis: principles and practice*, International Union of Crystallography, 2001.
2. Giacobozzo C. Editor. *Fundamentals of Crystallography*. IUCr[J]. 1992.
3. A. H. Windle, *A first course in Crystallography*, G. Bell, 1977.
4. T. Hahn, *International Tables for Crystallography, Space-Group Symmetry*, International Union of Crystallography, Springer, 2002.
5. A. Guinier, *X-ray diffraction: in crystals, imperfect crystals, and amorphous bodies*, Courier Dover Publications, 2013.
6. C. Hammond, *Basics of crystallography and diffraction*, Oxford, 2001.
7. W. Bragg, "The diffraction of short electromagnetic waves by a crystal", in *Proceedings of the Cambridge Philosophical Society*, 1913, pp. 43-57.
8. A. L. Patterson, *Physical Review*, 1934, **46**, 372-376.
9. An introduction to direct methods: The most important phase relationships and their application in solving the phase problem., by H. Schenk.
10. D. Sayre, *Acta Crystallogr.*, 1952, **5**, 60-65.
11. J. Karle and H. Hauptman, *Acta Crystallogr.*, 1956, **9**, 635-651.
12. W. Massa, *Crystal structure determination*, Springer, 2004.
13. G. M. Sheldrick, SHELXL97. Program for crystal structure refinement. 1997. University of Gottingen, Germany.
14. R. E. Dinnebier and S. J. Billinge, *Powder diffraction: theory and practice*, Royal Society of Chemistry, 2008.
15. M. M. Treacy and J. B. Higgins, *Collection of Simulated XRD Powder Patterns for Zeolites Fifth (5th) Revised Edition*, Elsevier, 2007.
16. R. A. Young and S. E. C. Netherland, *The rietveld method*, Oxford University Press Oxford, 1995.
17. H. Rietveld, *J. Appl. Crystallogr.*, 1969, **2**, 65-71.
18. C. Kunz and K. Codling, *Synchrotron radiation*, Springer Berlin, Heidelberg, New York, 1979.
19. J. B. Hastings, W. Thomlinson and D. E. Cox, *J. Appl. Crystallogr.*, 1984, **17**, 85-95.
20. P. J. Hore, *Nuclear magnetic resonance*, Oxford University Press New York, 1995.
21. Sharon Ashbrook, Lecture of "Solid-State NMR"
22. M. J. Duer, *Solid state NMR spectroscopy: principles and applications*, John Wiley & Sons, 2008.
23. A. Pines, M. G. Gibby and J. S. Waugh, *The Journal of Chemical Physics*, 1972, **56**, 1776-1777.
24. L. Frydman and J. S. Harwood, *J. Am. Chem. Soc.*, 1995, **117**, 5367-5368.
25. A. Medek, J. S. Harwood and L. Frydman, *J. Am. Chem. Soc.*, 1995, **117**, 12779-12787.
26. Wuzong Zhou, Lecture of "Introduction to electron microscopy"
27. K. Sing, D. Everett, R. Haul, L. Moscou, R. Pierotti, J. Rouquerol and T. Siemieniowska, *Pure Appl. Chem*, 1982, **54**, 2201.
28. S. Brunauer, P. H. Emmett and E. Teller, *J. Am. Chem. Soc.*, 1938, **60**, 309-319.
29. I. Langmuir, *J. Am. Chem. Soc.*, 1916, **38**, 2221-2295.
30. B. C. Lippens and J. H. de Boer, *J. Catal.*, 1965, **4**, 319-323.
31. E. P. Barrett, L. G. Joyner and P. P. Halenda, *J. Am. Chem. Soc.*, 1951, **73**, 373-380.
32. M. Thommes, in *Stud. Surf. Sci. Catal.*, eds. H. v. B. A. C. Jiří Čejka and S. Ferdi, Elsevier, 2007, vol. Volume 168, pp. 495-XIII.

# Chapter 4 Top-down and Post-Synthesis Treatment of Ge-zeolites

## 4.1 Introduction

One of the current research interests in the field of zeolites is synthesizing and tailoring new structure types.<sup>1-3</sup> Conventional hydrothermal synthetic routes have been proved to be the most important and effective method for zeolite preparation.<sup>4, 5</sup> However, other synthetic routes can lead to novel structures which have never been obtained by a direct hydrothermal route.<sup>6-8</sup> Recently, a top-down synthetic route has been reported.<sup>9</sup> In this method Ge-zeolites were selectively cleaved owing to specific sites being preferentially occupied by the hydrolytically sensitive Ge atoms.<sup>10</sup> These zeolites were treated through an “Assembly, Disassembly, Organization and Reassembly” process and transformed to new structures. The obtained materials were named as “ADORable zeolites”. The first example of ADOR manipulation was carried out by utilizing the **UTL** structure, which can be considered as layer structures pillared by double four rings (*D4Rs*).<sup>11, 12</sup> The Ge atoms are preferentially located in the *D4Rs* of **UTL**. After hydrolysis in an acidic medium the *D4Rs* dissolve, which result in a layered precursor for new zeolites. The reassembly of the layered precursor leads to two new zeolites (type codes **OKO**<sup>13</sup> and **PCR**<sup>9</sup>). The ADOR routes have been demonstrated in Chapter 1, Fig. 1-15. The **UTL** zeolite possesses 2-dimensional channels with 14- and 12-membered rings (called a 14 × 12 ring system).<sup>11</sup> The **UTL** zeolite was disassembled to a layer material due to the selective dissolution of the *D4Rs*. The following organization and reassembly processes can lead to two new structures with different pore sizes: when the layer materials were treated with organosilane species such as diethoxydimethylsilane (DEDMS), single 4-membered rings (*S4Rs*) were formed and connected the layers, resulting in an IPC-2 (structure type **OKO**) with a 12 × 10 ring system structure; when no extra tetrahedral atom species was added during the process, the layers were directly connected by bridging oxygen and an IPC-4 (structure type **PCR**) with an even smaller 10 × 8 ring system structure was obtained.

Computational modelling indicates that there are over 2 million unique predicted zeolite structures and at least 10 % of them are thermodynamically accessible.<sup>14</sup> However, there are only 218 zeolite structures that have been approved by the IZA Structure

commission. Many structures which may be important in different application fields have not been synthesized yet. The ADOR route establishes a new method to synthesize zeolites which cannot be achieved through the hydrothermal route and will lead to more real zeolite structures. Moreover, such a top-down treatment is distinct from the conventional hydrothermal route because the zeolites with desired pore sizes and chemical composition are controllable by the former. Another advantage is the structure of the “ADORable zeolites” obtained from the known zeolite is predictable by varying the limited connection possibilities of the layers. The structure can be simply solved by comparing the experimental powder diffraction pattern with the calculated ones.

Successful ADOR treatment relies on both structural and compositional characters of the **UTL** zeolites: a structure of layers connected by pillaring motifs, and the hydrolytically sensitive Ge atoms are preferentially occupied in the *D4R* pillaring motifs. Several other zeolites such as **IWW**,<sup>15</sup> **ITH**,<sup>16</sup> **ITR**,<sup>17</sup> **IWR**<sup>18</sup> and **IWV**<sup>19</sup> have similar structural character and are reported to be synthesized with Ge. Applying the similar top-down treatment to these materials would give the opportunities to create new zeolite structures.

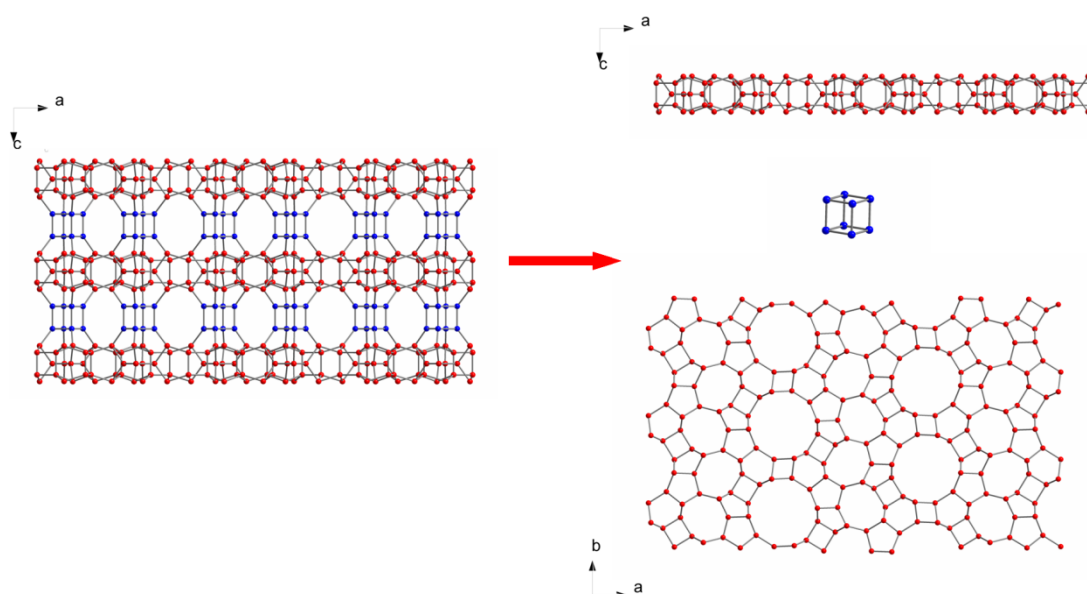
## **4.2 Aims**

The overall aim of this chapter is to carry out the top-down treatment of some zeolites which are constructed of layered structures and hydrolytically unstable pillaring motifs. Ge-containing **IWW** and **ITH**-type zeolites will be used in ADOR treatment. Zeolites with different chemical compositions will be treated under various hydrolysis conditions, such as pH, temperature and duration, in order to disassemble them appropriately. The effects of the Ge distribution and content on the disassembly process will be discussed. If the zeolites are proved to be appropriately disassembled then post-synthesis treatments such as organization, realumination or reassembly processes will be carried out to examine if any new zeolitic material with a tailored structure or composition can be obtained.

## 4.3 Top-down and post-synthesis treatment of IWW-type zeolite

### 4.3.1. Framework structure introduction to IWW-type zeolite

The first reported IWW-zeolite is ITQ-22,<sup>15</sup> which is a 3-dimensional zeolite with interconnected 8-, 10- and 12-membered ring pores. Scheme 4-1 illustrates the IWW structure in the view of combination of *D4Rs* and layers. The layers that possess alternating 8- and 12-membered rings are in the *ab* plane. These layers are pillared by *D4Rs* (shown in blue) along the *c* axis and the sinusoidal 10-membered rings that interconnect the 8- and 12-membered rings are formed.



Scheme 4-1. IWW framework structure displaying the layers (shown in red) and *D4R* pillars (shown in blue). T-O-T bridges are drawn as straight lines for clarity.

### 4.3.2 Experimental methods

#### 4.3.2.1 Synthesis of 1, 5-bis-(methylpyrrolidinium) pentane hydroxide

The SDA used in the preparation of IWW-zeolite is 1, 5-bis-(methylpyrrolidinium) pentane hydroxide (MPP(OH)<sub>2</sub>).<sup>15</sup> The MPP<sup>+</sup> cation was synthesized by reacting 20.0 g of N-Methylpyrrolidine (97 %, 0.235 mol, Aldrich) and 18.7 g of 1, 5-dibromopentane (97 %, 0.081 mol, Aldrich) in 300 ml of acetone (99 %, Fisher Chemical) under reflux. After 24 hours the solution was decanted and the produced precipitate was washed with acetone to give pure MPPBr<sub>2</sub>. The hydroxide form of MPP(OH)<sub>2</sub> was obtained by

anion-exchange of the  $\text{MPPBr}_2$  with Ambersep 900 OH form ion-exchange resin (Acros). The bromide salt and the anion-exchange resin were dissolved in distilled water in a weight ratio of 1: 1: 4. The mixture was stirred at room temperature for 10 hours. The same procedure was repeated 4 times to give full exchange. The filtrate was concentrated to an aqueous solution (13.6 wt %). The concentration of SDA was confirmed by titration of the hydroxide using phenolphthalein as indicator.

#### ***4.3.2.2 Synthesis of IWW-zeolites with different Si/Ge ratios***

Two **IWW**-type zeolites with different Si/Ge ratios were synthesized. The Ge-rich sample with a low synthetic precursor Si/Ge ratio of 2 was synthesized from a gel with a composition of 0.66  $\text{SiO}_2$ : 0.33  $\text{GeO}_2$ : 0.25  $\text{MPP(OH)}_2$ : 3.5  $\text{H}_2\text{O}$ . The Ge-poor sample that processes a higher synthetic precursor Si/Ge ratio of 6.6 was synthesized from a gel of 0.66  $\text{SiO}_2$ : 0.1  $\text{GeO}_2$ : 0.25  $\text{MPP(OH)}_2$ : 3.5  $\text{H}_2\text{O}$ . According to the synthetic composition, they are named IWW-2 for the Ge-rich sample and IWW-6 for the Ge-poor sample, respectively. In a typical synthesis of the IWW-2, 2.750 g of tetraethylorthosilicate (TEOS) (98 %, 13.2 mmol, Aldrich) and 0.691 g of  $\text{GeO}_2$  (99.9999 %, 6.6 mmol, Alfa Aesar) were added to 10 g of  $\text{MPP(OH)}_2$  solution (13.6 wt%, 5 mmol) under continuous stirring. To achieve the required gel composition, the resulting mixture was vigorously stirred to evaporate the excess water and the ethanol from the hydrolysis of TEOS. The gel was then heated in Teflon-lined stainless steel autoclaves at 175 °C for 11 days. For IWW-6 samples, 3.437 g of TEOS (98 %, 16.5 mmol, Aldrich) and 0.262 g of  $\text{GeO}_2$  (99.9999 %, 2.5 mmol, Alfa Aesar) were added to 10 g of  $\text{MPP(OH)}_2$  solution (13.6 wt%, 5 mmol) under continuous stirring. The resulting mixture was vigorously stirred to achieve the required gel composition. Hydrothermal synthesis took place in Teflon-lined stainless steel autoclaves at 175 °C for 7 days.

The products from the autoclaves were filtered, washed with water and dried at 100 °C overnight. The solid was calcined at 580 °C for 6 hours in air to remove the organic SDA before hydrolysis.

#### ***4.3.2.3 Hydrolysis of IWW-zeolites in acidic medium***

Hydrolysis was carried out with calcined samples in either dilute hydrochloric acid (HCl, 0.1 M) or concentrated HCl (12 M). Typically 0.2 g of solid was stirred in 20 ml

of HCl solution for 1-2 days. The products were collected by centrifugation and dried at 100 °C overnight.

#### ***4.3.2.4 Realumination of hydrolysed IWW***

Realumination was performed by reacting 0.2 g of AlCl<sub>3</sub> (99 %, 1.5 mmol, Lancaster) with 0.1 g of hydrolysed sample in 50 ml of 0.05 M HCl solution under reflux for 3 days. The solid was isolated by centrifugation, washed with water and dried overnight.

#### ***4.3.2.5 Restoration of hydrolysed IWW by Si***

0.2 g of hydrolysed IWW was treated with 0.2 g of diethoxydimethylsilane (DEDMS) (97 %, 1.3 mmol, Aldrich) in 10 mL of 1 M HNO<sub>3</sub> solution. The mixed suspension was heated at 170 °C for 16 hours in an autoclave. The product was collected by centrifugation, washed to neutral and calcined at 540 °C for 6 hours.

#### ***4.3.2.6 Organization and reassembly of hydrolysed IWW***

Organization followed the procedure described in the literature.<sup>9</sup> Hydrolysed IWW and octylamine (99 %, Aldrich) were mixed with a weight ratio of 1/100. The mixture was heated at 70 °C for 8 hours and then stirred at room temperature overnight. The supernatant liquid was decanted. The solid was heated at 90 °C in an open vessel in air for 2 hours.

#### ***4.3.2.7 Characterisation***

The powder X-ray diffraction patterns were collected on a STOE diffractometer using CuK $\alpha$ 1 radiation in Debye-Scherrer mode. The samples for data collection were filled in glass capillaries of 0.5 mm diameter. A chemical composition was obtained by Energy Dispersive X-Ray Spectroscopy (EDX) at the operating voltage of 25 kV with an Oxford Inca Energy system attached to a Jeol JSM 5600 instrument. Solid-state NMR spectra were acquired using 600 MHz Bruker Avance III spectrometer equipped with a wide-bore 14.1 T magnet. Powdered samples were packed into conventional 4 mm ZrO<sub>2</sub> rotors. <sup>29</sup>Si MAS NMR spectra were obtained using single-pulse experiments, with a recycle interval of 180 s. The MAS rate was 10 kHz. For the <sup>27</sup>Al MAS NMR the MAS rate of 14 kHz was used.

Synchrotron powder diffraction data were collected on the Materials Science-Powder X04SA Beamline at the Swiss Light Source (SLS), Paul Scherrer Institut in Villigen, Switzerland.<sup>20</sup> Data collection details are given in Table 4-1. The Rietveld refinement

was performed using the program package XRS-82.<sup>21</sup> The plots with observed, calculated and differences patterns were prepared with the programme ppp14.<sup>22</sup>

Table 4-1. Powder diffraction data collection parameters for IWW-zeolites

Synchrotron facility	SLS
Beamline	Material Science
Diffraction geometry	Debye-Scherrer
Monochromator	Si 111
Wavelength	1.000 Å
Sample	Rotating 0.3 mm capillary
Nominal step size	0.004 ° 2 $\theta$
Detector positions	4
Time per pattern	24 s
	1.0–120 ° 2 $\theta$
2 $\theta$ range	(only 2.4–45.0 ° 2 $\theta$ was used in the refinement)

Argon adsorption isotherms were measured on a Micromeritics ASAP 2020 static volumetric instrument at -186 °C. Prior to the sorption experiments, samples were outgassed at 110 °C under a turbo molecular pump vacuum until a residual pressure of 0.5 Pa was obtained. After further heating at 110 °C for 1 hour the temperature was increased to 300 °C at the temperature ramp of 1 °C·min<sup>-1</sup>. This temperature was maintained for 6 hours. The surface area was evaluated by BET method<sup>23</sup> using adsorption data in the  $p/p_0$  range of 0.05-0.20. The adsorbed amount at relative pressure  $p/p_0 = 0.98$  reflects the total adsorption capacity ( $V_{tot}$ ). The DFT algorithm (using standard Micromeritics software for cylindrical pores for Argon on oxides at -186 °C) was used to calculate the volume of micropores ( $V_{mic}$ ).

### 4.3.3 Results and Discussions

#### 4.3.3.1 Powder X-ray diffraction

PXRD patterns of calcined IWW-2 and IWW-6 are shown in Fig. 4-1. The experimental patterns are in good agreement with the theoretical reflections simulated from the IWW structure type. This good agreement indicates both samples are the IWW structure and in high purity. The samples were stable after being calcined to 580 °C in air. It is also noted that compared to IWW-2, all the reflections from IWW-6 are slightly shifted to higher  $2\theta$  values. In the unit cell of IWW-6, the content of Ge which has a larger atomic radius is low. Therefore IWW-6 should possess smaller unit cell sizes. This difference implies IWW-6 has less Ge in the unit cell than the IWW-2 does, which is consistent with the synthesis.

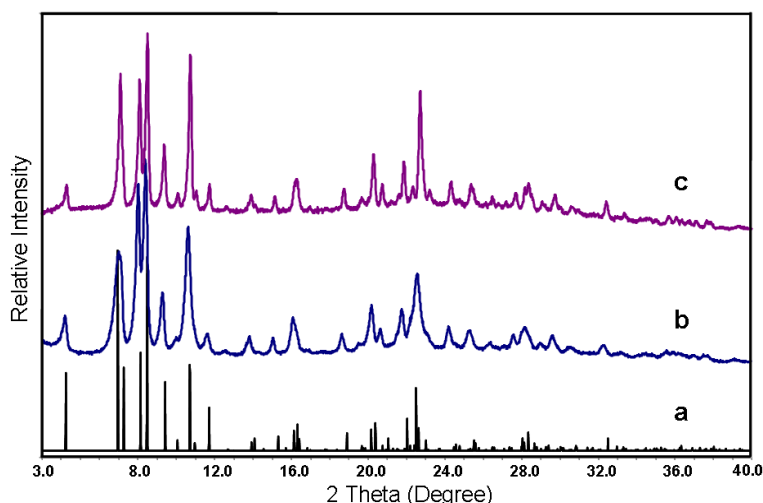


Fig. 4-1. (a) Simulated PXRD pattern of IWW structure type; experimental PXRD pattern of (b) calcined IWW-2 and (c) calcined IWW-6.

#### 4.3.3.2 Structure analysis by synchrotron powder X-ray diffraction

Synchrotron powder X-ray diffraction Data collection and Rietveld refinement were carried out by Dr. Ana B. Pinar from Laboratory of Crystallography, ETH Zürich.

PXRD patterns confirmed the structure and purity of the synthesized IWW samples. Detailed investigation of Ge atom locations were carried out with synchrotron powder X-ray diffraction and Rietveld refinement. The crystallographic data and the fit of the profile calculated for this model to the experimental data from Rietveld refinement are shown in Table 4-2 and Fig. 4-2, respectively.

Table 4-2. Crystallographic data from the Rietveld refinements of IWW-2 and IWW-6.<sup>a</sup>

Sample	IWW-2	IWW-6
Chemical composition	$[\text{H}_2\text{O}]_4[\text{Si}_{86.2}\text{Ge}_{25.8}\text{O}_{224}]$	$[\text{Si}_{96.2}\text{Ge}_{15.8}\text{O}_{224}]$
Unit cell		
<i>a</i>	42.0902(9) Å	41.9986(7) Å
<i>b</i>	12.9738(4) Å	12.9554(3) Å
<i>c</i>	12.6657 (3) Å	12.6100 (2) Å
Space Group	<i>Pba2</i>	<i>Pba2</i>
Standard peak ( <i>hkl</i> , 2θ)	3 1 0, 6.02°	2 0 0, 2.73°
Peak range (FWHM)	25	15
Data points	11037	10984
Contributing reflections	1619	1716
Geometric restraints	336	336
Si–O	1.61(1)-1.76(1) Å	80
O–Si–O	109.5(2)°	168
Si–O–Si	145(8)°	36
Si/Ge–O <sup>b</sup>	1.70(1)-1.76(1) Å	32
Si/Ge–O–Si/Ge <sup>c</sup>	135(8)°	20
Parameters		
structural	263	262
profile	8	8
<i>R<sub>F</sub></i>	0.100	0.078
<i>R<sub>wp</sub></i>	0.152	0.076
<i>R<sub>exp</sub></i>	0.036	0.029

a: The numbers given in parentheses are the esd's in the units of the least significant digit given. Each restraint was given a weight equivalent to the reciprocal of its esd.

b: The T–O bond distance restraint was adjusted to the Ge population at each T site.

c: The T–O–T bond angle restraint was set to 135° for those angles with at least one T site partially occupied by Ge.

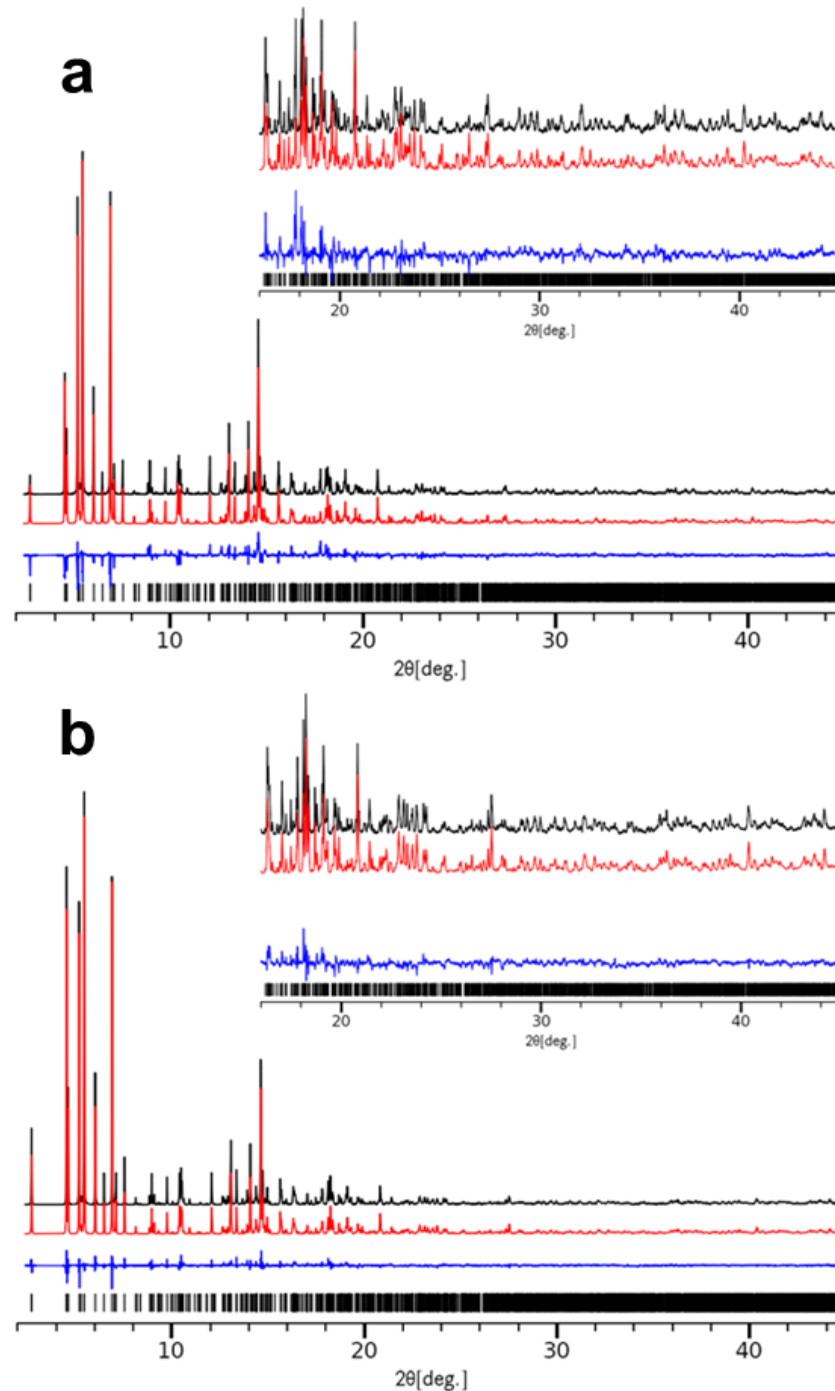


Fig. 4-2. The observed (black), calculated (red) and difference (blue) profiles for the Rietveld refinement of (a) IWW-2 and (b) IWW-6. The data in the inset have been scaled up by a factor of 6 to show more details at high angles. The tick marks indicate the positions of the reflections.

For IWW-6, the pattern contains two broad peaks of low intensity which do not belong to IWW. These two peaks were included in the background so they do not disturb the refinement. IWW-2 and IWW-6 were firstly indexed with the programme TREOR<sup>24</sup> implemented in the software CMPR<sup>25</sup> in an orthorhombic unit cell with parameters  $a =$

42.09 Å,  $b = 12.97$  Å,  $c = 12.66$  Å, for IWW-2, and  $a = 42.00$  Å,  $b = 12.96$  Å,  $c = 12.61$  Å, for IWW-6. The systematic absences were indicative of the extinction symbol  $Pba-$  (space groups  $Pbam$  and  $Pba2$ ). ITQ-22 was initially reported to be solved in  $Pbam$ ,<sup>15</sup> however, the mirror plane perpendicular to the  $c$ -axis divides the  $D4Rs$  into two symmetrically equivalent halves (see Fig. 4-3a), therefore the percentage of Ge in four T sites are necessarily equal to that of their four respective symmetrically equivalent T sites. To check if the Si/Ge fraction is actually different in each T sites of the  $D4R$ , the mirror plane was removed, reducing the symmetry to  $Pba2$ . This resulted in an increase in the number of T sites in the asymmetric unit from 16 to 28 and the T sites of  $D4R$  from 4 to 8 (Fig. 4-3b). For IWW-2, refinement of the occupancy parameters of the T sites showed that Ge was located exclusively in the eight T sites (T1-T8) that form the  $D4Rs$  in  $Pba2$ . The Rietveld refinement of the diffraction data of the IWW-6 sample was carried out similarly.

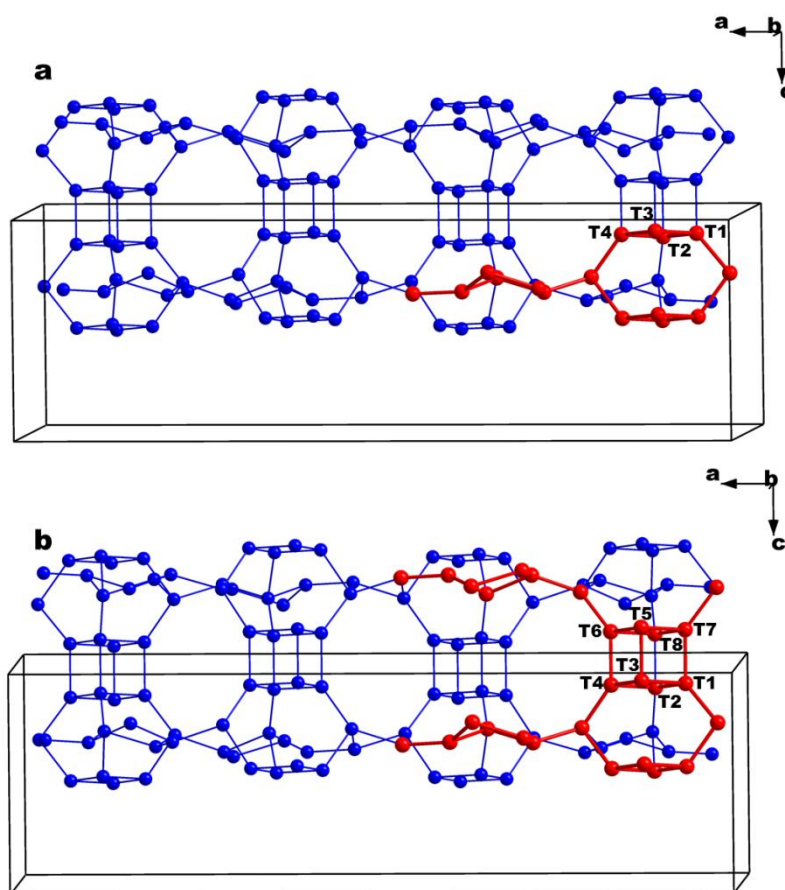


Fig. 4-3. (a) The framework structure of IWW-type zeolite and the asymmetric units in the space group of  $Pbam$ . (b) The framework structure of IWW-type zeolite and the asymmetric units in the space group of  $Pba2$ . T atoms represent with blue and red balls. Oxygen atoms have been omitted for clarity. The asymmetric units are shown in red.

Table 4-3. Atomic parameters for the T atoms of IWW-2 <sup>a,b</sup>.

Atom/site	x	y	z	U <sub>iso</sub>	% Ge <sup>c</sup>
T1	0.3899(2)	0.9157(6)	0.1110(1)	0.01	94(1)
T2	0.8837(2)	0.5679(6)	0.8549(2)	0.01	94(1)
T3	0.4312(2)	0.6955(7)	0.0953(10)	0.01	90(1)
T4	0.9258(2)	0.7814(7)	0.8381(2)	0.01	98(1)
T5	0.3617(2)	0.5645(6)	0.0852(12)	0.01	67(3)
T6	0.8575(2)	0.9144(7)	0.8292(13)	0.01	57(4)
T7	0.3215(2)	0.7806(8)	0.1097(8)	0.01	69(1)
T8	0.8170(2)	0.7037(9)	0.8593(11)	0.01	30(1)
T9	0.3844(2)	0.8965(6)	0.4879(9)	0.01	
T10	0.4201(2)	0.6877(7)	0.4670(10)	0.01	
T11	0.3541(2)	0.5672(7)	0.4673(11)	0.01	
T12	0.3182(2)	0.7753(8)	0.4885(10)	0.01	
T13	0.3529(2)	0.4106(7)	0.2705(10)	0.01	
T14	0.8454(2)	0.0870(7)	0.6670(10)	0.01	
T15	0.3818(2)	0.0592(6)	0.3022(8)	0.01	
T16	0.8802(2)	0.4319(6)	0.6597(8)	0.01	
T17	0.2794(2)	0.8670(8)	0.2924(10)	0.01	
T18	0.7800(2)	0.6427(7)	0.6711(10)	0.01	
T19	0.4647(2)	0.6170(6)	0.2877(10)	0.01	
T20	0.9669(2)	0.8722(5)	0.6527(10)	0.01	
T21	0.2896(2)	0.3035(7)	0.3457(10)	0.01	
T22	0.7875(2)	0.2067(7)	0.5952(10)	0.01	
T23	0.3086(2)	0.0764(8)	0.3387(10)	0.01	
T24	0.8077(2)	0.4292(7)	0.5903(10)	0.01	
T25	0.4074(2)	0.2756(7)	0.3581(8)	0.01	
T26	0.9045(2)	0.2135(7)	0.6066(9)	0.01	
T27	0.4680(2)	0.3923(6)	0.3597(9)	0.01	
T28	0.9650(2)	0.0992(6)	0.6087(9)	0.01	

a: T is used to designate the mixed Si/Ge T sites. The multiplicity of all atoms is 1.

b: Numbers in parentheses are the estimated standard deviations (esd's) in the units of the least significant digit given. Each restraint was given a weight equivalent to the reciprocal of its esd. Values without an esd were not refined.

c: The % of Si at each T site is the difference to 100 %. The T sites that are not part of D4R units (T9-T28) are 100 % siliceous.

Table 4-4. Atomic parameters for the T atoms of IWW-6 <sup>a,b</sup>.

Atom/site	x	y	z	U <sub>iso</sub>	% Ge <sup>c</sup>
T1	0.3869(2)	0.9183(5)	0.1941(5)	0.01	80(2)
T2	0.8833(2)	0.5730(5)	0.9343(5)	0.01	35(2)
T3	0.4259(1)	0.6980(6)	0.1881(10)	0.01	55(2)
T4	0.9227(2)	0.7860(6)	0.9239(10)	0.01	71(2)
T5	0.3580(2)	0.5749(5)	0.1823(10)	0.01	53(2)
T6	0.8566(2)	0.9128(6)	0.9245(11)	0.01	22(2)
T7	0.3192(2)	0.7897(6)	0.1977(7)	0.01	45(3)
T8	0.8174(2)	0.7048(8)	0.9392(7)	0.01	35(2)
T9	0.3841(2)	0.8965(5)	0.5599(7)	0.01	
T10	0.4195(1)	0.6904(6)	0.5590(10)	0.01	
T11	0.3544(2)	0.5689(5)	0.5610(11)	0.01	
T12	0.3193(2)	0.7762(6)	0.5641(8)	0.01	
T13	0.3539(2)	0.4163(6)	0.3601(9)	0.01	
T14	0.8451(2)	0.0882(6)	0.7576(10)	0.01	
T15	0.3820(2)	0.0606(5)	0.3813(6)	0.01	
T16	0.8792(2)	0.4380(5)	0.7434(6)	0.01	
T17	0.2763(1)	0.8662(6)	0.3834(8)	0.01	
T18	0.7828(2)	0.6354(7)	0.7507(8)	0.01	
T19	0.4625(2)	0.6160(5)	0.3760(10)	0.01	
T20	0.9661(2)	0.8715(5)	0.7424(10)	0.01	
T21	0.2927(2)	0.3033(5)	0.4396(9)	0.01	
T22	0.7866(2)	0.1999(6)	0.6810(9)	0.01	
T23	0.3090(1)	0.0724(6)	0.4376(10)	0.01	
T24	0.8085(1)	0.4237(6)	0.6834(10)	0.01	
T25	0.4071(2)	0.2799(5)	0.4378(8)	0.01	
T26	0.9028(2)	0.2222(6)	0.6857(8)	0.01	
T27	0.4690(2)	0.3916(5)	0.4460(8)	0.01	
T28	0.9645(1)	0.0998(5)	0.6929(9)	0.01	

a: T is used to designate the mixed Si/Ge T sites. The multiplicity of all atoms is 1.

b: Numbers in parentheses are the estimated standard deviations (esd's) in the units of the least significant digit given. Each restraint was given a weight equivalent to the reciprocal of its esd. Values without an esd were not refined.

c: The % of Si at each T site is the difference to 100 %. The T sites that are not part of D4R units (T9-T28) are 100 % siliceous.

For both IWW-2 and IWW-6, Ge atoms are located exclusively in the *D4R* positions, namely T1 to T8 out of 28 T atoms in the asymmetric unit, whose atomic parameters are listed in Table 4-3 and Table 4-4, respectively. For IWW-2, the total Ge occupancy is  $0.94 + 0.94 + 0.90 + 0.98 + 0.67 + 0.57 + 0.69 + 0.30 \approx 6$  T (5.99) out of 28 T sites. In this case the Si/Ge ratio of the whole IWW structure is  $28 - 6 / 6 = 3.7$ . Similarly, the total Ge occupancy of IWW-6 is  $0.80 + 0.35 + 0.55 + 0.71 + 0.53 + 0.22 + 0.45 + 0.35 \approx 4$  T (3.96) and the Si/Ge ratio calculated from the results of Ge occupancy is 6.1. The elemental analysis by EDX suggests the Si/Ge ratios of IWW-2 and IWW-6 are 3.6 and 6.4, respectively, which are consistent with the results obtained from the Rietveld refinement. Structure analysis suggests the chemical composition of the *D4R* in IWW-2 and IWW-6 are [6Ge, 2Si] and [4Ge, 4Si], respectively.

#### 4.3.3.3 Hydrolysis of IWW-zeolites

IWW-2 and IWW-6 were hydrolysed under different conditions. The effects of acid concentration and hydrolysis duration on the products were investigated. IWW-2 was hydrolysed in either 0.1 M or 12 M HCl aqueous solutions at room temperature and the PXRD patterns of the products are shown in Fig. 4-4.

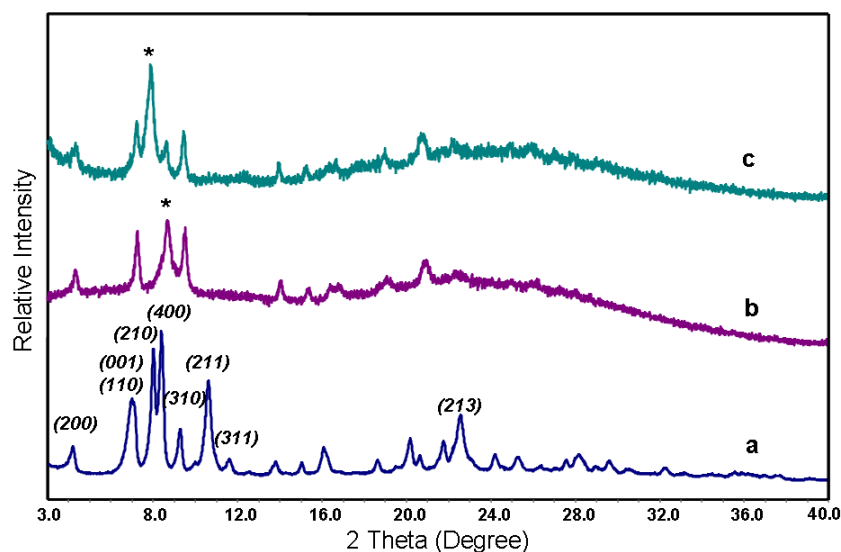


Fig. 4-4. PXRD patterns of (a) parental IWW-2, (b) IWW-2 hydrolysed in 0.1 M HCl solution and (c) IWW-2 hydrolysed in 12 M HCl solution for 48 hours. The peaks considered as the interlayer reflection of hydrolysed IWW-2 are marked by asterisks.

The *hkl* reflections of the parental **IWW** were indexed according to the reported reference.<sup>15</sup> The layers of **IWW** are parallel to the *ab* plane and stacked along the *c* direction by the *D4Rs* pillarings. If the *D4Rs* are dissolved, the product would lose

regularity in the  $c$  direction, in this case all the  $hkl$  reflections of which  $l$  are not equal to zero would disappear, or be shifted, after hydrolysis. Meanwhile, the  $(hk0)$  intralayer reflections should be retained after hydrolysis. This hypothesis was confirmed by the PXRD patterns of hydrolysed IWW-2. The interlayer  $(001)$  reflection is characteristic of the regularity of the layers stacked along  $c$  direction. However the position of  $(001)$  reflection ( $7.0^\circ 2\theta$ ,  $d$ -spacing =  $12.7 \text{ \AA}$ ) is close to the  $(110)$  reflection ( $7.1^\circ 2\theta$ ,  $d$ -spacing =  $12.4 \text{ \AA}$ ). The two nearby reflections resulted in a broad peak in the PXRD pattern of IWW-2. Disassembly of the **IWW** structure by removing the  $D4Rs$  should lead to the disappearance of the  $(001)$  reflection. However the preservation of the  $(110)$  reflection obstructed this disappearance from being observed. For both samples that were hydrolysed in 0.1 M HCl and in 12 M HCl for 48 hours, the remaining peaks were attributed to the  $(110)$  reflection of the **IWW** layers. The disappearance of the  $(001)$  reflection can be deduced from the peak shape alteration of the hydrolysed sample. The full width at half-maximum (FWHM) of this broad peak of parental IWW-2 was about  $0.462^\circ 2\theta$ , and got sharper after being hydrolysed in either 0.1 M HCl (*c.a.*  $0.210^\circ 2\theta$ ) or in 12 M HCl (*c.a.*  $0.252^\circ 2\theta$ ), which was due to the disappearance of the  $(001)$  reflection. Several other reflections such as  $(211)$ ,  $(311)$  and  $(213)$  of parental **IWW** disappeared, and the products retained some reflections in the positions of  $(200)$ ,  $(110)$ ,  $(400)$  and  $(310)$  of the parental **IWW**. Meanwhile, both of the hydrolysed samples exhibited a strong peak which was not observed in the parental **IWW**. They were assigned to be the interlayer reflection of hydrolysed IWW-2. For the sample hydrolysed in 0.1 M HCl, the peak was at  $8.7^\circ 2\theta$ , denoting to an interlayer distance of  $10.2 \text{ \AA}$ . It is believed that the interlayer distance decreased from  $12.7 \text{ \AA}$  of the parental IWW-2 to  $10.2 \text{ \AA}$  of the hydrolysed **IWW** was resulting from the dissolution of the  $D4Rs$ . For the sample hydrolysed in 12 M HCl the peak was at  $7.9^\circ 2\theta$ , indicating the interlayer distance decreased to  $11.2 \text{ \AA}$ .

It is noted that the interlayer distance of hydrolysed IWW-2 was flexible and related to the HCl concentration of the hydrolysis solution. In order to investigate the hydrolysis processes in detail, PXRD patterns of the samples hydrolysed for different durations were examined. The effects of the hydrolysis time are shown in Fig. 4-5 and Fig. 4-6. Either in 0.1 M HCl (Fig. 4-5) or in 12 M HCl (Fig. 4-6), IWW-2 was hydrolysed within 5 minutes, which was confirmed by the disappearance of the  $(211)$  and  $(213)$  reflections. This rapid structural alteration was also observed in the hydrolysis of zeolite

UTL.<sup>26</sup> For IWW-2 hydrolysed in 0.1 M HCl, there was no obvious further change after stirring IWW-2 in an acidic solution for 48 hours. For IWW-2 hydrolysed in 12 M HCl, at the beginning the products exhibited a similar PXRD pattern to those in 0.1 M HCl, indicating the same dissolution process occurred. After 24 hours, the interlayer reflection started to shift to lower  $2\theta$  values, indicating a rearrangement process of the layer structure had happened. After 48 hours this peak shifted to  $7.9^\circ 2\theta$ . The interlayer distance of the hydrolysed IWW-2 increased from  $10.2 \text{ \AA}$  to  $11.2 \text{ \AA}$ .

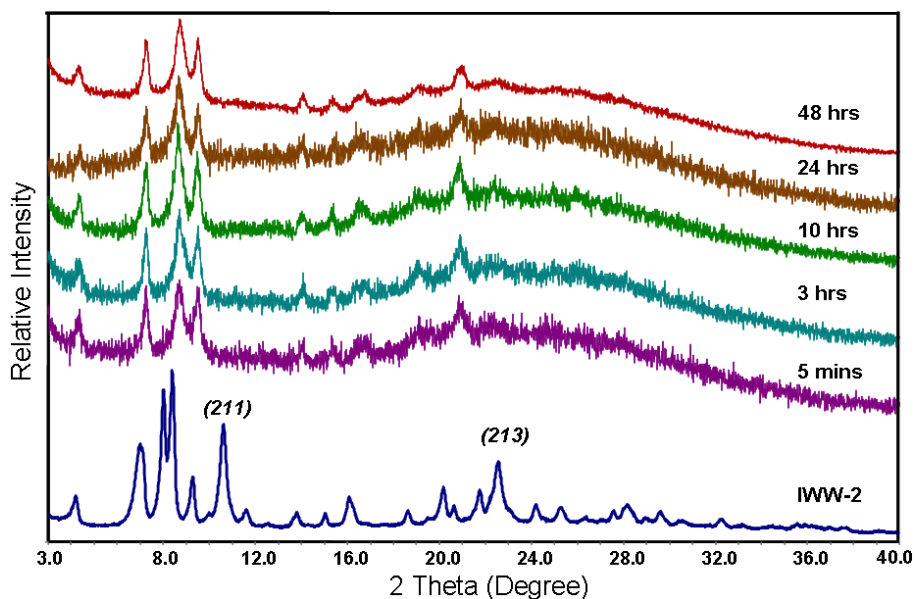


Fig. 4-5. PXRD patterns of parental IWW-2 and hydrolysed products in 0.1 M HCl for different durations.

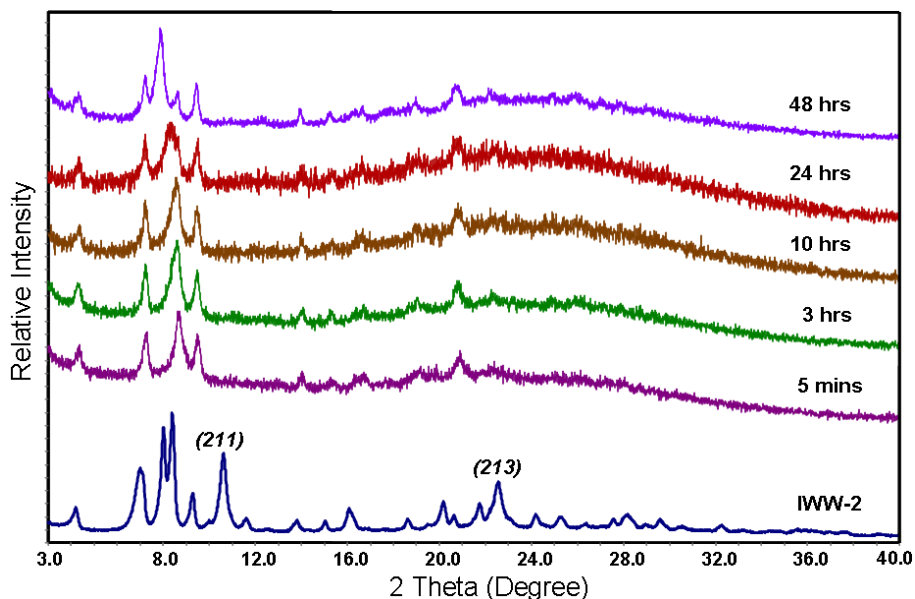


Fig. 4-6. PXRD patterns of parental IWW-2 and hydrolysed products in 12 M HCl for different durations.

It was reported when hydrolysing the **UTL** zeolites, a fast hydrolysis process was occurred first and a slow ripening stage was followed.<sup>26</sup> The hydrolysis of IWW-2 in acidic solution also presented a similar fast hydrolysis. However the PXRD patterns of hydrolysed IWW-2 in 12 M HCl indicate a different ripening process from the **UTL** zeolites: when hydrolysed in 12 M HCl, the *D4Rs* of IWW-2 were dissolved as quickly as in 0.1 M HCl. A layer rearrangement process occurred after 24 hours of acid treatment. The layer expansion of the hydrolysed IWW-2 in 12 M HCl is more than that in 0.1 M HCl. The low HCl concentration for hydrolysis resulted in a steady PXRD pattern after hydrolysis for 24 hours.

Hydrolysis of IWW-6 which has a lower Ge content was different from the hydrolysis of IWW-2. Fig. 4-7 shows the PXRD patterns of IWW-6 hydrolysed in 0.1 M HCl (Fig. 4-7b) and in 12 M HCl (Fig. 4-7c) at room temperature for 48 hours. Unlike IWW-2, the hydrolysis of IWW-6 in 0.1 M HCl and 12 M HCl produced samples with similar PXRD patterns. The HCl concentration of the hydrolysis solution didn't affect the structure of the products. Meanwhile, some reflections such as (211) and (311), which should have disappeared if the *D4Rs* were completely destroyed, were still observed in the powder patterns of hydrolysed samples. All these results indicated that the IWW-6 was not fully disassembled.

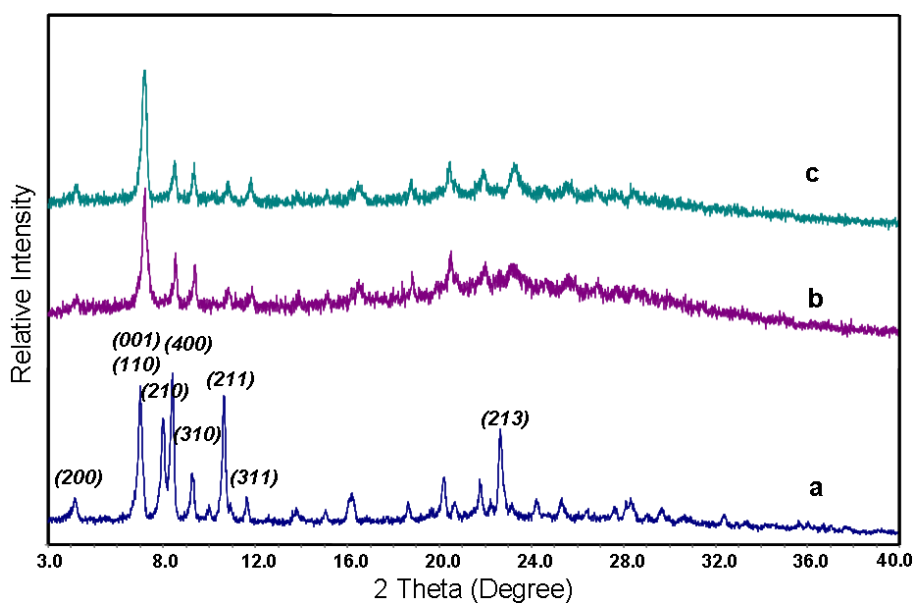


Fig. 4-7. PXRD patterns of (a) calcined parental IWW-6; (b) hydrolysed IWW-6 in 0.1 M HCl and (c) hydrolysed IWW-6 in 12 M HCl. Hydrolysis experiments were carried out at room temperature for 48 hours.

In Table 4-3 and 4-4, it is noted that all the sites in the *D4Rs* are not fully occupied by hydrolytically sensitive Ge atoms and the Ge occupancies in each sites are very different. In IWW-2 at least four *D4R* sites possess Ge occupancy over 90 % but in IWW-6 the highest Ge occupancy is 80 %. It is inferred the probability of two hydrolytically stable Si atoms linked along *c* direction would be higher in the *D4Rs* of IWW-6 than that in IWW-2. Thus more Si-O-Si units would exist in the hydrolysed IWW-6 and link the layers together, resulting in a connected material.

#### **4.3.3.4 Realumination of hydrolysed IWW**

Al and Si exhibit higher framework stability than Ge in zeolite frameworks. Moreover, Al atoms can introduce negative charge to zeolite frameworks and result in catalytic activity.<sup>27, 28</sup> Methods have been developed to incorporate Al by replacing less stable atoms like Ge.<sup>29</sup> Structural analysis of IWW-2 and IWW-6 have shown that Ge atoms are exclusively located in *D4Rs*. Replacing these sites by Al may lead to an **IWW**-type zeolite with aluminium only located in *D4Rs*. Directly synthesized Al-IWW would only result in randomly distributed Al sites. It would be a facile way to control the location of catalytically active atoms in a zeolite structure. Based on this idea, realumination processes of both IWW-2 and IWW-6 were carried out.

PXRD patterns of calcined, hydrolysed and realuminated IWW-2 and IWW-6 are compared in Fig. 4-8. IWW-2 was fully hydrolysed to the layer structure, but after realumination the product displayed poor crystallinity. Chemical composition analysis by EDX didn't give any signal of Al. Unlike IWW-2, realumination of the hydrolysed IWW-6 led to the recovery of the unit cell of original IWW-type structure. The reflections marked by asterisks in Fig. 4-8f are the newly appeared peaks after realumination. These peaks are in the same positions as those in parental IWW-6 which had disappeared after hydrolysis in 0.1 M HCl at room temperature. The appearance of these peaks indicates the realuminated IWW-6 has similar cell parameters to the parental IWW-6. The EDX analysis suggested the Si/Ge ratio increased from the 6.4 of parental IWW-6 to the 114.8 of realuminated IWW-6. Meanwhile Al signals were detected, indicating the Ge was replaced by Al after realumination. The Si/Al ratio of realuminated IWW-6 was 26.9. It can be calculated to be 1 Al atom out of 28 T atoms in the **IWW** framework. As it has been discussed above, there are 8 T atoms of one *D4R* and totally 28 T atoms in the **IWW** asymmetric unit, therefore it can be concluded that 1 out of 28 T sites is occupied by Al and this is a T site in the *D4R* motifs.

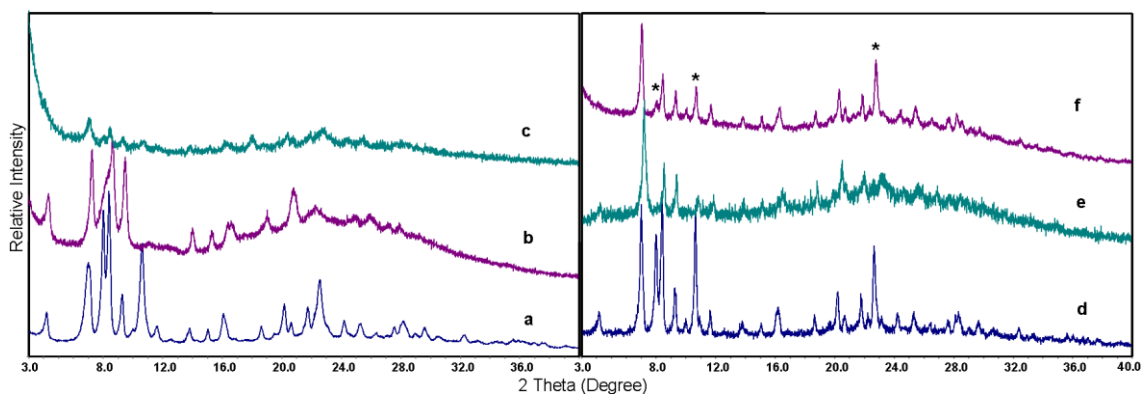


Fig. 4-8. PXRD patterns of (a) calcined parental IWW-2, (b) hydrolysed IWW-2 in 0.1 M HCl, (c) realuminated IWW-2, (d) calcined parental IWW-6, (e) hydrolysed IWW-6 in 0.1 M HCl and (f) realuminated IWW-6.

The  $^{27}\text{Al}$  solid state NMR is shown in Fig. 4-9. The major resonance at about 57 ppm is deemed to be the tetrahedrally coordinated Al, indicating the Al exists in the **IWW** framework. Meanwhile, the minor resonance at 0 ppm, which is usually considered to be octahedrally coordinated Al, indicates the existence of non-framework Al species.<sup>30</sup> It was the hydrolysis products of the  $\text{AlCl}_3$  in weak acidic solution and was difficult to be separated from the Al-IWW. Lower pH value can inhibit the production of the octahedrally coordinated Al, however the incorporation of the Al into the IWW framework is also prevented, resulting in a solid with poor crystallinity.

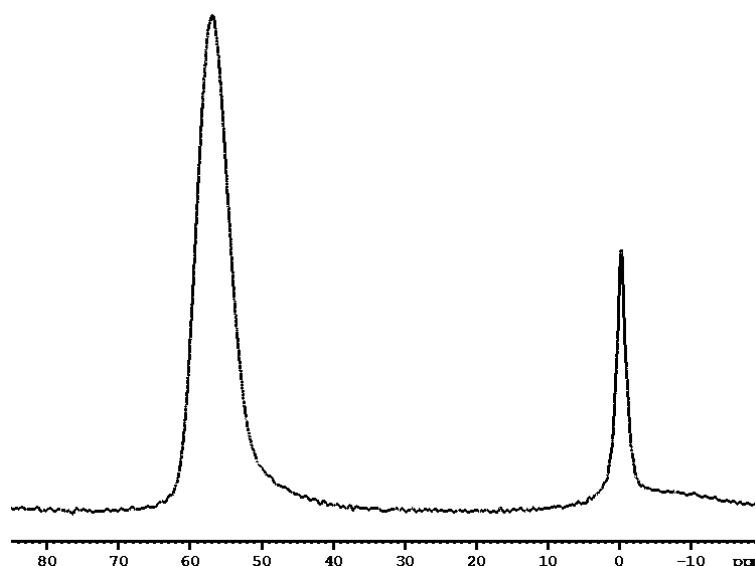


Fig. 4-9.  $^{27}\text{Al}$  MAS NMR spectrum of realuminated IWW-6. Solid-state NMR experiment was carried out by Dr. Daniel Dawson from University of St Andrews.

Corma and co-workers reported the unique catalysis performance of Al-IWW for alkylation reactions and studied the Al location by computational methods.<sup>31</sup> Theoretical calculations suggested a preferential distribution of Al atoms which led to about 1/3 of the total Brønsted acid sites located in the intersected 10- and 12-membered ring channels. The steric hindrance of 10-membered ring openings gave rise to good catalysis selectivity for mono- and dialkylation reactions. Al-IWW with a (Si + Ge)/Al molar ratio of 37 performed a higher selectivity for alkylating benzene to cumene than zeolite Beta with a 12 × 12 ring system did. However it was also found the Brønsted acid centres of the Al-IWW located in other positions such as in the 12-membered rings and in the cages which wouldn't benefit this catalysis selectivity. Differently, Al-IWW zeolites prepared from the proposed realumination procedure would have all the Al atoms in the *D4Rs* which are surrounded by the 10-membered rings. Therefore the realuminated IWW would have more Brønsted acid sites near the 10-membered rings than directly synthesized Al-IWW and perform better catalysis selectivity. This proposal will be true unless a rearrangement occurred.

Based on the above discussions, it is believed that synthesis of Al-IWW with (a) high Al content (about 1 Al atom per asymmetric unit) and (b) special Al distribution (only located in *D4Rs*) were achieved by a top-down treatment, which included a disassembly of the Ge-zeolite and the following realumination stage. This material would exhibit good catalysis selectivity on reactions such as mono- and dialkylation of the heavier compounds.

Failure to realuminate IWW-2 could be explained by Lowenstein's rule: the linkages of Al-O-Al are forbidden.<sup>32</sup> Hydrolysed IWW-2 is a structure of fully separated layers. To recover the **IWW** structure, *D4Rs* must be built between the layers. However Al atoms themselves can't form *D4Rs* as Al tetrahedron must connect to other tetrahedral atoms such as Si. While in hydrolysed IWW-6, *D4Rs* are not fully dissolved and Si-O-Si may link the layers. These can be considered as defected *D4Rs*. After realumination, the Al atoms went into these defects and restored the **IWW** structure.

#### 4.3.3.5 Restoration of hydrolysed IWW by Si

(The restoration of hydrolysed **IWW** by silicon insertion and the argon adsorption isotherm measurements were carried out by Pavla Chlubná-Eliášová from the Department of Synthesis and Catalysis, J. Heyrovský Institute of Physical Chemistry, Academy of Sciences of Czech Republic.)

One aim of this chapter is to synthesize zeolites with different pore sizes by reassembling the layers. Organization and reassembly were carried out on hydrolysed IWW-2 which was believed to be the layer structure. Unlike realumination, restoration by Si can be achieved in both IWW-2 and IWW-6 (Fig. 4-10). Reassembly of hydrolysed IWW-2 with organosilane compounds didn't form *S4R* motifs. Instead the restoration from the 2D layer structure to 3D original **IWW** structure occurred. The same restoration process was used on IWW-6 as well, in the aim of preparing hydrolytically stable **IWW** zeolites. For both IWW-2 and IWW-6, reflections such as (210), (211) and (213) (marked by asterisks) which have disappeared in the hydrolysed products were observed, indicating the recovery of the **IWW** unit cell. It was noted that these recovered peaks shift slightly to higher  $2\theta$  values, as was observed in the case of **UTL**,<sup>12</sup> which may be due to the contraction of the unit cell when Ge which has a large atomic radius is replaced by the smaller Si atoms.

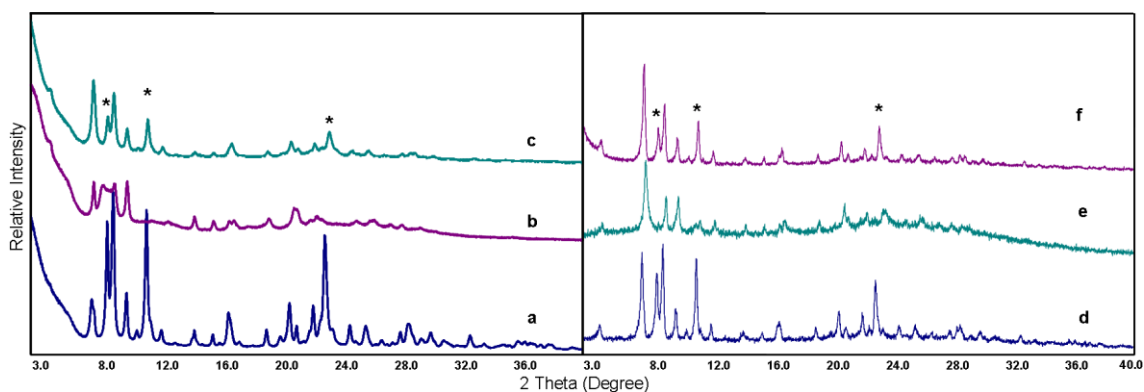


Fig. 4-10. PXRD patterns of (a) calcined parental IWW-2, (b) hydrolysed IWW-2 in 0.1 M HCl, (c) restored IWW-2, (d) calcined parental IWW-6, (e) hydrolysed IWW-6 in 0.1 M HCl and (f) restored IWW-6.

Textural properties and Ar adsorption isotherms of the IWW-2 and related materials are shown in Table 4-5 and Fig. 4-11, respectively. The Si/Ge ratios of these materials increased to 45.9 for hydrolysed IWW-2 and 76.4 for restored IWW-2, indicating the Ge was removed and Si was incorporated into the framework. The argon adsorption isotherm of IWW-2 is a typical type I curve, indicating the IWW-2 is a microporous

material and has a BET surface area of 416.1 m<sup>2</sup>/g. After hydrolysis, the product is still microporous but the BET surface area decreases to 123.6 m<sup>2</sup>/g. The collapse of the 3D IWW structure led to an obvious decrease of the surface area and micropore volume. Meanwhile, the 2D layer structure is retained so the isotherm is still a microporous adsorption. After restoration, the micropore volume increases to 0.146 cm<sup>3</sup>/g, which is close to the volume of the parental IWW-2 (0.169 cm<sup>3</sup>/g), due to the recovery of the 8-, 10-, 12- interconnected pore system.

Table 4-5. Textural properties of IWW-2 and its ADOR treatment products

	Si/Ge ratio by EDX	Argon adsorptions		
		BET (m <sup>2</sup> /g)	V <sub>mic</sub> (cm <sup>3</sup> /g)	V <sub>tot</sub> (cm <sup>3</sup> /g)
IWW-2	3.1	416.1	0.169	0.484
Hydrolysed IWW-2	45.9	123.6	0.030	0.213
Restored IWW-2	76.4	509.5	0.146	0.450

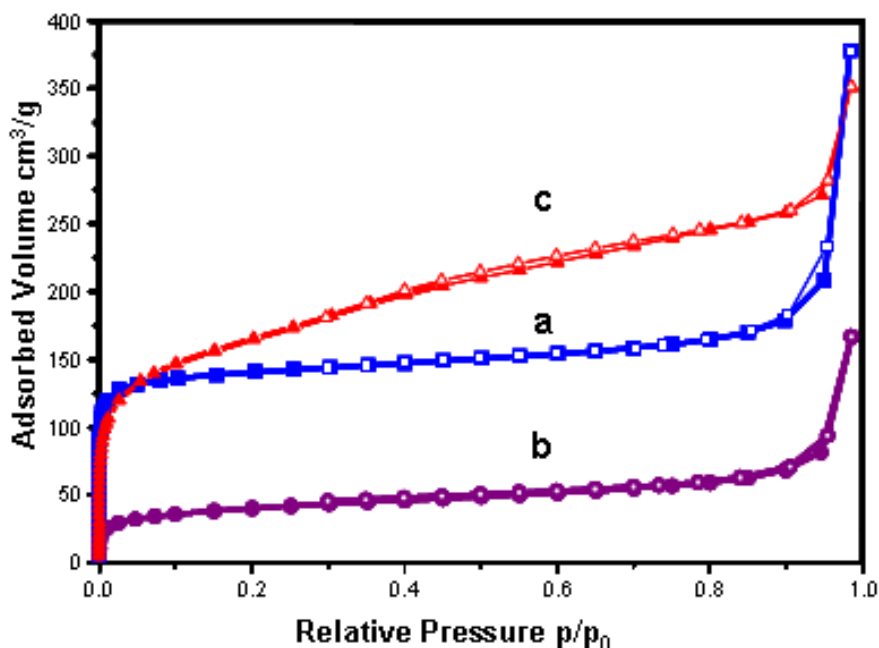


Fig. 4-11. Argon adsorption isotherms measured at -186°C. (a) Calcined parental IWW-2, (b) hydrolysed and calcined IWW-2 and (c) restored and calcined IWW-2.

The <sup>29</sup>Si solid state NMR spectra of IWW-2, hydrolysed IWW-2 and restored IWW-2 are shown in Fig. 4-12. The calcined IWW-2 (Fig. 4-12a) exhibited two separated resonances. The resonance at around -113 ppm is assigned to the Si(4Si) Q<sup>4</sup> signal, where silicon is surrounded by four silicon only. The chemical shift at around -109 ppm is the Si(nGe) Q<sup>4</sup> signal, which shows the silicon atoms are surrounded by at least one

Ge atom.<sup>33</sup> After hydrolysis, the resonance at -109 ppm disappeared (Fig. 4-12b). In addition a new resonance was observed at around -101 ppm, which is commonly assigned to the Q<sup>3</sup> signal resulting from the silanol defects.<sup>34</sup> Meanwhile a minor resonance at -91 ppm of Q<sup>2</sup> signal was also observed. The absence of Si(nGe) Q<sup>4</sup> signal and the present of the Q<sup>3</sup> and Q<sup>2</sup> resonances indicate the Ge atoms in the **IWW** framework have been dissolved. After restoration, the Q<sup>3</sup> and Q<sup>2</sup> resonances had almost faded away and only a Q<sup>4</sup> resonance was observed in the spectrum, indicating the recovery of the 3D connected structure.

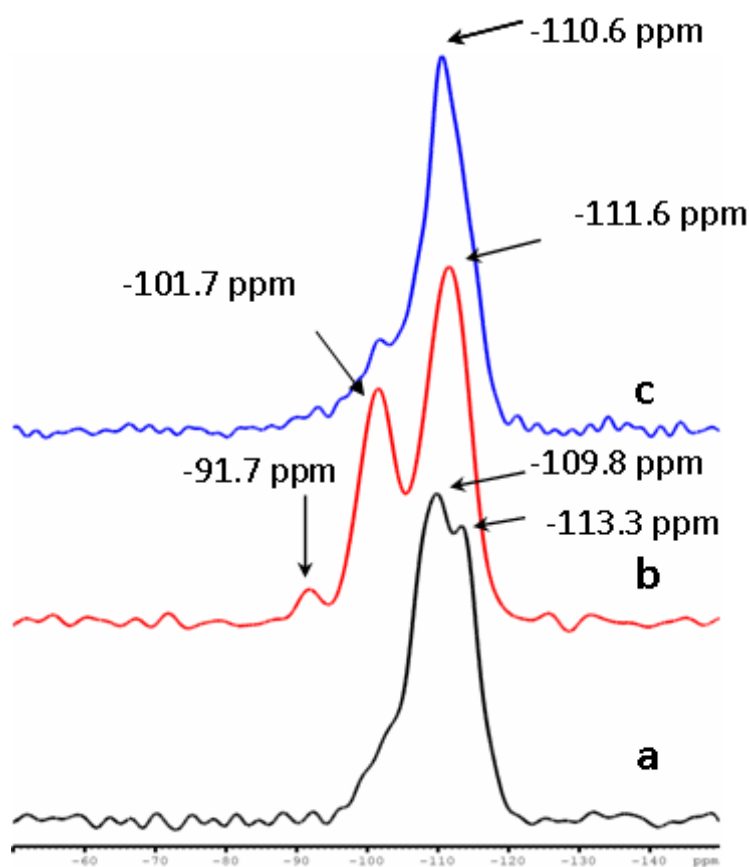


Fig. 4-12. <sup>29</sup>Si solid state NMR spectra of (a) IWW-2, (b) hydrolysed IWW-2 and (c) restored IWW-2. Solid-state NMR experiment was carried out by Dr. Daniel Dawson from University of St Andrews.

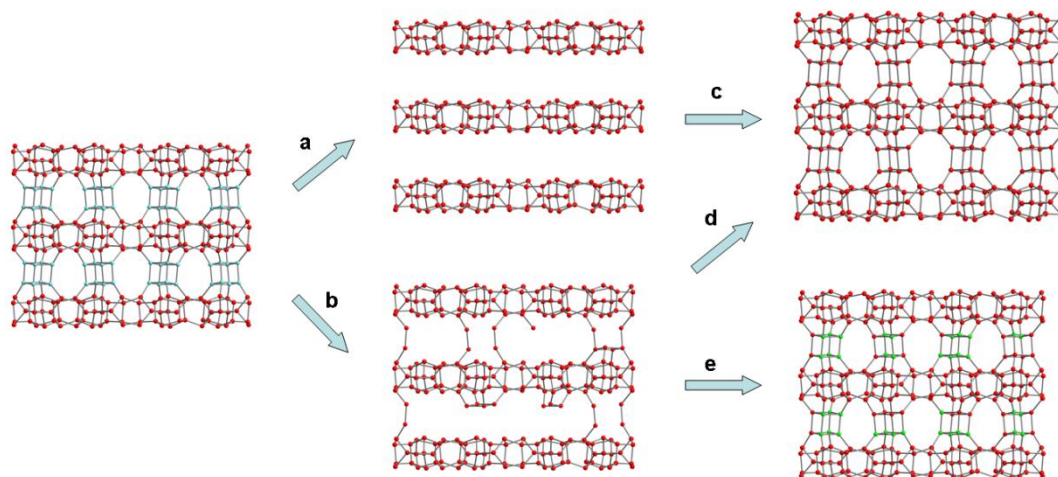
#### 4.3.3.6 Organization and reassembly of hydrolysed IWW

In order to build new zeolite structures from hydrolysed IWW, organization and reassembly of hydrolysed IWW-2 which is believed as a layered structure was carried out. However, PXRD shows only amorphous product is obtained after treating with octylamine. Failure to reassemble the hydrolysed IWW-2 in octylamine can be explained by the intrinsic property of the **IWW** type structure. The porous layers of

**IWW** which possess alternating 8- and 12-membered rings would be less stable in base solution than the dense layers of hydrolysed **UTL**. Thus direct reassembly in octylamine only resulted in amorphous solids. When the layers were reassembled with silane compounds, the recovery of the **IWW** type structure and the porous character indicates the hydrolysed **IWW** tend to form original **IWW** structure rather than new structures. *D4Rs* were more favourable than *S4Rs* when pillaring the **IWW** layers. This is probably due to an energetic reason, for example in analogy to the *D4Rs* in polymorph C of zeolite beta,<sup>10</sup> the bond tension between *S4Rs* and layers may be too high.

#### 4.3.4 Summary

In summary, this part of Chapter 4 investigated the top-down treatment applied to **IWW**-type zeolites. The main aim of this chapter was to synthesize new zeolites with different pore sizes through the top-down route. Despite the successful disassembling of the **IWW** with high Ge content in *D4Rs* to a layer material, the following organization and reassembly unexpectedly failed to give a new structure. Materials with the same framework structure but different chemical compositions were prepared. The main procedures of all the treatments are described in Scheme 4-2.



Scheme 4-2. Schematic illustration of top-down treatment procedures of **IWW**-type zeolites. (a) Hydrolysis of Ge-rich **IWW**-2; (b) hydrolysis of Ge-poor **IWW**-6; (c) restoration of hydrolysed **IWW**-2 by Si; (d) restoration of hydrolysed **IWW**-6 by Si and (e) Al-incorporation of **IWW**-6 by realumination. The hydrolytically stable structures are shown in red. Unstable Ge-containing *D4R* motifs are shown in blue. Al atoms are shown in green. Bridging oxygen atoms are omitted for clarity.

In detail, experiments showed that the structure of the disassembled product by hydrolysis is related to the chemical compositions of the framework. Structural analysis by synchrotron powder X-ray diffraction suggests the Ge is exclusively located in the *D4R* sites. IWW-type zeolite with a high Ge content (Si/Ge = 3.6) has a *D4R* composition of [6Ge, 2Si] while the zeolite with a low Ge content (Si/Ge = 6.4) has a *D4R* composition of [4Ge, 4Si]. The former (IWW-2) can be fully pulled apart into layer structures but the latter (IWW-6) retains the connected structure after acidic treatment. The hydrolysed products tend to be reassembled into the original **IWW** structure. IWW-6 can be restored by the incorporation of either Si or Al. IWW-2 can be restored by Si. However, due to the limitation of Lowenstein's rule, Al atoms can't form the *D4R* independently and fail to restore the IWW-2 structure when used alone.

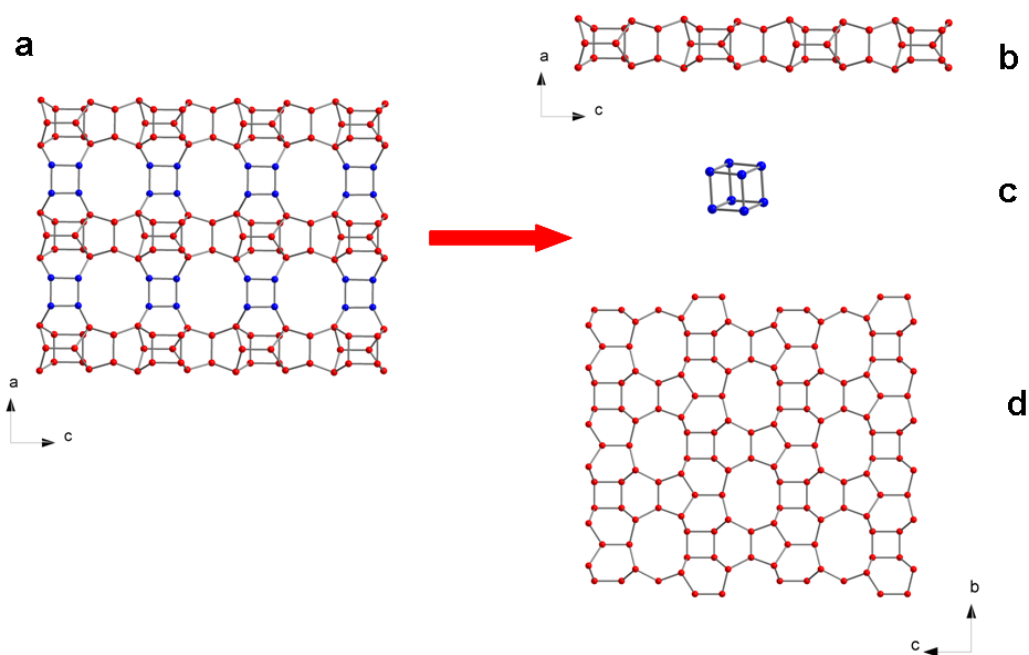
Although new structures from **IWW** were not achieved, investigation of the ADOR strategy applied to **IWW** zeolites also provided us ideas for further work.

- (A) realuminated IWW possesses higher Al content than directly synthesized Al-IWW and unique Al atom location. Incorporation of the Al into the *D4R* sites of the **IWW** framework created the Brønsted acidic sites near the 10-membered ring openings, which was reported to be beneficial to the catalytic selectivity on alkylation reactions. The catalytic performance of realuminated IWW will be investigated in the future.
- (B) Organization and reassembly of hydrolysed IWW in octylamine failed. It may be because the hydrolysed IWW which possesses a porous layered structure is not stable in base solvent. It was reported IPC-4 can be prepared with an ionic liquid, 1-ethyl-3-methylimidazolium bromide, instead of octylamine.<sup>9</sup> Our previous work also suggested the Si species were not soluble in the common ionic liquids.<sup>35, 36</sup> The further work will be finding out suitable ionic liquids for organizing and reassembling the hydrolysed IWW.
- (C) Reassembling the hydrolysed IWW with organosilane compounds tended to recover the original **IWW** structure. Layers of **IWW** connected by Si-containing *S4Rs* may be energetically unfavourable. To prepare zeolites with new structure types, other tetrahedral atoms or building units such as Ti, B and aluminophosphate will be employed as the pillaring motifs.

## 4.4 Top-down and post-synthesis treatment of ITH-type zeolites

### 4.4.1. Framework structure introduction to ITH-type zeolite

Another Ge-zeolite which possesses the structure of layers pillared by *D4Rs* is zeolite **ITH**. The first related material was ITQ-13 reported by Corma and co-workers in 2003.<sup>16</sup> In 2004 an identical structure, IM-7, was reported with a different synthetic temperature.<sup>37</sup> ITQ-13 and IM-7 can be synthesized from precursor gel compositions from purely siliceous to a Si/Ge ratio of 4. Recently, another related material with the **ITH** structure type has been reported.<sup>38</sup> This material named JLG-18 is synthesized from a non-concentrated gel system where the Si/Ge ratio of the gel can be reduced to 1. The structure of zeolite **ITH** is shown in Scheme 4-3. The **ITH** structure viewed in the *ac* plane projection (Scheme 4-3a) shows the layers (Scheme 4-3b) and the *D4R* pillars (Scheme 4-3c). 10-membered ring channels which are built up by the layers and pillars are formed along the *b* axis. The layer structure viewed in the *bc* plane projection shows the layer possesses 9-membered ring openings (Scheme 4-3d).



Scheme 4-3. **ITH** framework structure in the view of layers (shown in red) and *D4Rs* pillars (shown in blue). T-O-T bridges are drawn as straight lines for clarity.

## ***4.4.2 Experimental methods***

### ***4.4.2.1 Preparation of structure-directing agents***

**ITH**-type zeolites, including IM-7 and ITQ-13, were synthesized using hexamethonium hydroxide [HM(OH)<sub>2</sub>] as the SDA. The hydroxide form solution was obtained by 4-times anion-exchange of hexamethonium bromide (Aldrich) with Ambersep 900 OH form ion-exchange resin (Acros) in distilled water in a weight ratio of 1: 1: 4. Each anion-exchange took 10 hours at room temperature under stirring. Then the solution was filtered and new ion-exchange resin was added. The solution was then evaporated to achieve the required concentration of 45 wt%. The concentration of HM(OH)<sub>2</sub> was confirmed by hydroxide titration using phenolphthalein as indicator. The SDA for JLG-18 was N, N, N', N'- tetramethyl-1, 6-hexanediamine (TMHDA, 99 %, Aldrich) and was used without further purification.

### ***4.4.2.2 Synthesis of ITH-type zeolites with different Si/Ge ratios***

**ITH**-type zeolites with high Si/Ge ratios were synthesized following the procedure of IM-7.<sup>37</sup> The composition of the precursor gel was: (1-x) SiO<sub>2</sub>: x GeO<sub>2</sub>: 0.25 HM(OH)<sub>2</sub>: 0.5 HF: 5 H<sub>2</sub>O. TEOS (98%, Aldrich) and GeO<sub>2</sub> (99.9999%, Alfa Aesar) were added to HM(OH)<sub>2</sub> solution (45 wt%). Ethanol from hydrolysed TEOS and excess water were evaporated by continuous stirring at room temperature to achieve the required gel composition. HF (48 wt%, Aldrich) was added and the resulting gel was transferred to Teflon-lined stainless steel autoclaves. After being heated at 175 °C for 10 days, the autoclaves were opened and the products were isolated by filtration, washed with distilled water and dried at 100 °C overnight. Two batches of samples with different Ge contents were obtained: the sample with Si/Ge = 9 in a synthetic gel where x= 0.1 is named ITH-9 and the sample with Si/Ge= 5 where x= 0.17 is named ITH-5.

**ITH**-type zeolites with Si/Ge ratios below 5 can't be prepared using HM(OH)<sub>2</sub> as the SDA. **ITH** zeolites with higher Ge content were synthesized following the procedure of JLG-18.<sup>38</sup> The molar composition of the synthetic gel was: (1-x) SiO<sub>2</sub>: x GeO<sub>2</sub>: 7 TMHDA: 1.4 HF: 44 H<sub>2</sub>O. TEOS and GeO<sub>2</sub> were dissolved in the mixed solvent of TMHDA and water. After stirring overnight at room temperature, HF was added into the mixture and the synthetic gel was heated in autoclaves at 175 °C for 3 days. The products were washed with water, filtered and dried at 100 °C overnight. Two samples were obtained: A Si/Ge ratio in synthetic gel of 1 where x= 0.5 and a Si/Ge ratio of 2

where  $x = 0.33$ . These samples were named ITH-1 and ITH-2, respectively. All the **ITH** samples were calcined at 580 °C for 6 hours in air to remove the SDAs before hydrolysis. The Si/Ge ratios of the synthesized **ITH** zeolites were found to be different from the Si/Ge ratios in the synthetic gel. The ratios were measured with EDX and shown in Table 4-6 of 4.4.3.

#### ***4.4.2.3 Hydrolysis of ITH-zeolites***

Calcined **ITH**-zeolites were hydrolysed in HCl solution (0.1 M or 12 M) or in acetic acid ( $\geq 99.7\%$ , Aldrich). 0.2 g of calcined zeolite was stirred in 20 ml of acidic solution at room temperature or under reflux. The products were centrifuged and dried at 100 °C overnight.

#### ***4.4.2.4 Swelling of hydrolysed ITH***

Swelling was performed using a mixed solution of hexadecyltrimethylammonium chloride (CTAC, 25 wt%, Aldrich) and hexadecyltrimethylammonium hydroxide (CTAOH, 25 wt%, made by anion-exchange of CTAC with Ambersep 900 OH form ion-exchange resin) in a volume ratio of 1: 2. Typically 1 g of hydrolysed ITH was dispersed in 20 mL of the above mixed solution and stirred at ambient temperature for 8 hours. The slurry was centrifuged, washed with distilled water and dried at 60 °C overnight. The solid was calcined at 540 °C for 6 hours in air.

#### ***4.4.2.5 Organization of the hydrolysed ITH***

Organization followed the procedure described in the literature.<sup>9</sup> 0.2g of the hydrolysed ITH was mixed with 20 g of octylamine, heated at 70 °C for 8 hours and then stirred at room temperature overnight. The supernatant liquid was decanted. The solid was heated at 90 °C in an open vessel in air for 2 hours.

#### ***4.4.2.6 Characterisation***

PXRD patterns were collected on a STOE diffractometer under  $\text{CuK}\alpha 1$  radiation in Debye-Scherrer mode. The samples were filled in glass capillaries of 0.5 mm in diameter. Scanning electron microscopy (SEM) images were taken on a Jeol JSM 5600 instrument. The chemical analysis was obtained by EDX on the same instrument equipped with an Oxford Inca Energy EDX System at the operating voltage of 25 kV.

Solid-state NMR spectra were acquired using Bruker Avance III 600 MHz spectrometer equipped with a wide-bore 14.1 T magnet.  $^{29}\text{Si}$  MAS NMR spectra were obtained using

single-pulse experiments, with a recycle interval of 180 s. The MAS rate was 10 kHz. Powdered samples were packed into conventional 4 mm ZrO<sub>2</sub> rotors. Samples for <sup>19</sup>F Solid-state MAS NMR were loaded into 2.5 mm rotors and rotated at MAS rates of 25 kHz. The chemical shift scale was shown relative to CCl<sub>3</sub>F.

### 4.4.3 Results and discussions

#### 4.4.3.1 Powder X-ray diffraction

The PXRD patterns of calcined **ITH** zeolites with different Ge contents corresponded well to the simulated reflections (Fig. 4-13). The sharp peaks indicated the obtained **ITH** zeolites are well crystalline and thermally stable regardless of the Ge contents in the framework. A broad peak at about 9.7 ° 2θ of ITH-5 is attributed to zeolite **ITR** which is a polymorph of zeolite **ITH**. Zeolite **ITR** has the similar layer structure to zeolite **ITH** but a different stacking sequence.<sup>17</sup> Intergrown **ITH/ITR** was found to be synthesized in a wide composition range when using HM(OH)<sub>2</sub> as the SDA and the simulated PXRD shows the intergrowth **ITH/ITR** has peaks of different intensity.<sup>39</sup> No intergrown **ITR** was observed when the **ITH** zeolites were synthesized using TMHDA as SDA. Thus it is believed TMHDA was a suitable SDA for synthesis of **ITH** zeolites.

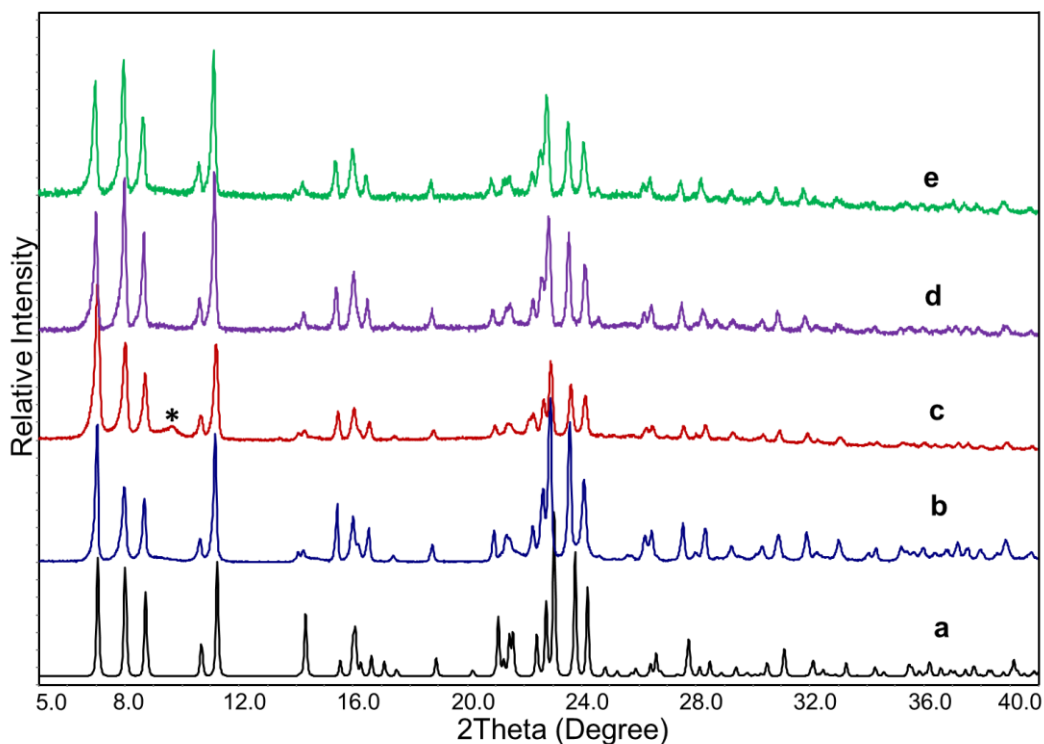


Fig. 4-13. PXRD patterns of (a) theoretical reflection from simulated **ITH** structure; (b) calcined ITH-9; (c) calcined ITH-5; (d) calcined ITH-2 and (e) calcined ITH-1. The reflection from **ITR** is marked by an asterisk.

#### 4.4.3.2 Morphology and chemical composition analysis of ITH-type zeolites

Fig. 4-14 shows the SEM images of (a) ITH-9, (b) ITH-5, (c) ITH-2 and (d) ITH-1. ITH-9 and ITH-5 exhibited needle-like crystals. ITH-2 and ITH-1 had plate shaped crystals. The crystal sizes of these samples were over 20  $\mu\text{m}$  in length. The Si/Ge ratios of the samples as determined by EDX are listed in Table 4-6.

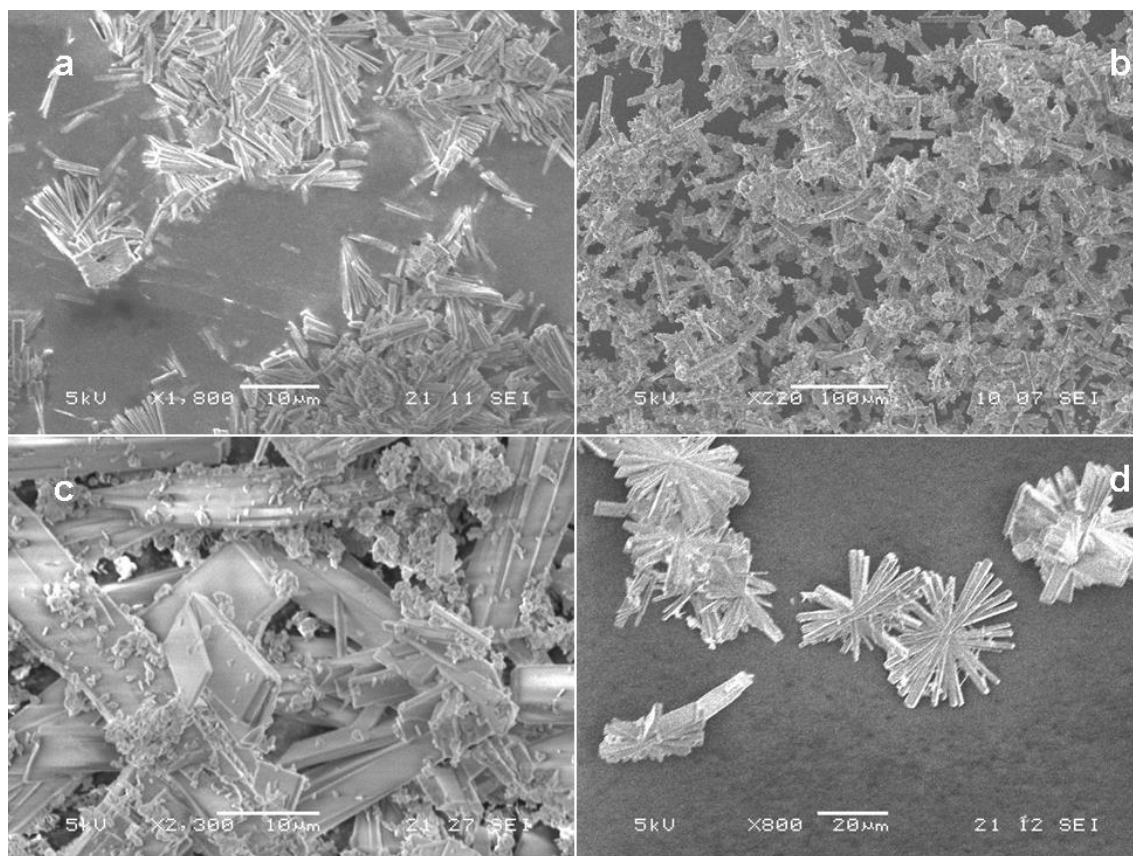


Fig. 4-14. SEM images of (a) ITH-9; (b) ITH-5; (c) ITH-2 and (d) ITH-1

Table 4-6. Chemical compositions of calcined **ITH**-type zeolites

	ITH-9	ITH-5	ITH-2	ITH-1
Si/Ge of synthetic gel	9	5	2	1
Si/Ge of as-made zeolites	15.7	8.3	4.4	2.5

In **ITH** zeolites there are 16 atoms in *D4R* sites out of the 56 atoms in the unit cell. To achieve full disassembly, at least half of the *D4R* sites should be occupied by Ge. In this case the highest Si/Ge ratio for successful hydrolysis should be  $(56-8)/8 = 6$ . However, ITH-9 and ITH-5 possess a Si/Ge ratio above 6. It can be predicted that ITH-9 and ITH-5 will be unable to be separated by hydrolysis.

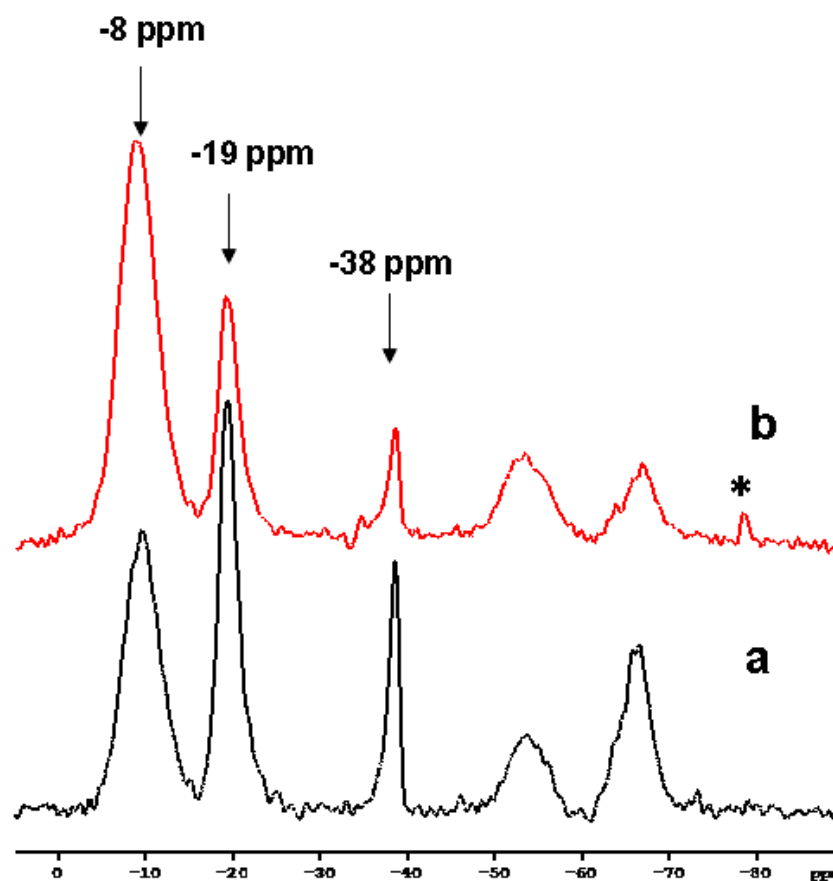


Fig. 4-15. The  $^{19}\text{F}$  MAS NMR spectra of (a) as-made ITH-9 and (b) as-made ITH-5. The resonance marked by the asterisk is the sideband of Teflon. Solid-state NMR experiment was carried out by Dr. Daniel Dawson from University of St Andrews.

$^{19}\text{F}$  MAS NMR spectrum has been used to study the Ge incorporation in *D4Rs* with different compositions (different  $n$  in  $[n\text{Si}, (8-n)\text{Ge}]$ ).<sup>40, 41</sup> In order to confirm the *D4R* compositions of ITH-9 and ITH-5,  $^{19}\text{F}$  MAS NMR was applied. As shown in Fig. 4-15, the resonances represented the local environments of  $\text{F}^-$  anions in the **ITH** framework. It has been reported that three resonances at -8, -19 and -38 ppm correspond to  $\text{F}^-$  located in  $[4\text{Si}, 4\text{Ge}]$  *D4Rs*,  $[7\text{Si}, 1\text{Ge}]$  *D4Rs* and purely siliceous *D4Rs*, respectively.<sup>42</sup> The integrals of each resonance suggested that ITH-5 possessed more  $[4\text{Si}, 4\text{Ge}]$  *D4Rs* than ITH-9 did, however there were still large amount of pure silica and high silica  $[7\text{Si}, 1\text{Ge}]$  *D4Rs*. The existence of these Si-rich *D4Rs* as evidenced by  $^{19}\text{F}$  MAS NMR spectra also supports the prediction that the calcined ITH-9 and ITH-5 would be stable under acidic treatments.

#### 4.4.3.3 Hydrolysis of ITH-9 and ITH-5

Hydrolysis of ITH-9 and ITH-5 in either dilute or concentrated HCl verified the above prediction. Fig. 4-16 and Fig. 4-17 are the PXRD patterns of ITH-9 and ITH-5 and their

hydrolysed products under different conditions. The peak positions didn't change after hydrolysis under variable conditions for up to 3 days, indicating the unit cell of **ITH**-zeolites remained identical. Chemical composition analysis by EDX shows the highest Si/Ge ratios of hydrolysed samples increased to 19.0 for ITH-9 and 11.5 for ITH-5 (Table 4-7). In ITH-9 and ITH-5 there are enough Si-O-Si bonds to hold the structure together, even though some Ge atoms are lost.

Although some Ge-zeolites are hydrolytically sensitive,<sup>43-45</sup> ITH-9 and ITH-5 with low Ge content were stable in acidic solution. The sustained PXRD patterns indicated the unit cells of ITH-9 and ITH-5 were retained. Calculation of Ge contents from the EDX results suggested that some Si-O-Ge bonds were acid-resistant.

A difference between ITH-5 and its hydrolysed product was the broad peak of ITH-5 from intergrown **ITR** was not observed after hydrolysis. This may imply that the **ITR** zeolites would be more hydrolytically sensitive than **ITH**. It is worth to investigate the hydrolysis behaviour of **ITR** zeolites in the future. However in this chapter the top-down treatment was not applied to **ITR** because the synthesis needs less economically efficient phosphonium cations as SDA.<sup>17</sup>

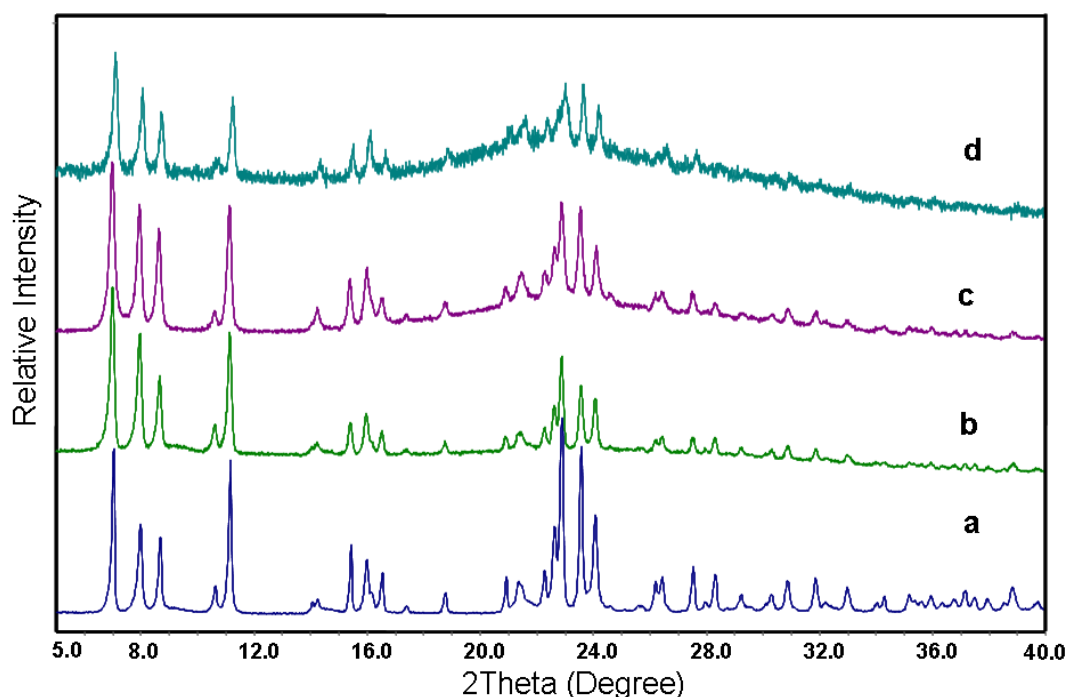


Fig. 4-16. PXRD patterns of (a) calcined ITH-9, (b) hydrolysed ITH-9 in 0.1 M HCl at room temperature, (c) hydrolysed ITH-9 in 0.1 M HCl under reflux and (d) hydrolysed ITH-9 in 12 M HCl at room temperature. All the hydrolysis treatments lasted for 3 days.

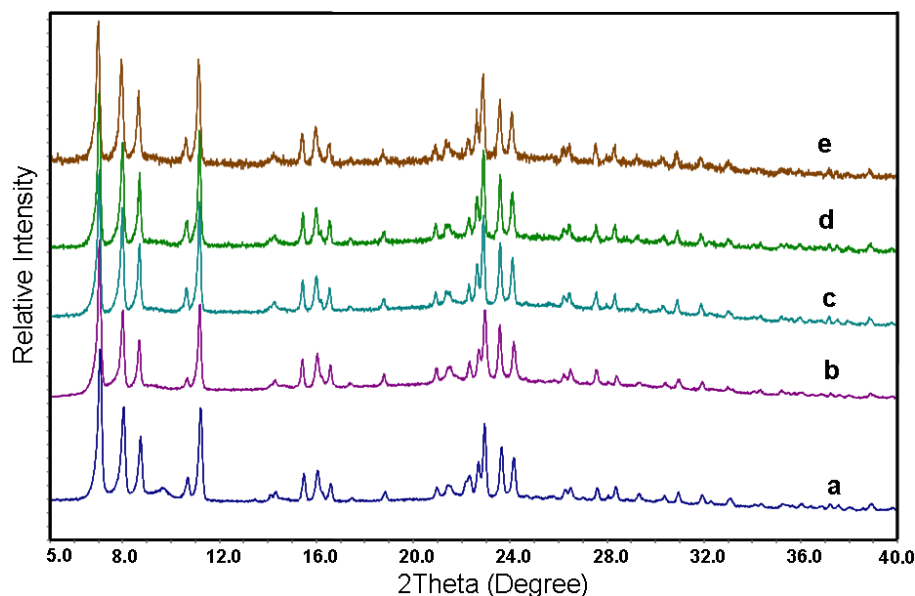


Fig. 4-17. PXRD patterns of (a) calcined ITH-5, (b) hydrolysed ITH-5 in 0.1 M HCl at room temperature, (c) hydrolysed ITH-5 in 0.1 M HCl under reflux, (d) hydrolysed ITH-5 in 12 M HCl at room temperature and (e) hydrolysed ITH-5 in 12 M HCl under reflux. All the hydrolysis treatments lasted for 3 days.

Table 4-7. Si/Ge ratios of Si-rich **ITH** zeolites and related products

samples	calcined	0.1 M HCl, room temperature	0.1 M HCl, reflux	12 M HCl, room temperature	12 M HCl, reflux
ITH-9	15.7	19.0	14.7	13.5	-
ITH-5	8.3	8.7	8.8	11.5	10.6

#### 4.4.3.4 Hydrolysis of ITH-2 and ITH-1

The chemical composition analysis shows the Si/Ge ratios of ITH-2 and ITH-1 were 4.4 and 2.5, respectively. The ratios were below the estimated value of when at least half of the *D4Rs* sites were occupied by Ge. This indicates there must be excess Ge in other sites in the framework, either in the layers or in the *D4Rs*.  $^{19}\text{F}$  MAS NMR spectra of as-made ITH-2 and ITH-1 are shown in Fig. 4-18. Neither of the samples possesses the resonance at -38 ppm, suggesting the absence of purely siliceous *D4Rs* in the frameworks. The major resonance at -8 ppm indicated [4Si, 4Ge] *D4Rs* are the dominant pillaring motifs of both samples. The spectrum of ITH-2 also exhibited a minor resonance at -19 ppm which indicated the existence of [7Si, 1Ge] *D4Rs*. No other F signals related to the *D4Rs* were observed, suggesting the excess Ge were located in the layers. For ITH-1, the Si/Ge ratio was about 2.5. There would be about 15 Ge atoms per 56 sites in the unit cell. In ITH-1 all *D4Rs* were [4Si, 4Ge] in composition. It means

there were 8 Ge atoms in 16 *D4R* sites of the **ITH** unit cell, with another 7 Ge atoms located in the 40 sites of the layers. Similarly it can be calculated that there would be about 2 Ge atoms in the layer of ITH-2. There was a broad minor resonance at about -55 ppm in both spectra. This is attributed to the F<sup>-</sup> anions located near to the Ge-containing [4<sup>1</sup>5<sup>2</sup>6<sup>2</sup>] cages in the layer structure.<sup>42</sup>

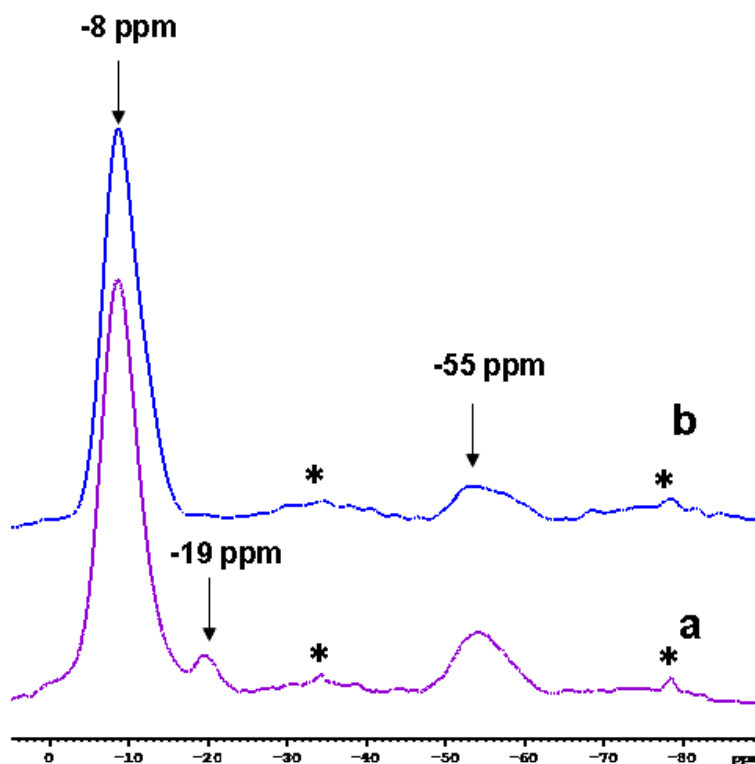


Fig. 4-18. <sup>19</sup>F NMR spectra of (a) as-made ITH-2 and (b) as-made ITH-1. The sidebands are marked by asterisks. Solid-state NMR experiment was carried out by Dr. Daniel Dawson from University of St Andrews.

Hydrolysis of ITH-2 under different conditions was investigated by PXRD (shown in Fig. 4-19). The layer structure of **ITH** framework is parallel to the *bc* projection, thus (*0kl*) reflections are the intralayer reflections. If the structure can be disassembled by removing *D4Rs*, the intralayer reflections would remain while the interlayer reflection of (*100*) at about 7.00 ° 2θ would be shifted or disappear. The PXRD pattern of samples that were hydrolysed in 12 M HCl at room temperature didn't change compared to parental ITH-2. When ITH-2 was treated in acidic solution under elevated temperature, either in 0.1 M HCl or in 12 M HCl, the alterations of the PXRD patterns were minimal: First, the intralayer reflections almost remained intact, but slightly shifted to higher 2θ values which may be due to the removal of Ge atoms. For example, the peak position of (*002*) shifted from 7.98 ° (*d* = 11.02 Å) to 8.09 ° (*d* = 10.90 Å), indicating the

contraction of the unit cell parameter  $c$  from 22.04 Å to 21.80 Å (a difference of 0.12 Å); Second, the interlayer reflection ( $100$ ) shifted from 7.00 ° to 7.19 ° after hydrolysis. The interlayer distance decreased from 12.64 Å to 12.29 Å. Compared to the 0.12 Å difference of the unit cell contraction, the interlayer distance decreased by 0.35 Å, indicating the decrease was not only caused by the removal of Ge; other changes also included the intensity of  $hkl$  reflections for which  $h$  is not equal to zero, such as ( $111$ ), decreased with respect to the intralayer reflections. Combining this with the chemical composition analysis by  $^{19}\text{F}$  NMR it is believed that a partial disassembly has occurred when ITH-2 was treated by an acidic solution at an elevated temperature: (a) the layer structure remained intact; (b) the interlayer distance decreased due to the destruction of  $[4\text{Si}, 4\text{Ge}]$   $D4Rs$  and (c) the hydrolytically stable  $[7\text{Si}, 1\text{Ge}]$   $D4Rs$  were still connecting the layer structures so an interlayer distance of hydrolysed ITH-2 didn't change too much.

Hydrolysed ITH-2 in 0.1 M HCl at room temperature has a similar PXRD pattern (Fig. 4-19d) to those hydrolysed under reflux, except the intensity of the interlayer reflection was low and the peak was broad. It can be explained by at room temperature, the destruction of the  $D4Rs$  resulted in some disrupted  $[7\text{Si}]$  units which pillared the layers, thus resulted in less regular stacked layers; while at higher temperature the pillaring units were more ordered and led to uniform interlayer distance.

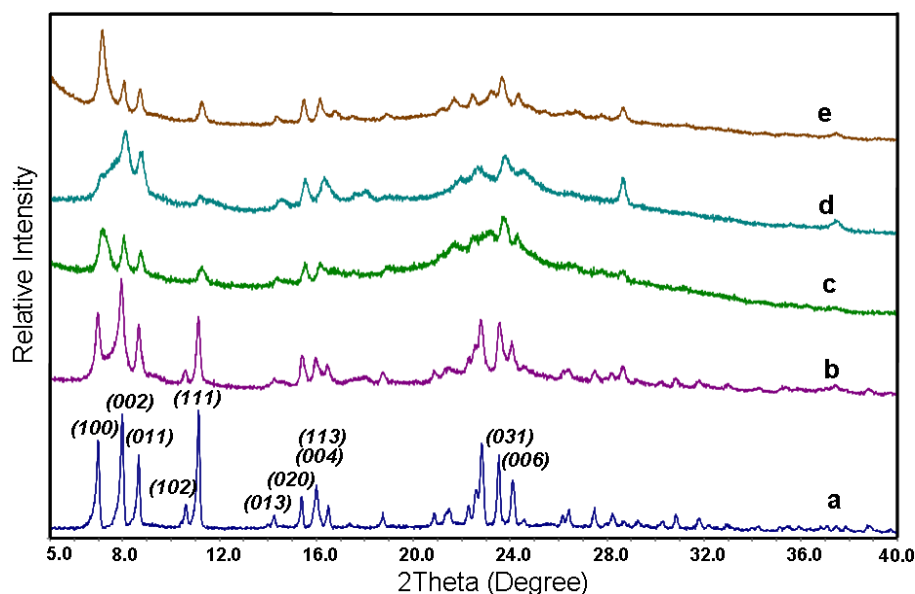


Fig. 4-19. PXRD patterns of (a) calcined parental ITH-2, (b) hydrolysed ITH-2 in 12 M HCl at room temperature, (c) hydrolysed ITH-2 in 12 M HCl under reflux, (d) hydrolysed ITH-2 in 0.1 M HCl at room temperature and (e) hydrolysed ITH-2 in 0.1 M HCl under reflux. All hydrolysis treatments were kept for 48 hours.

SEM images of the hydrolysed ITH-2 in 0.1 M HCl are shown in Fig. 4-20. Both samples that were hydrolysed at room temperature and under reflux possessed the same morphology as the parental ITH-2. The EDX analysis indicates the Si/Ge ratios of hydrolysed ITH-2 increased to 25.5 at room temperature and 30.5 under reflux. As it has been discussed, there were approximately 8 Ge in *D4R* sites and 2 Ge in T sites of layer structure out of 56 T sites of **ITH** unit cell. If the 8 Ge in *D4R* sites were dissolved out, the rest 48 T sites with Si/Ge ratios of 25.5 and 30.5 would contain 1.8 and 1.5 Ge atoms, respectively. These calculated numbers were in agreement with the estimated Ge quantities in the **ITH** layer T sites (2 Ge atoms in the layer of the unit cell). It is suggested that Ge atoms in *D4Rs* of ITH-2 were removed after acidic treatment.

Chemical composition analysis of hydrolysed ITH-9 and ITH-5 has shown some Si-O-Ge bonds stay intact after acidic treatment. By measuring the Si/Ge ratio and checking the PXRD reflections of the hydrolysed ITH-2, it can be concluded the **ITH** layers are of better hydrolytically stability than *D4Rs* in **ITH**.

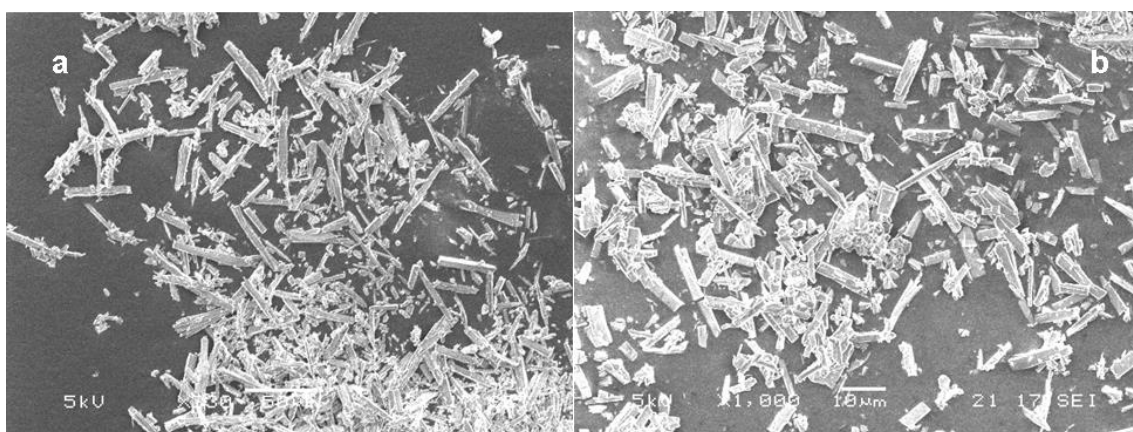


Fig. 4-20. SEM images of hydrolysed ITH-2 from 0.1 M HCl, (a) at room temperature and (b) under reflux.

In order to examine if the layers were fully separated or not, swelling with CTA<sup>+</sup> solution or organization with octylamine were also carried out to the hydrolysed sample that obtained from 0.1 M HCl under reflux. However, no obvious change of the interlayer reflection was observed in the PXRD patterns (Fig. 4-21). These unchanged PXRD patterns further confirmed that the hydrolysed ITH-2 was a connected 3D structure rather than a separated 2D layer structure.

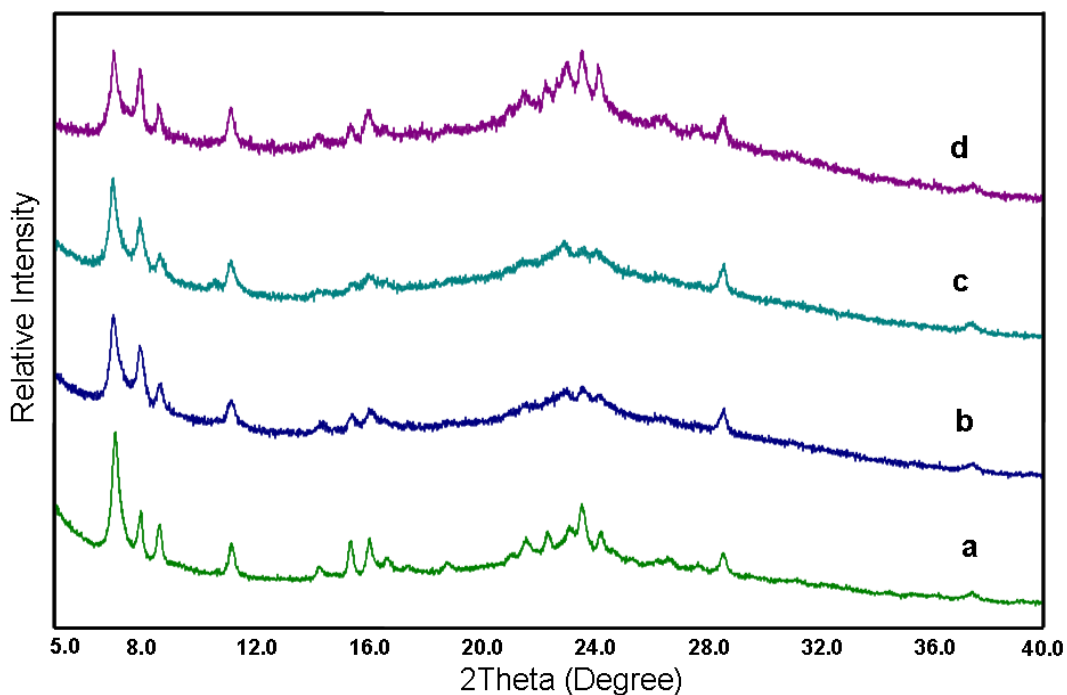


Fig. 4-21. PXRD patterns of (a) hydrolysed ITH-2 in 0.1 M HCl under reflux (b) hydrolysed ITH-2 swelled with CTA<sup>+</sup> surfactant (c) calcination of the swelling sample and (d) hydrolysed ITH-2 organized with octylamine.

Hydrolysis of ITH-1 was investigated following similar procedures to that of ITH-2. However the results were different, probably due to the different Ge distribution in the ITH structure, especially the different Ge distribution in *D4Rs*. Fig. 4-22 is the PXRD patterns of calcined parental ITH-1 and the products hydrolysed under different conditions. It was difficult to identify the intralayer reflections due to the low intensities of the hydrolysed samples. This may be because of the large proportion of Ge atoms in the layer (7 Ge atoms out of 40 sites). EDX analysis indicated that the Si/Ge ratio of hydrolysed ITH-1 in 12 M HCl at room temperature increased to 115.5. The high Si/Ge ratio suggests that Ge atoms in the layer have been dissolved out of the framework as well as any Ge in the *D4Rs*. Meanwhile, a strong, broad peak which was considered to be the interlayer reflection of the hydrolysed **ITH** layers appeared after hydrolysis. The peak position, which varied from 7.6 ° to 8.9 ° 2θ related to the hydrolysis solutions: In a solution at the same HCl concentration (b and c; d and e), the peak shifted to positions of higher 2θ values (lower *d*-spacing) at high temperature; At the same hydrolysis temperature, the peak shifted to positions of higher 2θ values in solutions with decreasing HCl concentration.

The changeable interlayer peak indicated that the ITH layers were fully separated. The difference between the ITH-1 and ITH-2 was that the  $^{19}\text{F}$  MAS NMR showed the resonance from  $[\text{7Si}, 1\text{Ge}] \text{D4Rs}$  were only present in the ITH-2 sample. The  $[\text{7Si}, 1\text{Ge}] \text{D4Rs}$  were believed to link the layers of the ITH-2 after hydrolysis. The absence of the  $[\text{7Si}, 1\text{Ge}] \text{D4Rs}$  caused the successful separation of the ITH-1. This indicates the chemical composition of  $\text{D4Rs}$  is an important parameter that can affect the top-down treatment.

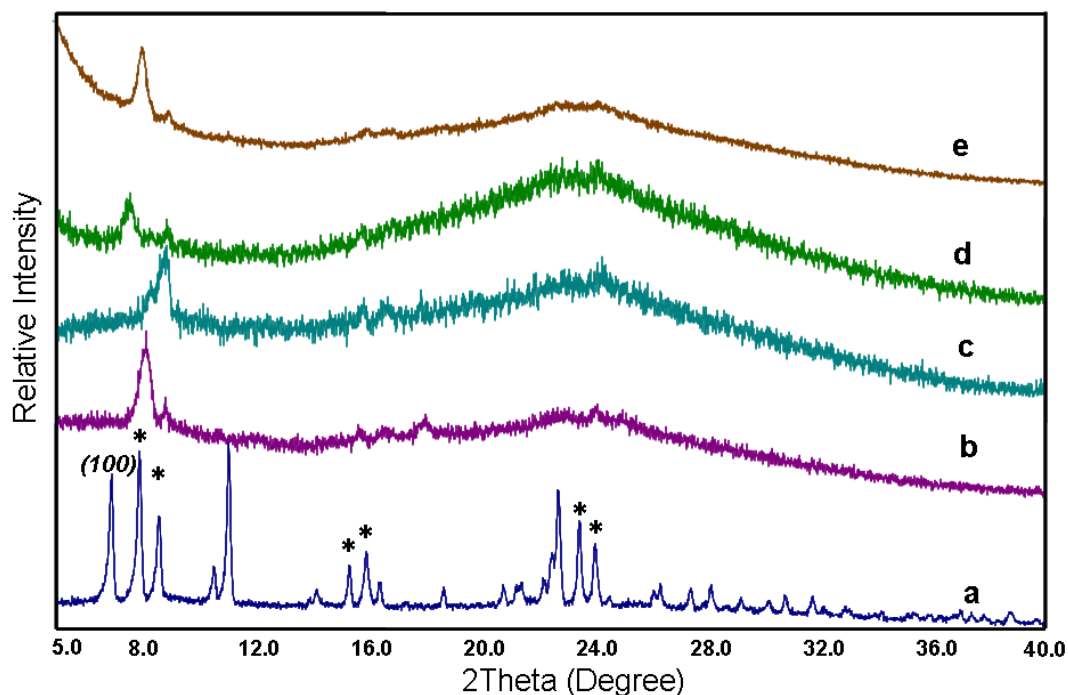


Fig. 4-22. PXRD patterns of (a) calcined parental ITH-1, (b) hydrolysed ITH-1 in 12 M HCl at room temperature, (c) hydrolysed ITH-1 in 12 M HCl at 85 C, (d) hydrolysed ITH-1 in 0.1 M HCl at room temperature and (e) hydrolysed ITH-1 in 0.1 M HCl at 85 C. All hydrolysis treatments were kept for 48 hours. The intralayer ( $0kl$ ) reflections are marked by asterisks.

According to Fig. 4-22, a hydrolysed sample with the best crystallinity was obtained in 12 M HCl at room temperature. A detailed investigation of the hydrolysis procedure under this condition was carried out. PXRD patterns of samples hydrolysed for different durations are shown in Fig. 4-23. Unlike **UTL** and the IWW-2 zeolites which can be fully hydrolysed within 5 minutes, the ITH-1 retained its structure after 1 hour of hydrolysis treatment. After treatment for 3 hours, a broad peak at  $8.8^\circ 2\theta$  appeared. This peak was deemed to be the interlayer reflection after the removal of the  $\text{D4R}$  pillars. Meanwhile, interlayer and intralayer reflections of parental ITH-1 were retained, indicating the separation of the layers was incomplete. Prolongation of the acidic

treatment up to 16 h resulted in the disappearance of intralayer reflections, indicating that the layers were destroyed.

The interlayer peak of the hydrolysed ITH-1 was getting sharper, which implies the layer stacking was getting more regular with the increasing hydrolysis time by a ripening procedure. The slow ripening stage was also observed in the hydrolysis process of the IWW-2 in 12 M HCl. When hydrolysing IWW-2 in 12 M HCl, a fast disassembly and the following slow ripening stage were observed. For the ITH-1, although the disassembly was not as fast as the IWW-2, a similar ripening process occurred.

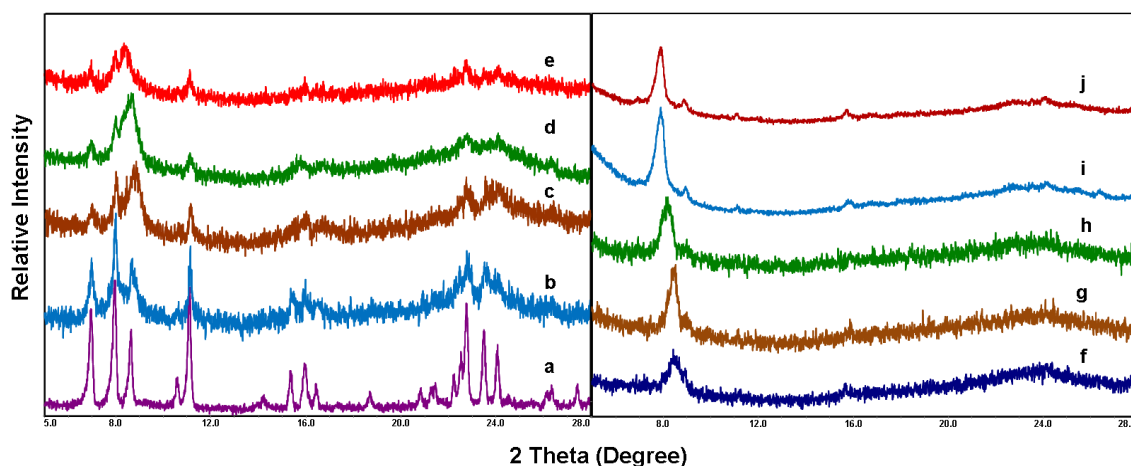


Fig. 4-23. PXRD patterns of hydrolysed ITH-1 in 12 M HCl at room temperature for (a) 5 min, (b) 1 h, (c) 3 h, (d) 6 h, (e) 10 h, (f) 16 h, (g) 24 h, (h) 30 h, (i) 36 h and (j) 42 h.

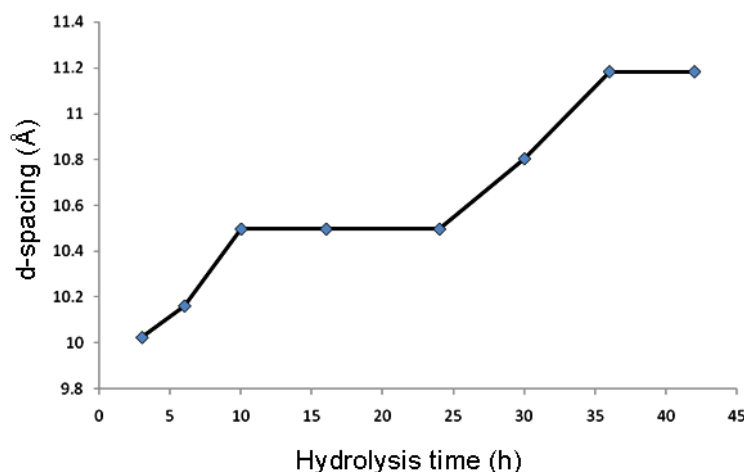


Fig. 4-24. Values of d-spacing of the hydrolysed ITH-1 interlayer reflection versus the hydrolysis time in 12 M HCl at room temperature.

The PXRD reflection position of the newly created interlayer peak shifted with hydrolysis time consecutively. The trend is plotted in Fig. 4-24. It shows two steps of structural changes. Firstly, the interlayer distance increased to about 10.5 Å within 10

hours, due to the destruction of the *D4R* pillars. Secondly, the layer distance increased to 11.2 Å was due to the rearrangement of the layer structures after the complete separation of the layer connections.

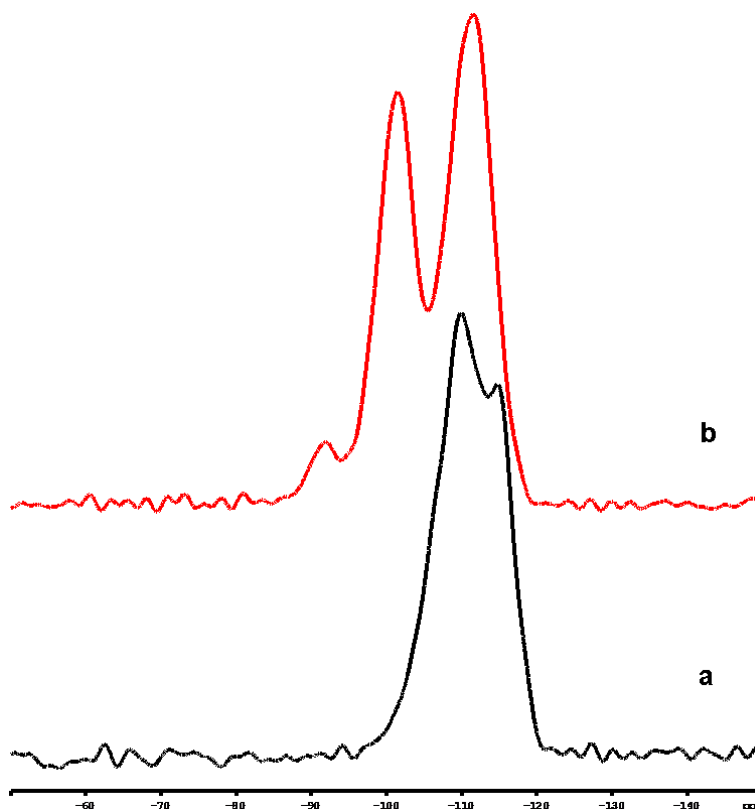


Fig. 4-25. <sup>29</sup>Si MAS NMR spectrum of (a) calcined parental ITH-1 and (b) hydrolysed ITH-1 in 12 M HCl at room temperature for 48 hours. Solid-state NMR experiment was carried out by Dr. Daniel Dawson from University of St Andrews.

<sup>29</sup>Si MAS NMR spectra of ITH-1 and hydrolysed ITH-1 in 12 M HCl at room temperature for 48 hours are shown in Fig. 4-25. Similarly to the spectra of parental **IWW** and hydrolysed **IWW**, the spectrum of parental ITH-1 exhibited two Q<sup>4</sup> resonances which refer to Si surrounded by 4 Si and Si surrounded by at least one Ge, respectively. The spectrum of hydrolysed ITH-1 exhibited an obvious Q<sup>3</sup> resonance and a minor Q<sup>2</sup> resonance, indicating the existence of silanol defects after acidic treatment.

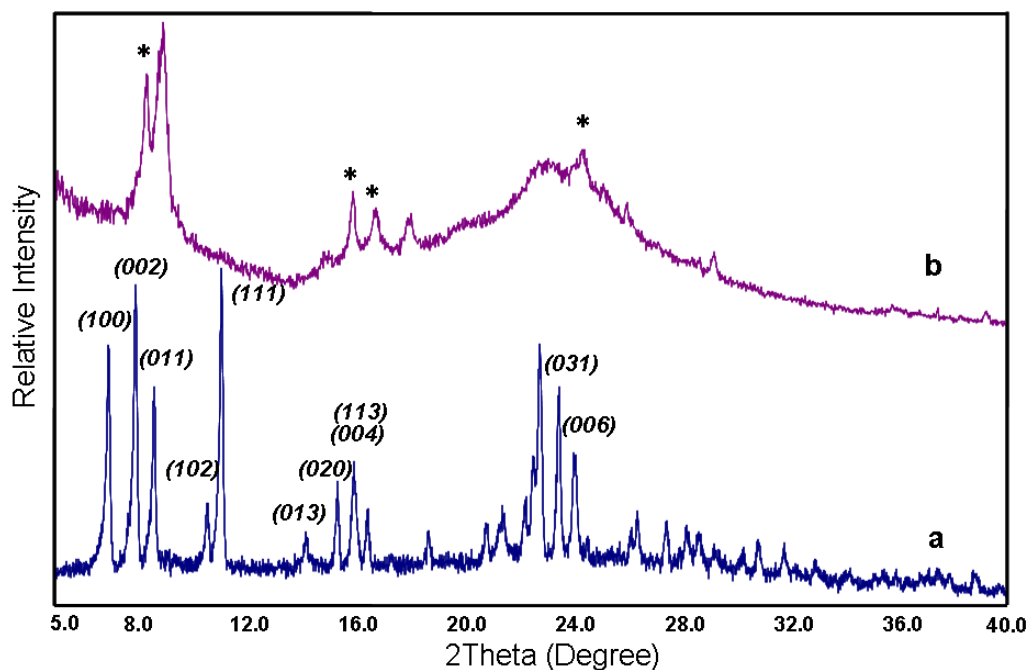


Fig. 4-26. PXRD patterns of (a) calcined parental ITH-1 and (b) hydrolysed ITH-1 in acetic acid. The intralayer reflections retained after acidic treatment are marked by asterisks.

The low intensity of the intralayer reflections after hydrolysis indicates that the layers were destroyed as well as the *D4R* pillars, which would obstruct the following organization and reassembly processes. In order to retain the layer structure, weak acid such as acetic acid was used for the hydrolysis treatment. The PXRD patterns of calcined parental ITH-1 and its hydrolysis product in pure acetic acid are shown in Fig. 4-26. Unlike the samples hydrolysed in HCl, a sample hydrolysed in weak acid for 48 hour retained the intralayer reflections such as (002), (020), (004) and (006), indicating the layer structure was more stable in acetic acid. Meanwhile, an interlayer reflection occurred at  $9.0^\circ 2\theta$  ( $d$ -spacing of  $9.8 \text{ \AA}$ ). However, a broad peak ranging from  $22^\circ$  to  $26^\circ$  indicates the product is also low in crystallinity. Compared with ITH-1 hydrolysed in HCl of which the Si/Ge ratio is 115.5, the Si/Ge ratio of hydrolysed ITH-1 in acetic acid is about 7.0. It can be concluded that after hydrolysis there were still considerable Ge atoms existed in the product. The results suggest although the dissolution of Ge from **ITH** zeolites is more difficult than that in HCl but **ITH** zeolite with high Ge content is still sensitive to acidic hydrolysis. Further swelling process has been carried out. However, the product was dissolved to form amorphous materials. This is probably due to the product not being stable in the basic solution during the swelling process.

#### 4.4.4 Summary

In this part of the chapter, the top-down treatment was applied to another Ge-zeolite, **ITH**, which is constructed by the layers and *D4R* pillars. **ITH**-type zeolites with different Si/Ge ratios (15 to 2.5) were synthesized. The disassembly of the **ITH** zeolites by chemically selective cleavage of interlayer Si-O-Ge bonds under appropriate acidic treatment was investigated. The chemical compositions of the parental zeolites proved to be important to its hydrolytic stability: for zeolites having less than 50 % Ge in *D4Rs* of **ITH** zeolite (Si/Ge > 6),  $^{19}\text{F}$  NMR indicates some of the *D4Rs* were purely siliceous or highly siliceous (such as [7Si, 1Ge]). These **ITH** zeolites were stable in acidic solutions. Hydrolysis treatments with acidic solution under different conditions were carried out but no changes were observed from the PXRD patterns. The chemical composition analysis by EDX showed that despite the loss of some Ge atoms, there were still enough Si-O-Si bonds to hold the structure together.

For the **ITH** zeolites with the Si/Ge ratio below 6, the  $^{19}\text{F}$  MAS NMR showed that the excess Ge went into the layers. Meanwhile, the **ITH** zeolite with the Si/Ge ratio of 4.4 still has Si-rich *D4Rs*. The presence of the Si-rich [7Si, 1Ge] *D4Rs* resulted in a partial separation of the layers after the hydrolysis but the hydrolysis product was still a connected structure.

If the Si/Ge ratios in the framework continuously decreased, the **ITH** zeolites with only *D4Rs* of [4Si, 4Ge] composition were synthesized. The layers can be pulled apart completely. However, Ge content in the layer was high as well, which resulted in the low hydrolytic stability of the layer structure. The **ITH** layers are less hydrolytically stable than the **IWW** layers. The difference can be explained by the different Ge distributions in the two zeolites. In **IWW**, Ge atoms exclusively occupy the sites in the *D4Rs*. The purely siliceous **IWW** layers are stable to the hydrolysis treatment with acidic solution. Differently, some Ge atoms locate in the sites of the layers of **ITH**. Although by decreasing the Ge content, the Ge atoms that incorporated in the layers were reduced, but at the same time it was leading to the presence of some Si-rich or purely siliceous *D4Rs*. This prevents the successful disassembly of **ITH** zeolites. Although using weak acid can retain the layer structure but the hydrolysed product is still of low-crystalline. Further work would be finding out appropriate mild conditions for hydrolysing the **ITH** zeolites to layers but retain the crystallinity. Reassembly of the layer structures directly or incorporating other units such as *S4Rs* would give the chance

of preparing new zeolite structures with different pore sizes. Moreover, the realumination and restoration of the layer structure by Al and Si compounds would be applied to the **ITH** layers, aiming at synthesizing materials with unique catalytic performance and good hydrothermal stability.

#### ***4.5 Summary of Chapter 4***

The disassembly of the germanosilicate **IWW** and **ITH** type zeolites with different Si/Ge ratios under acidic treatment was investigated. The preserved structure of original crystalline layers under hydrolysis conditions was confirmed by means of PXRD. Structural analysis by either synchrotron powder XRD analysis for **IWW** or chemical composition analysis by  $^{19}\text{F}$  MAS NMR spectrum for **ITH** revealed the Ge distribution in the corresponding structures. Results indicated that the Ge distribution and content were crucial for the disassembly process as well as the layer stability. Ge atoms are exclusively located in the *D4R* sites of the **IWW** framework. **IWW**-zeolites with high Ge content can be hydrolysed to a fully separated structure. Hydrolysis of Ge-poor **IWW**-zeolites led to a connected structure. Hydrolysed **IWW** of both high and low Ge content can be restored by incorporating Si to the framework, but only hydrolysed Ge-poor **IWW** can be restored by incorporation of Al due to the limitation of Lowenstein's rule.

Being different from the **IWW** zeolites, the occupancy of some Ge atoms in the layers of the **ITH** zeolites cannot be excluded. **ITH**-zeolites with Si/Ge ratios above 6 were hydrolytically stable to acid treatment, because the frameworks contain some pure silica or high silica *D4Rs*. These *D4Rs* are hydrolytically stable and connect the structure together. **ITH**-zeolites with a Si/Ge ratio of about 4 were partially hydrolysed to a connected structure due to the existence of high silica [7Si, 1Ge] *D4R* pillars. **ITH**-zeolites with only [4Si, 4Ge] *D4Rs* in the framework can be fully separated but the layer structure was unstable to harsh chemical treatment conditions. Suitable hydrolysis conditions such as time, pH, temperature, etc. will affect the final product layer structure and also will be important for the following reassembly process. A separated layer structure of **ITH** zeolite with low crystallinity was obtained by the disassembly process in weak acid.

## 4.6 References

1. M. E. Davis, *Chem. Mater.*, 2013, **26**, 239-245.
2. M. Moliner, F. Rey and A. Corma, *Angew. Chem. Int. Ed.*, 2013, **52**, 13880-13889.
3. R. Morris, *Top. Catal.*, 2010, **53**, 1291-1296.
4. C. S. Cundy and P. A. Cox, *Chem. Rev.*, 2003, **103**, 663-702.
5. V. Valtchev and L. Tosheva, *Chem. Rev.*, 2013, **113**, 6734-6760.
6. B. Yilmaz, U. Muller, M. Feyen, H. Zhang, F.-S. Xiao, T. De Baerdemaeker, B. Tijsebaert, P. Jacobs, D. De Vos, W. Zhang, X. Bao, H. Imai, T. Tatsumi and H. Gies, *Chem. Commun.*, 2012, **48**, 11549-11551.
7. Q. Huo, R. Xu, S. Li, Z. Ma, J. M. Thomas, R. H. Jones and A. M. Chippindale, *J. Chem. Soc., Chem. Commun.*, 1992, 875-876.
8. A. Corma, V. Fornes, S. B. Pergher, T. L. M. Maesen and J. G. Buglass, *Nature*, 1998, **396**, 353-356.
9. W. J. Roth, P. Nachtigall, R. E. Morris, P. S. Wheatley, V. R. Seymour, S. E. Ashbrook, P. Chlubná, L. Grajciar, M. Položij, A. Zukal, O. Shvets and J. Čejka, *Nature Chem.*, 2013, **5**, 628-633.
10. A. Corma, M. T. Navarro, F. Rey, J. Rius and S. Valencia, *Angew. Chem. Int. Ed.*, 2001, **40**, 2277-2280.
11. J.-L. Paillaud, B. Harbuzaru, J. Patarin and N. Bats, *Science*, 2004, **304**, 990-992.
12. W. J. Roth, O. V. Shvets, M. Shamzhy, P. Chlubná, M. Kubů, P. Nachtigall and J. Čejka, *J. Am. Chem. Soc.*, 2011, **133**, 6130-6133.
13. E. Verheyen, L. Joos, K. Van Havenbergh, E. Breynaert, N. Kasian, E. Gobechiya, K. Houthoofd, C. Martineau, M. Hinterstein, F. Taulelle, V. Van Speybroeck, M. Waroquier, S. Bals, G. Van Tendeloo, C. E. A. Kirschhock and J. A. Martens, *Nat. Mater.*, 2012, **11**, 1059-1064.
14. R. Pophale, P. A. Cheeseman and M. W. Deem, *Phys. Chem. Chem. Phys.*, 2011, **13**, 12407-12412.
15. A. Corma, F. Rey, S. Valencia, J. L. Jorda and J. Rius, *Nat. Mater.*, 2003, **2**, 493-497.
16. C. Avelino, P. Marta, R. Fernando, S. Gopinathan and J. T. Simon, *Angew. Chem. Int. Ed.*, 2003, **42**, 1156-1159.
17. A. Corma, M. J. Diaz-Cabanas, J. L. Jorda, F. Rey, G. Sastre and K. G. Strohmaier, *J. Am. Chem. Soc.*, 2008, **130**, 16482-16483.
18. R. Castañeda, A. Corma, V. Fornés, F. Rey and J. Rius, *J. Am. Chem. Soc.*, 2003, **125**, 7820-7821.
19. D. L. Dorset, G. J. Kennedy, K. G. Strohmaier, M. J. Diaz-Cabañas, F. Rey and A. Corma, *J. Am. Chem. Soc.*, 2006, **128**, 8862-8867.
20. A. Bergamaschi, A. Cervellino, R. Dinapoli, F. Gozzo, B. Henrich, I. Johnson, P. Kraft, A. Mozzanica, B. Schmitt and X. Shi, *Nucl. Instrum. Methods Phys. Res. A*, 2009, **604**, 136-139.
21. C. Baerlocher, *Acta Crystallographica Section A*, 1984, **40**, C368-C368.
22. Graesslin, J., Ph.D. Thesis, ETH Zuerich, 2013.
23. S. Brunauer, P. H. Emmett and E. Teller, *J. Am. Chem. Soc.*, 1938, **60**, 309-319.
24. P.-E. Werner, L. Eriksson and M. Westdahl, *J. Appl. Crystallogr.*, 1985, **18**, 367-370.
25. B. Toby, *J. Appl. Crystallogr.*, 2005, **38**, 1040-1041.
26. P. Chlubná, W. J. Roth, H. F. Greer, W. Zhou, O. Shvets, A. Zukal, J. Čejka and R. E. Morris, *Chem. Mater.*, 2013, **25**, 542-547.
27. W. Wang and M. Hunger, *Acc. Chem. Res.*, 2008, **41**, 895-904.
28. M. Hunger, in *Zeolites and Catalysis*, Wiley-VCH Verlag GmbH & Co. KGaA, 2010, pp. 493-546.
29. F. Gao, M. Jaber, K. Bozhilov, A. Vicente, C. Fernandez and V. Valtchev, *J. Am. Chem. Soc.*, 2009, **131**, 16580-16586.
30. J. A. van Bokhoven, D. C. Koningsberger, P. Kunkeler, H. van Bekkum and A. P. M. Kentgens, *J. Am. Chem. Soc.*, 2000, **122**, 12842-12847.
31. A. Corma, F. J. Llopis, C. Martínez, G. Sastre and S. Valencia, *J. Catal.*, 2009, **268**, 9-17.

32. Lowenstein, W. et. al., *Am. Mineral.*, 1954, **39**, 92-96.
33. H. Kosslick, V. A. Tuan, R. Fricke, C. Peuker, W. Pilz and W. Storek, *J. Phys. Chem.*, 1993, **97**, 5678-5684.
34. J. B. Nagy, Z. Gabelica and E. G. Derouane, *Chem. Lett.*, 1982, **11**, 1105-1108.
35. R. E. Morris, *Chem. Commun.*, 2009, 2990-2998.
36. P. S. Wheatley, P. K. Allan, S. J. Teat, S. E. Ashbrook and R. E. Morris, *Chem. Sci.*, 2010, **1**, 483-487.
37. N. Bats, L. Rouleau, J. L. Paillaud, P. Caultet, Y. Mathieu and S. Lacombe, in *Stud. Surf. Sci. Catal.*, eds. I. M. C. E. van Steen and L. H. Callanan, Elsevier, 2004, vol. Volume 154, Part A, pp. 283-288.
38. X. Ren, J. Liu, Y. Li, J. Yu and R. Xu, *J. Porous Mater.*, 2013, **20**, 975-981.
39. A. Corma, M. J. Diaz-Cabanas, J. L. Jorda, F. Rey, K. Boulahya and J. M. Gonzalez-Calbet, *J. Phys. Chem. C*, 2009, **113**, 9305-9308.
40. X. Liu, U. Ravon, F. Bosselet, G. Bergeret and A. Tuel, *Chem. Mater.*, 2012, **24**, 3016-3022.
41. X. Liu, U. Ravon and A. Tuel, *Chem. Mater.*, 2011, **23**, 5052-5057.
42. J. A. Vidal-Moya, T. Blasco, F. Rey, A. Corma and M. Puche, *Chem. Mater.*, 2003, **15**, 3961-3963.
43. Q. Li, A. Navrotsky, F. Rey and A. Corma, *Microporous Mesoporous Mater.*, 2003, **64**, 127-133.
44. P. S. Petkov, H. A. Aleksandrov, V. Valtchev and G. N. Vayssilov, *Chem. Mater.*, 2012, **24**, 2509-2518.
45. J. Jiang, J. L. Jorda, M. J. Diaz-Cabanas, J. Yu and A. Corma, *Angew. Chem. Int. Ed.*, 2010, **49**, 4986-4988.

# Chapter 5 Ionic Liquid Assisted Synthesis of Zeolites

## 5.1 Introduction

In 2012, Ren and co-workers reported a novel solvent free synthetic route to zeolites.<sup>1</sup> Unlike conventional hydrothermal synthesis in which reagents are dissolved in aqueous solution, in this solvent free method zeolite materials were obtained by mechanically mixing the raw materials of tetrahedral atom species and structure directing agents and the following thermal treatment in sealed autoclaves. The advantages of this method include high yields, high utilization of autoclaves, simplification of the synthetic procedure and minimal production of waste solvent.<sup>2</sup> It is believed that the solvent free synthesis of zeolites is a green procedure. Multiple zeolites with different structure types such as **MFI**, **FAU**, **MOR**, and **BEA** were successfully prepared by selecting appropriate SDAs.<sup>1</sup> Meanwhile, the method is not only limited to the aluminosilicate zeolites, recent research from the same group also confirmed that this strategy is feasible for the preparation of silicoaluminophosphates (SAPOs), aluminophosphates (AlPOs), and heteroatom aluminophosphates (MeAPOs, Me = Co and Mg), all of which are zeolite analogues.<sup>2,3</sup>

SDAs are a key parameter which would determine the framework type of the zeolitic materials obtained in this solvent free strategy. Both inorganic cations and organic quaternary ammonium salts were used in the solvent free strategy and led to multiple framework types. As described in Chapter 1, ionic liquids are structurally similar to organic quaternary ammonium compounds, which play the role of SDAs in zeolite synthesis.<sup>4-6</sup> Moreover, ionic liquids are considered to be designable compounds due to their synthetic flexibility.<sup>5-7</sup> There will be potential of obtaining zeolites with new pore architectures by replacing organic SDAs with ionic liquids.

Up to now ionothermal synthesis of siliceous or aluminosilicate zeolite remains a challenge, although syntheses of silica aerogel,<sup>8</sup> mesoporous materials,<sup>9, 10</sup> AlPOs<sup>11, 12</sup> and MOFs<sup>13, 14</sup> have been reported. Silica species are rarely dissolved in those commonly used ionic liquids. Meanwhile, ionic liquids also decrease the reactivity of water.<sup>9, 15</sup> These are possibly the reasons that prevent the formation of crystalline silicate based materials in ionic liquids. Only a few studies reported the synthesis of

siliceous zeolites with the aid of ionic liquids.<sup>16-18</sup> Yan and co-workers converted a dry gel precursor to **MFI**-type zeolite in ionic liquid under microwave heating.<sup>16</sup> Although water is used in their method, the reaction still occurred under ambient pressure due to the assistance of ionic liquid. Wheatley *et al.* reported the synthesis of siliceous **MFI** and **TON**-type zeolites in a partially hydroxide anion-exchanged ionic liquid,<sup>17</sup> which contains 1-butyl-3-methylimidazolium cations and approximately 65 %/ 35 % of OH<sup>-</sup>/ Br<sup>-</sup> mixed anions. Hydroxide anions were used as mineralizer and constructive for the dissolution of silicate precursor. From these examples it can be concluded that ionothermal synthesis of silicate based zeolites possesses advantages such as reducing the autogenous pressure in sealed autoclaves and developing new routes to synthesizing zeolites.

## ***5.2 Aims***

The overall aim of this chapter is to synthesize silicate based zeolites with the assistance of commonly used ionic liquids under “solvent free” conditions, and characterise the obtained materials. This synthetic route will be named ionic liquid assisted (ILA) synthesis. The roles of the ionic liquids and other synthetic conditions will be investigated. The aim of these investigations is to develop a new “green chemistry” synthetic route for zeolites and to improve our understanding about the target of ionothermal synthesis of silicate based zeolites.

## ***5.3 Ionic liquid assisted synthesis of zeolites***

### ***5.3.1 Experimental Sections***

#### ***5.3.1.1 Preparation of ionic liquids***

1-Ethyl-3-methylimidazolium chloride ([Emim]Cl), 1-Ethyl-3-methylimidazolium bromide ([Emim]Br), 1-Ethyl-3-methylimidazolium bis(trifluoromethylsulfonyl)imide ([Emim]Tf<sub>2</sub>N) and 1-Butyl-3-methylimidazolium Bromide ([Bmim]Br) were used in the ILA synthesis procedures. [Emim]Br and [Bmim]Br were prepared following the methods described in the literature.<sup>11</sup>

10.9 g of degassed ethylbromide (0.1 mol, Alfa Aesar) was dropped into 8.2 g of redistilled N-methyl imidazole (0.1 mol, Aldrich) with constant stirring under N<sub>2</sub> atmosphere conditions. The mixture was refluxed at 40 °C for 3 h and cooled down to room temperature. Ethyl acetate was added, and the white solids were precipitated from the solution. The products were filtered, washed with ethyl acetate and dried under vacuum at 50 °C for 10 h to give 17.8 g of EmimBr (Yields: 93.2 %). The ionic liquid was stored under an inert atmosphere. Successful preparation of [Emim]Br and its purity were confirmed by <sup>1</sup>H solution NMR (300 MHz, D<sub>2</sub>O): δ= 1.39 (t, 3H, CH<sub>3</sub>), 3.77 (s, 3H, NCH<sub>3</sub>), 4.11 (q, 2H, NCH<sub>2</sub>), 7.29-7.37 (d, 2H, NC(H)C(H)N), 8.60 (s, 1H, NC(H)N).

For the synthesis of [Bmim]Br, procedure was same as that described above for EmimBr, except for using 13.7 g of degassed butylbromide (0.1 mol, Alfa Aesar) instead of ethylbromide. The products were obtained as 19.5 g of white solids (Yields: 89.0 %). <sup>1</sup>H NMR (300 MHz, D<sub>2</sub>O): δ= 0.79 (t, 3H, CH<sub>3</sub>), 1.19 (m, 2H, CH<sub>2</sub>), 1.72 (m, 2H, CH<sub>2</sub>), 3.75 (s, 3H, NCH<sub>3</sub>), 4.05 (t, 2H, NCH<sub>2</sub>), 7.29-7.34 (d, 2H, NC(H)C(H)N), 8.57 (s, 1H, NC(H)N).

[Emim]Cl and [Emim]Tf<sub>2</sub>N were purchased from Aldrich and used without further purification.

### ***5.3.1.2 Ionic liquid assisted synthesis of zeolites***

A typical ILA synthesis procedure, which uses [Emim]Br as the SDA, is described as follows: 1.400 g of Na<sub>2</sub>SiO<sub>3</sub>·9H<sub>2</sub>O (5 mmol, Aldrich), 0.300 g of fumed silica (5 mmol, Cab-O-Sil M5, Acros) and 0.020 g of hydrated Al(OH)<sub>3</sub> (0.3 mmol, Aldrich) were ground in a mortar for 5 minutes. 0.400 g of NH<sub>4</sub>Cl (7.5 mmol, Fisher) and 0.190 g of [Emim]Br (1 mmol, home-made) were added into the mixture and ground for another 5 minutes. In the case of investigating the effect of moist air to the synthesis, 0.1 g of distilled water (5 mmol) was added to the mixture. White solid, or in some occasions such as grinding the mixture for over 20 min, white paste, would be formed as the synthetic precursor. The solid or paste was transferred into Teflon lined stainless steel autoclaves and heated at 175 °C for 48 hours. The product was washed with distilled water, filtered, and dried at 90 °C overnight. The products were calcined at 550 °C for 6 hours to remove the organic SDAs in the framework.

The synthesis and recovery procedures of ILA synthesis with other ionic liquids including [Emim]Cl, [Emim]Tf<sub>2</sub>N and [Bmim]Br were similar to the above methods.

### **5.3.1.3 Characterisations**

The samples were filled in glass capillaries of 0.5 mm diameter for PXRD analysis. The PXRD data were collected on a STOE diffractometer using CuK $\alpha$ 1 radiation in Debye-Scherrer mode. Thermal gravimetric analysis (TGA) was carried out in a Netzsch TG 209 instrument under air flow. The samples were heated in alumina crucibles at a heating ramp of 10 °C·min<sup>-1</sup>. The morphologies of the products were examined by scanning electron microscopy (SEM) using a Jeol JSM-5600 scanning electron microscope. A tungsten filament was used as the electron source and the operating high voltage was 5 kV. Chemical composition was investigated by Energy Dispersive X-rays Spectroscopy (EDX) with an Oxford Inca Energy system on the same SEM instrument at operating voltage of 25 kV. Surface area was examined with nitrogen adsorption isotherms at -196 °C using a Micromeritics ASAP 2020 instrument. The sample outgassing was carried out at 110 °C for 8 h and then the temperature was increased to 300 °C and maintained for 3 h. Solid-state NMR spectra were acquired using Bruker Avance III 600 MHz spectrometer equipped with a wide-bore 14.1 T magnet. Powder samples were packed into conventional 4 mm ZrO<sub>2</sub> rotors. <sup>13</sup>C NMR spectra were acquired using cross polarization (CP), with a contact pulse (ramped for <sup>1</sup>H) of 2 ms, and <sup>1</sup>H decoupling applied during acquisition. Chemical shifts were referenced to TMS for <sup>13</sup>C and <sup>1</sup>H using alanine as a secondary reference. The MAS rate was 12.5 kHz. For the <sup>27</sup>Al MAS NMR a MAS rate of 14 kHz was used.

## **5.3.2 Results and discussions**

### **5.3.2.1 Ionic liquid assisted synthesis with [Emim]Br**

The hydrated raw material of Na<sub>2</sub>SiO<sub>3</sub>·9H<sub>2</sub>O is a key compound in the “solvent free” synthetic route. It provides the Na<sub>2</sub>O and H<sub>2</sub>O which are crucial to create the suitable alkaline condition for zeolite crystallization. Thus the Na<sub>2</sub>O/H<sub>2</sub>O ratio was fixed unless extra H<sub>2</sub>O was added. The pH value of the precursor can be controlled by adding NH<sub>4</sub>Cl, which plays the role of buffering agent. The raw material also supplied a part of silica sources. By adding a second silica source such as fumed silica the ratios of Na<sub>2</sub>O/SiO<sub>2</sub> and H<sub>2</sub>O/SiO<sub>2</sub> can be adjusted. The SiO<sub>2</sub>/Al<sub>2</sub>O<sub>3</sub> ratio was controlled by adding Al sources such as Al(OH)<sub>3</sub> or aluminium isopropoxide. The synthetic precursor possessed

chemical composition of: *a* Na<sub>2</sub>O: *b* SiO<sub>2</sub>: *c* Al<sub>2</sub>O<sub>3</sub>: *d* NH<sub>4</sub>Cl: *e* [Emim]Br: *f* H<sub>2</sub>O. Systematic studies on the effects of several synthetic parameters on the products were carried out. Synthetic compositions are listed in Table. 5-1. The phases of the products were identified by means of PXRD.

Table 5-1. Synthetic compositions of the precursor for ILA synthesis <sup>a</sup>

Exp. No.	<i>a</i> Na <sub>2</sub> O mmol	<i>b</i> SiO <sub>2</sub> mmol	<i>c</i> Al <sub>2</sub> O <sub>3</sub> mmol	<i>d</i> NH <sub>4</sub> Cl mmol	<i>e</i> [Emim]Br mmol	<i>f</i> H <sub>2</sub> O mmol	Products
1	5	10	0.15	7.5	0	45	α-quartz
2	5	10	0.15	7.5	0	60	α-quartz
3	5	10	0.15	7.5	1	45	<b>TON</b>
4	5	10	0.15	7.5	2	45	<b>TON</b>
5	5	10	0	7.5	1	45	<b>TON+*MRE</b>
6	5	10	0	7.5	2	45	<b>TON+*MRE</b>
7	5	10	0.07	7.5	1	45	<b>TON</b>
8	5	10	0.25	7.5	1	45	<b>TON</b>
9	5	10	0.35	7.5	1	45	amorphous
10	5	10	0.35	7.5	2	60	amorphous
11	5	10	0.15	7.5	1	75	<b>TON</b>
12	5	10	0.15	7.5	1	60	<b>TON</b>
13	5	10	0.15	7.5	1	50	<b>TON</b>
14	5	10	0.15	7.5	1	30	amorphous

a. All the experiments occurred at 175 °C for 48 hours.

### ***Effect of [Emim]Br***

The effect of the [Emim]Br was investigated by comparing the products from the experiments with same compositions but different [Emim]Br contents. Two groups of the experiments, Exp. 1, 3, 4 and Exp. 2, 12, were used for the comparison. Their PXRD patterns are shown in Fig. 5-1. In both Exp. 1 and 2, no ionic liquid was added into the synthetic precursor. The products from both experiments were dense phase materials. PXRD identified that the products were α-quartz (Fig. 5-1a and d).

On addition of the [Emim]Br, the precursors with the same composition (Experiment No. 3, 4 and 12) produced the crystalline materials after being heated in the oven. The products synthesized from different experiments possess identical PXRD patterns which

are different from the dense  $\alpha$ -quartz (Fig. 5-1b c and e). The reflections identified the materials TON-type zeolites.<sup>19</sup>

Although sodium cations have been used as SDA for some zeolite frameworks such as LTA,<sup>20</sup> FAU<sup>21</sup> and TON,<sup>22</sup> the synthetic precursor containing sodium but no ionic liquid only resulted in dense silicate compounds. On addition of [Emim]Br a porous material was synthesized. These experiments indicate the [Emim]Br plays the role of SDA in this ionic liquid assisted synthesis. It is believed that the presence of ionic liquid is essential for successful formation of a zeolitic framework.

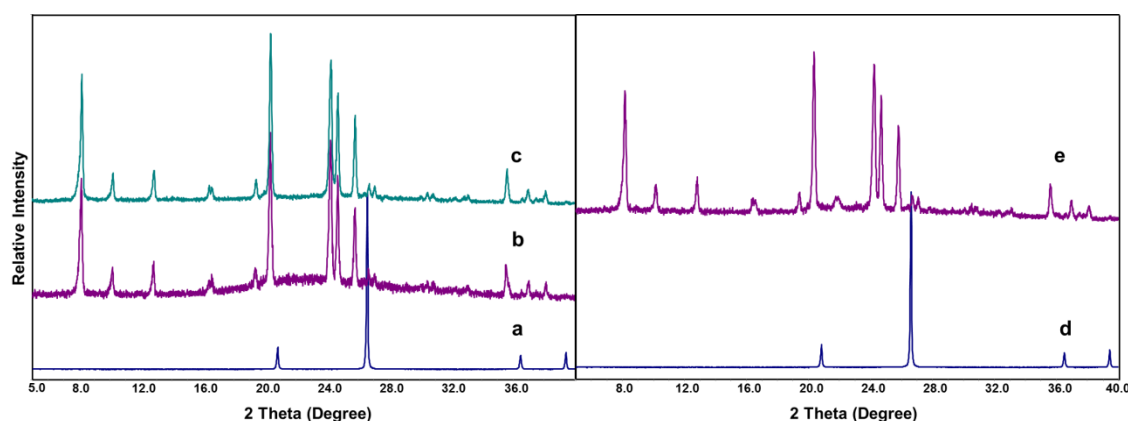


Fig. 5-1. PXRD patterns of (a) product of Exp. 1; (b) product of Exp. 3; (c) product of Exp. 4; (d) product of Exp. 2 and (e) product of Exp. 12.

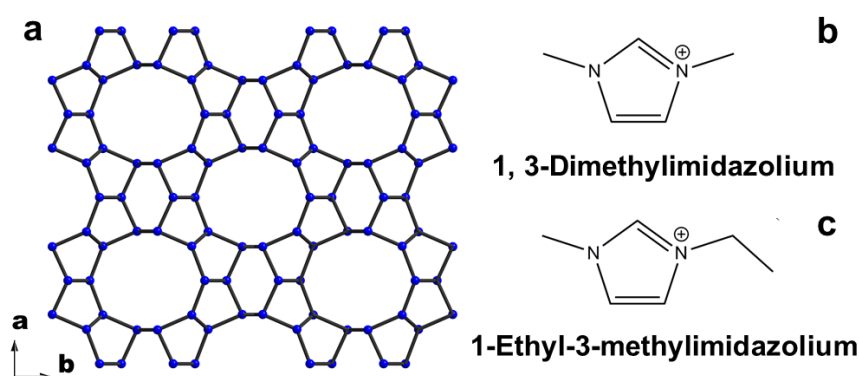


Fig. 5-2. (a) The *ab* plane projection of TON zeolite which shows the 10-membered ring channels. Blue spots represent the tetrahedral centres and the bonds between them are the bridging oxygen; (b) reported SDA structure for the synthesis of ZSM-22 and (c) structure of 1-ethyl-3-methylimidazolium cation for this ionic liquid assisted synthesis of TON zeolite.

TON-type zeolites which possess one-dimensional 10-membered ring channels<sup>22</sup> are widely used as catalysts.<sup>23-25</sup> It has been reported a ZSM-22 zeolite with TON-type framework was prepared by using 1, 3-dimethylimidazolium hydroxide as SDA which

is structurally similar to EmimBr (Fig. 5-2).<sup>26</sup> Wheatley and co-workers' work also proved that **TON**-type isostructural zeolite was crystallized using a partially hydroxide-exchanged ionic liquid with 1-butyl-3-methylimidazolium cations.<sup>17</sup> Therefore it is reasonable to consider that the imidazolium-based compounds are suitable SDAs for the synthesis of the one-dimensional **TON**-type zeolites.

<sup>13</sup>C CP/MAS NMR spectrum of the as-made **TON**-zeolite obtained from Exp. 3 is shown in Fig. 5-3. The spectrum corresponds well to the 1-ethyl-3-methylimidazolium cation structure. The <sup>13</sup>C CP/MAS NMR indicates the [Emim]Br was present in the zeolite framework and was intact after the synthetic procedure.

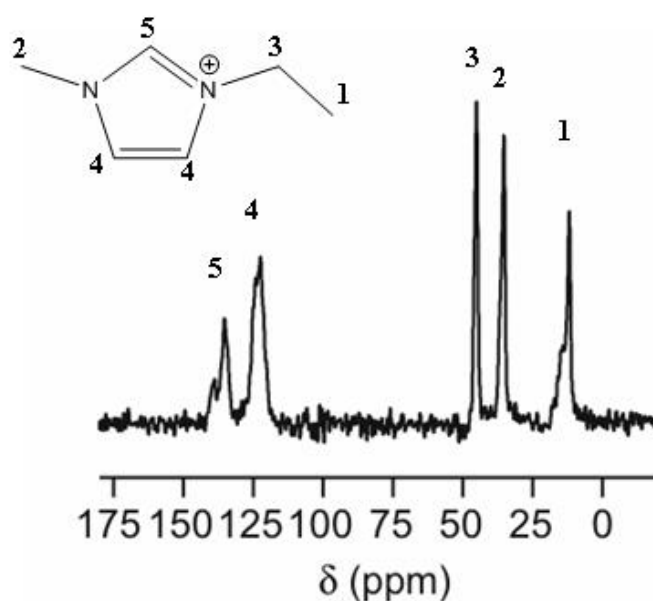


Fig. 5-3. <sup>13</sup>C CP/MAS NMR spectrum of as-made **TON**-zeolite: the inserted figure shows the structure of the used ionic liquid cation and the corresponding carbon atoms to the resonances. The spectrum is the result of averaging 8192 transients, with a recycle interval of 2 s. Solid-state NMR experiment was carried out by Dr. Valerie Seymour from University of St Andrews.

One advantage of using ionic liquids for zeolite synthesis is that the ionic liquids are recyclable. It is because the ionic liquids possess negligible vapour pressure so they are easily separated from the volatile solvent.<sup>27</sup> To successfully recycle the ionic liquids, their stability under the synthetic conditions is important. The product of Exp. 3 was washed with 10 mL of distilled water and filtered. The pH of the filtration was examined with a pH indicator and the value was 14. It indicated the ILA synthesis was carried out under alkaline condition. Previous ionothermal syntheses have shown some 1-alkyl-3-methylimidazolium based ionic liquids with different length of alkyl chains

were not stable.<sup>11</sup> On addition of HF, the cations were decomposed. The only exception was [Emim]<sup>+</sup> which remained intact after the reaction. In this ILA synthesis the <sup>13</sup>C MAS NMR spectrum suggests the [Emim]<sup>+</sup> was also stable after treatment in alkaline environment and is suitable for recycling.

### *Effect of SiO<sub>2</sub>/Al<sub>2</sub>O<sub>3</sub>*

The variation of the SiO<sub>2</sub>/Al<sub>2</sub>O<sub>3</sub> ratios in the synthetic precursor was achieved by changing the content of Al source. In Table 5-1, experiments with SiO<sub>2</sub>/Al<sub>2</sub>O<sub>3</sub> ratios from +∞ (0 mmol of Al<sub>2</sub>O<sub>3</sub>) to 28 (0.35 mmol of Al<sub>2</sub>O<sub>3</sub>) were carried out. Exp. 5 and 6 were the ILA synthesis that took place without adding any Al species. These experiments produced mixed solids with **TON**-type and **\*MRE**-type zeolites (Fig. 5-4d). The PXRD intensities of both phases suggested **TON**-type zeolite was the major product and a minor amount of **\*MRE** was considered as impurity. **\*MRE** has similar one-dimensional 10-membered rings and 5-membered ring building units to those also present in the **TON** framework.<sup>28</sup> The formation of **\*MRE** in the absence of aluminium was also observed when synthesizing other **TON** type zeolites such as Nu-10.<sup>29</sup>

Fig. 5-4c is the PXRD pattern of the products obtained from Exp. 7 where the precursor composition was 5 Na<sub>2</sub>O: 10 SiO<sub>2</sub>: 0.07 Al<sub>2</sub>O<sub>3</sub>: 7.5 NH<sub>4</sub>Cl: 1 EmimBr: 45 H<sub>2</sub>O. On addition of Al sources into the synthetic precursor, **TON** zeolite of high purity was selectively synthesized. Synthetic precursors with the SiO<sub>2</sub>/Al<sub>2</sub>O<sub>3</sub> ratios ranging from 40 to 140 resulted in pure **TON**-type zeolite as product after being heated in the oven (PXRD patterns shown in Fig. 5-1b, Fig. 5-4 b and c). However, **TON**-type zeolites with SiO<sub>2</sub>/Al<sub>2</sub>O<sub>3</sub> ratio below 20 in the synthetic precursor were inaccessible through the ILA synthetic route as the SiO<sub>2</sub>/Al<sub>2</sub>O<sub>3</sub> ratios below this composition only led to an amorphous product (Exp. 9 and 10). The crystallization of **TON** zeolite requires an appropriate SiO<sub>2</sub>/Al<sub>2</sub>O<sub>3</sub> ratio. This was also reported by other researchers. For example, in the synthesis of Nu-10, lower SiO<sub>2</sub>/Al<sub>2</sub>O<sub>3</sub> ratios resulted in less crystalline zeolites, and when the SiO<sub>2</sub>/Al<sub>2</sub>O<sub>3</sub> ratio was below 60, other phases such as ferrierite were formed.<sup>29</sup> This may be because the **TON** zeolites synthesized with ionic liquid as SDA are only stable at a low framework Al content. Incorporation of Al into the framework results in negative charge which needs to be balanced by cations. As discussed in Chapter 1, organic SDAs with large molecular volume favour the formation of high silica or purely siliceous zeolites.

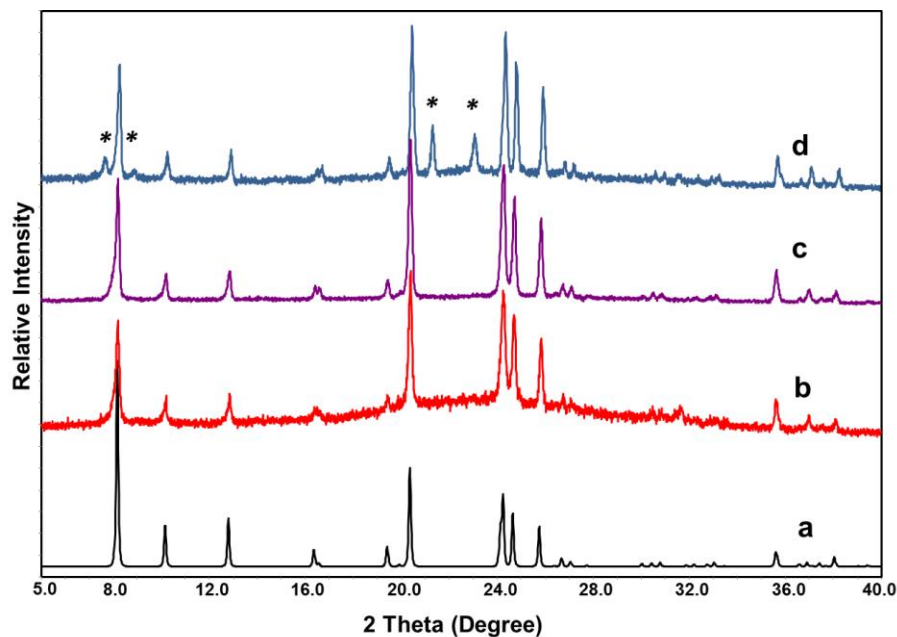


Fig. 5-4. PXRD patterns of (a) simulated **TON** type framework; (b) as-made product obtained from Exp. 8; (c) as-made product obtained from Exp. 7 and (d) as-made products of Exp. 5 which contains impurity of **\*MRE**. The asterisks in the figure indicate the reflections from the **\*MRE** impurity.

In Exp. 7, 3 and 8, the  $\text{SiO}_2/\text{Al}_2\text{O}_3$  ratios of the synthetic precursors were 140, 67 and 40, respectively. EDX was applied to examine the  $\text{SiO}_2/\text{Al}_2\text{O}_3$  ratios of the products. The results showed the corresponding  $\text{SiO}_2/\text{Al}_2\text{O}_3$  ratios of the products of Exp.7, 3 and 8 were 427, 78 and 18, respectively. The results indicate the  $\text{SiO}_2/\text{Al}_2\text{O}_3$  ratios of the **TON** zeolites synthesized through the ILA route can be easily varied from 430 to 18 by controlling the  $\text{SiO}_2/\text{Al}_2\text{O}_3$  ratios of the synthetic precursor.

Al atoms in the framework tetrahedral site can induce acidic sites which are important in catalysis reactions.<sup>30, 31</sup> To investigate the Al location in **TON**-zeolites,  $^{27}\text{Al}$  MAS NMR experiments were carried out.

The  $^{27}\text{Al}$  NMR spectra of calcined products with different Si/Al ratios are shown in Fig. 5-5. Each spectrum shows two major resonances at the chemical shift of 54 and 64 ppm, both of which are referred to tetrahedrally coordinated central atoms.<sup>32, 33</sup> **TON** zeolite contains four crystallographically independent T sites. It has been reported the Al were preferentially located in the T3 and T4 sites.<sup>33</sup> It is also observed that the integral of the resonance at 64 ppm has a higher population with increasing Al incorporation. An

empirical equation<sup>34</sup> that described the correlation between the <sup>27</sup>Al chemical shifts  $\delta$  and the corresponding mean Al-O-Si bond angles  $\alpha$  is:

$$\delta = -0.50 \alpha + 132 \text{ (ppm)} \quad (\text{eq. 5-1})$$

According to eq. 5-1, these two resonances are assigned to the Al atoms with the mean Al-O-Si angles of  $156^\circ$  ( $\delta = 54$  ppm) and  $136^\circ$  ( $\delta = 64$  ppm), respectively. The Si-O-Si bonds in zeolites are in the range of angles between  $140^\circ$  and  $180^\circ$ , and the angle below  $140^\circ$  was found to have high bond energy.<sup>35, 36</sup> Incorporation of Al into these energetically unfavourable sites even at low Al content explained why pure TON zeolites can be selectively synthesized with the addition of Al species. Meanwhile, I also conclude that the Al species were first incorporated into the sites with lower energy. The sites with higher T-O-T bond energy were gradually incorporated as the Al content increased, which is evidenced by the increasing integral of the resonance at 64 ppm with increasing Al incorporation.

A minor resonance at 6 ppm indicates a very small amount of octahedrally coordinated Al,<sup>37</sup> which may come from the unreacted Al species present in the product. The dominant resonance from the tetrahedral Al implies that almost all the Al species were in the framework and the SiO<sub>2</sub>/Al<sub>2</sub>O<sub>3</sub> ratios obtained from EDX were reliable to indicate the framework SiO<sub>2</sub>/Al<sub>2</sub>O<sub>3</sub> ratios.

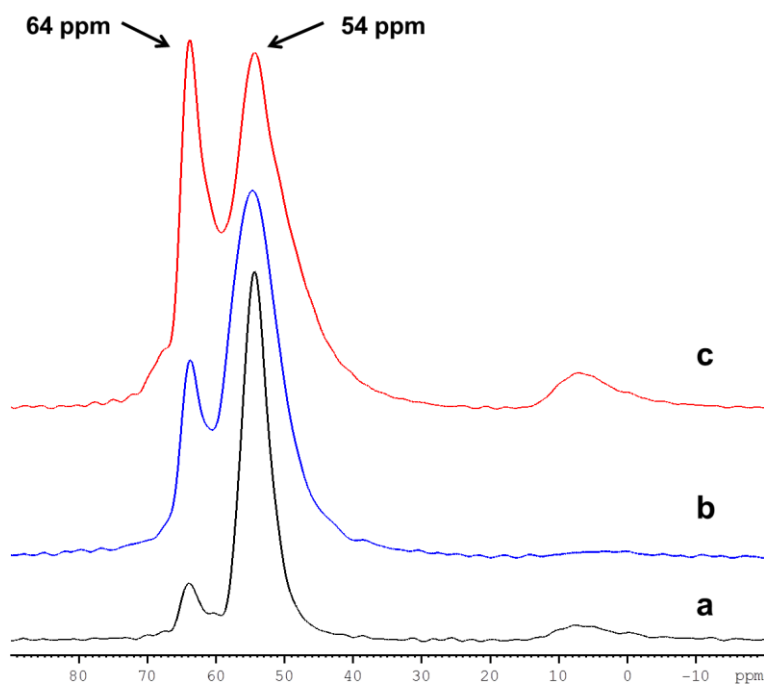


Fig. 5-5. <sup>27</sup>Al MAS spectrum of calcined products with the Si/Al ratio of (a) 427 (from Exp. 7); (b) 78 (from Exp. 3) and (c) 18 (from Exp. 8). Solid-state NMR experiment was carried out by Dr. Daniel Dawson from University of St Andrews.

### *Effect of H<sub>2</sub>O/SiO<sub>2</sub>*

Although the ILA synthesis is considered to be a solvent free method, water from the hydrated raw material proved necessary for zeolite crystallization: directly heating the precursor in an open vessel to the synthetic temperature only resulted in a dense phase product with low crystallinity. The ratio of H<sub>2</sub>O/SiO<sub>2</sub> was controlled by changing the content of the second Si source. Products of the Exp. 14, 3, 12 and 11 were examined where the H<sub>2</sub>O/SiO<sub>2</sub> ratios of the precursor were 3, 4.5, 6 and 7.5, respectively. PXRD patterns indicate when the H<sub>2</sub>O/SiO<sub>2</sub> ratio was below 4 (Fig. 5-6a), no crystalline products were obtained; while when the H<sub>2</sub>O/SiO<sub>2</sub> ratio is increased above 4 (Fig. 5-1b, Fig. 5-6c and d), all precursors led to the successful synthesis of **TON** zeolites. A minor reflection at 22.01° 2θ of products from Exp. 11 and 12 indicates an impurity (cristobalite) formed at the higher H<sub>2</sub>O/SiO<sub>2</sub> ratios. It is believed that water is necessary to hydrolyse and crystallize the raw materials to the zeolite materials. Strictly speaking, ILA synthesis is a solid state reaction rather than a solvent free synthesis as water is necessary for zeolite formation.

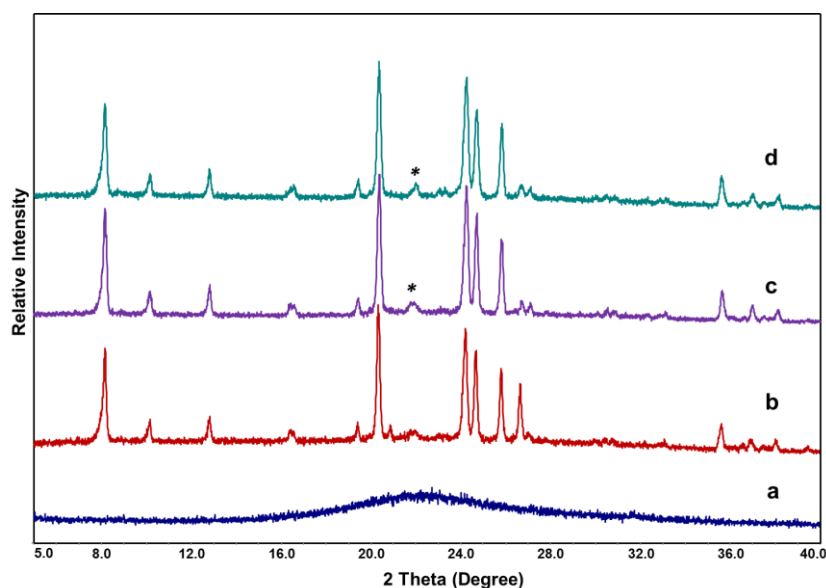


Fig. 5-6. PXRD patterns of products obtained from precursor with H<sub>2</sub>O/SiO<sub>2</sub> ratio of (a) 3 (from Exp. 14); (b) 5 (from Exp. 13); (c) 6 (from Exp.12) and (d) 7.5 (from Exp.11). The asterisks indicate the reflections from the impurity.

Moreover, the weight of the calcined products obtained from Exp. 3, 12 and 11 were 0.532 g, 0.353 g and 0.282 g, respectively. The corresponding yields based on SiO<sub>2</sub> were 88.3 % for the precursor H<sub>2</sub>O/SiO<sub>2</sub> ratio of 4.5, 78.4 % for the precursor H<sub>2</sub>O/SiO<sub>2</sub> ratio of 6 and 78.3 % for the precursor H<sub>2</sub>O/SiO<sub>2</sub> ratio of 7.5. It is noted that an ILA

synthesis with precursor H<sub>2</sub>O/SiO<sub>2</sub> ratio of 4.5 gave higher yields than the syntheses with higher H<sub>2</sub>O/SiO<sub>2</sub> ratios. ILA synthesis is considered to be a green chemistry procedure as it is more effective for zeolite preparation and produces less pollutant in the filtrate solution.

Although the experiments have proven that the changes of the H<sub>2</sub>O/SiO<sub>2</sub> ratio in the synthetic precursor by adding silica source have no effect on the product, it is also interesting whether excess water from the external environment would affect the structure and purity of the product. This is because the [Emim]Br used in this ILA synthesis is a hydrophilic compound and absorbs water strongly. If excess water prevents the formation of **TON** zeolites, a moisture free environment in the practical synthetic procedure will be required. This may increase the cost of operation for production of zeolites. To investigate the effect of absorbed water, a small amount of water was added into the synthetic precursor in some experiments. However, no obvious changes were observed by PXRD due to the addition of water (Fig. 5-6b). It is also noted that under moist atmosphere or long grind duration, the synthetic compounds transform from powder to paste. This transformation may be because the ionic liquid strongly absorbs the water molecules in air, changing the water content in the synthetic precursor. Both powder and paste were found to be successful precursors for zeolite formation, which implies the ILA synthesis of **TON** zeolite is a facile, repeatable method and tolerant of the operation environment.

### *Textural properties*

According to the above investigation, **TON**-type zeolite can be synthesized from a wide precursor composition by the ILA strategy. The morphology and the porous properties were studied with the product synthesized from Exp. 3.

It is noted that other zeolites which are synthesized from the solvent free route are usually large.<sup>1</sup> The hydrated raw materials in the synthetic precursor released the nutrients slowly when the water for Si dissolution was unavailable. The same results were also observed for the ILA synthesis of **TON** zeolites. The SEM images are shown in Fig. 5-7. The products were of rod shape. The crystal particles are up to 50 μm in length. Previous research reported many synthesized **TON**-zeolites were < 5 μm in length.<sup>22, 23, 38, 39</sup> Williams and co-workers<sup>40</sup> reported needle shaped **TON**-zeolites with up to 400 μm in length, of which the synthesis took 5 weeks through a bulk material dissolution method.

Zeolites with an appropriate size and morphology are demanded for either heterogeneous catalysis or ion-exchange in a liquid continuous flow process.<sup>41-44</sup> Zeolites with particle size below 5  $\mu\text{m}$  are unsuitable because they are difficult to fill in a column and cause high pressure drop.<sup>45, 46</sup> This ILA synthesis may contribute to the formation of large crystals of 50  $\mu\text{m}$  in length and provide a facile route to obtain large zeolite crystals.

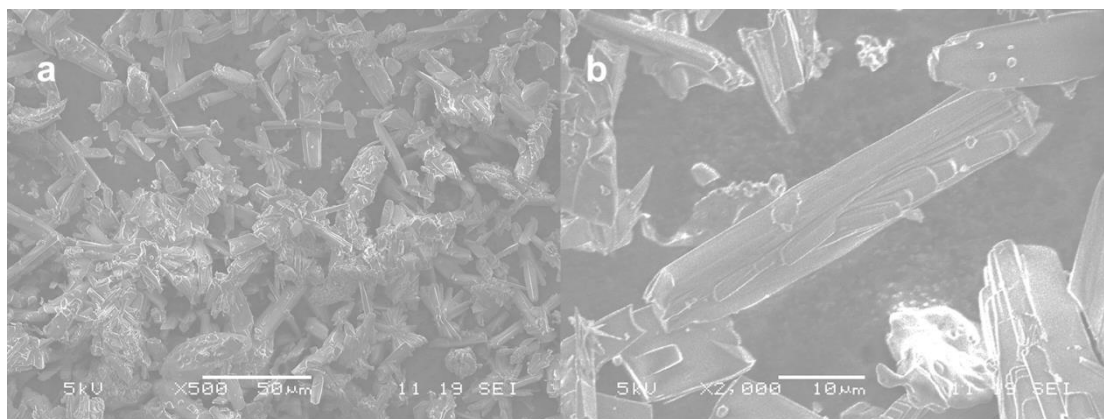


Fig. 5-7. SEM images of as-made TON crystals which were taken at (a) low magnification (scale bar is 50  $\mu\text{m}$ ) and (b) high magnification (scale bar is 10  $\mu\text{m}$ ).

Fig. 5-8 is the TGA trace of the as-made TON-zeolite. A gradual weight loss in the interval from 100 to 400  $^{\circ}\text{C}$  is attributed to the removal of the adsorbed water molecules in the channels. As the temperature increases to 800  $^{\circ}\text{C}$ , further loss of about 8.2 % is observed. This is considered as the pyrolytic decomposition of the organic SDA.

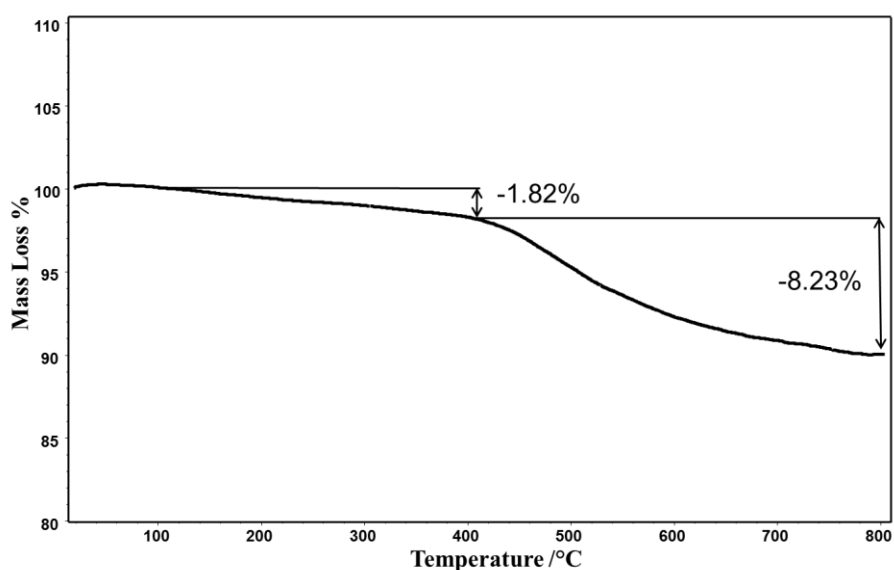


Fig. 5-8. TGA curve of as-made TON zeolite in air.

Porous properties of the prepared **TON** zeolites is characterised by nitrogen adsorption. The N<sub>2</sub> adsorption isotherm of the calcined sample shown in Fig. 5-9 is a typical type I adsorption, which indicates the microporous property of the product. The BET surface area of the calcined sample is calculated to be 170 m<sup>2</sup>/g and the micropore volume is 0.07 cm<sup>3</sup>/g. The surface area and the pore volume are slightly lower than the previously reported data (255 m<sup>2</sup>/g of surface area<sup>47</sup> and 0.1 cm<sup>3</sup>/g of pore volume<sup>22</sup>) but still considered to be comparable. The decreases may be caused by the large particle size of the **TON** crystals obtained from ILA synthesis.

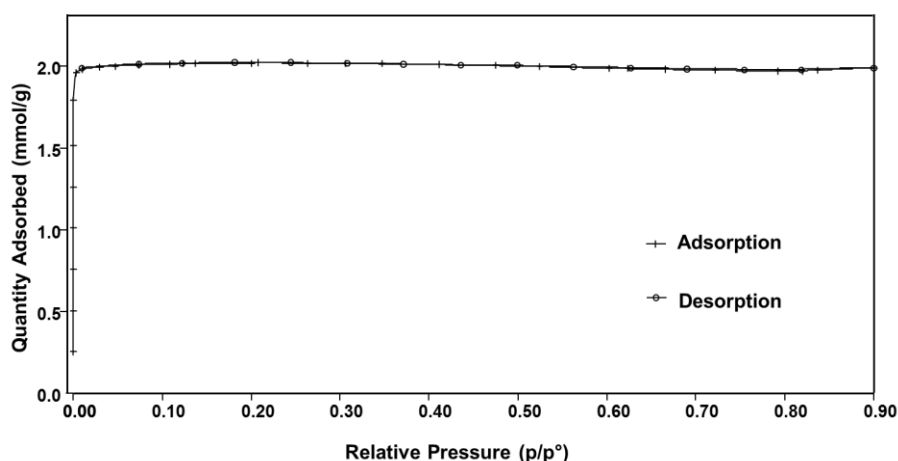


Fig. 5-9. N<sub>2</sub> isothermal plots of calcined **TON**-zeolites. N<sub>2</sub> sorption isotherm was measured by Dr Paul Wheatley from University of St Andrews.

### 5.3.2.2 Ionic liquid assisted synthesis with [Emim]Cl and [Emim]Tf<sub>2</sub>N

It has been reported that the anions in ionic liquids play a structure induction role in ionothermal synthesis.<sup>48,49</sup> In order to investigate the effect of the ionic liquid anions on the ILA synthesis, [Emim]Cl and [Emim]Tf<sub>2</sub>N were used in the ILA synthesis. The PXRD patterns of the products are shown in Fig. 5-10. Using [Emim]Cl as the SDA led to the formation of **TON**-type zeolites. Replacing Br<sup>-</sup> anion with Cl<sup>-</sup> has no effect on the product structure. Only the cations in ionic liquid play the role of SDA in ILA synthesis. However, the anions affect the physical properties of the ionic liquids. [Emim]Tf<sub>2</sub>N is a relatively hydrophobic compound and doesn't dissolve in water. Using [Emim]Tf<sub>2</sub>N as the SDA in ILA synthesis resulted in amorphous solids. Although [Emim]<sup>+</sup> cation is a suitable SDA for synthesizing **TON**-zeolites, hydrophobic ionic liquids are unable to mix with water and thus unable to play the role of SDA. This result suggests the attendance of both water and ionic liquid are important for successful preparation of zeolite materials.

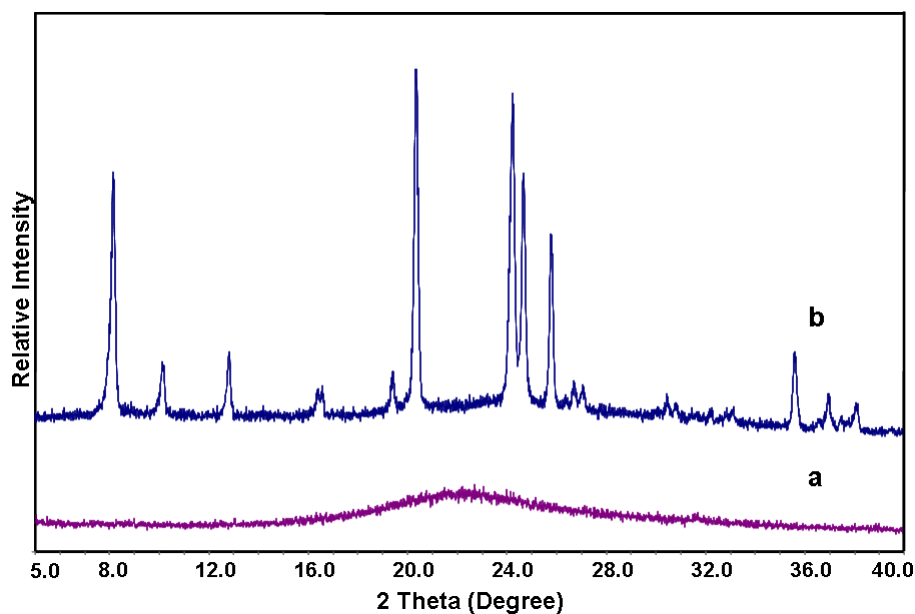


Fig. 5-10. PXRD patterns of the products obtained from ILA syntheses using (a) [Emim]Tf<sub>2</sub>N and (b) [Emim]Cl as SDA.

### 5.3.2.3 Ionic liquid assisted synthesis with [Bmim]Br

One potential advantage of ionic liquids for zeolite synthesis is their synthetic flexibility. There are many ionic liquids that are commercially available or synthesized in the literature.<sup>50-53</sup> 1-Butyl-3-methylimidazolium ([Bmim]<sup>+</sup>) is another commonly used ionic liquid cation. Using [Bmim]<sup>+</sup> as SDA in a ILA synthesis procedure may lead to zeolite structures other than **TON** framework. However, heating the synthetic precursor with chemical compositions of 0.5 Na<sub>2</sub>O: 1-1.5 SiO<sub>2</sub>: 0.75 NH<sub>4</sub>Cl: 0.1-0.2 Al<sub>2</sub>O<sub>3</sub>: 1 [Bmim]Br: 4.5 H<sub>2</sub>O gave mixed solids with a major  $\alpha$ -quartz phase and minor phases of  $\alpha$ -cristobalite and **MFI**-zeolite (Fig. 5-11). This result implies that different zeolite frameworks can be achieved by selecting the cations of ionic liquids although optimized conditions still need to be investigated for the synthesis of pure phase. Further work will be looking for suitable precursor compositions and synthetic conditions for synthesizing pure phase zeolite using other ionic liquids as SDAs.

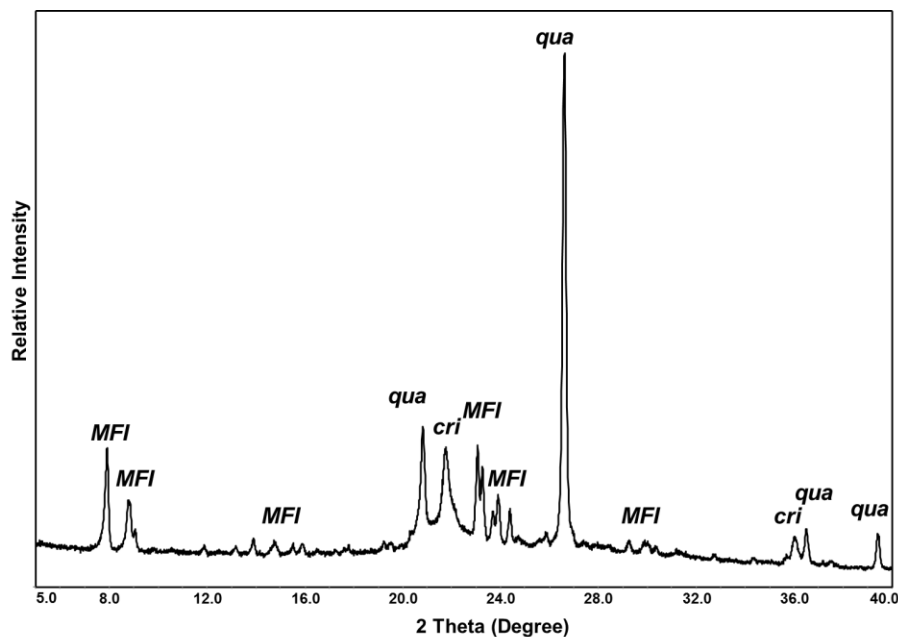


Fig. 5-11. PXRD pattern of the product from an ILA synthesis using [Bmim]Br as SDA. The corresponded phases to some reflections are indicated. *qua*:  $\alpha$ -quartz; *cri*:  $\alpha$ -cristobalite and *MFI*: MFI zeolite.

## 5.4 Summary

In this chapter some common ionic liquids were used in a solvent free procedure. The effects of ionic liquids,  $\text{SiO}_2/\text{Al}_2\text{O}_3$  and  $\text{H}_2\text{O}/\text{SiO}_2$  on the so-called “ionic liquid assisted synthesis” were investigated. The obtained materials were characterised by means of PXRD, solid-state NMR, EDX,  $\text{N}_2$  adsorption and other techniques. Addition of ionic liquid is a key parameter to obtain the porous solids so the ionic liquid is considered as the SDA in the ILA synthesis. 1-Ethyl-3-methylimidazolium bromide ([Emim]Br) was used as the SDA for the synthesis of the **TON** type zeolites. The  $^{13}\text{C}$  MAS NMR indicated the [Emim]<sup>+</sup> cations remained intact after thermal treatment.

Al was incorporated into the framework and tended to selectively form the pure **TON** zeolites. The selective formation of **TON** framework can be explained by examining the Al sites in the framework. The  $^{27}\text{Al}$  MAS NMR revealed the Al atoms preferentially occupied two tetrahedral sites in the **TON** framework. The Al atoms first occupied one tetrahedral T site and as then gradually incorporated into the other site which is high in bonding energy.

Investigations on the effects of the  $\text{H}_2\text{O}/\text{SiO}_2$  ratios indicates this ILA method is not a strict solvent free synthesis as small amount of water come from the raw reagent are

important for zeolite crystallization. With low  $\text{H}_2\text{O}/\text{SiO}_2$  ratio in the synthetic precursors, zeolite materials were synthesized in high yields and with minimal production of waste solution.

The effects of the anions and cations of the ionic liquids were also investigated by replacing the [Emim]Br with other ionic liquids as the SDAs. Anions of the ionic liquids have no effect on the framework structure of the obtained porous material, but they affect the physical properties of the ionic liquid. Hydrophobic ionic liquids are unable to mix with hydrated raw materials thus making them unsuitable as the SDA in the ILA synthesis. Ionic liquids are considered as designable compounds thus possess the potential to direct multiple zeolite structures. Another common ionic liquid, [Bmim]Br, was used as the SDA and **MFI** type zeolites were obtained, although other dense phase by-products were synthesized at the same time.

Compared to the conventional hydrothermal synthetic route to zeolites, this ILA synthesis exhibits several advantages:

- (a) Recyclable SDAs;
- (b) High yields of zeolite production;
- (c) Minimal production of waste solution;
- (d) Being tolerable to the external environment and easy for practical operation.

Moreover, using common ionic liquids is less expensive than the hydroxide form organic quaternary ammonium and easy to handle because time consuming anion-exchange procedures are not necessary. All these features suggest the ILA synthesis is a green chemical procedure.

## 5.5 References

1. L. Ren, Q. Wu, C. Yang, L. Zhu, C. Li, P. Zhang, H. Zhang, X. Meng and F.-S. Xiao, *J. Am. Chem. Soc.*, 2012, **134**, 15173-15176.
2. X. Meng and F.-S. Xiao, *Chem. Rev.*, 2013, **114**, 1521-1543.
3. Y. Jin, Q. Sun, G. Qi, C. Yang, J. Xu, F. Chen, X. Meng, F. Deng and F.-S. Xiao, *Angew. Chem. Int. Ed.*, 2013, **52**, 9172-9175.
4. M. Moliner, F. Rey and A. Corma, *Angew. Chem. Int. Ed.*, 2013, **52**, 13880-13889.
5. Z. Ma, J. Yu and S. Dai, *Adv. Mater.*, 2010, **22**, 261-285.
6. J. D. Holbrey and K. R. Seddon, *Clean Products and Processes*, 1999, **1**, 223-236.
7. R. E. Morris, *Chem. Commun.*, 2009, 2990-2998.
8. S. Dai, Y. H. Ju, H. J. Gao, J. S. Lin, S. J. Pennycook and C. E. Barnes, *Chem. Commun.*, 2000, 243-244.
9. Y. Zhou and M. Antonietti, *J. Am. Chem. Soc.*, 2003, **125**, 14960-14961.
10. T. Wang, H. Kaper, M. Antonietti and B. Smarsly, *Langmuir*, 2006, **23**, 1489-1495.
11. E. R. Parnham and R. E. Morris, *Chem. Mater.*, 2006, **18**, 4882-4887.
12. E. R. Parnham and R. E. Morris, *J. Am. Chem. Soc.*, 2006, **128**, 2204-2205.
13. L. Peng, J. Zhang, J. Li, B. Han, Z. Xue and G. Yang, *Chem. Commun.*, 2012, **48**, 8688-8690.
14. Z. Lin, A. M. Z. Slawin and R. E. Morris, *J. Am. Chem. Soc.*, 2007, **129**, 4880-4881.
15. E. Amigues, C. Hardacre, G. Keane, M. Migaud and M. O'Neill, *Chem. Commun.*, 2006, 72-74.
16. R. Cai, Y. Liu, S. Gu and Y. Yan, *J. Am. Chem. Soc.*, 2010, **132**, 12776-12777.
17. P. S. Wheatley, P. K. Allan, S. J. Teat, S. E. Ashbrook and R. E. Morris, *Chem. Sci.*, 2010, **1**, 483-487.
18. Y. C. Ma, S. J. Wang, Y. Song, Y. P. Xu, Z. J. Tian, J. Y. Yu and L. W. Lin, *Chinese J. Inorg. Chem.*, 2010, **26**, 1923-1926.
19. M. M. Treacy and J. B. Higgins, *Collection of Simulated XRD Powder Patterns for Zeolites Fifth (5th) Revised Edition*, Elsevier, 2007.
20. T. B. Reed and D. W. Breck, *J. Am. Chem. Soc.*, 1956, **78**, 5972-5977.
21. D. H. Olson, *Zeolites*, 1995, **15**, 439-443.
22. S. A. I. Barri, G. W. Smith, D. White and D. Young, *Nature*, 1984, **312**, 533-534.
23. R. Kumar and P. Ratnasamy, *J. Catal.*, 1989, **116**, 440-448.
24. J. A. Martens, G. Vanbutsele, P. A. Jacobs, J. Denayer, R. Ocakoglu, G. Baron, J. A. Muñoz Arroyo, J. Thybaut and G. B. Marin, *Catal. Today*, 2001, **65**, 111-116.
25. S. Teketel, W. Skistad, S. Benard, U. Olsbye, K. P. Lillerud, P. Beato and S. Svelle, *ACS Catal.*, 2011, **2**, 26-37.
26. S. I. Zones and A. W. Burton, *J. Mater. Chem.*, 2005, **15**, 4215-4223.
27. E. R. Cooper, C. D. Andrews, P. S. Wheatley, P. B. Webb, P. Wormald and R. E. Morris, *Nature*, 2004, **430**, 1012-1016.
28. J. L. Schlenker, W. J. Rohrbaugh, P. Chu, E. W. Valyocsik and G. T. Kokotailo, *Zeolites*, 1985, **5**, 355-358.
29. A. Araya and B. M. Lowe, *Zeolites*, 1984, **4**, 280-286.
30. A. Corma, *J. Catal.*, 2003, **216**, 298-312.
31. A. Corma, *Chem. Rev.*, 1995, **95**, 559-614.
32. A. Omegna, M. Vasic, J. Anton van Bokhoven, G. Pirngruber and R. Prins, *Phys. Chem. Chem. Phys.*, 2004, **6**, 447-452.
33. M. Derewinski, P. Sarv and A. Mifsud, *Catal. Today*, 2006, **114**, 197-204.
34. E. Lippmaa, A. Samoson and M. Magi, *J. Am. Chem. Soc.*, 1986, **108**, 1730-1735.
35. T. Blasco, A. Corma, M. J. Díaz-Cabañas, F. Rey, J. A. Vidal-Moya and C. M. Zicovich-Wilson, *J. Phys. Chem. B*, 2002, **106**, 2634-2642.
36. K. L. Geisinger, G. V. Gibbs and A. Navrotsky, *Phys. Chem. Miner.*, 1985, **11**, 266-283.
37. J. A. van Bokhoven, D. C. Koningsberger, P. Kunkeler, H. van Bekkum and A. P. M. Kentgens, *J. Am. Chem. Soc.*, 2000, **122**, 12842-12847.

38. B. Wang, Z. Tian, P. Li, L. Wang, Y. Xu, W. Qu, H. Ma, Z. Xu and L. Lin, *Mater. Res. Bull.*, 2009, **44**, 2258-2261.
39. S. Ernst, J. Weitkamp, J. A. Martens and P. A. Jacobs, *Applied Catalysis*, 1989, **48**, 137-148.
40. J. J. Williams, Z. A. D. Lethbridge, G. J. Clarkson, S. E. Ashbrook, K. E. Evans and R. I. Walton, *Microporous Mesoporous Mater.*, 2009, **119**, 259-266.
41. S. Radhakrishnan, G. Thoelen, J. Franken, J. Degreève, C. E. A. Kirschhock and J. A. Martens, *ChemCatChem*, 2013, **5**, 576-581.
42. S. Radhakrishnan, J. Franken and J. A. Martens, *Green Chem.*, 2012, **14**, 1475-1479.
43. Z. Milan, E. Sánchez, P. Weiland, C. de Las Pozas, R. Borja, R. Mayari and N. Roviroso, *Chem. Eng. J.*, 1997, **66**, 65-71.
44. A. Sachse, A. Galarneau, F. Fajula, F. Di Renzo, P. Creux and B. Coq, *Microporous Mesoporous Mater.*, 2011, **140**, 58-68.
45. M. Mańko, J. Vittenet, J. Rodriguez, D. Cot, J. Mendret, S. Brosillon, W. Makowski and A. Galarneau, *Microporous Mesoporous Mater.*, 2013, **176**, 145-154.
46. A. Galarneau, J. Iapichella, D. Brunel, F. Fajula, Z. Bayram-Hahn, K. Unger, G. Puy, C. Demesmay and J.-L. Rocca, *J. Sep. Sci.*, 2006, **29**, 844-855.
47. R. Byggningsbacka, N. Kumar and L. E. Lindfors, *J. Catal.*, 1998, **178**, 611-620.
48. E. R. Parnham and R. E. Morris, *J. Mater. Chem.*, 2006, **16**, 3682-3684.
49. Z. Lin, D. S. Wragg, J. E. Warren and R. E. Morris, *J. Am. Chem. Soc.*, 2007, **129**, 10334-10335.
50. C. Chiappe and D. Pieraccini, *J. Phys. Org. Chem.*, 2005, **18**, 275-297.
51. H. Xing, X. Zhao, R. Li, Q. Yang, B. Su, Z. Bao, Y. Yang and Q. Ren, *ACS Sustain. Chem. Eng.*, 2013, **1**, 1357-1363.
52. J. Sun, S. Zhang, W. Cheng and J. Ren, *Tetrahedron Lett.*, 2008, **49**, 3588-3591.
53. E. D. Bates, R. D. Mayton, I. Ntai and J. H. Davis, *J. Am. Chem. Soc.*, 2002, **124**, 926-927.

# Chapter 6 Ionothermal Synthesis of Aluminophosphates Large Single Crystals with a New Ionic Liquid

## 6.1 Introduction

As described in Chapter 1, ionothermal synthesis is a newly developed synthetic route to microporous materials. Unlike conventional hydrothermal synthesis, in which water is used as the reaction medium, in ionothermal synthesis ionic liquids play the role of a solvent and structure directing agent at the same time.<sup>1</sup> In recent years ionothermal synthesis has received increasing attention in the field of synthesizing microporous materials such as AIPOs,<sup>2,3</sup> MeAIPOs<sup>4,5</sup> and metal-organic frameworks.<sup>6-8</sup> Research has shown that the ionothermal synthetic route possesses many advantages, for example the negligible vapour pressure of the ionic liquids eliminates the safety concern of reactions occurring in sealed vessels;<sup>9</sup> ionic liquids are good microwave absorbers and suitable for quick syntheses of zeolitic materials;<sup>10,11</sup> moreover, the ionic liquids can be simply recycled and further used repeatedly.<sup>1</sup> Another potential advantage of ionothermal synthesis is the absence of other solvent such as water can consequentially result in the dominant interaction between the ionic liquids and the framework species. This feature is proposed to be “improved templating”.<sup>12</sup>

Based on Davis and Lobo’s definition of an SDA,<sup>13</sup> a large number of organic cations in hydrothermal synthesis are classified as space fillers rather than true SDAs. This may be because in hydrothermal synthesis the water and SDA molecules determine the structure together. A proposed mechanism of the relationship between the SDAs and the framework structure is shown in Fig. 6-1a. It suggests the Si species replace the water molecules in the hydrated spheres which are formed by the SDA and the solvent. Thus the interactions between the solvent and the SDA species are critical to the structure of the product.<sup>14,15</sup> In ionothermal synthesis the solvent and the SDAs are same, thus the ionic liquid would be the only species that interacts with the tetrahedral solids. Therefore the structure directing effect may be the more prevalent role of the organic cations in ionothermal synthesis process rather than their space filling role in hydrothermal synthesis. Moreover, the ionic liquids are considered to be synthetically

flexible and designable.<sup>16, 17</sup> The feature of improved templating might increase the possibility of synthesizing microporous materials with new framework types. The synthesis of zeolite analogues with ionic liquids in hydrothermal synthesis and ionothermal synthesis are shown in Fig. 6-1b and c for comparison.

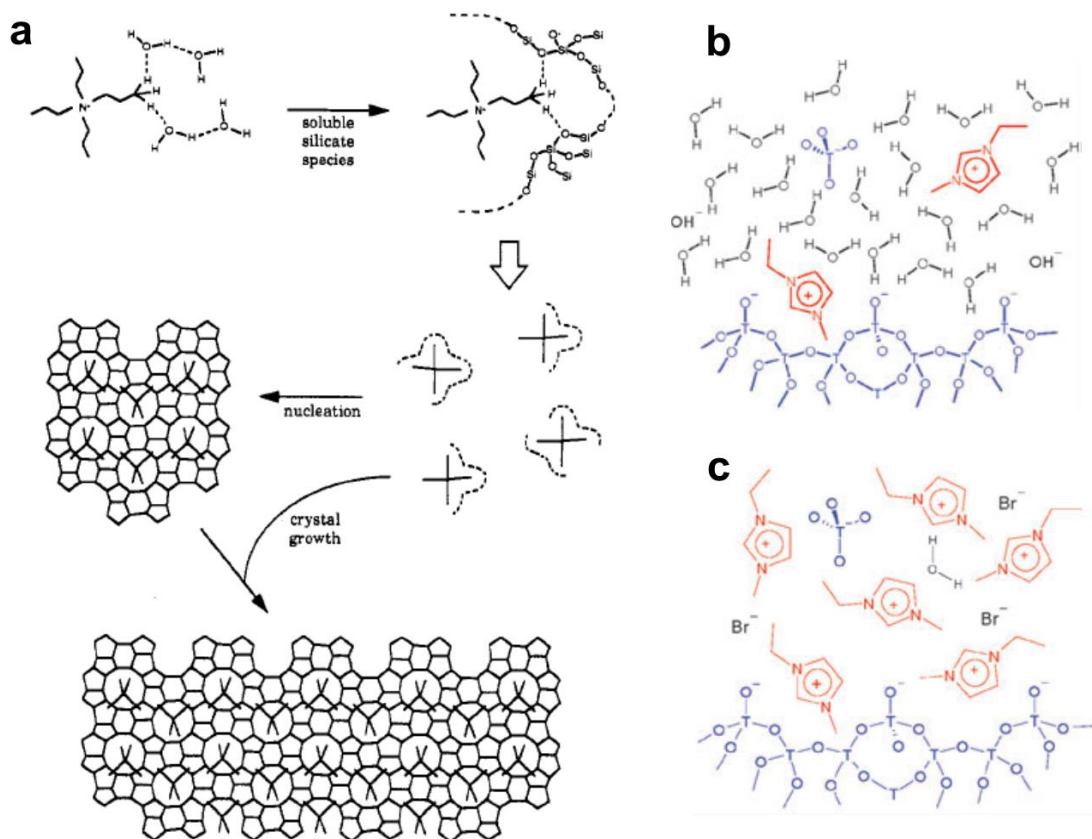


Fig. 6-1. (a) The proposed mechanism for hydrothermal synthesis of zeolites with organic SDAs. The picture is adapted from reference 14. (b) The mechanism of hydrothermal synthesis of microporous materials with ionic liquids and (c) the mechanism of ionothermal synthesis of microporous materials. The pictures are adapted from reference 12.

Up to now many zeolite analogues, especially AIPOs and MeAIPOs have been synthesized ionothermally. 1-Alkyl-3-methyl imidazolium based ionic liquids were one kind of ionic liquids that usually used for the ionothermal synthesis.<sup>2, 18, 19</sup> Other than alkyl-chain branching, ionic liquids with other functional groups such as hydroxyl have not been used as SDAs for zeolite synthesis. Their properties may be different to the commonly used SDAs due to the higher interaction with framework species through hydrogen bonding. In hydrothermal synthesis the hydroxyl functionalized organic compounds are not suitable as SDAs due to their strong hydrogen bonding interaction with water, which prevents the replacement of solvent by tetrahedral species,<sup>20, 21</sup> while

ionothermal syntheses using such hydroxyl functionalized ionic liquids as the SDAs may result in zeolite analogues with new structures.

Zeolite single crystals are of wide interest in research fields for structure analysis and their applications as host materials.<sup>22-25</sup> Due to the sophisticated crystallization process which is affected by multiple synthetic factors, it is difficult to find a routine strategy to obtain zeolite single crystals. Many effective methods for synthesizing large single crystals of zeolites and zeolite analogues have been reported. The basic principle is to control the rate of nucleation and crystal growth.<sup>26</sup> For example, large single crystals of zeolite **LTA** and **FAU** were synthesized using triethanolamine as the chelating agent to suppress the nucleation,<sup>27, 28</sup> zeolite silicalite-I single crystals with size in the mm scale were synthesized by a Bulk-Material Dissolution method.<sup>29</sup> The solubility of the starting material affects the rates of nucleation and crystal growth, which are critical in determining crystal sizes; another effective strategy is the fluoride route. The F<sup>-</sup> can form complexes with Al and P and releases them gradually as the nutrients for crystal growth. Large single crystals of AlPO<sub>4</sub>-5, AlPO<sub>4</sub>-11 and AlPO<sub>4</sub>-34 were synthesized in the presence of HF;<sup>26, 30</sup> besides those synthesized by the hydrothermal route, large single crystals can also be synthesized through the solvothermal route in organic solvents. Compared with water, the organic solvents usually possess higher viscosity. The mass transfer by convection and diffusion is reduced. The inhibited secondary nucleation and crystal growth result in the formation of large single crystals.<sup>15</sup> Giant aluminosilicate and aluminophosphate single crystals were obtained in organic solvents including triethylamine, pyridine and polyethylene glycol.<sup>31</sup> Although there are many published examples that prepare large single crystals of the microporous materials by hydrothermal and solvothermal routes, reports on obtaining large single crystals by the ionothermal route are rare. Tian *et al.* reported the synthesis of Gallophosphate (GaPO<sub>4</sub>) with the **LTA** type structure in 1-alkyl-3-methylimidazolium bromide ionic liquids.<sup>32</sup> The size of the produced crystals decreases with the increasing of the alkyl chain length of the ionic liquids. The GaPO<sub>4</sub>-**LTA** synthesized in the ionic liquid with alkyl chain length of 2 carbons is 400 μm in size. Morris and Parnham reported the synthesis of AlPOs in 1-alkyl-3-methylimidazolium bromide ionic liquids.<sup>2</sup> Zeolite single crystals of **CHA** type with the crystal size of 200 μm were prepared.

## **6.2 Aims**

The overall aim of this chapter is to synthesize zeolite analogues with a new ionic liquid. 1-(2-hydroxyethyl)-3-methylimidazolium chloride ([HOEmim]Cl) which is an imidazolium based ionic liquid with a hydroxyl group will be synthesized and used as the solvent and SDA for the synthesis of AlPO materials. The idea of selecting this ionic liquid is that the hydroxyl group may bring this compound higher interaction strength with the framework species than the alkyl imidazolium based ionic liquids.<sup>33</sup> If zeolite analogues can be prepared from the selected ionic liquid, the next target will be optimizing the synthetic conditions to prepare large single crystals for structural analysis. The relationship between this ionic liquid and the framework will be investigated.

## **6.3 Ionothermal synthesis of AlPOs with a new ionic liquid**

### **6.3.1 Experimental methods**

#### **6.3.1.1 Preparation of [HOEmim]Cl**

Preparation of [HOEmim]Cl was following the reported procedure.<sup>34</sup> The reaction was carried out under an inert gas atmosphere. 49 g of N-methyl imidazole (99 %, 0.6 mol, Aldrich) and 48 g of 2-chloroethanol (99 %, 0.6 mol, Aldrich) were reacted at 80 °C under reflux for 5 days. The obtained liquid was recrystallized in acetonitrile (HPLC grade, Fisher) to give 89 g of white solid (Yields: 91.0 %). Successful preparation of [HOEmim]Cl was confirmed by <sup>1</sup>H NMR (300 MHz, d<sub>6</sub>-DMSO): δ= 9.34 (s, 1H, NC(H)N), 7.79 (d, 2H, NC(H)C(H)N), 5.49 (s, 1H, OH), 4.26 (t, 2H, NCH<sub>2</sub>), 3.89 (s, 3H, NCH<sub>3</sub>), 3.72 (t, 2H, OCH<sub>2</sub>).

#### **6.3.1.2 Synthesis of aluminophosphate in [HOEmim]Cl**

In a typical synthesis, 2.282 g of ionic liquid [HOEmim]Cl (14.00 mmol) was melted at 70 °C in a beaker. 0.102 g of Aluminium isopropoxide (98 %, 0.50 mmol, Alfa Aesar) and 0.15 g of orthophosphoric acid (85 wt% in H<sub>2</sub>O, 1.30 mmol, Aldrich) were added into the melted ionic liquid and stirred for 5 min. The mixture was transferred to a Teflon lined stainless steel autoclave. 0.015 g of hydrofluoric acid (48 wt% in H<sub>2</sub>O, 0.36 mmol, Aldrich) or 0.36 g of HCl (37 wt% in H<sub>2</sub>O, 0.36 mmol, Fisher) was dropped in the liner. The autoclaves were sealed and heated for 3 days at temperatures of 150,

175 or 210 °C. The obtained solids were filtered with distilled water and dried at 80 °C overnight.

### **6.3.1.3 Characterisation**

The samples were filled in glass capillaries of 0.5 mm diameter for Powder X-ray diffraction. The data were collected on a STOE diffractometer using CuK $\alpha$ 1 radiation in Debye-Scherrer mode. Sample morphology was examined through a Jeol JSM 5600 scanning electron microscope. Solid-state NMR spectra were recorded using a 400 MHz Bruker Avance III spectrometer equipped with a 9.4 T superconducting magnet. Powdered samples were packed into standard ZrO<sub>2</sub> rotors with outer diameters of 4 mm. The <sup>13</sup>C NMR spectra were recorded with cross polarisation from <sup>1</sup>H. A spin-lock period of 0.5 ms was used, with a ramped pulse (90-100%) applied to <sup>1</sup>H. High-power TPPM-15 <sup>1</sup>H decoupling was applied during acquisition. The MAS rate was 12.5 kHz. For the <sup>27</sup>Al and <sup>31</sup>P MAS NMR the MAS rate of 14 kHz were used, respectively. Thermogravimetric analysis was carried out on a Netzsch TG 209 instrument. The sample was put in an alumina crucible and heated to 800 °C under air flow. The heating rate was 10 °C·min<sup>-1</sup>. Single crystal analysis was performed with the as-synthesized crystals in order to investigate the framework structure and the ionic liquid location. Data were collected at Station 11.3.1 of the Advanced Light Source, Lawrence Berkeley National Laboratory, using a wavelength of  $\lambda = 0.7749$  Å. Data collection was carried out on a Bruker AXS APEXII diffractometer and the corresponding Bruker AXS APEXII software was used during data collection and reduction. Data was collected at -173 °C. Only the non-hydrogen atoms were solved and refined. The structure was solved using direct method by the program SHELXS-97 and then refined on  $F^2$  using SHELXTL-97.<sup>35</sup>

### **6.3.2 Results and discussions**

The synthetic precursors with composition of 1 Al<sub>2</sub>O<sub>3</sub>: 2.6 P<sub>2</sub>O<sub>5</sub>: 56 [HOEmim]Cl: 1.4 HF: 6.8 H<sub>2</sub>O were heated in autoclaves. The water comes from the solution of orthophosphoric acid and hydrofluoric acid. It is considered to be a true ionothermal synthesis as the ionic liquid is the dominant solvent in the reaction. The PXRD patterns of the products are shown in Fig. 6-2. Crystalline materials with the identical PXRD patterns can be successfully synthesized at the three different temperatures. The PXRD patterns identify the crystals to be the SIZ-4 structure which is a triclinic deformation of **CHA** type framework.<sup>1</sup>

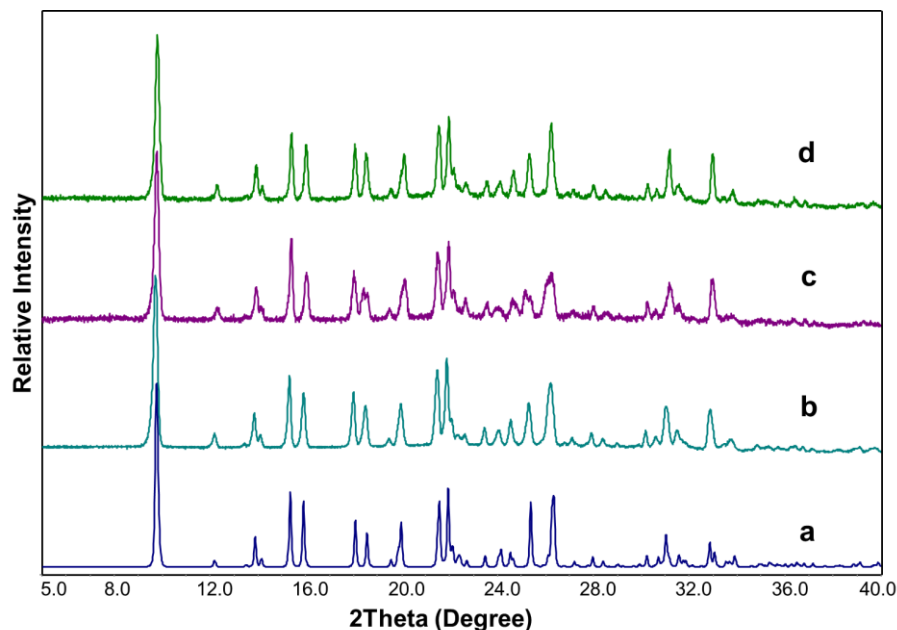


Fig. 6-2. PXRD patterns of (a) theoretical simulated pattern of SIZ-4 which possesses the triclinic **CHA**-type framework structure; (b) zeolite analogues synthesized with [HOEmim]Cl at 150 °C; (c) zeolite analogues synthesized with [HOEmim]Cl at 175 °C and (d) zeolite analogues synthesized with [HOEmim]Cl at 210 °C.

**CHA** is a small-pore microporous framework with 8-membered ring openings and 3-dimensional channels. The structure can be described as double-6-rings (*d6rs*) connected by bridging oxygen atoms, which form the single-4-rings (*s4rs*).<sup>36</sup> Related materials such as SSZ-13 and SAPO-34 are important catalysts for Methanol-to-Olefin (MTO) reaction<sup>37-39</sup> and materials for methane/carbon dioxide separation.<sup>40-42</sup> The **CHA** type zeolite is a rhombohedral structure of the trigonal system. However, direct synthesis of rhombohedral **CHA** type AlPO materials was unsuccessful. Only the triclinic deformation of the **CHA** type structure AlPO material named AlPO-34 was synthesized in the presence of HF. The fluorine was reported to bond to the octahedral Al atoms, resulting in the deformation of the **CHA** framework (Fig. 6-3).<sup>43, 44</sup>

The synthetic precursors with compositions of 1 Al<sub>2</sub>O<sub>3</sub>: 2.6 P<sub>2</sub>O<sub>5</sub>: 56 [HOEmim]Cl: 0 HF: 5 H<sub>2</sub>O and 1 Al<sub>2</sub>O<sub>3</sub>: 2.6 P<sub>2</sub>O<sub>5</sub>: 56 [HOEmim]Cl: 1.4 HCl: 10 H<sub>2</sub>O were heated in autoclaves to investigate the effect of HF. When acid was absent in the synthetic precursor, the products were amorphous solids. If HF was replaced with hydrochloric acid of the same molar content, mixed phases of **AEL** and **CHA**-type framework were obtained (Fig. 6-4). The results indicate that the crystallization of AlPO materials is favoured under acidic conditions. Moreover, HF is a crucial species for selectively preparing **CHA**-type zeolite analogue.

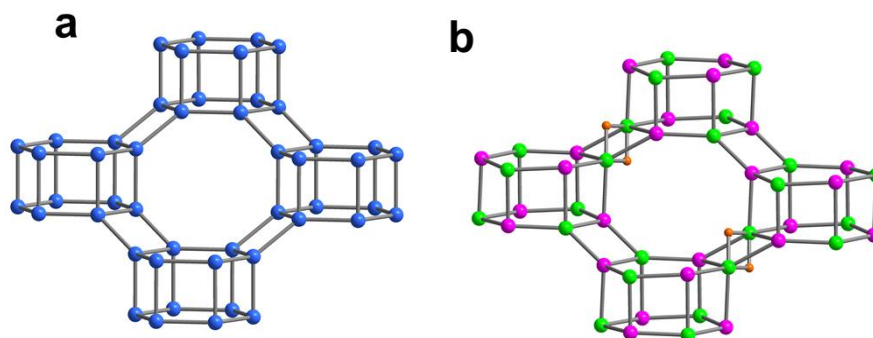


Fig. 6-3. The structures of (a) rhombohedral **CHA** framework and (b) SIZ-4 with triclinic deformation of **CHA** framework. The blue balls are the tetrahedral atoms in **CHA** framework; the green balls and pink balls are the Al and P atoms in SIZ-4, respectively; the orange balls are the F atoms bonding to Al. T-O-T bridges are drawn as straight lines.

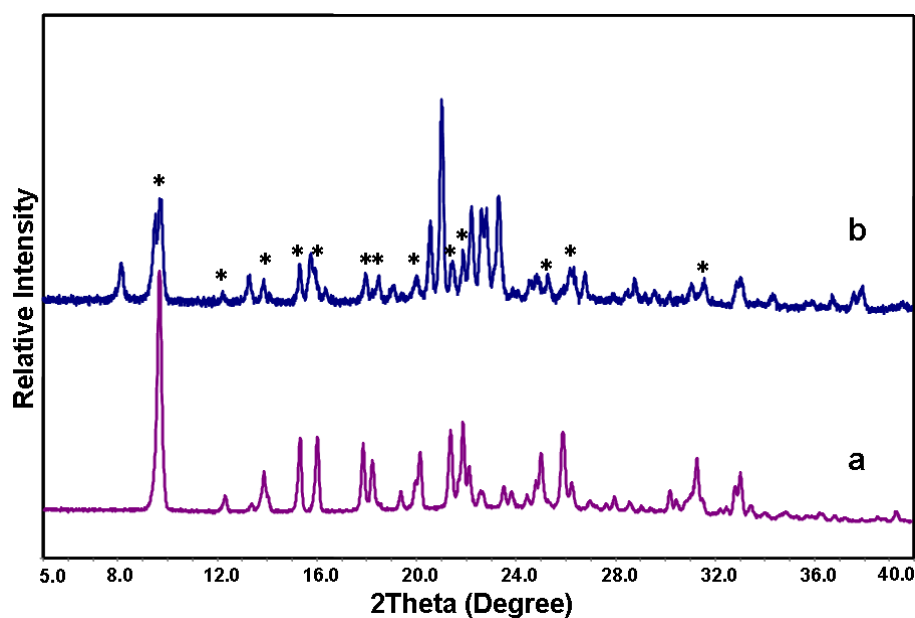


Fig. 6-4. PXRD patterns of zeolite analogues synthesized in [HOEmim]Cl at 175 °C. (a) Samples synthesized with HF indicate the pure triclinic **CHA** framework was prepared; (b) samples synthesized in the presence of HCl instead of HF. Asterisks marked the reflections from **CHA**-type framework.

When the ionothermal synthesis occurs in one of the most commonly used ionic liquids, 1-ethyl-3-methylimidazolium bromide ([Emim]Br), different structures including **CHA** type were prepared from different synthetic precursor compositions.<sup>1</sup> The interrupted SIZ-1 structure was synthesized in the absence of HF and the SIZ-3 with an **AEL** type framework was synthesized in the presence of HF. SIZ-4 was ionothermally synthesized when the reaction was taking place in completely dry conditions. Other work also reported the synthesis of **CHA**-zeolite in [Emim]Br with the aid of a co-SDA such as a

heterocyclic aromatic amine<sup>45</sup> or 1, 6-hexadamine.<sup>46</sup> Ionothermal synthesis of SIZ-4 from [HOEmim]Cl provides a facile route to synthesize the small pore zeolite analogue. A moisture free environment or other SDAs are not necessary, which reduces the cost of the synthetic operation and the production of waste organic compounds.

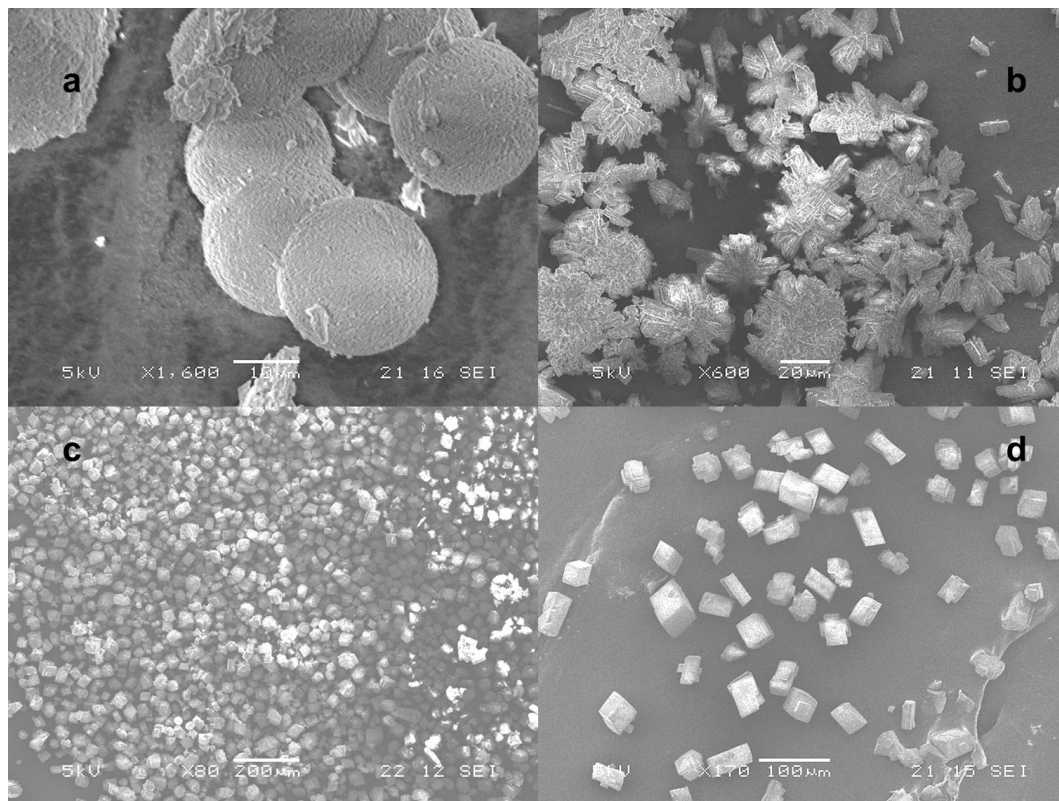


Fig. 6-5. SEM images of the products obtained from (a) 150 °C, the scale bar is 10 μm; (b) 175 °C, the scale bar is 20 μm; (c) 210 °C, low magnification, the scale bar is 200 μm and (d) 210 °C, high magnification, the scale bar is 100 μm.

SEM was applied to examine their sizes and morphologies. Although the PXRD patterns in Fig. 6-2 indicate the products synthesized at different temperatures have the same framework structure, crystals with different sizes and shapes were synthesized at different synthesis temperatures. Fig. 6-5 shows the SEM images of the samples obtained from 150, 175 and 210 °C, respectively. The crystals obtained at 150 °C (Fig. 6-5a) are spherical aggregations with 20 μm diameter. The surface stripe of the spheres indicates they are made up of small crystals. The crystals obtained at 175 °C are also aggregated particles with size of 20 μm but the size of the small crystals which make up the aggregations are larger than the crystals obtained at 150 °C. Some stick shaped small crystals are also observed (Fig. 6-5b). Rhombohedral shaped large single crystals with sizes of about  $70 \times 50 \times 50 \mu\text{m}^3$  were prepared at 210 °C. The SEM images of these crystals are of well-defined shape and uniform in size.

The successful synthesis of the single crystals at high temperature provides an opportunity for solving the framework structure. Meanwhile, single crystal analysis could also provide the information for understanding the relationship between the framework and the guest molecules by examining the location of the SDA in the framework. Synchrotron diffraction data was collected using the crystals synthesized at 210 °C. Single crystal data were collected by Dr. Laura McCormick. The data collection and refinement details are listed in Table 6-1.

Table 6-1. Crystal data and refinement results of the AlPOs crystal

Compound	AlPOs
Formula	C10 Al6 F2 N4 O24 P6
Formula weight	945.84
Crystal system	Triclinic
Space group	P -1
<i>a</i> (Å)	9.1025(13)
<i>b</i> (Å)	9.1938(13)
<i>c</i> (Å)	9.2943(13)
$\alpha$ (°)	76.283(2)
$\beta$ (°)	87.094(2)
$\gamma$ (°)	89.550(2)
<i>V</i> (Å <sup>3</sup> )	754.65(18)
<i>Z</i>	1
<i>D<sub>c</sub></i> (g/cm <sup>-3</sup> )	2.081
<i>F</i> (000)	466
$\mu$ (mm <sup>-1</sup> )	0.651
$\theta$ for data collection (°)	3.06 to 34.93
Reflections collected	11481
Unique reflections	4718
<i>R<sub>int</sub></i>	0.1797
Data/restraints/parameters	4718 / 0 / 235
Goodness-of-fit on <i>F</i> <sup>2</sup>	1.005
<i>R</i> <sub>1</sub> , <i>wR</i> <sub>2</sub> [ <i>I</i> > 2σ( <i>I</i> )]	<i>R</i> <sub>1</sub> = 0.0730, <i>wR</i> <sub>2</sub> = 0.2012
<i>R</i> <sub>1</sub> , <i>wR</i> <sub>2</sub> (all data)	<i>R</i> <sub>1</sub> = 0.0783, <i>wR</i> <sub>2</sub> = 0.2079

$$R_1 = \frac{\sum(|F_o| - |F_c|)}{\sum|F_o|}, wR_2 = [\frac{\sum w(F_o^2 - F_c^2)^2}{\sum w(F_o^2)^2}]^{1/2}.$$

Both the framework structure and the SDA molecules were solved. The framework is the triclinic **CHA** structure. The *d6rs* were connected by *s4rs*. 3D 8-membered ring channels were formed. Two Al atoms in one *s4r* were bridged by two fluorine atoms. The 1, 3-dimethylimidazolium cations were located inside the channel of the framework (Fig. 6-6).

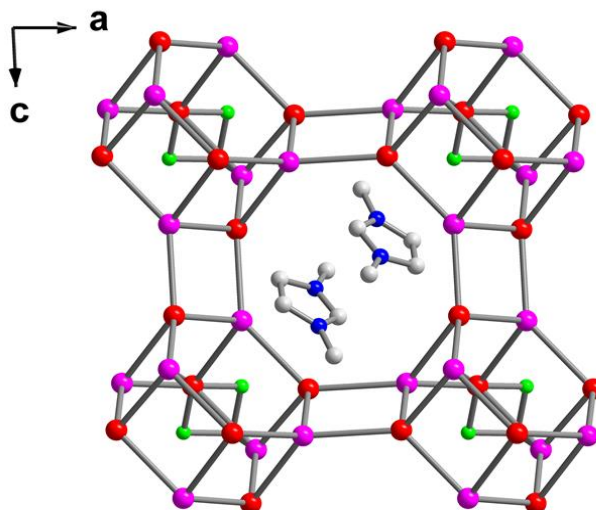


Fig. 6-6. Structure of the triclinic **CHA** type AlPOs crystals obtained from 210 °C. The structure is viewed along the *b*-axis. Al: red; P: pink; F: green, N: blue; C: grey. T-O-T bridges are drawn as straight lines for clarity.

The side-views of the structure are shown in Fig. 6-6. In this direction, the **CHA** structure is made up of *d6rs* with a stacking sequence ABCABC... (Fig. 6-7a). A CBU cage named *cha* or  $[4^{12}6^28^6]$  is formed (Fig. 6-7b). Two 1, 3-dimethylimidazolium cations are located in this cage. The distance between two imidazole planes (represented by the distance of N-N) is 3.6211(73) Å, which is considered to be typical of  $\pi$ - $\pi$  interactions.<sup>47</sup> A similar structure-directing effect of the self-assembled molecules by  $\pi$ - $\pi$  interactions was also observed in the synthesis of pure siliceous **LTA** zeolites, ITQ-29.<sup>48</sup>

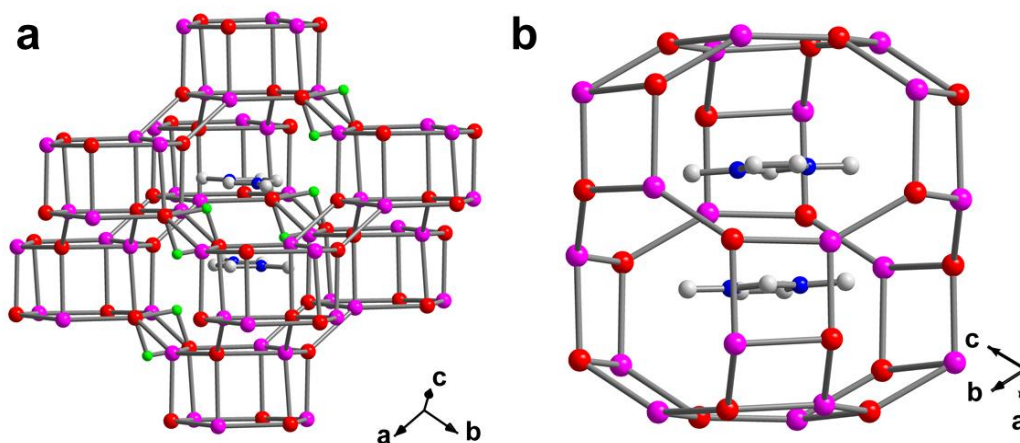


Fig. 6-7. (a) side-view of triclinic **CHA** framework with the SDAs in the cage; (b) the structure of *cha* cage and the SDAs inside the cage. Al: red; P: pink; F: green, N: blue; C: grey. The T-O-T bridges are drawn as straight lines for clarity.

The structure-directing effect of the [HOEmim]Cl is analogous to the effect of the long branching chain 1-alkyl-3-methylimidazolium based ionic liquids. It was reported these alkyl-methylimidazolium ionic liquids with an alkyl chain length above 3 carbons were decomposed to the 1, 3-dimethylimidazolium cations which then played the role of SDA.<sup>2</sup> Successful preparation of **CHA**-type zeolite analogue in [HOEmim]Cl may be also because of the longer branching chain on the imidazolium based ionic liquids. The triclinic **CHA**-type AlPOs with 1, 3-dimethylimidazolium in the channels were named SIZ-10a to SIZ-10e, depending on the ionic liquids used in the synthesis. For clarity the AlPO material obtained from the [HOEmim]Cl is named SIZ-10f in the following discussions.

The <sup>13</sup>C CP/MAS NMR spectra of the as-synthesized SIZ-10f from 150 °C and 210 °C are shown in Fig. 6-8. Both spectra indicate the main species in the samples are 1, 3-dimethylimidazolium cations. The spectrum of SIZ-10f obtained from 150 °C still has the minor resonances from the [HOEmim]Cl which are marked by asterisks in Fig. 6-8a. These resonances are absent in the spectrum of the as-synthesized SIZ-10f obtained at 210 °C, indicating no [HOEmim] cations are left in the framework. Moreover, an obvious resonance at 50 ppm appearing in the SIZ-10f at 210 °C is attributed to the methanol absorbed in the *cha* cages.<sup>49</sup> Methanol is the other product of the decomposed ionic liquid.

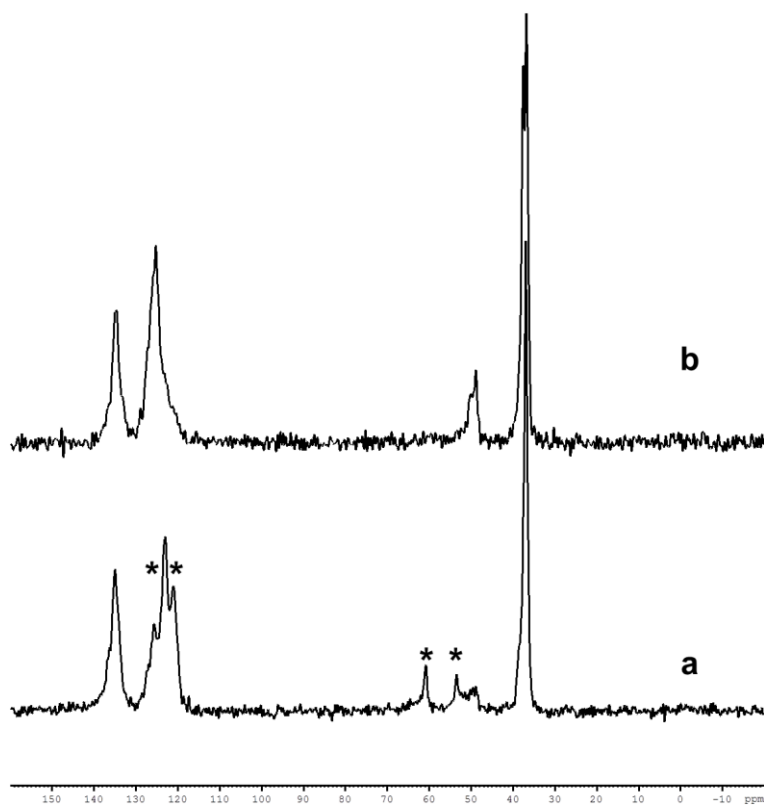


Fig. 6-8. The  $^{13}\text{C}$  MAS NMR spectra of (a) SIZ-10f obtained from 150 °C, the spectrum was recorded with signal averaging for 3584 transients with a recycle interval of 3 s; and (b) SIZ-10f obtained from 210 °C, the spectrum was recorded with signal averaging for 4096 transients with a recycle interval of 3 s. The asterisks indicate the resonances from the [HOEmim] cations in the framework. Solid-state NMR experiment was carried out by Dr. Daniel Dawson from University of St Andrews.

The  $^{13}\text{C}$  MAS NMR spectra indicate the [HOEmim]Cl in the framework was partially decomposed at a temperature of 150 °C but completely decomposed at 210 °C. Both the [HOEmim]Cl and its decomposition product 1, 3-dimethylimidazolium cations were located in the *cha* cages of the triclinic **CHA** framework. The samples obtained from different synthetic temperatures have the same structure but are different in size and shape. Decomposition of the [HOEmim]Cl at higher temperature may provide more 1, 3-dimethylimidazolium which is the best SDA for nucleation of AlPO-**CHA** structure. The concentration of the SDA resulted in an optimized balance between the nucleation and growth rate. These optimized nucleation and growth rates may be the possible reason that the large single crystal of AlPOs materials with a well-defined shape were obtained at a high temperature.

Several works on the ionothermal synthesis of large single crystal microporous materials have been reported. The work of Morris *et al.* showed that the AlPO-**CHA** synthesized in 1-alkyl-3-methylimidazolium bromide ionic liquids with longer alkyl

chains were much larger than the crystals synthesized in [Emim]Br. It was reasoned that the former tend to suppress the nucleation when the SDA was produced through the decomposition of the solvent.<sup>2</sup> Tian *et al.* reported the synthesis of GaPO-LTA single crystals up to 400  $\mu\text{m}$  in size in 1-alkyl-3-methylimidazolium bromide. In their work the size of the crystals dramatically decreased with increasing alkyl chain length. They believe the growth of the nonpolar alkyl chain domains decreases the polarity of the ionic liquids, which accordingly increases the supersaturation level in the synthetic precursor. This leads to the different sizes of the crystals synthesized in ionic liquids with different alkyl chains.<sup>32</sup>

In this chapter, the synthesis of the AlPO-CHA reveals another strategy for the ionothermal synthesis of microporous single crystals, which is clearly different from the previously reported ones. In the syntheses, the hydroxyl functionalized ionic liquid was used as a solvent. The decomposition of the solvent provided the SDA required for the crystallization of the microporous material. At higher temperature, single crystals of tens of micrometres were synthesized. While the ionothermal syntheses occurring at lower temperatures only gave intergrown crystal aggregations. Although the single crystal structural analysis and the  $^{13}\text{C}$  solid state NMR have proven the SDA comes from the decomposition of the ionic liquid, the growth of the large single crystals is unlikely the result of suppressed nucleation as in the example reported by Morris *et al.*<sup>2</sup> In this chapter's case, the temperature is the predominant factor. Increasing the crystallizing temperature may enhance the mass transfer, which results in increasing crystal growth. At a lower temperature, the rates of both nucleation and crystal growth are reduced, resulting in small crystals that easily aggregate. While at a higher temperature, a suitable balance between the nucleation and the crystal growth is established. Therefore large single crystals are synthesized at high temperature.

TGA was carried out to investigate the removal of the volatile species and the organic SDAs in the SIZ-10f samples that were obtained from different temperatures. The TGA curves of the as-synthesized SIZ-10f obtained from 150  $^{\circ}\text{C}$  and 210  $^{\circ}\text{C}$  are shown in Fig. 6-9 and Fig. 6-10, respectively. Both curves exhibit two stages of weight loss: one happened below 400  $^{\circ}\text{C}$  and the other happened from 400  $^{\circ}\text{C}$  to 800  $^{\circ}\text{C}$ . The weight losses in the first stage are attributed to the removal of the volatile species such as absorbed water and methanol. The weight losses that happened above 400  $^{\circ}\text{C}$  are assigned to the decomposition and escape of the organic SDAs and the fluorine. For

SIZ-10f obtained at 150 °C, the weight loss of the first stage is -1.58 % and the second stage is -25.1 %. For the SIZ-10f obtained at 210 °C the changes of both two weight losses happened in an opposite trend. The first stage exhibits a higher weight loss of -2.53 % but the second stage decreases to -24.32 %.

Considering the information obtained from the  $^{13}\text{C}$  MAS NMR, the changes in different trend are reasonable. For the samples obtained at 210 °C the 1, 3-dimethylimidazolium cations and methanol, which were the decomposition products of the [HOEmim]Cl, were located in the cavities of SIZ-10f. While in the samples obtained at 150 °C the [HOEmim]Cl was partially decomposed, resulting in the existence of the [HOEmim]Cl, methanol and 1, 3-dimethylimidazolium in the same cavities, but the weak  $^{13}\text{C}$  NMR signal from methanol indicates the absorbed methanol molecules were fewer than the methanol in the samples obtained at a higher temperature. Therefore when heated below 400 °C, the higher weight loss of the sample obtained at a high temperature is due to the removal of more methanol in the cavities. The weight losses between 400 to 800 °C are attributed to the removal of organic SDAs and the fluorine. For the sample obtained at 210 °C the 1, 3-dimethylimidazolium cations are the only organic compound in the cages and are well resolved by single crystal structural analysis. The calculated weight loss based on this compound and F should be 24.07 % in total. The experimental result agrees with the calculated value (24.32 % in Fig. 6-10). However, for the samples obtained at 150 °C, the experimental results show a greater weight loss (25.1 %) due to the existence of the heavier [HOEmim]Cl molecules, which is evidenced by  $^{13}\text{C}$  MAS NMR.

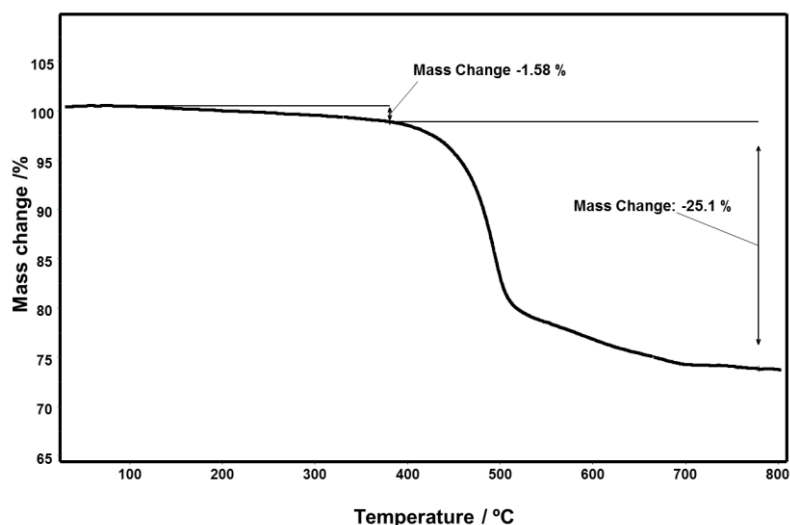


Fig. 6-9. TGA curve of the as-synthesized SIZ-10f obtained from 150 °C.

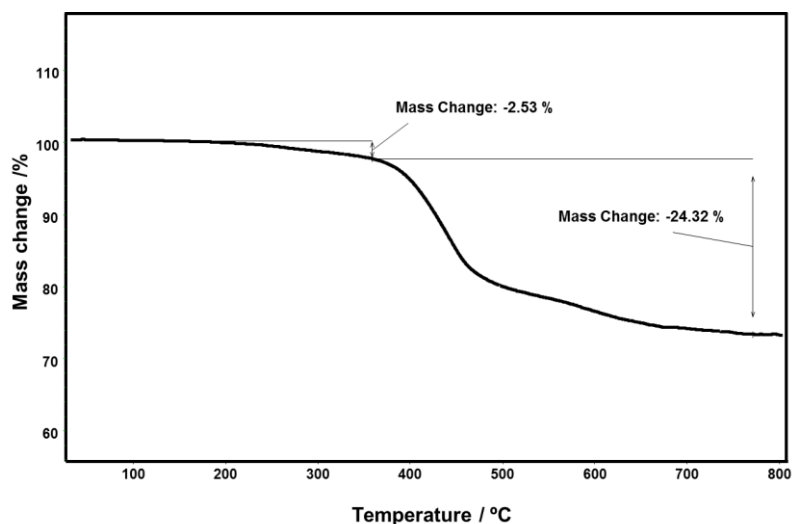


Fig. 6-10. TGA curve of the as-synthesized SIZ-10f obtained from 210 °C.

The  $^{27}\text{Al}$  and  $^{31}\text{P}$  solid state NMR spectra of as-synthesized SIZ-10f obtained at 210 °C are shown in Fig. 6-11 and Fig. 6-12, respectively. Both spectra are consistent with the structure of the triclinic CHA framework. Two resonances at 44 ppm and -6 ppm with an integral ratio of 2: 1 are observed in the  $^{27}\text{Al}$  MAS NMR spectrum of SIZ-10f. These resonances correspond to the tetrahedrally and octahedrally coordinated Al atoms in the as-synthesized SIZ-10f in an atomic ratio of 2: 1, respectively. For the  $^{31}\text{P}$  MAS NMR spectrum of the same sample, three resonances at -8, -24 and -29 ppm are observed. They are assigned to the three crystallographically independent P atoms with a different average P-O-Al angle.<sup>50, 51</sup>

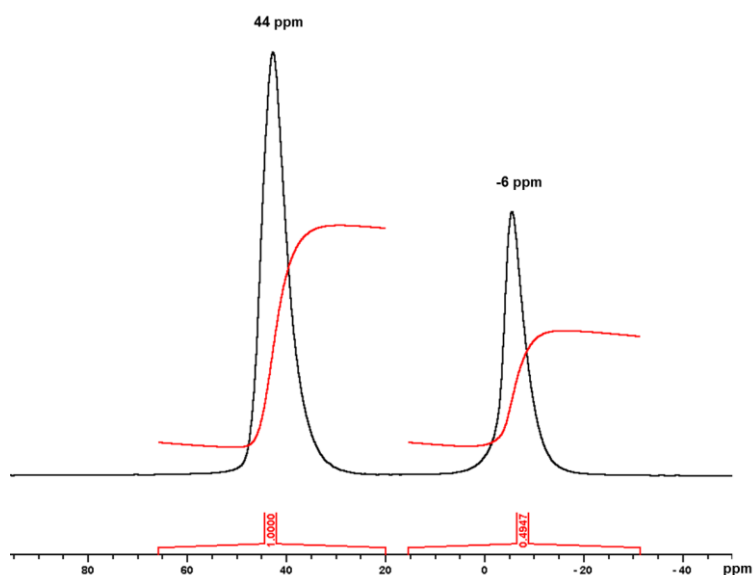


Fig. 6-11. The  $^{27}\text{Al}$  MAS NMR spectrum of the as-made SIZ-10f obtained from 210 °C. The spectrum was recorded with signal averaging for 128 transients with a recycle interval of 5 s. Solid-state NMR experiment was carried out by Dr. Daniel Dawson from University of St Andrews.

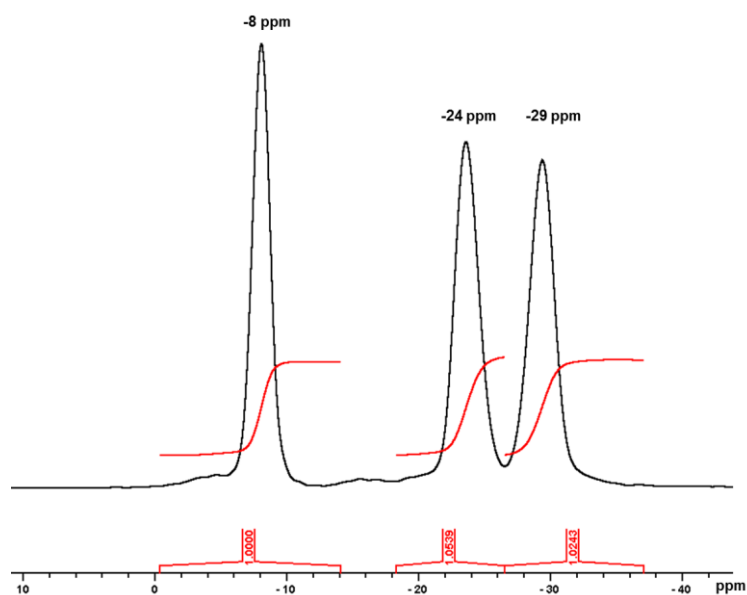


Fig. 6-12. The  $^{31}\text{P}$  MAS NMR spectrum of the as-made SIZ-10f obtained from 210 °C. The spectrum was carried out with signal averaging for 800 transients with a recycle interval of 60 s. Solid-state NMR experiment was carried out by Dr. Daniel Dawson from University of St Andrews.

## 6.4 Summary

In conclusion, in this chapter an ionic liquid with a hydroxyl group, 1-(2-hydroxyethyl)-3-methylimidazolium chloride ([HOEmim]Cl), was applied to the ionothermal synthesis of AlPO materials. The PXRD identified the framework of the product was structurally identical to SIZ-4 or SIZ-10, which were ionothermally synthesized from [Emim]Br and other alkyl-methylimidazolium based ionic liquids, respectively. The water from the orthophosphoric acid and hydrofluoric acid solution was not required to be removed from the synthetic precursor. The synthetic temperature was proved to strongly affect the sizes and shapes of the products. At a temperature of 210 °C, large single crystals with sizes of approximately  $70 \times 50 \times 50 \mu\text{m}^3$  were synthesized. Single crystal analysis by synchrotron diffraction solved both the framework structure and the SDA location in the product. Single crystal analysis confirmed the product was the triclinic deformation of **CHA** type framework. It also revealed the 1, 3-dimethylimidazolium cations that had resulted from the decomposition of the [HOEmim] cations were self-assembled through  $\pi$ - $\pi$  interaction and located in the *cha* cage of the framework. The formation of the large single crystals may be due to the enhanced mass transfer with the increasing of the temperature.

The  $^{13}\text{C}$  MAS NMR spectra indicate that at 210 °C the  $[\text{HOEmim}]^+$  decomposed to 1, 3-dimethylimidazolium cations and methanol. Both compounds were located in the *cha* cages. However, for the syntheses occurring at 150 °C, the ionic liquid in the framework was only partially decomposed, resulting in both  $[\text{HOEmim}]^+$  and 1, 3-dimethylimidazolium cations in the framework.

The work in this chapter shows the 1, 3-dimethylimidazolium cation is a suitable SDA for the synthesis of triclinic deformation **CHA** type framework. Although the hydroxyl group functionalized ionic liquids only directed to a known structure under this synthetic condition, its structure directing effects are still interesting due to the strong hydrogen bonding interaction which are not suitable in conventional hydrothermal synthesis. Other milder synthetic conditions that can avoid the decomposition of the ionic liquid will be investigated in the further work.

## 6.5 References

1. E. R. Cooper, C. D. Andrews, P. S. Wheatley, P. B. Webb, P. Wormald and R. E. Morris, *Nature*, 2004, **430**, 1012-1016.
2. E. R. Parnham and R. E. Morris, *Chem. Mater.*, 2006, **18**, 4882-4887.
3. Y. Wei, B. Marler, L. Zhang, Z. Tian, H. Graetsch and H. Gies, *Dalton Trans.*, 2012, **41**, 12408-12415.
4. E. R. Parnham and R. E. Morris, *J. Am. Chem. Soc.*, 2006, **128**, 2204-2205.
5. X. Zhao, H. Wang, B. Dong, Z. Sun, G. Li and X. Wang, *Microporous Mesoporous Mater.*, 2012, **151**, 56-63.
6. Z. Lin, A. M. Z. Slawin and R. E. Morris, *J. Am. Chem. Soc.*, 2007, **129**, 4880-4881.
7. L. Xu, S. Yan, E.-Y. Choi, J. Y. Lee and Y.-U. Kwon, *Chem. Commun.*, 2009, 3431-3433.
8. H. Fu, C. Qin, Y. Lu, Z.-M. Zhang, Y.-G. Li, Z.-M. Su, W.-L. Li and E.-B. Wang, *Angew. Chem. Int. Ed.*, 2012, **51**, 7985-7989.
9. R. E. Morris, *Angew. Chem. Int. Ed.*, 2008, **47**, 442-444.
10. J. Hoffmann, M. Nuchter, B. Ondruschka and P. Wasserscheid, *Green Chem.*, 2003, **5**, 296-299.
11. R. Cai, M. Sun, Z. Chen, R. Munoz, C. O'Neill, D. E. Beving and Y. Yan, *Angew. Chem. Int. Ed.*, 2008, **47**, 525-528.
12. R. E. Morris, *Chem. Commun.*, 2009, 2990-2998.
13. M. E. Davis and R. F. Lobo, *Chem. Mater.*, 1992, **4**, 756-768.
14. S. L. Burkett and M. E. Davis, *J. Phys. Chem.*, 1994, **98**, 4647-4653.
15. R. E. Morris and S. J. Weigel, *Chem. Soc. Rev.*, 1997, **26**, 309-317.
16. R. D. Rogers and K. R. Seddon, *Science*, 2003, **302**, 792-793.
17. S. Dai, Y. H. Ju, H. J. Gao, J. S. Lin, S. J. Pennycook and C. E. Barnes, *Chem. Commun.*, 2000, 243-244.
18. E. R. Parnham and R. E. Morris, *Acc. Chem. Res.*, 2007, **40**, 1005-1013.
19. Y.-P. Xu, Z.-J. Tian, S.-J. Wang, Y. Hu, L. Wang, B.-C. Wang, Y.-C. Ma, L. Hou, J.-Y. Yu and L.-W. Lin, *Angew. Chem. Int. Ed.*, 2006, **45**, 3965-3970.
20. H. Gies and B. Marker, *Zeolites*, 1992, **12**, 42-49.
21. S. L. Burkett and M. E. Davis, *Chem. Mater.*, 1995, **7**, 1453-1463.

22. J. P. Hofmann, D. Mores, L. R. Aramburo, S. Teketel, M. Rohnke, J. Janek, U. Olsbye and B. M. Weckhuysen, *Chem.-Eur. J.*, 2013, **19**, 8533-8542.
23. J. Caro, G. Finger, J. Kornatowski, J. Richter-Mendau, L. Werner and B. Zibrowius, *Adv. Mater.*, 1992, **4**, 273-276.
24. F. Gao, G. Zhu, Y. Chen, Y. Li and S. Qiu, *J. Phys. Chem. B*, 2004, **108**, 3426-3430.
25. L. Liu, Z.-B. Yu, H. Chen, Y. Deng, B.-L. Lee and J. Sun, *Cryst. Growth Des.*, 2013, **13**, 4168-4171.
26. S. Qiu, J. Yu, G. Zhu, O. Terasaki, Y. Nozue, W. Pang and R. Xu, *Microporous Mesoporous Mater.*, 1998, **21**, 245-251.
27. J. F. Charnell, *J. Cryst. Growth*, 1971, **8**, 291-294.
28. M. Morris, A. G. Dixon, A. Sacco jr and R. W. Thompson, *Zeolites*, 1993, **13**, 113-121.
29. S. Shimizu and H. Hamada, *Angew. Chem. Int. Ed.*, 1999, **38**, 2725-2727.
30. S. Qiu, W. Pang, H. Kessler and J.-L. Guth, *Zeolites*, 1989, **9**, 440-444.
31. A. Kuperman, S. Nadimi, S. Oliver, G. A. Ozin, J. M. Garces and M. M. Olken, *Nature*, 1993, **365**, 239-242.
32. H. Ma, R. Xu, W. You, G. Wen, S. Wang, Y. Xu, B. Wang, L. Wang, Y. Wei, Y. Xu, W. Zhang, Z. Tian and L. Lin, *Microporous Mesoporous Mater.*, 2009, **120**, 278-284.
33. S. Zhang, X. Qi, X. Ma, L. Lu and Y. Deng, *J. Phys. Chem. B*, 2010, **114**, 3912-3920.
34. L. C. Branco, J. N. Rosa, J. J. Moura Ramos and C. A. M. Afonso, *Chem.-Eur. J.*, 2002, **8**, 3671-3677.
35. Sheldrick, G. M., University of Gottingen, Germany, 1997.
36. L. S. Dent and J. V. Smith, *Nature*, 1958, **181**, 1794-1796.
37. J. W. Park and G. Seo, *Applied Catalysis A: General*, 2009, **356**, 180-188.
38. J. Q. Chen, A. Bozzano, B. Glover, T. Fuglerud and S. Kvisle, *Catal. Today*, 2005, **106**, 103-107.
39. S. Xu, A. Zheng, Y. Wei, J. Chen, J. Li, Y. Chu, M. Zhang, Q. Wang, Y. Zhou, J. Wang, F. Deng and Z. Liu, *Angew. Chem. Int. Ed.*, 2013, **52**, 11564-11568.
40. J. C. Poshusta, V. A. Tuan, E. A. Pape, R. D. Noble and J. L. Falconer, *AIChE J.*, 2000, **46**, 779-789.
41. M. A. Carreon, S. Li, J. L. Falconer and R. D. Noble, *Adv. Mater.*, 2008, **20**, 729-732.
42. Y. Tian, L. Fan, Z. Wang, S. Qiu and G. Zhu, *J. Mater. Chem.*, 2009, **19**, 7698-7703.
43. M. M. Harding and B. M. Kariuki, *Acta Crystallographica Section C*, 1994, **50**, 852-854.
44. N. Rajić, R. Gabrovšek, A. Ristić and V. Kaučič, *Thermochim. Acta*, 1997, **306**, 31-36.
45. R. Pei, Z. Tian, Y. Wei, K. Li, Y. Xu, L. Wang and H. Ma, *Mater. Lett.*, 2010, **64**, 2384-2387.
46. M. Musa, Thesis, University of St Andrews.
47. C. Janiak, *J. Chem. Soc., Dalton Trans.*, 2000, 3885-3896.
48. A. Corma, F. Rey, J. Rius, M. J. Sabater and S. Valencia, *Nature*, 2004, **431**, 287-290.
49. W. Song, J. F. Haw, J. B. Nicholas and C. S. Heneghan, *J. Am. Chem. Soc.*, 2000, **122**, 10726-10727.
50. K. Kanehashi, T. Nemoto and K. Saito, *J. Non-Cryst. Solids*, 2007, **353**, 4227-4231.
51. Z. Yan, B. Chen and Y. Huang, *Solid State Nucl. Magn. Reson.*, 2009, **35**, 49-60.

# Chapter 7 Targeted Synthesis of a Hemilabile Metal-Organic Frameworks

## 7.1 Introduction

The past two decades have witnessed the rapid development of the Metal-Organic Frameworks (MOFs, also known as coordination polymers, CPs). These materials exhibit properties such as adjustable pore sizes,<sup>1-3</sup> high surface area<sup>4-6</sup> and various compositions,<sup>7-10</sup> therefore are interesting for their applications in gas separation,<sup>11-13</sup> gas storage,<sup>14-16</sup> drug delivery,<sup>17, 18</sup> catalysis,<sup>19, 20</sup> and so forth.<sup>21</sup> One of the attractive properties of MOFs is that some of them possess structural flexibility.<sup>22, 23</sup> These materials can transform to another structure when responding to external stimuli such as guest removal and guest exchange. In the cases where the structural transformations are induced by guest molecules, this kind of compounds is classified as “third generation”.<sup>24</sup> Many MOF compounds which can respond to the changing of guest molecules have been reported.<sup>25-27</sup> The change of temperature also can cause structure transformation as the increase of temperature usually assists in removing the volatile guests from the framework of the flexible materials, and this process is named activation.<sup>28, 29</sup> These materials are attractive in many fields, especially in selective gas adsorption<sup>30</sup> and sensing.<sup>31</sup> Sometimes the transformations of MOF materials can take place from single crystal to single crystal reversibly.<sup>32-34</sup> However, in most cases the reversible Single-Crystal to Single-Crystal transformable MOFs were synthesized by trial and error. Predicting the structure of MOF materials and their properties is still a challenge due to the multifarious coordination modes of organic ligands to metal atoms.<sup>35</sup>

In 2009, Xiao *et al.* reported the synthesis of a flexible MOF named Cu-SIP-3.<sup>36</sup> The ligand of Cu-SIP-3 is 5-sulfoisophthalic acid (SIP), which was carefully selected as it contains two strongly bonding carboxylate groups and one weakly bonding sulfonate group. When the compound was heated, the coordinated water molecules were removed and resulted in unsaturated metal sites. The weak bonding sulfonate groups changed their coordination mode and moved so that the sulfonate groups could bind to the unsaturated metal sites. These changes led to a structural transformation. Meanwhile the

strongly bonding carboxylate groups retain their coordinating mode and thus keep the single crystal stable. The structural transformation and the changes of the ligand coordination modes are illustrated in Fig. 7-1.

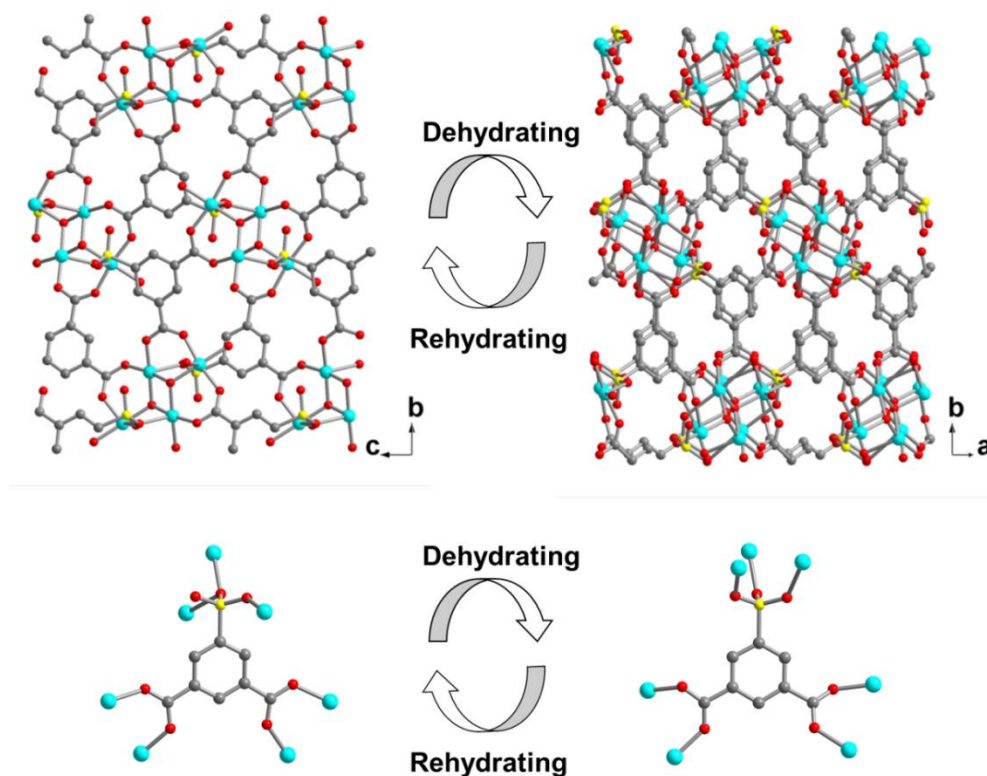


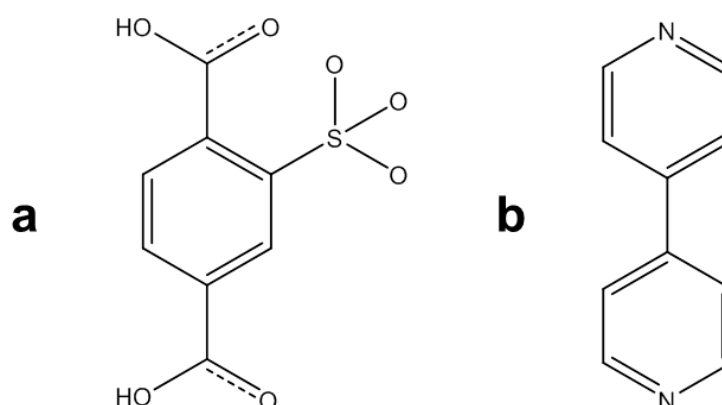
Fig. 7-1. The picture shows the reversible changes of the Cu-SIP-3 (upper) and the changes of the coordination modes of 5-sulfoisophthalic acid in Cu-SIP-3 upon a hydration-dehydration process. (Cu: aqua blue, O: red, S: yellow, C: grey. Hydrogen on ligand is not shown for clarity)

This example demonstrates a strategy toward targeted synthesis of transformable materials by selecting appropriate ligands. The materials synthesized by this strategy are dubbed “hemilabile MOFs”, as the selected ligands are analogous to the multidentate ligands in homogenous catalysis where the ligands can have different coordinating groups of varying strengths.<sup>37-39</sup>

The compounds that can exhibit structural transformation and maintain single crystallinity at the same time provide an opportunity to study these transformations *in situ* using single crystal diffraction<sup>40</sup>. Moreover, the hemilabile property of Cu-SIP-3 makes the material interesting for gas adsorption: coordinating gases such as NO, which is a biological active compound,<sup>41-43</sup> are selectively adsorbed over other gases such as H<sub>2</sub>, N<sub>2</sub>, CO<sub>2</sub>, CO, and *etc.*, and a “gate opening pressure” for NO was observed.<sup>36</sup>

## 7.2 Aims

The aim of this chapter is to prove that the synthetic strategy for Cu-SIP-3 can be generalized to other compounds and can prepare hemilabile MOFs. Other ligands which also contain both strong and weaker coordinating groups will be selected to build MOF materials. The sulfonate group is usually regarded as a poor coordination group.<sup>44, 45</sup> In this chapter 2-sulfoterephthalic acid (STP) will be selected as the hemilabile ligand (Scheme 7-1a). It contains one sulfonate group and two carboxylate groups, which is structurally similar to 5-sulfoisophthalic acid. The 4, 4'-bipyridine (Bpy) will be used as the auxiliary ligand to help the crystallization (Scheme 7-1b). In order to investigate the relationship between structure and hemilability of the MOF materials, variable temperature single crystal structure analysis will be carried out. The flexible property will also be investigated by other techniques such as powder X-ray diffraction (PXRD), thermal gravimetric analysis (TGA) and elemental analysis.



Scheme 7-1. Schematic shows the structure of the ligands which will be used in this chapter: (a) 2-sulfoterephthalic acid and (b) 4, 4'-bipyridine.

## 7.3 Cu-STP-Bpy

### 7.3.1 Experimental methods

#### 7.3.1.1 Synthesis of hydrated compound

To synthesize the hydrated compound, 2-sulfoterephthalic acid (STP) which contains two carboxylate groups and one sulfonate group was selected as the hemilabile ligand. Meanwhile, 4, 4'-bipyridine (Bpy) was selected as the auxiliary ligand. The hydrated compound named Cu-STP-Bpy-H<sub>2</sub>O was prepared by solvothermally heating the above ligands with Cu(NO<sub>3</sub>)<sub>2</sub>·3H<sub>2</sub>O in the mixed solvent of water and ethanol. All the reagents

were obtained from commercial sources and used as purchased. The synthetic molar composition was  $\text{Cu}(\text{NO}_3)_2 \cdot 3\text{H}_2\text{O}$ : STP: Bpy:  $\text{H}_2\text{O}$ : ethanol = 1: 1: 1: 400: 200. In a typical synthesis, 0.242 g of  $\text{Cu}(\text{NO}_3)_2 \cdot 3\text{H}_2\text{O}$  (98 %, 1 mmol, Alfa Aesar), 0.268 g of 2-sulfoterephthalic acid monosodium salt (98 %, 1 mmol, TCI) and 0.156 g of 4, 4'-bipyridine (98 %, 1 mmol, Aldrich) were dispersed in a mixed solvent of 7.2 g of distilled water (400 mmol) and 9.2 g of ethanol (99.8 %, 200 mmol, VWR). The suspension was stirred at room temperature for 15 min. The mixture was transferred to a 50ml Teflon-lined autoclave and heated at 110 °C for 3 days. Blue prism-shaped crystals were obtained, collected by vacuum filtration, washed with distilled water and dried at 80 °C overnight. 0.274 g (91 % yield based on Cu) of product was obtained.

### ***7.3.1.2 Dehydration and rehydration processes***

The dehydrated compound named Cu-STP-Bpy was obtained by heating Cu-STP-Bpy- $\text{H}_2\text{O}$  under vacuum. The dehydration temperature was determined to be 240 °C based on the result of TGA.

The hydrated compound samples were packed into glass capillaries of 0.5 mm diameter and laid in a schlenk apparatus. They were heated to 240 °C in a furnace under vacuum. The colour of the sample changed from blue to dark green within 12 hours at elevated temperature under vacuum, indicating the coordinating water molecules were removed and dehydrated compound was obtained. The capillaries were quickly sealed under Ar flow to prevent rehydration occurring.

In order to obtain the rehydrated sample, the dehydrated samples were exposed to open air for 24 hours until the sample colour returned to blue.

### ***7.3.1.3 Characterisation***

TGA was run on a Netzsch TG 209 instrument under air flow. The sample was heated to 600 °C in an alumina crucible at a heating rate of 10 °C·min<sup>-1</sup>. PXRD patterns of each sample were collected in a STOE diffractometer under  $\text{CuK}\alpha$  radiation in Debye-Scherrer mode. Hydrated, dehydrated and rehydrated samples were sealed in glass capillaries of 0.5 mm diameter to prevent the further structure changes during the data collection. The elemental analysis on C, H, N and S of the hydrated sample took place on a Carlo Erba CHNS analyser.

Single crystal data of hydrated and dehydrated samples were collected at Station 11.3.1 of the Advanced Light Source, Lawrence Berkeley National Laboratory, using a

wavelength of  $\lambda = 0.7749 \text{ \AA}$ . A Bruker AXS APEXII diffractometer was used for data collection. Data collection and reduction were carried out with the corresponding Bruker AXS APEXII software. Hydrated sample data were collected at  $-123 \text{ }^\circ\text{C}$ . Dehydrated sample data were collected at  $227 \text{ }^\circ\text{C}$ . Variable temperatures in single crystal analysis were achieved via the Cryostream with a ramp rate of  $6 \text{ }^\circ\text{C}\cdot\text{min}^{-1}$ .

All the structures were solved by direct methods using the program SHELXS-97 and then refined on  $F^2$  using SHELXL-97<sup>46</sup>. Three non-hydrogen atoms of the dehydrated structure were refined isotropically for a satisfactory refinement at high temperature. Other non-hydrogen atoms of both hydrated and dehydrated structures were refined anisotropically. Hydrogen atoms on the coordinated water molecules were fixed with DFIX restraints. Other hydrogen atoms were fixed based on idealized coordinates and refined with values of  $U_{\text{iso}}$  set to 1.2 times that of the carrier atoms.

### 7.3.2 Results and discussions

The single crystal diffraction data of the Cu-STP-Bpy- $\text{H}_2\text{O}$  and the Cu-STP-Bpy were collected at  $-123 \text{ }^\circ\text{C}$  and  $227 \text{ }^\circ\text{C}$ , respectively. The structures of both compounds were solved and refined. Single crystal data were collected by Dr. Catherine Renouf from University of St Andrews. The crystal data and refinement results are listed in Table 7-1.

Table 7-1. Crystal data and refinement results of Cu-STP-Bpy- $\text{H}_2\text{O}$  and Cu-STP-Bpy

Compound	<b>Cu-STP-Bpy-<math>\text{H}_2\text{O}</math></b>	<b>Cu-STP-Bpy</b>
Formula	$\text{Cu}_3(\text{C}_8\text{S}_1\text{O}_7\text{H}_3)_2(\text{C}_{10}\text{N}_2\text{H}_8)(\text{H}_2\text{O})_4$	$\text{Cu}_3(\text{C}_8\text{S}_1\text{O}_7\text{H}_3)_2(\text{C}_{10}\text{N}_2\text{H}_8)$
Formula weight	905.20	833.13
Crystal system	Monoclinic	Monoclinic
Space group	$P2_1/c$	$P2_1/c$
$a$ ( $\text{\AA}$ )	11.017(5)	10.075(5)
$b$ ( $\text{\AA}$ )	11.814(5)	12.806(5)
$c$ ( $\text{\AA}$ )	12.135(5)	19.502(5)
$\alpha$ ( $^\circ$ )	90.000(5)	90.000(5)
$\beta$ ( $^\circ$ )	109.701(5)	95.342(5)
$\gamma$ ( $^\circ$ )	90.000(5)	90.000(5)
$V$ ( $\text{\AA}^3$ )	1487.0(11)	2505.2(17)
$Z$	2	4
$D_c$ ( $\text{g}/\text{cm}^3$ )	2.022	2.209

$F(000)$	910	1660
$\mu$ (mm <sup>-1</sup> )	2.890	3.409
$\theta$ for data collection (°)	2.85 to 34.65	2.96 to 22.79
Reflections collected	21375	23264
Unique reflections	4736	2610
$R_{\text{int}}$	0.0578	0.0959
Data/restraints/parameters	4736/ 6/ 244	2610 / 0 / 412
Goodness-of-fit on $F^2$	1.023	1.067
$R_1, wR_2 [I > 2\sigma(I)]$	0.0327, 0.0904	0.0685, 0.1887
$R_1, wR_2$ (all data)	0.0378, 0.0938	0.1000, 0.2155

$$R_1 = \frac{\sum(|F_o| - |F_c|)}{\sum|F_o|}, wR_2 = \left[ \frac{\sum w(F_o^2 - F_c^2)^2}{\sum w(F_o^2)^2} \right]^{1/2}.$$

The formula of the Cu-STP-Bpy-H<sub>2</sub>O is Cu<sub>3</sub>(STP)<sub>2</sub>(Bpy)·4H<sub>2</sub>O. Based on its molecular formula, the calculated weight contents of C, H, N and S are 34.49 %, 2.43 %, 3.10 % and 7.08 %, respectively. The elemental analysis of the compound gave consistent results, of which the weight contents of C, H, N and S are 35.94 %, 2.51 %, 3.65 % and 7.05 %, respectively. The single crystal analysis also indicates the Cu-STP-Bpy-H<sub>2</sub>O possesses two H<sub>2</sub>O per asymmetric unit. According to the formula, the calculated weight loss for complete removal of the water from the Cu<sub>3</sub>(STP)<sub>2</sub>(Bpy)·4H<sub>2</sub>O is 7.95 %.

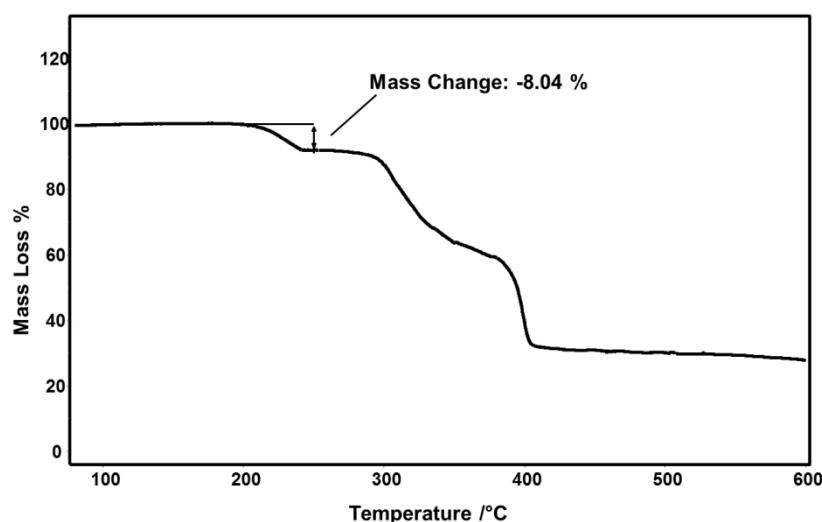


Fig. 7-2. TGA curve of heating hydrated compound Cu-STP-Bpy-H<sub>2</sub>O under air.

The TGA curve of Cu-STP-Bpy-H<sub>2</sub>O shown in Fig. 7-2 exhibits a weight loss of about 8.04 % in the temperature range between 200 °C and 240 °C. The weight loss observed

in TGA is considered to be caused by the removal of coordinating water molecules. Therefore the consistency of experimental and calculated results indicates the coordinated water molecules are completely removed after dehydration. The loss of coordinated water molecules led to the formation of the Cu-STP-Bpy, of which the molecular formula would be  $\text{Cu}_3(\text{STP})_2(\text{Bpy})$ , which is consistent with the single crystal structure analysis.

The reversible transformation between the Cu-STP-Bpy- $\text{H}_2\text{O}$  and the Cu-STP-Bpy was verified by PXRD patterns in Fig. 7-3. The PXRD patterns of hydrated, dehydrated and rehydrated compounds indicate all the samples were crystalline. The differences between the PXRD patterns of the hydrated and dehydrated samples indicate that a structural rearrangement had occurred (Fig. 7-3a and Fig. 7-3b). The dehydrated compound was reversibly rehydrated when it was exposed to the moist air, which is supported by the identical PXRD pattern of rehydrated compound to the pattern of the hydrated one (Fig. 7-3c and Fig. 7-3a).

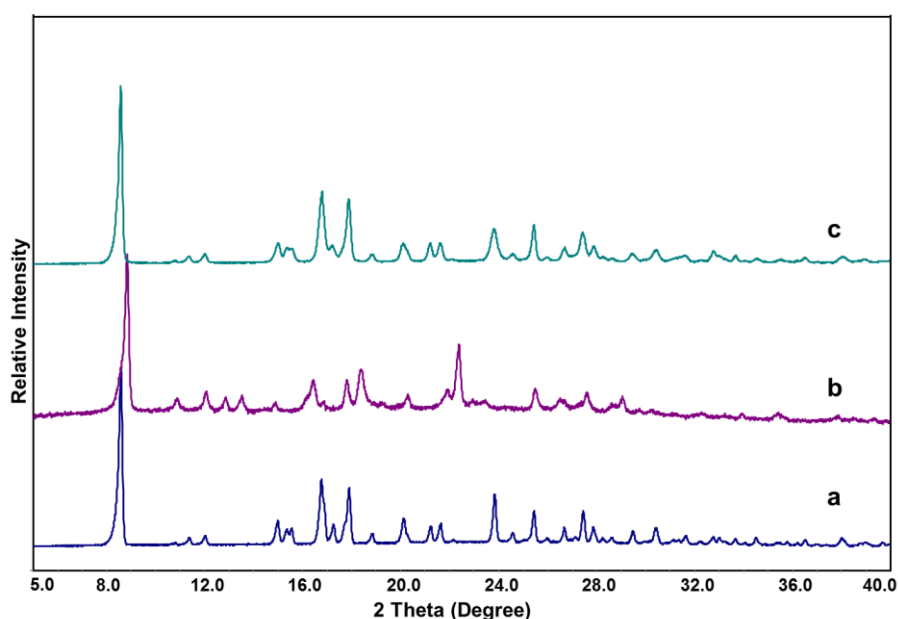


Fig. 7-3. PXRD patterns of (a) hydrated compound, Cu-STP-Bpy- $\text{H}_2\text{O}$ ; (b) dehydrated compound, Cu-STP-Bpy and (c) rehydrated compound, Cu-STP-Bpy- $\text{H}_2\text{O}$ .

The single crystal analysis reveals that the hydrated compound, Cu-STP-Bpy- $\text{H}_2\text{O}$ , has two kinds of crystallographically distinct copper atoms, denoted Cu1 and Cu2. In one Cu-STP-Bpy- $\text{H}_2\text{O}$  asymmetric unit, there is one Cu1 atoms, which have the square pyramidal coordination environment and half equivalent Cu2 atom which has an octahedral coordination environment. The coordination environment of Cu1 is shown in

Fig. 7-4a. Each Cu1 atom is coordinated by three independent STP molecules and two coordinated water. Two of the three STP ligand molecules coordinate to the Cu1 with the carboxylate groups and both of them are monodentate. The bond lengths of these two carboxylate oxygen to the Cu1 are 1.9913(16) Å and 1.9322(16) Å, respectively. The rest of the STP ligand molecules coordinate to the Cu1 with one oxygen atom from the sulfonate group. The bond length of sulfonate oxygen to the Cu1 is 2.2896(17) Å. Besides the three STP ligands, two water molecules also coordinate to each Cu1 atom of the Cu-STP-Bpy-H<sub>2</sub>O. The bond lengths of the water oxygen atoms to the Cu1 are 1.9758(19) Å and 1.9909(18) Å, respectively.

The coordination geometry of Cu2 of the Cu-STP-Bpy-H<sub>2</sub>O is shown in Fig. 7-4b. The Cu2 atom is coordinated by two STP ligands and two Bpy ligands. The STP and Bpy ligands are located around the inversion centre which is Cu2. The STP ligand chelates to Cu2 with the sulfonate oxygen and its ortho-carboxylate oxygen. The bond length of sulfonate oxygen to Cu2 is 2.2886(17) Å, and the bond length of carboxylate oxygen to Cu2 is 2.0435(16) Å. The pyridine is a strong binding group and in the Cu-STP-Bpy-H<sub>2</sub>O the length of the Cu-N bond is 1.9744(20) Å.

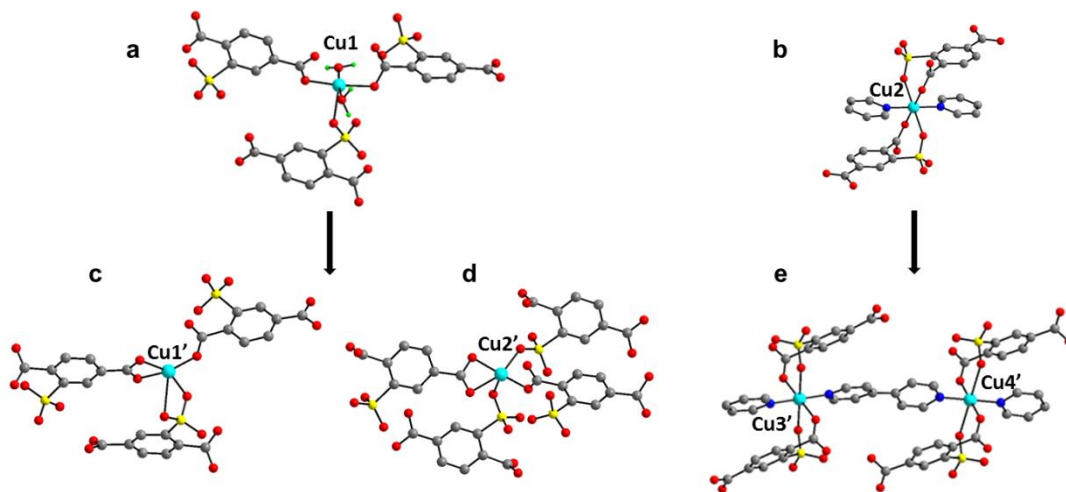


Fig. 7-4. Schematic showing the copper coordination environments of the Cu-STP-Bpy-H<sub>2</sub>O in (a) and (b) and the Cu-STP-Bpy in (c), (d) and (e). (Cu: aqua blue; O: red; S: yellow; C: grey; N: blue; H: green. Only water hydrogen atoms are present for clarity.)

The coordination geometries of both Cu1 and Cu2 exhibit the typical Jahn-Teller distortion.<sup>47</sup> For Cu1 (Fig. 7-5a), the two water molecules and two carboxylate oxygen atoms locate in the basal plane. The sulfonate oxygen atom is in the elongated axial site.

For Cu2 (Fig. 7-5b), the two nitrogen atoms and two carboxylate oxygen atoms locate in the equatorial plane, and the sulfonate oxygen atoms locate in the Jahn-Teller elongated coordination sites again.

Clearly, for both Cu1 and Cu2, the Cu-O(S) bonds are longer than the Cu-O(C) bonds, indicating the coppers attract to carboxylate more strongly than to sulfonate. Thus in the Cu-STP-Bpy-H<sub>2</sub>O, the binding strength of oxygen atoms to Cu1 is in the order of Cu1-O(C) > Cu1-O(S).

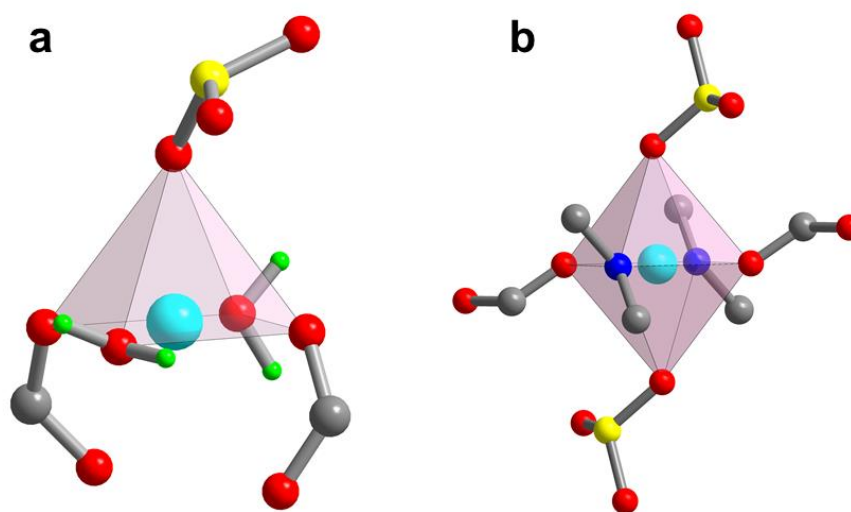


Fig. 7-5. The coordination geometries of Cu1 (a) and Cu2 (b) of the Cu-STP-Bpy-H<sub>2</sub>O. (Cu: aqua blue; O: red; S: yellow, C: grey; N: blue; H: green. Only water hydrogen atoms are present for clarity.)

After the dehydration process, the water molecules that coordinated to Cu1 were removed. The removal of the coordinated water led to the structural transformation of the Cu-STP-Bpy-H<sub>2</sub>O to the Cu-STP-Bpy. The coordination environments of both Cu1 and Cu2 in the Cu-STP-Bpy-H<sub>2</sub>O are changed. There are four independent Cu atoms in the Cu-STP-Bpy. In order to distinguish the copper atoms of the Cu-STP-Bpy from the ones of the Cu-STP-Bpy-H<sub>2</sub>O, the names of the atoms from the dehydrated Cu-STP-Bpy are marked by an apostrophe. The two copper atoms originating from Cu1 are named Cu1' and Cu2', respectively. Both of them are 5-coordinate. The corresponding coordination environments are shown in Fig. 7-4c and Fig. 7-4d, respectively. The other two crystallographically distinct copper atoms, which result from the transformation of Cu2, are named Cu3' and Cu4', respectively, and have octahedral coordination environments (Fig. 7-4e).

The Cu1' is coordinated by three distinct STP molecules. Unlike the Cu-STP-Bpy-H<sub>2</sub>O of which all the three STP ligands monodentate bind to the Cu1 centre, in the Cu-STP-Bpy one sulfonate group and one carboxylate group from two distinct STP chelate to Cu1'. The other STP binds in a monodentate fashion to Cu1' by one carboxylate group (Fig. 7-4c and Fig. 7-6a). The bond lengths of carboxylate oxygen to Cu1' are 1.8252(58) Å, 1.9070(69) Å and 1.9463(58) Å, respectively, which are comparable with the Cu-O(C) bond lengths of the Cu-STP-Bpy-H<sub>2</sub>O. However the Cu-O(S) bond lengths in the Cu-STP-Bpy-H<sub>2</sub>O and the Cu-STP-Bpy are different. In the Cu-STP-Bpy, one of the Cu1'-O(S) bond is decreased to 1.9621(55) Å, indicating this sulfonate oxygen is strongly binding to Cu1' atom after the removal of coordinated water. While the other sulfonate oxygen binds to Cu1' weakly and the bond length is 2.5357(66) Å. The coordination geometry of Cu1' is shown in Fig. 7-6a. It presents a distorted trigonal bipyramidal structure which is similar to some [Cu(Bpy)Cl]<sup>+</sup> complexes.<sup>48</sup>

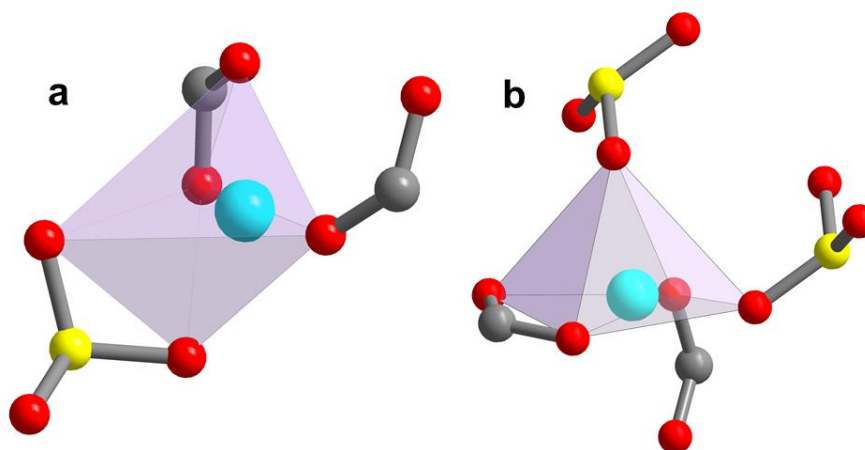


Fig. 7-6. Coordination geometries of Cu1' (a) and Cu2' (b) in the Cu-STP-Bpy. (Cu: aqua blue; O: red; S: yellow, C: grey.)

The Cu2' of the Cu-STP-Bpy is also 5-coordinate. The five coordinate oxygen atoms come from four STP ligands molecules (Fig. 7-4d and Fig. 7-6b). Two STP molecules coordinate to Cu2' with their carboxylate groups: one is monodentate and the other is bidentate. The bond lengths of these three carboxylate oxygen atoms to Cu2' are 1.8564(61) Å, 1.8747(66) Å and 2.136(8) Å, respectively. Another two STP molecules coordinate to Cu2' with their sulfonate group and both of them are monodentate. The newly sulfonate-coordinating STP ligand was not coordinated to Cu1 in the Cu-STP-

Bpy-H<sub>2</sub>O before dehydration. The single crystal analysis of the Cu-STP-Bpy-H<sub>2</sub>O indicates the distance between this oxygen to the nearest Cu1 was about 4 Å. After dehydration the sulfonate oxygen coordinates to this Cu atom and the distance between them decreases to 1.9731(59) Å. The other Cu-O(s) bond length is 2.1932(65) Å. Both of the Cu-O(S) distances in the Cu-STP-Bpy are shorter than the Cu-O(S) bond distance in the Cu-STP-Bpy-H<sub>2</sub>O, indicating the sulfonate groups bind to the metal site more strongly after removal of water. Fig. 7-6b shows the coordination geometry of the Cu2'.

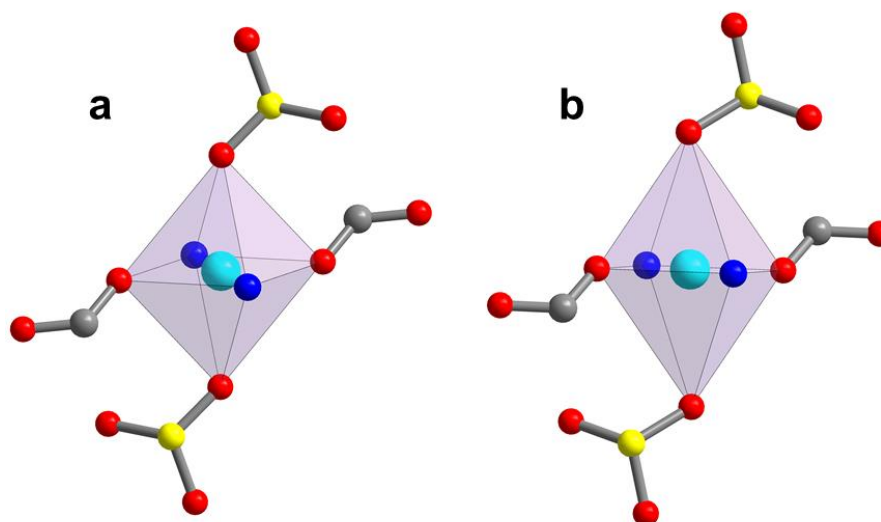


Fig. 7-7. Coordination geometries of Cu3' (a) and Cu4' (b) in the Cu-STP-Bpy. (Cu: aqua blue; O: red; S: yellow, C: grey; N: blue.)

Cu3' and Cu4' originate from the Cu2 of Cu-STP-Bpy-H<sub>2</sub>O. Similar to Cu2, they are both octahedrally coordinated. Two bidentate STP ligands and two monodentate Bpy ligands coordinate to the metal centre (Fig. 7-4e and Fig. 7-7). The coordination geometries of both Cu3' and Cu4' are shown in Fig. 7-7. The copper atoms present elongated octahedral geometries due to the Jahn-Teller effect. Similar to the sulfonate oxygen in the Cu-STP-Bpy-H<sub>2</sub>O, the sulfonate oxygen atoms of the Cu-STP-Bpy locate in the elongated axial sites. Although Cu3' and Cu4' have similar coordination geometries to Cu2 of the Cu-STP-Bpy-H<sub>2</sub>O, there are still several differences between hydrated and dehydrated compounds. First, the bond lengths of sulfonate oxygen to copper atoms of the Cu-STP-Bpy increase to 2.3389(63) Å for Cu3'-O(S) and 2.6606(55) Å for Cu4'-O(S); Second, the Cu-Bpy-Cu chain is twisted due to the structure transformation. The torsion angle between two pyridine planes is 19.131(821)° (Fig. 7-4e).

The coordination modes of the STP ligands in the Cu-STP-Bpy-H<sub>2</sub>O and Cu-STP-Bpy are shown in Fig. 7-8. For the Cu-STP-Bpy-H<sub>2</sub>O, each STP ligand coordinates to four Cu atoms (Fig. 7-8a). After dehydration, half of the ligands still coordinate to four Cu atoms, despite some monodentate groups now bidentate to Cu atoms (Fig. 7-8c). The rest of the STP ligands coordinate to five Cu atoms (Fig. 7-8b). The reversibility of the compound can be achieved by a rehydration process.

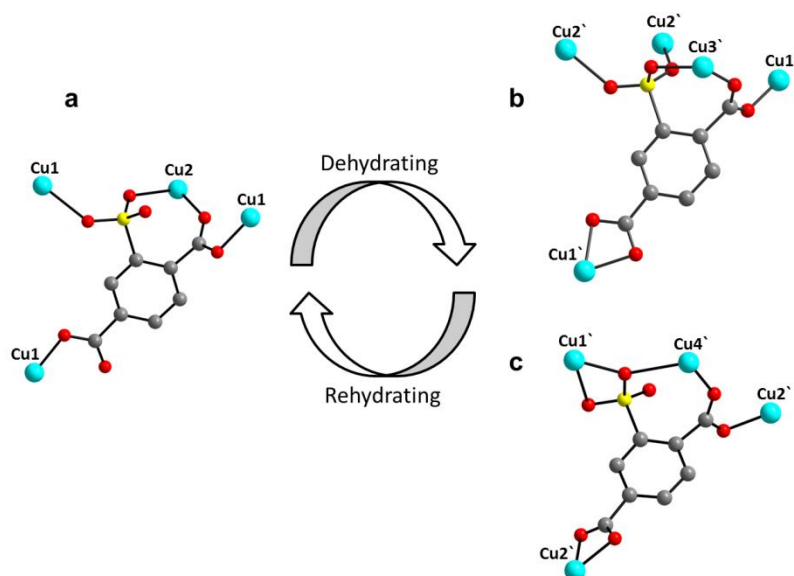


Fig. 7-8. (a) is the coordination modes of the STP ligand in the Cu-STP-Bpy-H<sub>2</sub>O, (b) and (c) are the coordination modes of the STP ligands in the Cu-STP-Bpy(Cu: blue, O: red, S: yellow, C: grey. Hydrogen is not shown for clarity).

An overall description about the structural transformation process between the Cu-STP-Bpy-H<sub>2</sub>O and the Cu-STP-Bpy is as follows: as soon as the coordinated water molecules were removed from the Cu-STP-Bpy-H<sub>2</sub>O, unsaturated copper sites were formed. The uncoordinated sulfonate oxygen atoms around the unsaturated Cu atoms were strongly attracted by the unsaturated Cu atoms. The Cu-O(S) distance changed from about 4 Å to 2 Å and resulted in the formation of the coordination bonds between Cu and sulfonate oxygen. However, the compound formed after dehydration may tend to recover to the original structure due to the binding of water to Cu being more stable than the binding between sulfonate and Cu. Therefore the Cu-STP-Bpy is less stable than its hydrated form. When it exposed to moist air the structure reversibly transformed to the Cu-STP-Bpy-H<sub>2</sub>O.

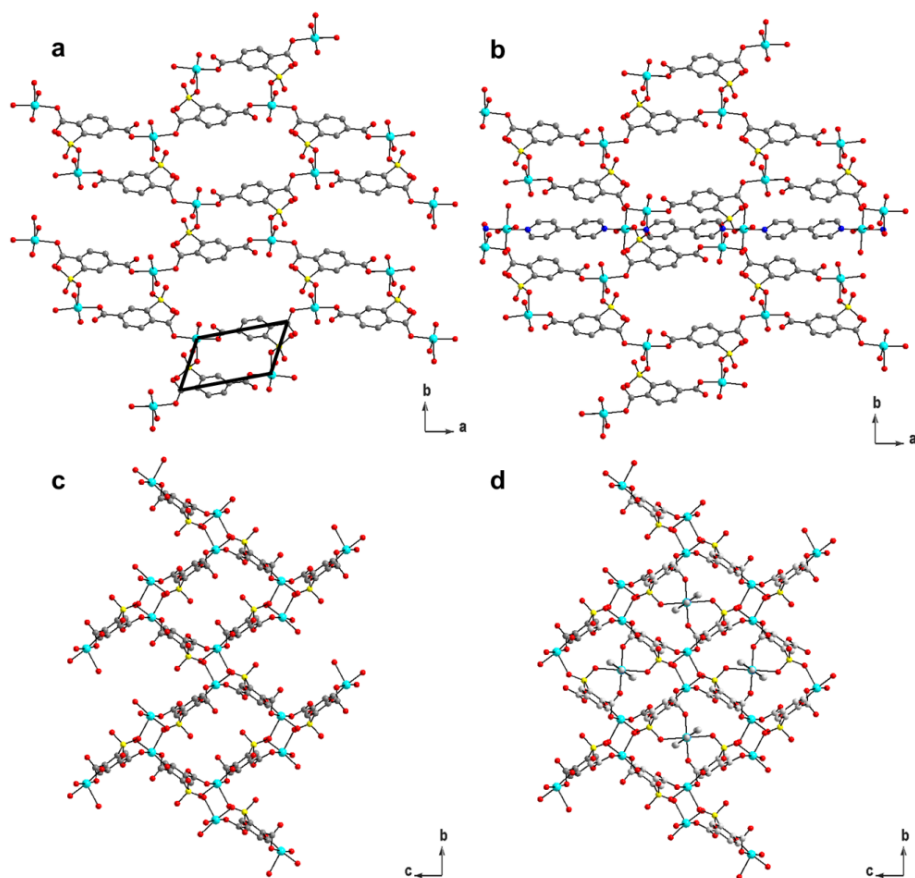


Fig. 7-9. Structure descriptions of the Cu-STP-Bpy-H<sub>2</sub>O. (a) a single 2D layer structure viewed along the *c* axis, the Cu<sub>2</sub>(STP)<sub>2</sub> building units are marked by the black frame at the bottom. The Cu<sub>2</sub> atoms and the Bpy ligands are not shown; (b) the same layer with one Cu-Bpy-Cu chain penetrating through this layer; (c) one 2D layer structure viewed along the *a* axis; (d) the same layer with four Cu-Bpy-Cu chains penetrating through it. (Cu: Aqua blue, O: red, S: yellow, C: grey, N: blue. Hydrogen atoms are not shown for clarity)

Fig. 7-9 illustrates the entire structure of the Cu-STP-Bpy-H<sub>2</sub>O. Two STP molecules and two Cu1 atoms link together and form a quadrilateral Cu<sub>2</sub>(STP)<sub>2</sub> building unit which are shown as the black frame in Fig. 7-9a. These building units connect together in a corner-sharing way continuously to form a 2-dimensional layer structure. Fig. 7-9a and Fig. 7-9c show the structure of a single layer viewed along the *c* axis and the *a* axis, respectively. Meanwhile, each STP molecule also chelates to one Cu<sub>2</sub> atom by one sulfonate oxygen and one carboxylate oxygen atom. As discussed above, every Cu<sub>2</sub> atom is coordinated in an inversion mode by two STP ligands. These two ligands respectively come from two neighbouring layers. Thus the 2D layers are linked together by the Cu<sub>2</sub> atoms to form a 3-dimensional extended structure. The Cu<sub>2</sub> atoms are also linked by the Bpy molecules. The Cu-Bpy-Cu chains penetrate through the layer. Fig. 7-

9b and Fig. 7-9d show a single layer with one and four Cu-Bpy-Cu chains, respectively. In Fig. 7-10a three 2D layers are shown in different colours. Their connections by Cu-Bpy-Cu chains (shown in yellow) are shown in different directions in Fig. 7-10b and Fig. 7-10c, respectively.

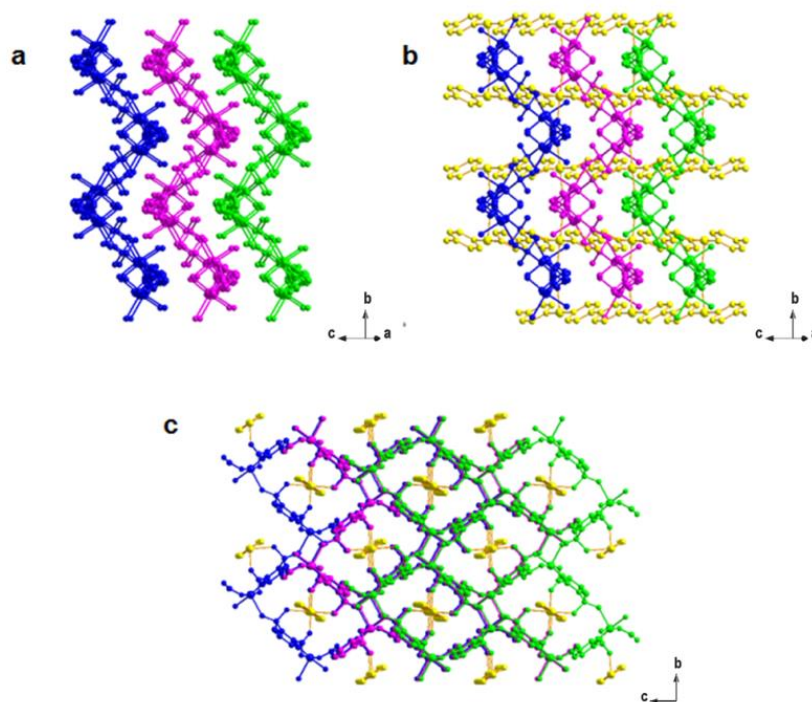


Fig. 7-10. The structure of Cu-STP-Bpy-H<sub>2</sub>O shown in different colours. (a) Three 2D layers shown in blue, purple and green, respectively; (b) the three 2D layers with the Cu-Bpy-Cu chains (yellow) penetrating through them and (c) the same structure of fig. 7-7b viewed along the *a* axis.

The structures of the Cu-STP-Bpy are shown in Fig. 7-11. The hemilabile STP ligand changes its coordinating mode after dehydration. These changes lead to the structural transformation of the hemilabile MOF compound. Half of the Cu1 atoms in the 2D layer of the Cu-STP-Bpy-H<sub>2</sub>O are coordinated by two sulfonate groups from two adjacent layers after dehydration. Thus the double-layer structure in the Cu-STP-Bpy are formed which originate from the adjacent single layer structures in the Cu-STP-Bpy-H<sub>2</sub>O. One double-layer structure is shown in Fig. 7-11a. Similar to the Cu-STP-Bpy-H<sub>2</sub>O, the double layer structures are connected into a 3D framework by the copper atoms on the Cu-Bpy-Cu chains. The whole structure of the Cu-STP-Bpy is shown in Fig. 7-11b with the layers and the Cu-Bpy-Cu chains in different colours.

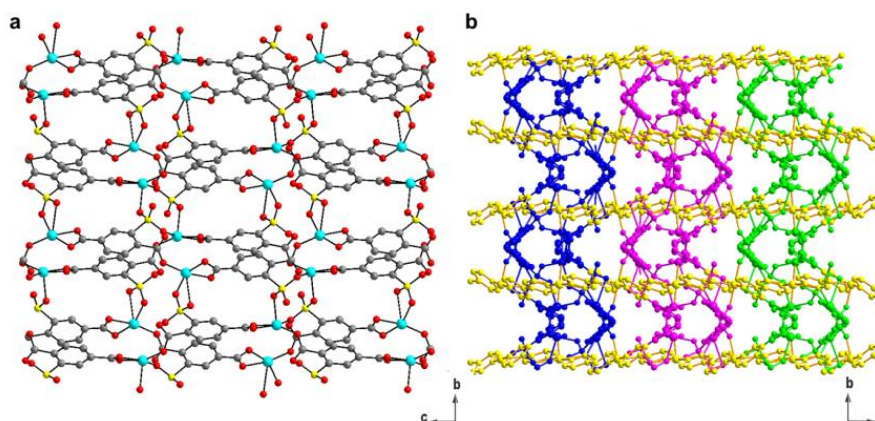


Fig. 7-11. (a) Double layer structure of the Cu-STP-Bpy viewed along the *a* axis. (Cu: aqua blue, O: red, S: yellow, C: grey. Cu3', Cu4', Bpy and hydrogen atoms are not shown for clarity); (b) complete crystal structure of the Cu-STP-Bpy viewed along the *c* axis to show three double-layer structures in different colours and the Cu-Bpy-Cu chains (shown in yellow) penetrating through them.

## 7.4 Summary

To conclude, a hemilabile copper MOF material was synthesized using STP and Bpy as the ligands. The single crystal analysis indicates the material contains coordinated water molecules. At elevated temperature the compound loses the coordinated water which results in a structural transformation. TGA results show that at temperature ranges between 200 and 240 °C the water molecules are completely removed. The PXRD pattern of the compound dehydrated at this temperature range indicates the MOF material transformed to a new structure after removal of water. The dehydrated compound can recover to the hydrated structure when exposed to the moist air. A reversible single crystal to single crystal transformation between the hydrated compound and the dehydrated compound occurs. Variable temperature single crystal analysis solved both hydrated and dehydrated structures. The structure analysis revealed the structural transformation between the hydrated and the dehydrated structures was caused by the changes of the weakly coordinated sulfonate groups. The removal of the coordinated water molecules resulted in unsaturated metal sites, which attracted the sulfonate oxygen strongly. The newly formed coordination bonds are considered less stable than the bonds between water and Cu. When water contacts the dehydrated compound, the sulfonate-copper bond breaks easily and the structure recovers to the hydrated one reversibly.

## 7.5 References

1. M. Eddaoudi, J. Kim, N. Rosi, D. Vodak, J. Wachter, M. O'Keeffe and O. M. Yaghi, *Science*, 2002, **295**, 469-472.
2. D. N. Dybtsev, M. P. Yutkin, E. V. Peresypkina, A. V. Virovets, C. Serre, G. Férey and V. P. Fedin, *Inorg. Chem.*, 2007, **46**, 6843-6845.
3. R. Banerjee, A. Phan, B. Wang, C. Knobler, H. Furukawa, M. O'Keeffe and O. M. Yaghi, *Science*, 2008, **319**, 939-943.
4. K. Koh, A. G. Wong-Foy and A. J. Matzger, *J. Am. Chem. Soc.*, 2009, **131**, 4184-4185.
5. H. K. Chae, D. Y. Siberio-Perez, J. Kim, Y. Go, M. Eddaoudi, A. J. Matzger, M. O'Keeffe and O. M. Yaghi, *Nature*, 2004, **427**, 523-527.
6. D. Yuan, D. Zhao, D. Sun and H.-C. Zhou, *Angew. Chem. Int. Ed.*, 2010, **49**, 5357-5361.
7. L. Ma, J. M. Falkowski, C. Abney and W. Lin, *Nature Chem.*, 2010, **2**, 838-846.
8. K.-J. Wei, Y.-S. Xie, J. Ni, M. Zhang and Q.-L. Liu, *Cryst. Growth Des.*, 2006, **6**, 1341-1350.
9. F. Luo, S. R. Batten, Y. Che and J.-M. Zheng, *Chem.-Eur. J.*, 2007, **13**, 4948-4955.
10. P. D. C. Dietzel, P. A. Georgiev, J. Eckert, R. Blom, T. Strassle and T. Unruh, *Chem. Commun.*, 2010, **46**, 4962-4964.
11. J.-R. Li, R. J. Kuppler and H.-C. Zhou, *Chem. Soc. Rev.*, 2009, **38**, 1477-1504.
12. B. Chen, C. Liang, J. Yang, D. S. Contreras, Y. L. Clancy, E. B. Lobkovsky, O. M. Yaghi and S. Dai, *Angew. Chem. Int. Ed.*, 2006, **45**, 1390-1393.
13. H. Guo, G. Zhu, I. J. Hewitt and S. Qiu, *J. Am. Chem. Soc.*, 2009, **131**, 1646-1647.
14. R. E. Morris and P. S. Wheatley, *Angew. Chem. Int. Ed.*, 2008, **47**, 4966-4981.
15. S. Ma and H.-C. Zhou, *Chem. Commun.*, 2010, **46**, 44-53.
16. B. Xiao, P. S. Wheatley, X. Zhao, A. J. Fletcher, S. Fox, A. G. Rossi, I. L. Megson, S. Bordiga, L. Regli, K. M. Thomas and R. E. Morris, *J. Am. Chem. Soc.*, 2007, **129**, 1203-1209.
17. P. Horcajada, R. Gref, T. Baati, P. K. Allan, G. Maurin, P. Couvreur, G. Férey, R. E. Morris and C. Serre, *Chem. Rev.*, 2011, **112**, 1232-1268.
18. P. Horcajada, C. Serre, M. Vallet-Regí, M. Sebban, F. Taulelle and G. Férey, *Angew. Chem. Int. Ed.*, 2006, **45**, 5974-5978.
19. J. Lee, O. K. Farha, J. Roberts, K. A. Scheidt, S. T. Nguyen and J. T. Hupp, *Chem. Soc. Rev.*, 2009, **38**, 1450-1459.
20. L. Ma, C. Abney and W. Lin, *Chem. Soc. Rev.*, 2009, **38**, 1248-1256.
21. H. Furukawa, K. E. Cordova, M. O'Keeffe and O. M. Yaghi, *Science*, 2013, **341**.
22. G. Férey and C. Serre, *Chem. Soc. Rev.*, 2009, **38**, 1380-1399.
23. S. Kitagawa and K. Uemura, *Chem. Soc. Rev.*, 2005, **34**, 109-119.
24. K. Uemura, R. Matsuda and S. Kitagawa, *J. Solid State Chem.*, 2005, **178**, 2420-2429.
25. E. J. Cussen, J. B. Claridge, M. J. Rosseinsky and C. J. Kepert, *J. Am. Chem. Soc.*, 2002, **124**, 9574-9581.
26. K. Uemura, S. Kitagawa, M. Kondo, K. Fukui, R. Kitaura, H.-C. Chang and T. Mizutani, *Chem.-Eur. J.*, 2002, **8**, 3586-3600.
27. T. Loiseau, C. Serre, C. Huguenard, G. Fink, F. Taulelle, M. Henry, T. Bataille and G. Férey, *Chem.-Eur. J.*, 2004, **10**, 1373-1382.
28. B. Rather and M. J. Zaworotko, *Chem. Commun.*, 2003, 830-831.
29. Z. Su, M. Chen, T.-a. Okamura, M.-S. Chen, S.-S. Chen and W.-Y. Sun, *Inorg. Chem.*, 2011, **50**, 985-991.
30. X. Zhao, B. Xiao, A. J. Fletcher, K. M. Thomas, D. Bradshaw and M. J. Rosseinsky, *Science*, 2004, **306**, 1012-1015.
31. Y. Qi, F. Luo, Y. Che and J. Zheng, *Cryst. Growth Des.*, 2007, **8**, 606-611.
32. T. K. Maji, G. Mostafa, R. Matsuda and S. Kitagawa, *J. Am. Chem. Soc.*, 2005, **127**, 17152-17153.
33. C.-D. Wu and W. Lin, *Angew. Chem. Int. Ed.*, 2005, **44**, 1958-1961.
34. H. J. Choi and M. P. Suh, *J. Am. Chem. Soc.*, 2004, **126**, 15844-15851.

35. D. J. Tranchemontagne, J. L. Mendoza-Cortes, M. O'Keeffe and O. M. Yaghi, *Chem. Soc. Rev.*, 2009, **38**, 1257-1283.
36. B. Xiao, P. J. Byrne, P. S. Wheatley, D. S. Wragg, X. Zhao, A. J. Fletcher, K. M. Thomas, L. Peters, J. S. O. Evans, J. E. Warren, W. Zhou and R. E. Morris, *Nature Chem.*, 2009, **1**, 289-294.
37. J. C. C. Chen and I. J. B. Lin, *Organometallics*, 2000, **19**, 5113-5121.
38. M. Nandi, J. Jin and T. V. RajanBabu, *J. Am. Chem. Soc.*, 1999, **121**, 9899-9900.
39. A. Bader and E. Lindner, *Coord. Chem. Rev.*, 1991, **108**, 27-110.
40. P. K. Allan, B. Xiao, S. J. Teat, J. W. Knight and R. E. Morris, *J. Am. Chem. Soc.*, 2010, **132**, 3605-3611.
41. P. S. Wheatley, A. R. Butler, M. S. Crane, S. Fox, B. Xiao, A. G. Rossi, I. L. Megson and R. E. Morris, *J. Am. Chem. Soc.*, 2005, **128**, 502-509.
42. R. F. Furchgott and J. V. Zawadzki, *Nature*, 1980, **288**, 373-376.
43. R. M. J. Palmer, A. G. Ferrige and S. Moncada, *Nature*, 1987, **327**, 524-526.
44. A. P. Côté and G. K. H. Shimizu, *Coord. Chem. Rev.*, 2003, **245**, 49-64.
45. G. K. H. Shimizu, G. D. Enright, C. I. Ratcliffe, K. F. Preston, J. L. Reid and J. A. Ripmeester, *Chem. Commun.*, 1999, 1485-1486.
46. Sheldrick, G. M., University of Gottingen, Germany, 1997.
47. H. A. Jahn and E. Teller, *Proceedings of the Royal Society of London. Series A - Mathematical and Physical Sciences*, 1937, **161**, 220-235.
48. W. D. Harrison, D. M. Kennedy, M. Power, R. Sheahan and B. J. Hathaway, *J. Chem. Soc., Dalton Trans.*, 1981, 1556-1564.

# Chapter 8 Conclusions and Future Work

## 8.1 Conclusions

The overall aim of this thesis was to synthesize crystalline microporous materials through several new synthetic routes which are different from the conventional hydrothermal route or trial-and-error method. In Chapter 4, 5 and 6, top-down treatment methods, ionic liquid assisted routes and ionothermal synthesis were applied for synthesizing zeolites and zeolite analogues, respectively. In Chapter 7, a MOF material was synthesized targeting the hemilabile property by carefully selecting the ligands.

Two Ge-zeolites, **IWW** and **ITH**, were selected for the top-down treatments.<sup>1</sup> The experiments showed that the chemical compositions and the Ge distributions in the parental zeolites had crucial effects on the structure of the products. A suitable chemical composition of the pillar units was a key parameter for the successful disassembly process. The **IWW** zeolite with a *D4R* composition of [6Ge, 2Si] was fully pulled apart into layer structures but the **IWW** zeolite with a *D4R* composition of [4Ge, 4Si] was only disassembled to a connected structure after acidic treatment. For **ITH** zeolites, the experiments indicated that if the framework contained some pure silica or high silica *D4Rs*, the zeolites were hydrolytically stable to acidic treatment or partially hydrolysed. **ITH**-zeolites with only [4Si, 4Ge] *D4Rs* in the framework can be fully separated. Meanwhile, the Ge distribution also affected the structures of the products from the top-down treatment. For **IWW** zeolites, the Ge occupied the *D4R* sites exclusively. The layer structure kept intact after hydrolysis. Attempts at reassembling the hydrolysis products to the 3D zeolitic structures led to the recovery of the **IWW** structure. However, for the **ITH** zeolites, the Ge atoms locate in both the layer and the *D4R* sites. The **ITH** zeolites with low Si/Ge ratio can be successfully separated but the layer structure was unstable to harsh chemical treatment conditions, which obstructed the following reassembly treatment.

In Chapter 7, a copper MOF material was synthesized using 2-sulfoterephthalic acid (STP) and 4, 4'-bipyridine (Bpy) as the ligands. The STP contains one sulfonate and two carboxylate groups. The variable temperature single crystal structure analysis revealed that the MOF material obtained was flexible and can reversibly transform to a

new structure upon dehydration. The weakly bonded sulfonate group changed its coordination mode upon dehydration, leading to the structural transformation. Meanwhile, the carboxylate groups were strong enough to retain crystallinity and the framework. The successful synthesis of such a hemilabile MOF material proved that the strategy of targeted synthesis of the flexible MOFs with ligands containing both weaker and stronger coordinating groups could be generalized to other compounds.

In these two chapters, both the Ge-zeolites and the sulfonate-containing MOF show structural flexibility and thus are used to induce targeted structural transformations. Both of the designable compounds have a common feature, which is that they contain weaker bonds in their structures: the Ge-zeolites contain Ge-O bonds that are less hydrolytically stable than a Si-O bond; for the sulfonate-containing MOF, the bonding strengths of the sulfonate-metal bonds are weaker than the carboxylate-metal bonds. Transformations are implemented by exploiting these weaker bonds in the structures. It is noted that to achieve a designable transformation, the weaknesses should be in the right place. The differences in bonding strength make it possible to exploit the weakness while keeping the rest of the structure intact. The work in these two chapters inspire a new way of tailoring crystalline microporous materials.

In Chapter 5, an ionic liquid assisted strategy for the synthesis of zeolites was described. A **TON** zeolite was synthesized using [Emim]Br as the SDA. The synthetic conditions were investigated and the products were characterised. The results indicated that the presence of the ionic liquid was important for the crystallization of the zeolite and played the role of SDA. The ILA strategy exhibits many advantages such as the readily recyclable SDA; the high yield of the zeolites and the minor production of waste water. This ILA strategy is thus considered as a new “green chemistry” synthetic route for zeolites.

In Chapter 6, a new ionic liquid, 1-(2-hydroxyl-ethyl)-3-methylimidazolium chloride ([HOEmim]Cl), was synthesized and used as an SDA and solvent for the ionothermal synthesis of aluminophosphates. The product was a triclinic deformed **CHA** type framework. Moreover, large single crystals were obtained at higher temperature, which may be because of the increase of the mass transfer of the crystal growth. The structural analysis indicated the [HOEmim] cations were decomposed to 1, 3-dimethyl imidazolium cations as the SDA for **CHA** framework.

In Chapter 5 and 6, utilizing ionic liquids for the syntheses of microporous materials was investigated. To conclude, ionic liquids are suitable SDAs for the synthesis of both zeolites and zeolite analogues. The synthetic flexibility of ionic liquids indicates the possibility of synthesizing zeolites and zeolite analogues with different framework structures. For instance, in the synthesis of aluminophosphates, the ionic liquids can simultaneously play the role of the solvent and this is known as ionothermal synthesis strategy, however, for the synthesis of zeolites using common ionic liquids, a certain content of water is still required. Although a true ionothermal synthesis of zeolites was not achieved in Chapter 5, utilizing ionic liquids to assist the synthesis of zeolites still has some advantages, especially for environmental benefit.

## ***8.2 Future work***

Compared with the conventional hydrothermal and trial-and-error synthetic routes, the experiments in this thesis have shown that novel non-hydrothermal synthesis and targeted synthesis possess unique features. Based on the obtained results and the conclusions, some investigations are now in progress or expected.

The main aim of the top-down treatment is to synthesize zeolite materials with controlled structures and pore sizes. For the **IWW** zeolites, the layer structure obtained from the disassembly process tends to recover to the original **IWW** structure after reassembly by silane compounds. It is still interesting if other units such as B and Ti can intercalate into the layers and create new structures. Meanwhile, for the disassembled **ITH** layers which are less hydrolytically stable, mild and suitable reassembling conditions are needed to retain the layers. Moreover, according to our proposal, the Al-**IWW** obtained from the realumination should possess different Al distribution from the hydrothermally synthesized one.<sup>2</sup> The catalytic performance of the former is worthy of further investigation.

The ionic liquid assisted route is considered as a “green chemistry” strategy for zeolite preparation. Currently only the synthesis of **TON** zeolite using [Emim]<sup>+</sup> cations as the SDA was successful. Further work would be using other cations of ionic liquids as the SDAs for the synthesis of other zeolite frameworks.

Other ionic liquids with functionalized groups will be used in ionothermal synthesis to investigate if other zeolite analogues can be synthesized. Mild synthetic conditions are required to keep them stable during the synthesis.

The experiments have shown that the hemilabile MOFs can be successfully synthesized through the strategy of selecting the ligands with both stronger and weaker coordinating groups. The next work is to generalize the strategy to other ligands and metals to prepare other hemilabile MOFs. Meanwhile, considering the removal of the coordinated water molecules resulted in the unsaturated metal sites and may selectively adsorb coordinating gas such as NO, the gas sorption properties of the synthesized Cu-STP-Bpy are under investigation.

### ***8.3 References***

1. W. J. Roth, P. Nachtigall, R. E. Morris, P. S. Wheatley, V. R. Seymour, S. E. Ashbrook, P. Chlubná, L. Grajciar, M. Položij, A. Zukal, O. Shvets and J. Čejka, *Nature Chem.*, 2013, **5**, 628-633.
2. A. Corma, F. J. Llopis, C. Martínez, G. Sastre and S. Valencia, *J. Catal.*, 2009, **268**, 9-17.

## APPENDIX

The crystallographic information files (CIFs) of IWW-2, IWW-6, SIZ-10f, Cu-SIP-Bpy-H<sub>2</sub>O and Cu-SIP-Bpy are attached on data CD.

### *Appendix I Crystallographic Information of SIZ-10f*

Table I-1 Crystal data and structure refinement for SIZ-10f

Identification code	SIZ-10f	
Empirical formula	C10 Al6 F2 N4 O24 P6	
Formula weight	945.84	
Temperature	100(2) K	
Wavelength	0.77490 Å	
Crystal system	Triclinic	
Space group	P -1	
Unit cell dimensions	$a = 9.1025(13) \text{ \AA}$	$\alpha = 76.283(2)^\circ$
	$b = 9.1938(13) \text{ \AA}$	$\beta = 87.094(2)^\circ$
	$c = 9.2943(13) \text{ \AA}$	$\gamma = 89.550(2)^\circ$
Volume	$754.65(18) \text{ \AA}^3$	
Z	1	
Density (calculated)	2.081 Mg/m <sup>3</sup>	
Absorption coefficient	0.651 mm <sup>-1</sup>	
F (000)	466	
Crystal size	0.058 × 0.023 × 0.012 mm <sup>3</sup>	
Theta range for data collection	3.06 to 34.93 °	
Index ranges	-13 ≤ h ≤ 13, -13 ≤ k ≤ 13, -13 ≤ l ≤ 13	
Reflections collected	11481	
Independent reflections	4718 [R (int) = 0.1797]	
Completeness to theta = 32.50°	98.6 %	
Refinement method	Full-matrix least-squares on F <sup>2</sup>	
Data / restraints / parameters	4718 / 0 / 235	
Goodness-of-fit on F <sup>2</sup>	1.005	
Final R indices [I > 2σ(I)]	R <sub>1</sub> = 0.0730, wR <sub>2</sub> = 0.2012	
R indices (all data)	R <sub>1</sub> = 0.0783, wR <sub>2</sub> = 0.2079	
Largest diff. peak and hole	2.078 and -1.149 e.Å <sup>-3</sup>	

Table I-2 Atomic coordinates ( $\times 10^4$ ) and equivalent isotropic displacement parameters ( $\text{\AA}^2 \times 10^3$ ) for SIZ-10f. U(eq) is defined as one third of the trace of the orthogonalized  $U^{ij}$  tensor.

	x	y	z	U(eq)
N(1)	1115(5)	593(5)	8044(6)	42(1)
N(2)	1176(7)	2171(7)	9418(7)	59(2)
C(5)	636(7)	-167(7)	6959(8)	51(2)
C(3)	2403(8)	1184(8)	9759(9)	55(2)
C(2)	2319(9)	258(8)	8835(8)	55(2)
C(1)	421(8)	1745(8)	8386(7)	49(1)
C(4)	747(10)	3421(11)	10065(10)	76(3)
P(1)	1873(1)	3807(1)	4041(1)	5(1)
P(3)	3813(1)	6273(1)	8242(1)	5(1)
Al(1)	4346(1)	1328(1)	4131(1)	6(1)
Al(2)	3827(1)	6095(1)	1577(1)	6(1)
Al(3)	1592(1)	6254(1)	5750(1)	6(1)
P(2)	3541(1)	8321(1)	3536(1)	6(1)
F(1)	3939(2)	-153(2)	5843(2)	7(1)
O(2)	3493(2)	18(2)	3117(2)	7(1)
O(3)	4988(2)	7422(2)	7623(2)	7(1)
O(4)	4673(2)	7664(2)	4654(2)	8(1)
O(5)	2464(2)	6429(2)	7311(2)	8(1)
O(6)	3239(3)	6462(2)	9772(2)	9(1)
O(7)	3828(3)	7790(2)	2090(2)	8(1)
O(8)	4422(2)	4684(2)	8402(2)	9(1)
O(9)	1952(3)	4514(2)	5377(2)	10(1)
O(10)	2610(2)	2308(2)	4324(2)	8(1)
O(11)	258(2)	3609(2)	3757(3)	9(1)
O(12)	2537(3)	4895(2)	2656(2)	10(1)
O(1)	1998(2)	7694(2)	4184(2)	8(1)

Table I-3 Bond lengths [Å] and angles [°] for SIZ-10f

---

N(1)-C(1)	1.324(8)
N(1)-C(2)	1.344(8)
N(1)-C(5)	1.441(9)
N(2)-C(1)	1.339(9)
N(2)-C(3)	1.433(9)
N(2)-C(4)	1.460(9)
C(3)-C(2)	1.350(10)
P(1)-O(10)	1.500(2)
P(1)-O(11)	1.527(2)
P(1)-O(12)	1.531(2)
P(1)-O(9)	1.537(2)
P(3)-O(3)	1.502(2)
P(3)-O(5)	1.524(2)
P(3)-O(8)	1.535(2)
P(3)-O(6)	1.538(2)
Al(1)-O(10)	1.835(2)
Al(1)-O(3)#1	1.835(2)
Al(1)-F(1)	1.8555(19)
Al(1)-O(4)#1	1.882(2)
Al(1)-O(2)	1.890(2)
Al(1)-F(1)#2	1.889(2)
Al(1)-Al(1)#2	2.8750(17)
Al(2)-O(12)	1.725(2)
Al(2)-O(7)	1.735(2)
Al(2)-O(6)#3	1.742(2)
Al(2)-O(8)#1	1.742(2)
Al(3)-O(5)	1.729(2)
Al(3)-O(11)#4	1.734(2)
Al(3)-O(9)	1.741(2)
Al(3)-O(1)	1.745(2)
P(2)-O(2)#5	1.517(2)
P(2)-O(4)	1.519(2)
P(2)-O(7)	1.544(2)
P(2)-O(1)	1.559(2)
F(1)-Al(1)#2	1.889(2)
O(2)-P(2)#6	1.517(2)
O(3)-Al(1)#1	1.835(2)
O(4)-Al(1)#1	1.882(2)
O(6)-Al(2)#7	1.742(2)
O(8)-Al(2)#1	1.742(2)
O(11)-Al(3)#4	1.734(2)
C(1)-N(1)-C(2)	110.3(6)
C(1)-N(1)-C(5)	124.0(5)
C(2)-N(1)-C(5)	125.7(5)
C(1)-N(2)-C(3)	108.3(6)
C(1)-N(2)-C(4)	123.6(7)
C(3)-N(2)-C(4)	128.1(7)
C(2)-C(3)-N(2)	104.4(6)
N(1)-C(2)-C(3)	109.2(6)
N(1)-C(1)-N(2)	107.8(6)
O(10)-P(1)-O(11)	108.91(13)
O(10)-P(1)-O(12)	112.14(13)
O(11)-P(1)-O(12)	106.46(13)
O(10)-P(1)-O(9)	111.40(13)

O(11)-P(1)-O(9)	108.58(13)
O(12)-P(1)-O(9)	109.17(13)
O(3)-P(3)-O(5)	113.68(13)
O(3)-P(3)-O(8)	110.72(13)
O(5)-P(3)-O(8)	108.28(12)
O(3)-P(3)-O(6)	109.50(12)
O(5)-P(3)-O(6)	105.32(12)
O(8)-P(3)-O(6)	109.14(12)
O(10)-Al(1)-O(3)#1	96.61(10)
O(10)-Al(1)-F(1)	93.20(9)
O(3)#1-Al(1)-F(1)	169.99(10)
O(10)-Al(1)-O(4)#1	93.01(10)
O(3)#1-Al(1)-O(4)#1	95.18(10)
F(1)-Al(1)-O(4)#1	86.25(9)
O(10)-Al(1)-O(2)	93.31(10)
O(3)#1-Al(1)-O(2)	91.46(10)
F(1)-Al(1)-O(2)	85.99(9)
O(4)#1-Al(1)-O(2)	170.26(10)
O(10)-Al(1)-F(1)#2	172.89(10)
O(3)#1-Al(1)-F(1)#2	90.50(9)
F(1)-Al(1)-F(1)#2	79.70(9)
O(4)#1-Al(1)-F(1)#2	86.32(9)
O(2)-Al(1)-F(1)#2	86.50(9)
O(10)-Al(1)-Al(1)#2	133.48(9)
O(3)#1-Al(1)-Al(1)#2	129.88(9)
F(1)-Al(1)-Al(1)#2	40.28(6)
O(4)#1-Al(1)-Al(1)#2	85.16(8)
O(2)-Al(1)-Al(1)#2	85.11(8)
F(1)#2-Al(1)-Al(1)#2	39.42(6)
O(12)-Al(2)-O(7)	110.32(11)
O(12)-Al(2)-O(6)#3	106.08(12)
O(7)-Al(2)-O(6)#3	106.86(11)
O(12)-Al(2)-O(8)#1	112.82(11)
O(7)-Al(2)-O(8)#1	111.79(11)
O(6)#3-Al(2)-O(8)#1	108.62(11)
O(5)-Al(3)-O(11)#4	103.46(11)
O(5)-Al(3)-O(9)	110.67(11)
O(11)#4-Al(3)-O(9)	110.10(12)
O(5)-Al(3)-O(1)	114.02(12)
O(11)#4-Al(3)-O(1)	107.42(11)
O(9)-Al(3)-O(1)	110.83(11)
O(2)#5-P(2)-O(4)	114.67(12)
O(2)#5-P(2)-O(7)	107.41(12)
O(4)-P(2)-O(7)	110.52(12)
O(2)#5-P(2)-O(1)	109.41(12)
O(4)-P(2)-O(1)	108.27(12)
O(7)-P(2)-O(1)	106.22(13)
Al(1)-F(1)-Al(1)#2	100.30(9)
P(2)#6-O(2)-Al(1)	126.57(13)
P(3)-O(3)-Al(1)#1	141.04(15)
P(2)-O(4)-Al(1)#1	126.73(13)
P(3)-O(5)-Al(3)	151.51(15)
P(3)-O(6)-Al(2)#7	138.28(15)
P(2)-O(7)-Al(2)	136.50(14)
P(3)-O(8)-Al(2)#1	135.04(15)

P(1)-O(9)-Al(3)	136.82(15)
P(1)-O(10)-Al(1)	144.82(15)
P(1)-O(11)-Al(3)#4	150.04(16)
P(1)-O(12)-Al(2)	157.26(17)
P(2)-O(1)-Al(3)	127.91(14)

Symmetry transformations used to generate equivalent atoms:

#1 -x+1,-y+1,-z+1 #2 -x+1,-y,-z+1 #3 x,y,z-1  
 #4 -x,-y+1,-z+1 #5 x,y+1,z #6 x,y-1,z #7 x,y,z+1

Table I-4 Anisotropic displacement parameters ( $\text{\AA}^2 \times 10^3$ ) for SIZ-10f. The anisotropic displacement factor exponent takes the form:  $-2\pi^2 [ h^2 a^{*2} U^{11} + \dots + 2 h k a^* b^* U^{12} ]$

	$U^{11}$	$U^{22}$	$U^{33}$	$U^{23}$	$U^{13}$	$U^{12}$
N(1)	31(2)	28(2)	57(3)	7(2)	4(2)	7(2)
N(2)	56(4)	46(3)	72(4)	-13(3)	21(3)	0(3)
C(5)	41(3)	37(3)	69(4)	-5(3)	7(3)	13(2)
C(3)	41(3)	54(4)	68(4)	-9(3)	-11(3)	-4(3)
C(2)	65(4)	42(3)	56(4)	-8(3)	-20(3)	24(3)
C(1)	55(4)	51(3)	44(3)	-17(3)	-10(3)	9(3)
C(4)	80(6)	88(6)	79(5)	-61(5)	30(4)	-37(5)
P(1)	7(1)	2(1)	9(1)	-3(1)	-1(1)	1(1)
P(3)	7(1)	2(1)	7(1)	-3(1)	-2(1)	1(1)
Al(1)	8(1)	2(1)	8(1)	-3(1)	-2(1)	1(1)
Al(2)	8(1)	3(1)	8(1)	-3(1)	-2(1)	1(1)
Al(3)	7(1)	3(1)	8(1)	-3(1)	-1(1)	1(1)
P(2)	9(1)	2(1)	8(1)	-3(1)	-2(1)	0(1)
F(1)	8(1)	3(1)	10(1)	-2(1)	0(1)	1(1)
O(2)	10(1)	3(1)	10(1)	-4(1)	-4(1)	1(1)
O(3)	9(1)	3(1)	11(1)	-2(1)	-1(1)	-1(1)
O(4)	10(1)	4(1)	10(1)	-3(1)	-4(1)	2(1)
O(5)	8(1)	9(1)	9(1)	-5(1)	-4(1)	2(1)
O(6)	12(1)	9(1)	7(1)	-5(1)	-3(1)	2(1)
O(7)	14(1)	5(1)	8(1)	-4(1)	-1(1)	1(1)
O(8)	9(1)	4(1)	15(1)	-4(1)	-2(1)	2(1)
O(9)	16(1)	6(1)	11(1)	-5(1)	-2(1)	2(1)
O(10)	9(1)	2(1)	14(1)	-2(1)	-2(1)	2(1)
O(11)	6(1)	9(1)	14(1)	-3(1)	-2(1)	0(1)
O(12)	12(1)	6(1)	12(1)	-3(1)	1(1)	-1(1)
O(1)	10(1)	4(1)	11(1)	-2(1)	-2(1)	0(1)

## *Appendix II Crystallographic Information of Cu-STP-Bpy-H<sub>2</sub>O*

Table II-1 Crystal data and structure refinement for Cu-STP-Bpy-H<sub>2</sub>O

Identification code	Cu-STP-Bpy-H <sub>2</sub> O	
Empirical formula	C <sub>26</sub> H <sub>22</sub> Cu <sub>3</sub> N <sub>2</sub> O <sub>18</sub> S <sub>2</sub>	
Formula weight	905.20	
Temperature	150(2) K	
Wavelength	0.77490 Å	
Crystal system	Monoclinic	
Space group	<i>P</i> 2 <sub>1</sub> / <i>c</i>	
Unit cell dimensions	<i>a</i> = 11.017(5) Å	<i>α</i> = 90.000(5) °
	<i>b</i> = 11.814(5) Å	<i>β</i> = 109.701(5) °
	<i>c</i> = 12.135(5) Å	<i>γ</i> = 90.000(5) °
Volume	1487.0(11) Å <sup>3</sup>	
Z	2	
Density (calculated)	2.022 Mg/m <sup>3</sup>	
Absorption coefficient	2.890 mm <sup>-1</sup>	
F (000)	910	
Crystal size	0.12 × 0.09 × 0.03 mm <sup>3</sup>	
Theta range for data collection	2.85 to 34.65 °	
Index ranges	-16 ≤ <i>h</i> ≤ 15, -16 ≤ <i>k</i> ≤ 17, -17 ≤ <i>l</i> ≤ 17	
Reflections collected	21375	
Independent reflections	4736 [ <i>R</i> (int) = 0.0578]	
Completeness to theta = 34.65°	96.2 %	
Absorption correction	Semi-empirical from equivalents	
Max. and min. transmission	1.000 and 0.750	
Refinement method	Full-matrix least-squares on <i>F</i> <sup>2</sup>	
Data / restraints / parameters	4736 / 6 / 244	
Goodness-of-fit on <i>F</i> <sup>2</sup>	1.023	
Final <i>R</i> indices [ <i>I</i> > 2σ( <i>I</i> )]	<i>R</i> <sub>1</sub> = 0.0327, <i>wR</i> <sub>2</sub> = 0.0904	
<i>R</i> indices (all data)	<i>R</i> <sub>1</sub> = 0.0378, <i>wR</i> <sub>2</sub> = 0.0938	
Largest diff. peak and hole	0.625 and -0.787 e.Å <sup>-3</sup>	

Table II-2 Atomic coordinates ( $\times 10^4$ ) and equivalent isotropic displacement parameters ( $\text{\AA}^2 \times 10^3$ ) for Cu-STP-Bpy- $\text{H}_2\text{O}$ .  $U(\text{eq})$  is defined as one third of the trace of the orthogonalized  $U^{ij}$  tensor.

	x	y	z	U(eq)
Cu(1)	6819(1)	8658(1)	4949(1)	12(1)
Cu(2)	15000	10000	10000	10(1)
S(1)	13802(1)	9232(1)	7144(1)	12(1)
N(1)	13231(2)	9962(1)	10057(1)	12(1)
O(1W)	7037(1)	7594(1)	3773(1)	21(1)
O(2W)	6507(1)	9571(1)	6207(1)	16(1)
O(3)	8663(1)	8674(1)	5738(1)	17(1)
O(4)	8248(1)	7743(1)	7174(1)	19(1)
O(5)	14923(1)	6539(1)	9192(1)	14(1)
O(6)	15137(1)	8281(1)	9891(1)	14(1)
O(7)	14241(1)	10138(1)	8002(1)	15(1)
O(8)	14829(1)	8436(1)	7171(1)	19(1)
O(9)	13119(1)	9665(1)	5976(1)	16(1)
C(1)	9003(2)	8171(2)	6729(2)	15(1)
C(2)	10439(2)	8051(2)	7357(2)	13(1)
C(3)	10859(2)	7354(2)	8340(2)	16(1)
C(4)	11344(2)	8587(2)	6962(2)	13(1)
C(5)	12164(2)	7168(2)	8912(2)	15(1)
C(6)	12657(2)	8438(2)	7568(2)	12(1)
C(7)	13079(2)	7717(2)	8541(2)	12(1)
C(8)	14480(2)	7525(2)	9256(2)	11(1)
C(9)	12313(2)	10527(2)	9226(2)	16(1)
C(10)	12895(2)	9427(2)	10887(2)	19(1)
C(11)	11650(2)	9439(2)	10905(2)	21(1)
C(12)	11041(2)	10539(2)	9171(2)	17(1)
C(13)	10684(2)	9996(2)	10021(2)	13(1)

Table II-3 Bond lengths [ $\text{\AA}$ ] and angles [ $^\circ$ ] for Cu-STP-Bpy- $\text{H}_2\text{O}$

Cu(1)-O(3)	1.9321(17)
Cu(1)-O(1W)	1.9758(16)
Cu(1)-O(2W)	1.9909(16)
Cu(1)-O(5)#1	1.9914(16)
Cu(1)-O(9)#2	2.2895(16)
Cu(2)-N(1)#3	1.9744(18)
Cu(2)-N(1)	1.9744(18)
Cu(2)-O(6)	2.0435(16)
Cu(2)-O(6)#3	2.0435(16)
Cu(2)-O(7)	2.2886(17)
Cu(2)-O(7)#3	2.2886(17)
S(1)-O(9)	1.4552(15)
S(1)-O(7)	1.4570(15)
S(1)-O(8)	1.4636(16)
S(1)-C(6)	1.7815(19)
N(1)-C(9)	1.341(2)
N(1)-C(10)	1.342(2)
O(1W)-H(1A)	0.920(17)
O(1W)-H(1B)	0.912(17)
O(2W)-H(2A)	0.917(16)
O(2W)-H(2B)	0.932(16)

O(3)-C(1)	1.278(2)
O(4)-C(1)	1.242(2)
O(5)-C(8)	1.275(2)
O(5)-Cu(1)#4	1.9914(16)
O(6)-C(8)	1.241(2)
O(9)-Cu(1)#2	2.2895(16)
C(1)-C(2)	1.513(3)
C(2)-C(3)	1.395(3)
C(2)-C(4)	1.395(3)
C(3)-C(5)	1.387(3)
C(3)-H(3)	0.9500
C(4)-C(6)	1.395(3)
C(4)-H(4)	0.9500
C(5)-C(7)	1.395(3)
C(5)-H(5)	0.9500
C(6)-C(7)	1.402(3)
C(7)-C(8)	1.511(2)
C(9)-C(12)	1.380(3)
C(9)-H(9)	0.9500
C(10)-C(11)	1.380(3)
C(10)-H(10)	0.9500
C(11)-C(13)	1.395(3)
C(11)-H(11)	0.9500
C(12)-C(13)	1.380(3)
C(12)-H(12)	0.9500
C(13)-C(13)#5	1.491(4)

O(3)-Cu(1)-O(1W)	90.06(7)
O(3)-Cu(1)-O(2W)	92.21(7)
O(1W)-Cu(1)-O(2W)	172.98(6)
O(3)-Cu(1)-O(5)#1	173.60(6)
O(1W)-Cu(1)-O(5)#1	87.53(6)
O(2W)-Cu(1)-O(5)#1	89.52(6)
O(3)-Cu(1)-O(9)#2	91.95(6)
O(1W)-Cu(1)-O(9)#2	99.54(7)
O(2W)-Cu(1)-O(9)#2	87.02(6)
O(5)#1-Cu(1)-O(9)#2	94.29(6)
N(1)#3-Cu(2)-N(1)	180.000(1)
N(1)#3-Cu(2)-O(6)	85.69(6)
N(1)-Cu(2)-O(6)	94.32(6)
N(1)#3-Cu(2)-O(6)#3	94.31(6)
N(1)-Cu(2)-O(6)#3	85.68(6)
O(6)-Cu(2)-O(6)#3	180.000(1)
N(1)#3-Cu(2)-O(7)	88.48(6)
N(1)-Cu(2)-O(7)	91.52(6)
O(6)-Cu(2)-O(7)	90.62(5)
O(6)#3-Cu(2)-O(7)	89.38(5)
N(1)#3-Cu(2)-O(7)#3	91.52(6)
N(1)-Cu(2)-O(7)#3	88.48(6)
O(6)-Cu(2)-O(7)#3	89.38(5)
O(6)#3-Cu(2)-O(7)#3	90.62(5)
O(7)-Cu(2)-O(7)#3	180.000(1)
O(9)-S(1)-O(7)	112.10(9)
O(9)-S(1)-O(8)	112.92(9)
O(7)-S(1)-O(8)	112.84(9)

O(9)-S(1)-C(6)	106.44(9)
O(7)-S(1)-C(6)	106.08(9)
O(8)-S(1)-C(6)	105.79(9)
C(9)-N(1)-C(10)	118.07(16)
C(9)-N(1)-Cu(2)	117.75(13)
C(10)-N(1)-Cu(2)	124.17(13)
Cu(1)-O(1W)-H(1A)	113.5(18)
Cu(1)-O(1W)-H(1B)	130.1(19)
H(1A)-O(1W)-H(1B)	110(2)
Cu(1)-O(2W)-H(2A)	105.8(18)
Cu(1)-O(2W)-H(2B)	117.6(18)
H(2A)-O(2W)-H(2B)	108(2)
C(1)-O(3)-Cu(1)	112.81(13)
C(8)-O(5)-Cu(1)#4	116.20(12)
C(8)-O(6)-Cu(2)	135.65(12)
S(1)-O(7)-Cu(2)	128.29(9)
S(1)-O(9)-Cu(1)#2	133.68(9)
O(4)-C(1)-O(3)	124.79(18)
O(4)-C(1)-C(2)	118.86(17)
O(3)-C(1)-C(2)	116.28(17)
C(3)-C(2)-C(4)	119.47(17)
C(3)-C(2)-C(1)	118.40(17)
C(4)-C(2)-C(1)	122.10(17)
C(5)-C(3)-C(2)	120.70(18)
C(5)-C(3)-H(3)	119.7
C(2)-C(3)-H(3)	119.7
C(6)-C(4)-C(2)	119.74(17)
C(6)-C(4)-H(4)	120.1
C(2)-C(4)-H(4)	120.1
C(3)-C(5)-C(7)	120.38(18)
C(3)-C(5)-H(5)	119.8
C(7)-C(5)-H(5)	119.8
C(4)-C(6)-C(7)	120.74(17)
C(4)-C(6)-S(1)	119.38(14)
C(7)-C(6)-S(1)	119.81(14)
C(5)-C(7)-C(6)	118.90(17)
C(5)-C(7)-C(8)	117.07(16)
C(6)-C(7)-C(8)	123.99(16)
O(6)-C(8)-O(5)	122.72(17)
O(6)-C(8)-C(7)	121.15(16)
O(5)-C(8)-C(7)	116.10(16)
N(1)-C(9)-C(12)	122.52(18)
N(1)-C(9)-H(9)	118.7
C(12)-C(9)-H(9)	118.7
N(1)-C(10)-C(11)	122.27(18)
N(1)-C(10)-H(10)	118.9
C(11)-C(10)-H(10)	118.9
C(10)-C(11)-C(13)	119.81(19)
C(10)-C(11)-H(11)	120.1
C(13)-C(11)-H(11)	120.1
C(9)-C(12)-C(13)	119.96(18)
C(9)-C(12)-H(12)	120.0
C(13)-C(12)-H(12)	120.0
C(12)-C(13)-C(11)	117.30(17)
C(12)-C(13)-C(13)#5	120.7(2)

C(11)-C(13)-C(13)#5 122.0(2)

Symmetry transformations used to generate equivalent atoms:

#1 x-1,-y+3/2,z-1/2 #2 -x+2,-y+2,-z+1 #3 -x+3,-y+2,-z+2

#4 x+1,-y+3/2,z+1/2 #5 -x+2,-y+2,-z+2

Table II-4 Anisotropic displacement parameters ( $\text{\AA}^2 \times 10^3$ ) for Cu-STP-Bpy- $\text{H}_2\text{O}$ . The anisotropic displacement factor exponent takes the form:  $-2\pi^2 [ h^2 a^{*2} U^{11} + \dots + 2 h k a^* b^* U^{12} ]$

	$U^{11}$	$U^{22}$	$U^{33}$	$U^{23}$	$U^{13}$	$U^{12}$
Cu(1)	8(1)	14(1)	15(1)	0(1)	2(1)	0(1)
Cu(2)	5(1)	11(1)	13(1)	-1(1)	4(1)	0(1)
S(1)	9(1)	14(1)	12(1)	1(1)	3(1)	-1(1)
N(1)	7(1)	12(1)	15(1)	-1(1)	4(1)	-1(1)
O(1W)	13(1)	27(1)	23(1)	-7(1)	8(1)	-4(1)
O(2W)	14(1)	16(1)	19(1)	2(1)	6(1)	3(1)
O(3)	9(1)	24(1)	16(1)	3(1)	2(1)	1(1)
O(4)	10(1)	23(1)	24(1)	4(1)	6(1)	1(1)
O(5)	9(1)	13(1)	20(1)	0(1)	2(1)	1(1)
O(6)	9(1)	13(1)	16(1)	-1(1)	2(1)	0(1)
O(7)	13(1)	18(1)	13(1)	-3(1)	4(1)	-5(1)
O(8)	15(1)	20(1)	25(1)	4(1)	12(1)	5(1)
O(9)	18(1)	17(1)	12(1)	1(1)	2(1)	-4(1)
C(1)	10(1)	14(1)	18(1)	-1(1)	2(1)	1(1)
C(2)	8(1)	15(1)	16(1)	-1(1)	2(1)	0(1)
C(3)	11(1)	18(1)	17(1)	2(1)	4(1)	-1(1)
C(4)	9(1)	14(1)	14(1)	1(1)	2(1)	1(1)
C(5)	11(1)	17(1)	16(1)	3(1)	3(1)	-1(1)
C(6)	9(1)	12(1)	13(1)	-1(1)	3(1)	-1(1)
C(7)	8(1)	13(1)	13(1)	0(1)	2(1)	0(1)
C(8)	7(1)	13(1)	13(1)	2(1)	2(1)	0(1)
C(9)	10(1)	18(1)	20(1)	5(1)	7(1)	2(1)
C(10)	9(1)	28(1)	20(1)	7(1)	4(1)	0(1)
C(11)	9(1)	35(1)	21(1)	9(1)	6(1)	1(1)
C(12)	9(1)	20(1)	21(1)	6(1)	6(1)	2(1)
C(13)	7(1)	16(1)	17(1)	0(1)	5(1)	-1(1)

### Appendix III Crystallographic Information of Cu-STP-Bpy

Table III-1 Crystal data and structure refinement for Cu-STP-Bpy.

Identification code	Cu-STP-Bpy	
Empirical formula	C <sub>26</sub> H <sub>14</sub> Cu <sub>3</sub> N <sub>2</sub> O <sub>14</sub> S <sub>2</sub>	
Formula weight	833.13	
Temperature	500(2) K	
Wavelength	0.77490 Å	
Crystal system	Monoclinic	
Space group	<i>P</i> 2 <sub>1</sub> / <i>c</i>	
Unit cell dimensions	<i>a</i> = 10.075(5) Å	$\alpha = 90.000(5)^\circ$
	<i>b</i> = 12.806(5) Å	$\beta = 95.342(5)^\circ$
	<i>c</i> = 19.502(5) Å	$\gamma = 90.000(5)^\circ$
Volume	2505.2(17) Å <sup>3</sup>	
Z	4	
Density (calculated)	2.209 Mg/m <sup>3</sup>	
Absorption coefficient	3.409 mm <sup>-1</sup>	
F (000)	1660	
Crystal size	0.12 × 0.09 × 0.03 mm <sup>3</sup>	
Theta range for data collection	2.96 to 22.79 °	
Index ranges	-10 ≤ <i>h</i> ≤ 10, -12 ≤ <i>k</i> ≤ 12, -19 ≤ <i>l</i> ≤ 19	
Reflections collected	23264	
Independent reflections	2610 [ <i>R</i> (int) = 0.0959]	
Completeness to theta = 22.79°	99.8 %	
Absorption correction	Semi-empirical from equivalents	
Max. and min. transmission	1.000 and 0.750	
Refinement method	Full-matrix least-squares on <i>F</i> <sup>2</sup>	
Data / restraints / parameters	2610 / 0 / 412	
Goodness-of-fit on <i>F</i> <sup>2</sup>	1.067	
Final R indices [ <i>I</i> > 2σ( <i>I</i> )]	<i>R</i> <sub>1</sub> = 0.0685, <i>wR</i> <sub>2</sub> = 0.1887	
R indices (all data)	<i>R</i> <sub>1</sub> = 0.1000, <i>wR</i> <sub>2</sub> = 0.2155	
Largest diff. peak and hole	2.649 and -0.977 e.Å <sup>-3</sup>	

Table III-2 Atomic coordinates ( $\times 10^4$ ) and equivalent isotropic displacement parameters ( $\text{\AA}^2 \times 10^3$ ) for Cu-STP-Bpy. U(eq) is defined as one third of the trace of the orthogonalized  $U^{ij}$  tensor.

	x	y	z	U(eq)
Cu(1)	227(2)	1494(2)	5642(1)	60(1)
Cu(2)	3152(2)	6437(1)	4028(1)	55(1)
Cu(3)	-5000	0	5000	44(1)
Cu(4)	0	5000	5000	50(1)
S(1)	-1904(4)	548(3)	4559(2)	48(1)
S(2)	2943(4)	4306(3)	4234(2)	50(1)
N(1)	1007(13)	4940(9)	5870(6)	49(3)
N(2)	-4267(11)	-198(9)	5918(6)	46(3)
O(1)	2264(9)	5239(7)	4413(4)	47(2)
O(2)	3237(11)	3653(8)	4799(6)	72(3)
O(3)	3984(10)	4594(9)	3860(6)	73(3)
O(4)	-1513(10)	1214(8)	5122(5)	61(3)
O(5)	848(10)	-144(8)	5749(5)	57(3)
O(6)	-4558(9)	1525(7)	5180(4)	46(2)
O(7)	-3534(10)	2990(7)	5119(4)	51(2)
O(8)	-2811(10)	-210(7)	4723(5)	55(3)
O(9)	960(10)	1999(8)	4869(5)	54(3)
O(10)	-425(16)	1532(12)	6508(6)	100(5)
O(11)	1624(17)	1686(12)	6516(6)	109(5)
O(12)	179(10)	3505(7)	5021(4)	45(2)
O(13)	2393(11)	6175(9)	3088(5)	60(3)
O(14)	4062(12)	7081(9)	3325(5)	73(3)
C(1)	1803(16)	1271(11)	8004(9)	57(4)
C(2)	1793(14)	1350(10)	8691(6)	40(3)
C(3)	-2818(13)	1315(10)	3943(7)	40(3)
C(4)	-3320(18)	1654(11)	2107(8)	52(4)
C(5)	-2693(14)	1201(11)	3290(7)	44(3)
C(6)	-3745(13)	1959(10)	4165(6)	41(3)
C(7)	-3484(14)	1713(11)	2817(6)	42(3)
C(8)	-3942(13)	2163(11)	4902(7)	39(3)
C(9)	-3261(15)	-803(11)	6067(7)	53(4)
C(10)	-4708(15)	369(11)	6418(7)	51(4)
C(11)	-4155(17)	335(12)	7043(7)	59(4)
C(12)	-2650(15)	-843(12)	6711(7)	57(4)
C(13)	-3077(14)	-251(11)	7211(7)	46(4)
C(14)	-2396(15)	-220(11)	7882(7)	48(4)
C(15)	1140(16)	4463(12)	7003(7)	57(4)
C(16)	839(15)	3102(11)	3946(7)	46(4)
C(17)	-126(17)	2678(13)	3522(8)	66(5)
C(18)	813(19)	1703(12)	7583(7)	59(4)
C(19)	-4541(16)	2482(11)	3695(7)	55(4)
C(20)	-4396(17)	2329(13)	3021(7)	59(4)
C(21)	-139(19)	2811(14)	2853(8)	71(5)
C(22)	2936(16)	5153(14)	6589(8)	66(5)
C(23)	2188(17)	5232(13)	5977(7)	64(5)
C(24)	479(15)	4546(12)	6395(7)	54(4)
C(25)	702(13)	2880(11)	4681(6)	36(3)
C(26)	730(30)	1636(13)	6810(10)	76(5)

Table III-3. Bond lengths [Å] and angles [°] for Cu-STP-Bpy.

---

Cu(1)-O(9)	1.855(9)
Cu(1)-O(10)	1.868(12)
Cu(1)-O(4)	1.975(10)
Cu(1)-O(11)	2.120(14)
Cu(1)-O(5)	2.193(10)
Cu(1)-C(26)	2.29(2)
Cu(2)-O(7)#1	1.825(8)
Cu(2)-O(14)	1.907(10)
Cu(2)-O(13)	1.948(9)
Cu(2)-O(1)	1.960(9)
Cu(2)-C(4)#2	2.253(15)
Cu(2)-S(2)	2.769(4)
Cu(3)-N(2)	1.889(12)
Cu(3)-N(2)#3	1.889(12)
Cu(3)-O(6)	2.026(9)
Cu(3)-O(6)#3	2.026(9)
Cu(3)-O(8)#3	2.334(10)
Cu(3)-O(8)	2.334(10)
Cu(4)-N(1)#1	1.895(13)
Cu(4)-N(1)	1.895(13)
Cu(4)-O(12)#1	1.923(9)
Cu(4)-O(12)	1.923(9)
S(1)-O(5)#4	1.372(10)
S(1)-O(8)	1.390(10)
S(1)-O(4)	1.416(10)
S(1)-C(3)	1.747(13)
S(2)-O(3)	1.381(11)
S(2)-O(2)	1.394(12)
S(2)-O(1)	1.437(10)
S(2)-C(2)#5	1.714(14)
N(1)-C(23)	1.246(19)
N(1)-C(24)	1.299(18)
N(2)-C(9)	1.287(17)
N(2)-C(10)	1.325(17)
O(5)-S(1)#4	1.372(10)
O(6)-C(8)	1.187(15)
O(7)-C(8)	1.200(15)
O(7)-Cu(2)#1	1.825(8)
O(9)-C(25)	1.207(15)
O(10)-C(26)	1.26(2)
O(11)-C(26)	1.12(2)
O(12)-C(25)	1.192(16)
O(13)-C(4)#2	1.209(17)
O(14)-C(4)#2	1.204(17)
C(1)-C(2)	1.35(2)
C(1)-C(18)	1.35(2)
C(2)-C(16)#6	1.324(19)
C(2)-S(2)#6	1.714(14)
C(3)-C(5)	1.298(19)
C(3)-C(6)	1.347(18)
C(4)-O(14)#7	1.204(17)
C(4)-O(13)#7	1.209(17)
C(4)-C(7)	1.41(2)
C(4)-Cu(2)#7	2.253(15)

C(5)-C(7)	1.334(19)
C(6)-C(19)	1.340(18)
C(6)-C(8)	1.492(18)
C(7)-C(20)	1.30(2)
C(9)-C(12)	1.346(19)
C(10)-C(11)	1.29(2)
C(11)-C(13)	1.34(2)
C(12)-C(13)	1.34(2)
C(13)-C(14)	1.42(2)
C(14)-C(22)#8	1.30(2)
C(14)-C(15)#8	1.33(2)
C(15)-C(24)	1.31(2)
C(15)-C(14)#9	1.33(2)
C(16)-C(2)#5	1.324(19)
C(16)-C(17)	1.33(2)
C(16)-C(25)	1.481(19)
C(17)-C(21)	1.31(2)
C(18)-C(21)#6	1.30(2)
C(18)-C(26)	1.50(2)
C(19)-C(20)	1.349(19)
C(21)-C(18)#5	1.30(2)
C(22)-C(14)#9	1.30(2)
C(22)-C(23)	1.35(2)

O(9)-Cu(1)-O(10)	157.6(6)
O(9)-Cu(1)-O(4)	92.7(4)
O(10)-Cu(1)-O(4)	95.7(6)
O(9)-Cu(1)-O(11)	109.1(5)
O(10)-Cu(1)-O(11)	62.2(6)
O(4)-Cu(1)-O(11)	157.7(5)
O(9)-Cu(1)-O(5)	106.2(4)
O(10)-Cu(1)-O(5)	93.5(5)
O(4)-Cu(1)-O(5)	96.2(4)
O(11)-Cu(1)-O(5)	82.7(5)
O(9)-Cu(1)-C(26)	135.4(7)
O(10)-Cu(1)-C(26)	33.2(6)
O(4)-Cu(1)-C(26)	128.8(7)
O(11)-Cu(1)-C(26)	29.0(6)
O(5)-Cu(1)-C(26)	87.0(5)
O(7)#1-Cu(2)-O(14)	114.0(4)
O(7)#1-Cu(2)-O(13)	163.2(4)
O(14)-Cu(2)-O(13)	64.6(4)
O(7)#1-Cu(2)-O(1)	91.7(4)
O(14)-Cu(2)-O(1)	151.8(4)
O(13)-Cu(2)-O(1)	94.2(4)
O(7)#1-Cu(2)-C(4)#2	144.8(5)
O(14)-Cu(2)-C(4)#2	32.3(5)
O(13)-Cu(2)-C(4)#2	32.4(5)
O(1)-Cu(2)-C(4)#2	123.5(5)
O(7)#1-Cu(2)-S(2)	106.1(3)
O(14)-Cu(2)-S(2)	125.4(4)
O(13)-Cu(2)-S(2)	86.4(3)
O(1)-Cu(2)-S(2)	29.6(3)
C(4)#2-Cu(2)-S(2)	106.1(4)
N(2)-Cu(3)-N(2)#3	180.000(2)

N(2)-Cu(3)-O(6)	84.5(4)
N(2)#3-Cu(3)-O(6)	95.5(4)
N(2)-Cu(3)-O(6)#3	95.5(4)
N(2)#3-Cu(3)-O(6)#3	84.5(4)
O(6)-Cu(3)-O(6)#3	180.000(1)
N(2)-Cu(3)-O(8)#3	95.2(4)
N(2)#3-Cu(3)-O(8)#3	84.8(4)
O(6)-Cu(3)-O(8)#3	92.7(4)
O(6)#3-Cu(3)-O(8)#3	87.3(4)
N(2)-Cu(3)-O(8)	84.8(4)
N(2)#3-Cu(3)-O(8)	95.2(4)
O(6)-Cu(3)-O(8)	87.3(4)
O(6)#3-Cu(3)-O(8)	92.7(4)
O(8)#3-Cu(3)-O(8)	180.000(1)
N(1)#1-Cu(4)-N(1)	180.000(3)
N(1)#1-Cu(4)-O(12)#1	84.2(4)
N(1)-Cu(4)-O(12)#1	95.8(4)
N(1)#1-Cu(4)-O(12)	95.8(4)
N(1)-Cu(4)-O(12)	84.2(4)
O(12)#1-Cu(4)-O(12)	180.000(2)
O(5)#4-S(1)-O(8)	113.0(6)
O(5)#4-S(1)-O(4)	113.3(6)
O(8)-S(1)-O(4)	112.6(6)
O(5)#4-S(1)-C(3)	106.9(7)
O(8)-S(1)-C(3)	103.6(6)
O(4)-S(1)-C(3)	106.6(6)
O(3)-S(2)-O(2)	117.5(7)
O(3)-S(2)-O(1)	108.0(6)
O(2)-S(2)-O(1)	112.1(7)
O(3)-S(2)-C(2)#5	108.0(7)
O(2)-S(2)-C(2)#5	106.0(7)
O(1)-S(2)-C(2)#5	104.4(6)
O(3)-S(2)-Cu(2)	65.7(5)
O(2)-S(2)-Cu(2)	133.8(5)
O(1)-S(2)-Cu(2)	42.3(4)
C(2)#5-S(2)-Cu(2)	116.7(5)
C(23)-N(1)-C(24)	116.0(13)
C(23)-N(1)-Cu(4)	124.2(10)
C(24)-N(1)-Cu(4)	119.8(10)
C(9)-N(2)-C(10)	118.3(13)
C(9)-N(2)-Cu(3)	121.7(10)
C(10)-N(2)-Cu(3)	119.7(10)
S(2)-O(1)-Cu(2)	108.2(5)
S(1)-O(4)-Cu(1)	132.6(6)
S(1)#4-O(5)-Cu(1)	123.0(6)
C(8)-O(6)-Cu(3)	134.4(9)
C(8)-O(7)-Cu(2)#1	135.5(9)
S(1)-O(8)-Cu(3)	128.9(6)
C(25)-O(9)-Cu(1)	118.8(9)
C(26)-O(10)-Cu(1)	92.3(13)
C(26)-O(11)-Cu(1)	84.1(15)
C(25)-O(12)-Cu(4)	134.6(9)
C(4)#2-O(13)-Cu(2)	87.8(9)
C(4)#2-O(14)-Cu(2)	89.9(10)
C(2)-C(1)-C(18)	120.1(14)

C(16)#6-C(2)-C(1)	119.2(14)
C(16)#6-C(2)-S(2)#6	120.0(10)
C(1)-C(2)-S(2)#6	120.7(12)
C(5)-C(3)-C(6)	121.1(12)
C(5)-C(3)-S(1)	121.2(11)
C(6)-C(3)-S(1)	117.4(11)
O(14)#7-C(4)-O(13)#7	117.2(14)
O(14)#7-C(4)-C(7)	122.7(16)
O(13)#7-C(4)-C(7)	120.1(15)
O(14)#7-C(4)-Cu(2)#7	57.8(8)
O(13)#7-C(4)-Cu(2)#7	59.8(8)
C(7)-C(4)-Cu(2)#7	175.3(11)
C(3)-C(5)-C(7)	121.1(13)
C(19)-C(6)-C(3)	118.4(13)
C(19)-C(6)-C(8)	116.5(12)
C(3)-C(6)-C(8)	125.1(12)
C(20)-C(7)-C(5)	118.7(12)
C(20)-C(7)-C(4)	118.9(14)
C(5)-C(7)-C(4)	122.3(14)
O(6)-C(8)-O(7)	128.5(13)
O(6)-C(8)-C(6)	116.3(12)
O(7)-C(8)-C(6)	115.0(12)
N(2)-C(9)-C(12)	121.1(13)
C(11)-C(10)-N(2)	122.1(14)
C(10)-C(11)-C(13)	121.2(14)
C(13)-C(12)-C(9)	120.5(14)
C(11)-C(13)-C(12)	116.7(13)
C(11)-C(13)-C(14)	121.5(14)
C(12)-C(13)-C(14)	121.8(14)
C(22)#8-C(14)-C(15)#8	116.0(13)
C(22)#8-C(14)-C(13)	122.7(15)
C(15)#8-C(14)-C(13)	121.2(14)
C(24)-C(15)-C(14)#9	121.7(14)
C(2)#5-C(16)-C(17)	119.7(13)
C(2)#5-C(16)-C(25)	127.0(13)
C(17)-C(16)-C(25)	113.2(13)
C(21)-C(17)-C(16)	120.2(15)
C(21)#6-C(18)-C(1)	118.9(14)
C(21)#6-C(18)-C(26)	117.3(17)
C(1)-C(18)-C(26)	123.8(17)
C(6)-C(19)-C(20)	118.7(15)
C(7)-C(20)-C(19)	122.0(14)
C(18)#5-C(21)-C(17)	121.8(16)
C(14)#9-C(22)-C(23)	119.1(15)
N(1)-C(23)-C(22)	124.8(14)
N(1)-C(24)-C(15)	122.3(15)
O(12)-C(25)-O(9)	123.6(12)
O(12)-C(25)-C(16)	119.7(12)
O(9)-C(25)-C(16)	115.9(13)
O(11)-C(26)-O(10)	121(2)
O(11)-C(26)-C(18)	123(2)
O(10)-C(26)-C(18)	116.1(19)
O(11)-C(26)-Cu(1)	66.9(13)
O(10)-C(26)-Cu(1)	54.5(10)
C(18)-C(26)-Cu(1)	170.6(18)

Symmetry transformations used to generate equivalent atoms:

#1 -x,-y+1,-z+1 #2 -x,y+1/2,-z+1/2 #3 -x-1,-y,-z+1  
 #4 -x,-y,-z+1 #5 x,-y+1/2,z-1/2 #6 x,-y+1/2,z+1/2  
 #7 -x,y-1/2,-z+1/2 #8 -x,y-1/2,-z+3/2 #9 -x,y+1/2,-z+3/2

Table III-4 Anisotropic displacement parameters ( $\text{\AA}^2 \times 10^3$ ) for Cu-STP-Bpy. The anisotropic displacement factor exponent takes the form:  $-2\pi^2 [ h^2 a^{*2} U^{11} + \dots + 2 h k a^* b^* U^{12} ]$

	$U^{11}$	$U^{22}$	$U^{33}$	$U^{23}$	$U^{13}$	$U^{12}$
Cu(1)	85(2)	70(1)	23(1)	1(1)	-8(1)	2(1)
Cu(2)	78(1)	63(1)	23(1)	-2(1)	-2(1)	-11(1)
Cu(3)	67(2)	47(2)	14(1)	2(1)	-16(1)	-6(1)
Cu(4)	82(2)	45(2)	16(1)	-2(1)	-22(1)	5(1)
S(1)	61(2)	55(2)	25(2)	0(2)	-11(2)	9(2)
S(2)	55(2)	51(2)	44(2)	5(2)	-5(2)	2(2)
O(1)	60(6)	48(6)	30(5)	-10(4)	-5(4)	-2(5)
O(2)	71(7)	66(7)	75(8)	6(6)	-20(6)	3(6)
O(3)	57(7)	69(7)	94(9)	3(6)	10(6)	1(6)
O(4)	75(7)	73(7)	31(6)	-10(5)	-16(5)	14(5)
O(5)	66(7)	67(7)	35(6)	-7(5)	-10(5)	10(5)
O(6)	72(6)	42(6)	23(5)	-2(4)	0(4)	-8(5)
O(7)	79(7)	46(6)	26(5)	-11(4)	-1(4)	-12(5)
O(8)	71(7)	53(6)	39(6)	9(5)	-5(5)	0(5)
O(9)	77(7)	51(7)	33(6)	3(5)	4(5)	13(5)
O(10)	115(11)	151(14)	30(7)	-13(7)	-9(7)	13(10)
O(11)	159(14)	145(13)	28(8)	-27(7)	33(8)	-52(11)
O(12)	82(7)	36(6)	17(5)	-3(4)	-1(5)	3(5)
O(13)	76(7)	79(8)	25(6)	8(5)	0(5)	-6(6)
O(14)	105(9)	98(9)	15(6)	-7(5)	-6(6)	-34(7)
C(1)	74(11)	43(9)	57(12)	5(8)	19(9)	3(8)
C(2)	59(9)	45(8)	16(8)	-7(6)	0(6)	-5(7)
C(3)	43(8)	33(8)	41(11)	2(6)	-15(7)	-1(7)
C(4)	80(12)	45(9)	30(11)	0(7)	-3(9)	12(8)
C(5)	50(9)	63(10)	18(9)	4(7)	1(7)	1(7)
C(6)	56(9)	43(8)	24(8)	2(7)	-1(7)	4(7)
C(7)	57(9)	61(9)	7(8)	-6(7)	-3(7)	3(8)
C(9)	72(10)	59(9)	27(9)	0(7)	-4(7)	21(8)
C(10)	57(9)	63(10)	33(9)	2(7)	2(7)	15(7)
C(11)	84(12)	64(10)	25(9)	-10(7)	-13(8)	10(9)
C(12)	72(11)	72(10)	22(9)	-4(8)	-20(7)	19(8)
C(13)	53(9)	56(9)	26(9)	3(7)	-11(7)	7(8)
C(14)	59(11)	67(10)	12(8)	-5(7)	-18(7)	2(8)
C(15)	74(12)	71(11)	23(9)	14(7)	-11(8)	-13(9)
C(16)	68(10)	43(8)	27(9)	-6(7)	0(8)	1(8)
C(17)	84(12)	86(12)	28(10)	-5(8)	3(8)	-31(10)
C(18)	104(13)	56(10)	16(9)	-5(7)	7(9)	4(10)
C(19)	88(11)	56(9)	19(9)	4(7)	-3(8)	17(8)
C(20)	85(12)	71(11)	17(9)	12(7)	-10(7)	4(10)
C(21)	99(13)	82(12)	29(10)	-4(8)	-9(9)	-26(11)
C(22)	59(10)	107(14)	29(10)	16(9)	-15(8)	-18(9)
C(23)	92(13)	87(12)	14(8)	13(7)	10(8)	4(10)
C(24)	51(9)	87(11)	21(8)	4(7)	-7(7)	-11(8)
C(25)	54(8)	35(9)	17(8)	11(7)	-17(6)	-4(7)
C(26)	126(19)	48(10)	55(15)	-11(9)	19(14)	6(11)